Experimental and theoretical studies of lightning arcs and their interaction with aeronautical materials

Rafael Sousa Martins

NNT : 2016SACLC080

THESE DE DOCTORAT
DE
L'UNIVERSITE PARIS-SACLAY
PREPAREE A
ÉCOLE CENTRALE PARIS

ECOLE DOCTORALE N° 579
Sciences mécaniques et énergétiques, matériaux et géosciences

Spécialité de doctorat : Energétique

Par

Rafael Sousa Martins

Experimental and theoretical studies of lightning arcs and their interaction with aeronautical materials

Thèse présentée et soutenue à Châtenay-Malabry, le 15 novembre 2016

Composition du Jury :

M. Paillol, Jean	Professeur, Université de Pau et des Pays de l'Adour	Président du Jury / Rapporteur
M. Hong, Dunpin	Professeur, Université d'Orléans	Rapporteur
M. Chemartin, Laurent	Ingénieur de Recherche, ONERA	Examinateur
M. Lago, Frédéric	Chef du Département Foudre et DES, DGA TA	Examinateur
M. Stancu, Gabi-Daniel	Maître de Conférences, CentraleSupélec	Examinateur
M. Gleizes, Alain	Directeur de Recherche CNRS, Université Paul-Sabatier	Invité
M. Soufiani, Anouar	Directeur de Recherche CNRS, CentraleSupélec	Directeur de thèse

Aos meus queridos pais e avós
e ao amor da minha vida.
Obrigado por tudo que vocês sempre fizeram
por mim e por esse amor incondicional.
Essa obra pertence a todos vocês.

Acknowledgements

Firstly, I would like to direct my sincerest thankfulness to Jean Paillol and Dunpin Hong for having accepted to review this dissertation. Equally appreciated, I would like to share my gratitude to all the members of the thesis committee, Alain Gleizes, Gabi-Daniel Stancu and Frédéric Lago for having accepted to participate on my thesis defense. All their comments and suggestions thoroughly made on the dissertation and the thesis defense were taken in consideration contributing to this final version and for future works.

Secondly, it is with my deepest gratitude I express my tribute to my thesis adviser Anouar Soufiani for his pedagogy, his knowledge, his availability and help in engaging me moving forward in this thesis on highest rigor and accuracy standards.

Fairly esteemed, I likewise designate my most virtuous appreciation to my Onera adviser Laurent Chemartin for these three years we have completed together and for his attention and his confidence on me and on my work. It was an enriching and pleasant experience working with him during these years, even though our bureau being located at different Onera sites we always found a way to exchange our ideas. Duly, I would like to thank Clément Zaepffel, who collaborated with me all along this thesis on a daily basis routine. Sometimes it was hard and tiring, nevertheless, at the end, every single effort was undoubtedly rewarded.

Conjointly, I address a genuine recognition to thank Philippe Lalande, the head of *Foudre, Plasma et Applications* (FPA) unit, who trusted me and my work, and motivated me to accomplish this thesis in the best way possible. Furthermore, I would like to thank all FPA unit, but mainly those who were closer to me during these years; Denis Packan, Paul-Quentin Elias, Julien Jarrige, Julien Labaune and Fabien Tholin. Please, accept my sincerest gratitude for you all for always being open to interesting and productive discussions, either in theoretical and experimental fields. These discussions certainly contributed with improvements to my formation and had a significant impact on this thesis.

Moreover, I am thankful to all PhD students, postdocs and interns who have shared these three years with me at Onera, especially to those who could be present at the thesis defense; Philippe Castera, Sébastien Rassou, Théo Vialis, Sara Correyero, Malik Nafa, Gautier Vilmart and Raphael Duque.

Beyond, my gratitude to the Onera's members who always gave their support, Nicolas Fdida, Nelly Dorval, François Charbonnier also to all others members of the *Département Mesures*

Physiques (DMPH). In this respect, I voice a particular gratitude to Michel Lefevre, the DMPH director, who was present at the thesis defense sharing his support.

Lastly and deservedly I utter my profoundest gratitude to Brigitte Attal-Tretout, who in the first place, brought to light the opportunity to discover Onera by sharing with me the internship offer and thereafter continuously following my thesis progress.

Finalmente, gostaria de redigir algumas poucas palavras na minha língua nativa para fazer um verdadeiro agradecimento para todos vocês que foram e continuam sendo tão importantes na minha vida e em toda essa jornada até aqui.

Primeiramente, agradeço a Deus por ter me dado saúde, força, capacidade, motivação e coragem ao longo de toda minha vida.

Em seguida, quero agradecer a todos que contribuíram de uma forma ou de outra ao longo da minha vida pessoal e acadêmica. Agradeço a todos os professores com os quais eu tive a oportunidade de conviver, ouvir, admirar, aprender, trabalhar e, obviamente em alguns (poucos) casos, irritar. Certamente cada elemento nessa sólida estrutura tem a vossa contribuição e eu serei eternamente grato. Deixo uma menção especial aos dois professores que tiveram uma significante participação no início da minha carreira acadêmica, Régis e Júlio César. Obrigado por todos os conselhos, atenção, ajuda e apoio.

Igualmente, gostaria de agradecer aos meus grandes amigos de Anápolis, de ensino médio e pré-vestibular, Douglas e Edson, pelo companheirismo, força, incentivo e amizade ao longo desses anos, mesmo que nossos encontros tenham se tornados tão raros. Da mesma forma, um obrigado aos meus colegas e amigos de Campinas, da minha turma da elétrica e de outras turmas da Unicamp, com quem eu tive o prazer e a oportunidade de compartilhar o inicio do meu ensino superior. Um abraço em especial ao meu grande irmão e companheiro de moradia, José Augusto e ao meu amigo de futebol e de moda de viola, João Paulo. Um agradecimento especial aos amigos que fiz em Bauru e que me acompanharam em grande parte dessa jornada, Hanna, Melissa, Nathália, Letícia e Tiago. Seguindo em ordem cronológica, obrigado aos meus amigos feitos em Marseille, Alessandra e Joaquim. Nós conhecemos em um momento que o simples fato de terminar a Centrale e suportar a vida do duplo-diploma já parecia algo extremamente difícil (não podíamos estar mais enganados!), e que por fim se tornaram grandes companheiros ao longo de toda essa jornada. Em Paris, na última etapa, não fiz grandes amizades na universidade ou no trabalho, mas fiz grandes amigos pelas idas e vindas do destino, Juliana e Lucas, e tios Aurea e Keko. Agradeço a vocês pelo grande companheirismo e pelas ótimas discussões científicas, técnicas, gastronômicas, sociais e, principalmente, filosóficas.

ACKNOWLEDGEMENTS

Enfim, gostaria de dedicar essa ultima parte para agradecer as minhas duas famílias.

Primeiro para a família que me "adotou" nessa praticamente uma década, a família March(qu)esini. Gostaria de dizer um muito obrigado ao Jesus, Nice e Gabriel por todo carinho e apoio durante esses anos, e especialmente ao Bruno e a Marilia que puderam estar presentes no dia da defesa para dar força, partilhar e animar esse momento tão importante. Obrigado aos que considero como meus irmãos mais novos, José Ricardo, Luiz Henrique e Maria Laura, assim como para Ana Flávia, Julia e Daniel. Obrigado pelo carinho, pelas revisões de inglês, pela animação, pelos diversos e deliciosos momentos gastronômicos e de diversão. Nesses últimos anos, saber que podíamos contar com vocês nos fins de semanas ou nos períodos de férias, era sempre uma grande motivação para continuar firme no trabalho. Enfim, um muitíssimo obrigado ao Antônio e a Matilde, por sempre me tratarem e cuidarem de mim como um filho, e os quais eu sempre considero e considerarei como pais. Vocês acompanharam grande parte da minha jornada e sempre estiveram dispostos e solícitos nos momentos importantes que passei, assim como puderam compartilhar comigo os momentos de conquista.

Para minha querida família, gostaria de agradecer primeiramente meus tios, Nair e João Paulo, Roberto e Michelle, meus tios-padrinhos, Nilza e Carlos, a minha tia e mãe de leite, Madalena, e ao meu tio Ivan. O carinho, amor e consideração que vocês tiveram comigo ao longo de toda minha vida são enormes, e eu sou, e serei sempre, extremamente grato por tudo. Obrigado igualmente aos meus irmãos e primos mais velhos, Marcos, Alexandre, Alessandra, Chrisley, Jefferson, Leandro e Luciana, assim como aos meus primos mais novos, Mário, Ginger, Gabriella, Natália, Miguel e Carlos Filho. Agradeço pelo companheirismo, conselhos, apoio e amizade, e espero que meu trabalho possa servir de inspiração a todos vocês. Um grande obrigado aos meus queridos irmãos, Rávilla Karolina, Gabriel Felipe e Daniel Luís. Por mais que eu tenha vivido longe de vocês nesses últimos anos, em um momento de tanta importância e mudança em vossas vidas, vocês são uma parte que me motiva, a cada dia, a querer vencer e ir mais longe, com o objetivo de iniciar um caminho que um dia vocês também irão trilhar e alcançar.

Obrigado aos meus avós, José Lico e Cascilda, ao meu avô Manuel, e um agradecimento especial ao avô que ganhei por volta dos meus dez anos, Sebastião Monteiro de Alarcão. Obrigado por toda sabedoria, amor e atenção ao longo desses anos. Todo teu apoio foi, certamente, fundamental para que eu me tornasse a pessoal que sou hoje. Um imenso obrigado do fundo do coração a minha avó Rita, que sempre luta e batalha pela sua família e tem um amor irrestrito a todos seus filhos e netos como se fossem únicos. Evidentemente, por ser o neto

mais velho, sou o que mais pude aproveitar e conviver com todo esse amor e carinho, que certamente me ajudou e ajuda a ser uma pessoal melhor a cada dia.

Finalmente, gostaria de agradecer meus queridos pais, Ademir e Neide, por esse amor incondicional que vocês têm por mim. A pessoa que me tornei é fruto de todo vosso esforço e dedicação. Normalmente, o filho precisa sair de casa pra enxergar o verdadeiro significado e a importância dos pais em suas vidas. Felizmente, parti cedo do ninho, e desde então a vontade de fazer vocês se sentirem orgulhosos e felizes pelo filho que criaram me guia e me motiva a cada dia.

Por último, um agradecimento mais do que especial ao amor da minha vida, Maria Cecília, que me acompanha cotidianamente desde o inicio da minha carreira acadêmica, e que foi e é fundamental no meu crescimento pessoal ao longo de todos esses anos. Esse trabalho é uma consequência direta de tudo que você fez e faz por mim e por nossas vidas. Obrigado por todos os momentos que passamos juntos e por toda força e amor que permitiram que todos esses árduos anos de estudo e trabalho tenham passado de maneira tão agradável e prazerosa. Que venham os próximos cem!

Agora, convido a todos que tenham tido a consideração e paciência de ler até aqui, para me seguir e continuarmos juntos essa aventura em uma interessante e empolgante leitura (quase mitológica) sobre aviões, raios e trovões...

Abstract

The extensive use of composite materials in aeronautical construction leads to new questions on the direct effects of lightning. While aluminum structures show limited and well-known damaging when a lightning strike occurs, carbon composite structures are associated with several complex phenomena. The understanding of these physical mechanisms is an important concern for the design and the optimization of aeronautical structures. Nowadays, the study of lightning direct effects could be possible with simulation tools, but the lack of reliable experimental database for code validation prevents this approach.

The main goal of this work is to provide an experimental database based on the characterization of standardized lightning arcs, similar to those of certification process. This database could be used for both understanding of direct effects, and for validation of lightning arc physical models.

First, the free arc channel, without interaction with electrodes, is investigated. The macroscopic properties of the arc, as the shape, the characteristic lengths, the impedance and the shock wave propagation are assessed with different experimental methods. An investigation of the temperature, electronic density, and pressure distribution within the arc column is performed using optical emission spectroscopy. A method is developed to assess time- and space-resolved properties in a non-optically thin plasma, by solving the radiative transfer equation. For a 100 kA arc, it is shown that the temperature reaches 37400 K in the arc axis at 2 µs after arc ignition, with a corresponding pressure of 45 bar.

Second, the interaction between the lightning arc and aeronautical materials is studied. The temporal dynamics and the spatial form of the arc root zones are determined for different materials, such as aluminum and carbon fiber composite. The influence of the surface coating is also considered and shows a significant impact in the arc root behavior. In the case of carbon fiber composite panels, the arc root shows a complex shape, and seems to be highly influenced by the orientation of the surface fibers. The shock wave near to the attachment point is also studied and is compared to the results obtained by the free arc column. The thermal constraints imposed by the arc on the material are discussed and rear surface temperature measurements are performed. The mechanical constraints are assessed by fast deflection measurements of the panel center, and an evaluation of the pressure that acts at this point is proposed.

Keywords: Lightning, electric arc, optical diagnostics, plasma, arc roots, aeronautical materials

Résumé

L’utilisation massive des matériaux composites dans la construction aéronautique a conduit à de nouvelles questions scientifiques dans le domaine des effets directs de la foudre. Alors que les structures en aluminium présentent des endommagements relativement modérés et répétables, les structures en composite à fibre de carbone ont un comportement très complexe vis-à-vis de cette agression. La compréhension des phénomènes est un enjeu essentiel pour optimiser ces structures et garantir leur tenue. Aujourd’hui, l’étude des effets directs de la foudre pourrait être réalisée, au moins en partie, à l’aide d’outils de simulation. Néanmoins, le manque de données expérimentales sur la phase d’arc ne permet pas de valider le caractère prédictif des outils de simulation. L’objectif de cette thèse est de réaliser une base de données expérimentale en s’appuyant sur une caractérisation des arcs de foudre dans une situation standardisée, semblable à celle employée en ingénierie aéronautique et dans le processus de certification des aéronefs contre la foudre. Ces données peuvent être utilisées pour la compréhension des phénomènes observés lors des essais, mais surtout comme référence comparable aux outils de simulation.

Dans un premier temps, on s’intéresse à la colonne d'arc libre dans l’air, hors interaction avec les électrodes. Les propriétés macroscopiques comme la forme, la taille, l’impédance, ainsi que les caractéristiques de l’onde de choc associée, sont évaluées par différentes techniques expérimentales. Les effets des conditions d’essais, comme le niveau de courant, la longueur de l’arc ou la nature du fil d’amorce sont analysés. Par ailleurs, l’évaluation des profils spatiaux et temporels de la température, de la densité électronique et de la pression à l’intérieur de la colonne d'arc est réalisée en utilisant la technique de spectroscopie d'émission. Une méthodologie a été développée pour évaluer ces profils dans le plasma sous l’hypothèse d’un milieu non optiquement mince. On retrouve, pour un arc de 100 kA, une température maximale de 37400 K sur l'axe de la colonne à 2 µs après l’amorçage, avec une pression de 45 bar.

Dans un second temps, on s’intéresse à l'interaction de l'arc de foudre avec des matériaux aéronautiques. La dynamique du pied d'arc ainsi que les caractéristiques de l’onde de choc sont analysées sur différents matériaux aéronautiques tels que de l’aluminium ou le matériau composite à fibre de carbone. L'influence de la présence du revêtement de surface est également considérée. Enfin, les contraintes thermomécaniques subies par les matériaux sont étudiées à l’aide de mesures thermographiques infra rouge, et de mesures de déflection au centre du matériau, qui ont permis une évaluation de la pression exercée par l’arc au point d’impact.

Mots-clés : Foudre, arc électrique, diagnostics optiques, plasma, pied d’arc, matériaux aéronautiques.

Resumo

O uso extensivo de materiais compósitos de fibra de carbono na construção aeronáutica nós leva a novas questões sobre os efeitos diretos dos raios em aeronaves. Enquanto estruturas em alumínio apresentam danos moderados e repetitivos, estruturas em compósitos de carbono estão associadas a diversos fenômenos complexos. A compreensão física desses mecanismos é uma das grandes preocupações durante a fase de concepção e optimização de estruturas aeronáuticas. Hoje em dia, o estudo dos efeitos diretos dos raios poderia ser possível, pelo menos em parte, com ferramentas de simulação. Entretanto, a falta de dados experimentais confiáveis impossibilita a validação de modelos e códigos, limitando assim a utilização de uma abordagem computacional. O principal objetivo deste trabalho é fornecer uma base de dados experimental baseada na caracterização dos arcos de raio padronizados, semelhantes aos utilizados no processo de certificação aeronáutica. Esta base de dados poderá ser usada tanto para à compreensão dos efeitos diretos, quanto para a validação de modelos físicos de arco de raio.

Primeiramente, o canal de arco livre, sem interação com eletrodos, é investigado. As propriedades macroscópicas desse canal, como a forma, os comprimentos característicos, a impedância e a propagação de ondas de choque são avaliados a partir de diferentes métodos experimentais. Uma investigação da distribuição de temperatura, densidade eletrônica e pressão no interior do canal do arco é realizada utilizando espectroscopia de emissão. Um método é desenvolvido para realizar uma avaliação espaço-temporal das propriedades de um plasma não-opticamente fino, a partir da solução da equação de transferência radiativa. Para um arco de 100 kA, a temperatura atinge 37400 K no eixo do canal de arco, 2 µs depois da ignição, com uma pressão correspondente de 45 bar.

Em seguida, a interação entre o arco de raio e materiais aeronáuticos é estudada. A dinâmica e a forma espacial da zona de contato do arco são determinadas para diferentes materiais, como o alumínio e os compósitos de fibra de carbono. O efeito do revestimento é igualmente considerado e apresenta um impacto significativo no comportamento do contato do arco. Em painéis compósitos de fibra de carbono, o contato do arco assume uma forma complexa, sendo altamente influenciado pela orientação das fibras. A onda de choque perto do ponto de contato do arco também é estudada e comparada aos resultados obtidos para o canal de arco livre. Os estresses térmicos impostos pelo arco no o material são discutidos e medições de temperatura de superfície são realizadas usando termografia infravermelha. Os estresses mecânicos são avaliados por meio de medidas de deflexão rápida, permitindo a dedução da pressão exercida.

Palavras-chaves: Raio, arco elétrico, diagnósticos óticos, plasma, materiais aeronáuticos.

Table of Contents

Chapter V. Temperature, electron density and pressure profile determination of the free lightning arc during the high current phase using optical emission spectroscopy

Chapter VI. Characterization of the interaction between the transient lightning arc and aeronautical materials

Introduction

Lightning is a natural atmospheric phenomenon which is a result of the electrical activity of thunderclouds. Aeronautics is highly concerned about this phenomenon, once, on average, an aircraft can expect roughly one lightning strike every 1500 flight hours. Lightning is a possible safety hazard for aircraft, through different types of direct effects on aeronautical structures, such as thermo-mechanical constraints, and also with indirect effects, such as electromagnetic coupling with the aircraft's systems and cables. Most modern aircraft are designed to operate regardless the atmospheric conditions and, even if a lightning strike occurs, they must preserve their flyability, offering total security to the crew and passengers. The protection against lightning is based on standards and certification processes that specify and justify lightning protection requirements, and validate the implementation on aircraft.

Recently, fuel saving and greenhouse gas emission reductions became major concerns for the automotive and aircraft industries. To achieve these objectives, one of the current ways considered is the reduction of the vehicle's weight by using lighter materials. In aeronautics, the replacing of metallic materials, mainly used on previous aircraft generations, by the carbon fiber composite materials, which are lighter and show outstanding mechanical properties, accomplishes this weight reduction. The recent airliner programs, as the Boeing 787 Dreamliner and the Airbus A350XWB, employ carbon fiber composite in around 50% of the aircraft weight. They are used in zones highly exposed to the lightning strike such as fuselages and wings, which leads to new concerns. The carbon fiber composites are more vulnerable to the lightning constraints, once their thermal and electrical conductivity are lower than metals'. Therefore, additional lightning protection solutions must be adopted and yet the most common is the use of a metallic mesh on the surface of the composite parts. However, the implementations of these extra protections and their certification have an impact on the aircraft weight, the design manufacturing costs and the program delay. For instance, after having solved some lightning problems associated to fasteners, Airbus Operations was able to increase its production rate by 30% on the A350XWB program.

The evaluation of the lightning mechanical and thermal constraints for engineering purposes requires a deep understanding of the physical phenomena involved in lightning arcs. The knowledge of these constraints serves as a basis for aircraft manufacturers for optimization of aeronautical protections, and in the same time, it may help for the cost reduction by avoiding the need to perform numerous lightning tests for certification. In addition to these objectives, there

is a progressive need for reliable computational tools able to better predict the behavior of lightning arcs. Simulation codes require inputs and validations taken from experimental databases. Nevertheless, sufficient and accurate data is yet missing for high current arcs. The lack of understanding is principally related to the transient phase of the lightning arc, which can reach thousands of amperes in a few microseconds.

In order to answer the scientific needs, the present study consists of developing methods and experimental diagnostics, to obtain physical properties of lightning arc plasma and its interaction with aeronautical materials. The main quantities considered to be important to analyze and characterize can be separated into three groups. First, we study the macroscopic properties of the arc column, as the shape, the characteristic lengths, the shock wave propagation induceed by the arc expansion and the effect of the material on those quantities. Second, we characterize the electrical properties of the arc column, such as the arc resistance, the plasma conductivity and the electric power loss in the arc column. Finally, we assess the intensive thermodynamic properties as the temperature, the electronic density and the pressure distribution of the arc column. All these information will serve to build an experimental database for the understanding of the phenomenon, comparison and model validation.

Concisely, the study aims to answer the following questions:

- How is the evolution over time of the lightning arc? What is its size and shape? Is there an influence of the current level? Is there a strong shock wave induced by the arc expansion? What are the characteristics of this wave?
- What are the arc electrical characteristics? How the conductivity varies with time? What electrical energy does the lightning arc absorb?
- What are the temperature and pressure distributions of the arc columns? How do they change with time and with the arc current?
- Are there some differences between a free arc column and an arc interacting with aeronautical materials? How do the arc properties change when applied to different materials and surface coatings?

The dissertation is structured into six chapters as follows:

Chapter I is dedicated to a general overview of lightning and the lightning strike in the aeronautical context. We briefly describe the aircraft lightning protection processes, and we present an overview of previous studies on lightning arcs, which covers both theoretical and experimental studies. We present the main objectives of this work as a conclusion of this chapter.

Chapter II is devoted to the description of the experimental tools used to achieve the objectives. We present the lightning current generator utilized to create the transient lightning arcs studied in this work. Furthermore, we introduce the employed electrical and optical diagnostics, and also their main characteristics and limitations.

Chapter III investigates the hydrodynamic properties of the free arc channel. The study includes the characterization of macroscopic quantities, as the evolution over time of the channel arc shape, the luminous arc radius, the propagation of the shock wave induced by the arc expansion and the mass density distribution in the shock wave.

Chapter IV deals with the characterization of the electrical properties of the lightning arc. The geometry and the evolution over time of the arc shape, obtained in Chapter III, are used to develop an electrical model for the arc. This model allows us to determine the time-dependent impedance of the arc and the estimation of other useful characteristics, as the electrical conductivity, and the power and energy loss by Joule effect in the arc column.

Chapter V is dedicated to the study of the intensive thermodynamic properties of the lightning arc. Optical emission spectroscopy is employed to assess space- and time-resolved properties that include temperature, electron density and pressure distribution of the arc column. The absorption coefficients of nitrogen and oxygen ionic lines are calculated, and the radiative transfer equation is solved across the arc column. The pressure within the arc is estimated using the determined temperature and electron density profiles. These results are utilized to estimate the electrical conductivity of the arc column, to have it compared to the results obtained in chapter IV.

Chapter VI investigates the interaction between the high current arc and aeronautical materials. Different materials and surface coatings are analyzed, and many physical properties and constraints of this interaction are studied, which includes: the temporal dynamics and spatial shape of the arc roots, the shock wave propagation near to the attachment point and the thermo-mechanical constraints imposed by the arc on the material.

Chapter I.

Overview of lightning strike to aircraft

In this chapter, we present a general overview of lightning and the lightning strike in the aeronautical context. Furthermore, the processes of aircraft lightning protection are briefly descripted, as well as the main physical phenomena of lightning arcs. Then, we present an overview of previous studies on lightning arcs, which covers both theoretical and experimental studies. Finally, the main objectives of this work are presented and summarized.

I.1 Lightning overview

Lightning is a natural and atmospheric transient, high current electrical discharge, having a path length which is normally expressed in kilometers and attempts to equalize regions of opposite electrical charges (Rakov and Uman (2003); Bazelyan and Raizer (2000)). In the following sections we briefly present an introduction to the main features of the lightning phenomenon.

I.1.1 Historical introduction

Lightning are present on Earth since long before the appearance of life. It is even possible that lightning played an important role in the creation of organic molecules necessary for the formation of every life form (Rakov and Uman (2003)). The first interactions of early humans with lightning were certainly fascinating and terrifying. Since the ancient Egypt, going through Greeks, Scandinavians, Indian tribes of North America and southern Africa, until arrive to the middle ages, all those ancient civilizations incorporated lightning and thunder in their religious beliefs (Rakov and Uman (2003); Cooray (2015)). During the middle ages, lightning had been considered as a divine expression, a scary phenomenon against which people had only two alternatives for protections; the pray and the ringing of the church bells. Ironically, churches were often struck by lightning because of the high elevation of their towers (Becerra (2008)). It was only in 1752 that Benjamin Franklin provides the first scientific evidence that thunderclouds contain electricity, even if many scientists had previously noted the similarity between laboratory sparks and lightning. In that year, he published the first instructions of a lightning protection system, often referred to as Franklin's rod system or as lightning rod, which is a rod or object made of metal, installed on the top of elevated structures. An ample and interesting overview of the historical aspects and scientific progress involving lightning can be found in the literature (Rakov and Uman (2003); Becerra (2008); Cooray (2015)). The electricity presents in thunderclouds is the origin of the lightning phenomenon. The formation and electrification of thunderclouds was the subject of many studies. In the next section we give a short discussion of the main aspects of the thunderclouds.

I.1.2 Thundercloud formation and electrification

Thunderclouds, also known as *cumulonimbus*, are the result of atmospheric instabilities that causes air convections, combined with a significant level of humidity. Warm and moist parcels of air rise in the inner of cold air mass due their low density. During the parcel's rise, condensation of water vapor cause the formation of water droplets, and the continuous reduction of temperature in the vertical direction induces the development of ice crystals.

The different phase changes of water, changing to liquid and then to solid state, release energy through latent heat, which supplies the upward motion of convective currents, resulting in the formation of the thundercloud. The upward convection can reach speeds of the order of 5 to 35 m s^{-1}, which causes the expansion of the thundercloud by raising the lighter hydrometeors[1] up (Stolzenburg and Marshall (2008)). The vertical thundercloud development is stopped above the tropopause (around 8 to 16 km, depending on latitude) by the significant horizontal winds of the stratosphere combined with the increase of the temperature in this portion of the atmosphere (Marshall et al. (1989)). The maturity stage of the thundercloud is associated with heavy rainfall, and the appearance of lightning flashes reaches its maximum frequency. The dissipation stage occurs when the upward convection is no longer strong enough to support the hydrometeors suspended in the cloud, and the electrical activity of the storm fade. The air temperature in the thundercloud ranges from about -60 °C in higher altitudes to around 5 °C at its base (Malan and Schonland (1951)).

The presence of electric charges in thunderclouds occurs as a result of complex processes of freezing and melting, and by collisions and splintering (MacGorman and Rust (1998)). Currently, there are a variety of hypotheses for the thundercloud electrification phenomenon, but the most accepted ones involve rebounding collisions between ice crystals and graupel pellets (Schoene (2007); Soula (2012)). In the graupel-ice mechanism, the lighter particles that rise come into collisions with heavier particles that have a downward motion. During the collisions, a charge exchange takes place. The sign and the amount of transferred charge depend on two parameters; the ambient temperature and the liquid water content of the hydrometeor (Takahashi (1978)). After the collision, the particle is charged positively for warmer temperatures and for either very high or low cloud liquid water content. Conversely, this is charged negatively for colder temperatures and for the mid-range of cloud liquid water content. Each transferred electric charge is estimated to about 33 fC (Takahashi (1978)).

Generally, most positive charges accumulate at the top of the thunderclouds and the lower regions are formed by negative charges, producing a positive dipole structure, although there may be a small positive region near the base (Stolzenburg and Marshall (2008)). The result is the typical structure presented in Figure I.1 depicted by Malan and Schonland (1951), which produces a vertical electric field.

[1]Any product of condensation or deposition of atmospheric water vapor, whether formed in the free atmosphere or at the earth's surface (*American Meteorological Society (2012)*)

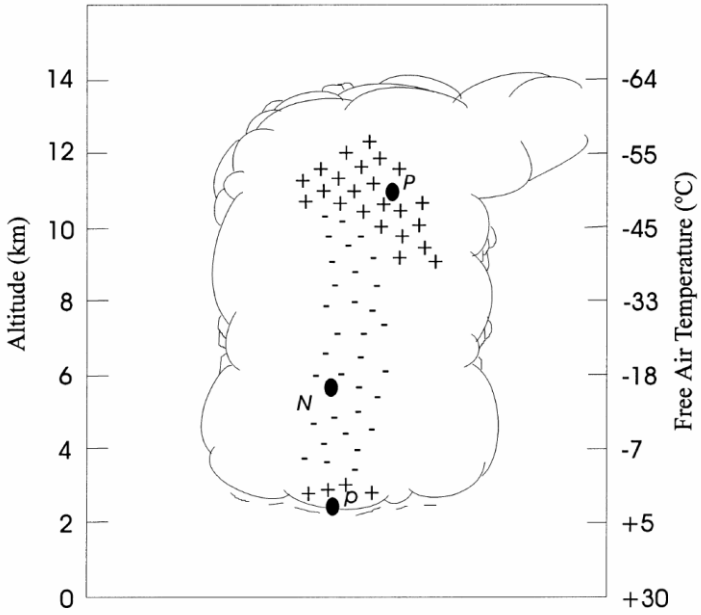

Figure I.1. Generalized diagram showing distribution of electrical charge in a typical cumulonimbus cloud (ARP5412A (2005)). 'P' indicates the positive charge regions and 'N' indicates the negative ones.

I.1.3 Lightning initiation and development

As most of electrical sparks, lightning is initiated via an electron avalanche that occur when energetic electrons are accelerated by electric fields to velocities sufficient to produce new energetic electrons during ionizing collisions with nitrogen or oxygen molecules. For the case of thunderstorm, Marshall et al. (1995) suggested that the condition required to induce the avalanche is a thunderstorm electric field higher than a critical value, called the breakeven field. Although the field strength for dielectric breakdown in dry air at ambient pressure is about 3 MV m^{-1}, the breakeven field is considerable lower at any altitude. It is estimated equal to 200 kV m^{-1} at ground level and decreases with the increase of altitude. Using balloon-borne electric field meters, Marshall et al. (1995) measured thunderstorm electric fields as a function of altitude. They correlated the maximum value reached by the electric field for a given altitude with the occurrence of lightning flashes. Figure I.2 shows an example of measured electric field. The two vertical curves, that enclose the electric field, represent the breakeven field, which can be written as $E_{be}(z) \approx \pm 200\exp(-z/8.4)$, where E_{be} is the breakeven field in kV m^{-1} and z is the altitude in kilometers. The measurements have shown that the electric field in the cloud is rarely higher than that given by the breakeven curve. When this value approaches to the critical field, a lightning flash occurs and reduces the thundercloud electric field.

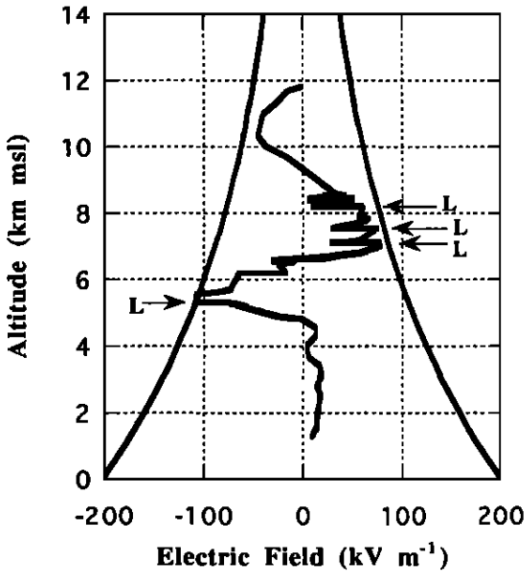

Figure I.2. Thundercloud electric field and breakeven field as a function of altitude. Each "L" marks a horizontal discontinuity in electric field produced by a lightning flash occurrence (Marshall et al. (1995)).

There are two most accepted hypotheses to explain how lightning flashes can occur while the thundercloud electric field is approximately fifteen times lower than the threshold for dielectric breakdown of dry air. The first one suggests that the water droplets and hydrometeor shapes present in the thundercloud locally enhance the electric field (Solomon et al. (2001); Cooray (2015)). A recent study performed by Rison et al. (2016), investigated high-power discharges inside the thundercloud, known as narrow bipolar events (NBEs), by measurements of its VHF (Very High Frequency, from 30 to 300 MHz) radiation. They reported that a system of positive streamers in a locally intense electric field seems to be the main cause of lightning flashes initiation. The second mechanisms is called runaway breakdown. The presence of high-energy electrons, originated from cosmic rays or terrestrial sources of ionizing radiation, accelerated over long distances in the thundercloud electric fields give rise to new runaway electrons, triggering the avalanche effect (Gurevich et al. (1999); Solomon et al. (2001)).

Theoretical and experimental studies of the physical processes that occur during the development of lightning flashes indicate that lightning originates from a bi-directional leader propagation, which remains a zero-net-charge channel (Kasemir (1960); Mazur and Ruhnke (1998); Mazur (2002)). From the lightning initiation zone, a positive electrical discharge, called positive leader, propagates in the direction of the thundercloud electric field to a negatively charged region, while a negative discharge (negative leader) propagates in the opposite direction, towards a positively charged regions. The bi-directional propagation speed is estimated to approximately 10^5 m s^{-1} for both negative and positive leaders

(Mazur and Ruhnke (1998)). The leader propagation creates a conductive path and produces a current of a few hundred amperes inside the channel. For the case of a bi-directional propagation between a thundercloud and the ground, the negative leader that propagates toward the ground is called stepped leader. When the leader reaches the ground, establishing the connection with the thundercloud, a high pulsed current, known as return stroke, takes place. The return stroke moves from the ground toward the thundercloud charged region and its current can reach thousands of amperes in a few microseconds. This pulsed current is followed by a continuous phase, with a current in the order of a few hundred amperes and duration of some hundreds of milliseconds. During the continuous phase, once the high conductive channel is established, others pulsed currents generally occur (Rakov and Uman (2003)). Figure I.3 shows the development of the bi-directional leader for the case of a *negative ground lightning* (see section I.1.4).

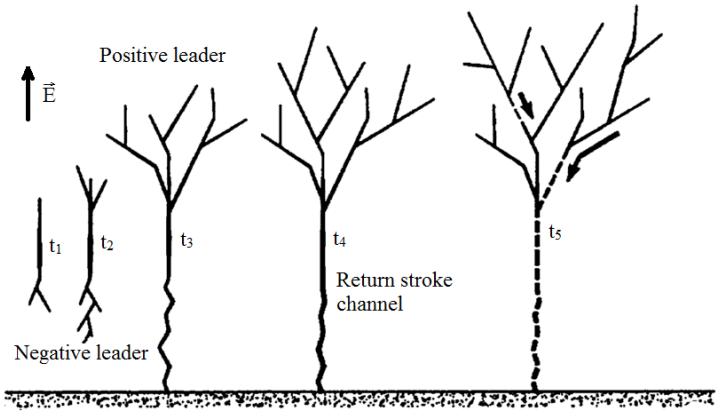

Figure I.3. Development of a bi-directional, bi-polar lightning 'tree' made of positive leaders above and negative leaders below for a negative ground lightning (Mazur (2002)). The different instants t_i illustrate the progression of the leaders.

I.1.4 Classification of lightning flashes

There are different types of lightning flashes. They can be classified depending on the regions between which the lightning takes place and the polarity of the charge transferred from one region to another. The most common occurs between two charged regions inside a single thundercloud and is called *intracloud lightning* (IC). The lightning flash may arise between opposite charged regions of two different clouds, and in this case it is known as *intercloud lightning* (CC). When a lightning flash takes place between cloud and ground, this is called *cloud-to-ground lightning* (CG). This category of lightning is also classified by the polarity of the transported charges. Around 90% of lightning flashes that strike ground come from the negative charged regions of clouds, and are named *negative ground lightning* (-CG). The others 10% are called *positive ground lightning* (+CG) and come from the positive charged regions of

cloud (Rakov and Uman (2003); Cooray (2015)). Figure I.4 illustrate the different types of lightning flashes.

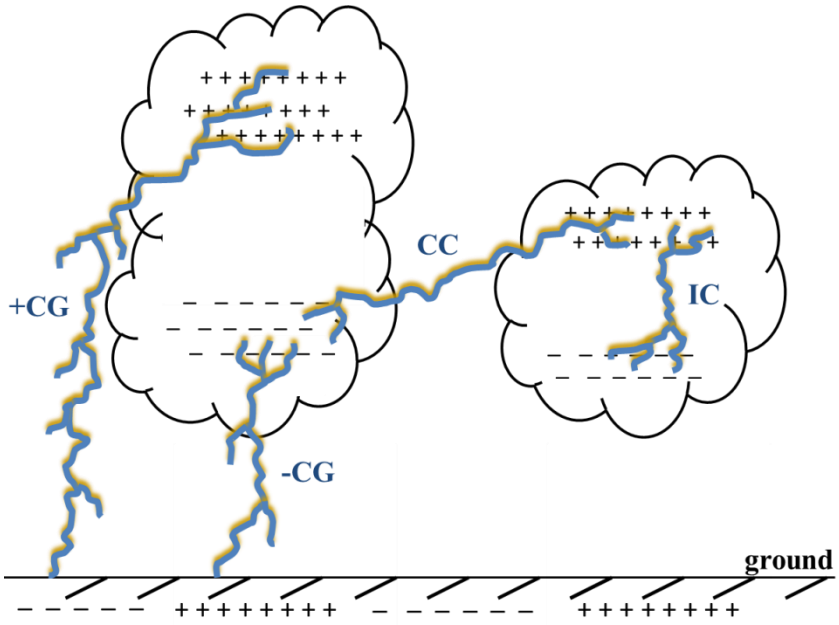

Figure I.4. Illustration of four types of lightning flashes.

The precise distribution of the electrical activity of thunderclouds remains unclear. The investigations of the partitioning of lightning flashes (IC and GC flashes compared to total electrical activity) are the subject of many studies (Christian et al. (1992); Boccippio et al. (2001); Christian et al. (2003)). As an example, the ratio IC/GC, known as Z ratio, may depend of several factors, as latitude, longitude, storm morphology and electrical parameters. Boccippio et al. (2001) reported the Z ratio obtained from observations made during four years over the continental United States. The average value over this region was between 2.64 to 2.94, with a peak as high as 9 in the central-upper Great Plains, and values as low as 1 or less over the Rocky and Appalachian Mountains.

I.2 Lightning strike to aircraft

Statistical in-flight analysis on airliner shows that the average probability of a lightning strike to a given aircraft is somewhere between one strike per 1000 and 10000 flight hours (Fisher et al. (1988); Jones et al. (2001)). This probability depends on different parameters; the local climate, flight profile, type of aircraft, etc. For a commercial airliner, this is roughly equivalent to one lightning strike each year. These data are based on reported strikes, which are noticed due to atypical incidents as the bright light, especially at night, the loud noises, or the associated

physical damage effects, interference and damage to cockpit avionics. Other strikes to aircraft certainly occur, however, they are unnoticed or are not reported (ARP5412A (2005)).

The problematic of lightning strike to aircraft presents some differences compared to lightning strike to grounded structures. In both cases, the shape of the stroked object locally enhances the electric field. In the case of an aircraft, the amplification coefficient of the electric field, defined by the ratio of the local field over the ambient atmospheric field, may reach 5 to 10 at the extremities, as for instance at the wings and stabilizers tips, or at the fuselage zone, as illustrated in figure I.5. It could initiate corona discharges and eventually a positive leader is initiated.

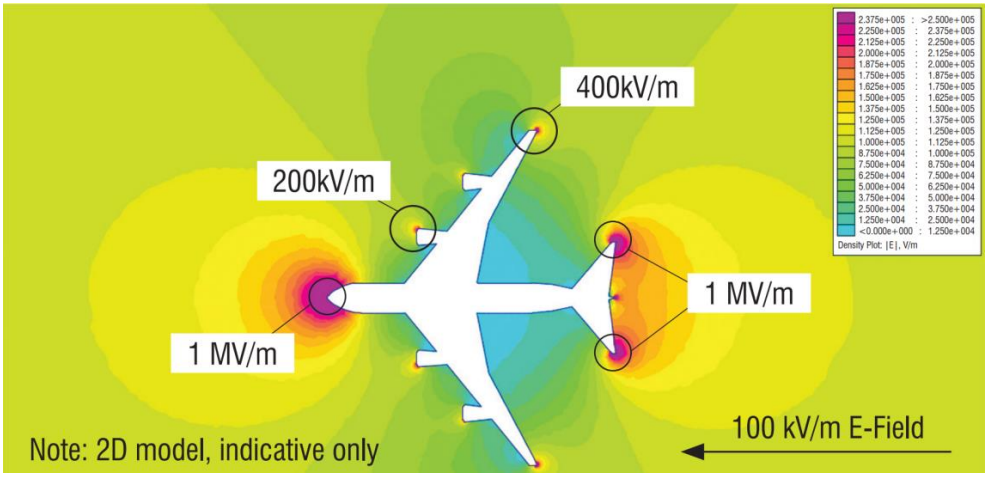

Figure I.5. Indicative 2D electrostatic model of an aircraft in a 100 kV m^{-1} ambient field calculated by Morgan et al. (2012).

The differences with grounded structures come from the floating and conductive characteristics of aircraft in flight. First, the aircraft must be a part of the global lightning current path; it cannot accumulate the transferred charges during the lightning flash. As a result, there are at least two conductive paths connected to the aircraft during the flash. Moreover, as a floating conductive body, the aircraft accumulates static charges from hydrometeors and by triboelectric charging. In some cases, if the electric potential is not perfectly equal over the aircraft surface (dielectric layers, radome, etc.), it could be locally polarized, with positively charged zones and negatively charged zones.

There are two main situations of lightning strike to aircraft. The most frequent case, corresponding to approximately 90% of events, is the lightning triggered by the presence of an aircraft. During the propagation of the positive leader, the aircraft becomes negatively charged, which causes the negative leader to trigger at an opposing extremity. This bi-directional leader constitutes the beginning of a lightning flash (Lalande et al. (1999); Larsson et al. (2000a)). The second case is the interception by the aircraft of a branch of a natural lightning

(Lalande et al. (1999)). The two mentioned cases correspond to the phase of lightning initiation, and can last for a few microseconds. This phase of initiation is then followed by the lightning high current phase, with typical duration from tens to hundreds of milliseconds. This phase is characterized by the displacement along the aircraft of the lightning attachment point and the occurrence of the different high current components of the lightning flash. The different phases are described in the following subsections.

I.2.1 Aircraft lightning initiation

A characteristic of both lightning triggered or intercepted by aircraft is that the lightning strike starts with the development of a positive discharge from the aircraft, followed by, a few milliseconds later, the inception of a negative discharge propagating in the opposite direction, forming a bi-directional leader (Castellani et al. (1998); Larsson (2002)). Figure I.6 shows the two different processes of aircraft lightning initiation. During the lightning flash, the aircraft forms a part of the lightning current path. Consequently, there are generally two attachment points on the aircraft for the lightning current: one entry point and one exit point. The entry and exit points are defined as to the direction of the current. Therefore, the exit point of the current will be at an anodic surface (positive electrode) and the entry point at a cathodic surface (negative electrode). As a result, the exit point is the attachment point of the positive leader and the entry point is the attachment point of the negative leader (Larsson (2002)). The aircraft is a part of the current path of an intracloud or an intercloud lightning flash if the discharge is bi-directional during the whole flash. If one of the bi-directional leaders reaches the ground, the aircraft forms a part of a cloud-to-ground lightning. The latter is the case in 25% of low-altitude strikes (<7 km) (Lalande et al. (1999); Larsson (2002)).

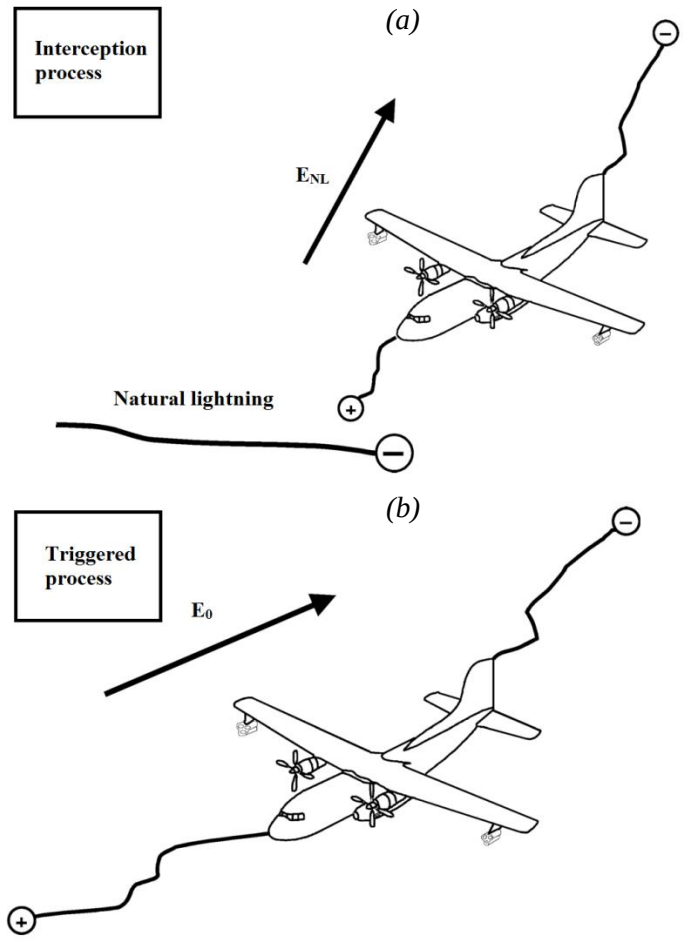

Figure I.6. The two different processes that lead to a lightning strike to an aircraft through a bi-directional leader process. (a) The interception by the aircraft of a natural lightning discharge. (b) The aircraft itself triggers the lightning discharge (Larsson (2002)).

I.2.2 Lightning high current stage

Once the lightning channel has been established, the lightning arc essentially develops between a stationary electrode (the cloud or the ground) and a moving electrode (the aircraft). The aircraft length and speed are of the order of 10 m and 100 m s^{-1}, respectively. Since the duration of the lightning flash is of the order of 100 ms, the lightning channel can be displaced along the whole aircraft length (Larsson et al. (2000a)). The motion of the lightning attachment point is known as the *swept stroke* phenomenon (ARP5412A (2005)). Figure I.7 illustrates the swept mechanism. In the frame of reference of the aircraft, the lightning channel is moving and the attachment point, initially at the nose radome (t_1), moves under the aircraft's surface until reaching the aircraft's tail (t_4). During that time, the portion of the channel attached to the aircraft's tail, elongates progressively. At the time (t_5), the two attachment points meet,

the swept phase ends and the lightning channel is no more connected to the aircraft, although the flash can continue for several milliseconds (Chemartin (2008)).

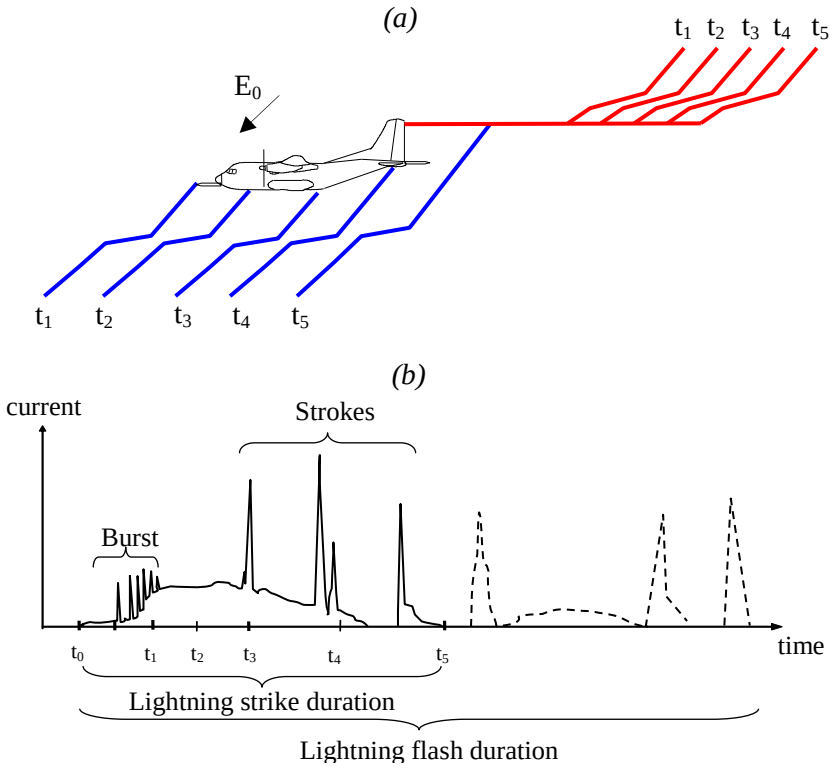

Figure I.7. Illustration of the swept stroke process. (a) The swept represented in the frame of reference of the aircraft for different times t_i. (Chemartin (2008)). (b) Typical current waveform obtained by in-flight measurements (Lalande et al. (1999)).

The sweeping phase is also characterized by a current higher than the initiation phase. The current typically consists of a continuous component of several hundred amperes on which are superimposed current pulses of several tens of kA, called return strokes. The continuous component of current lasts several hundreds of milliseconds while the pulses have duration of a few hundred microseconds. A typical current waveform is shown in figure I.7.

I.2.3 In service lightning strike on aircraft statistics

Data about in service incidents due to lightning strike bring out valuable information in order to improve the phenomenology understanding of the lightning strike on aircraft. These data are an important feedback for aircraft manufactures in the definition process of the most susceptive lightning zones in the aircraft.

Recent published studies present the results of in service lightning event experience for different kinds of aircraft, as for instance airliners, private jets and helicopters (Roussel et al. (2015); Fay and Bigand (2015); Zehar et al. (2013)). Figure I.8*(a)* shows an example of statistical data

obtained from 3708 lightning strikes on airlines from the Airbus family in the period from 2008 to 2014 (Fay and Bigand (2015)). It can be seen that the strikes frequency seems to have a proportional relation with the aircraft size.

(a)

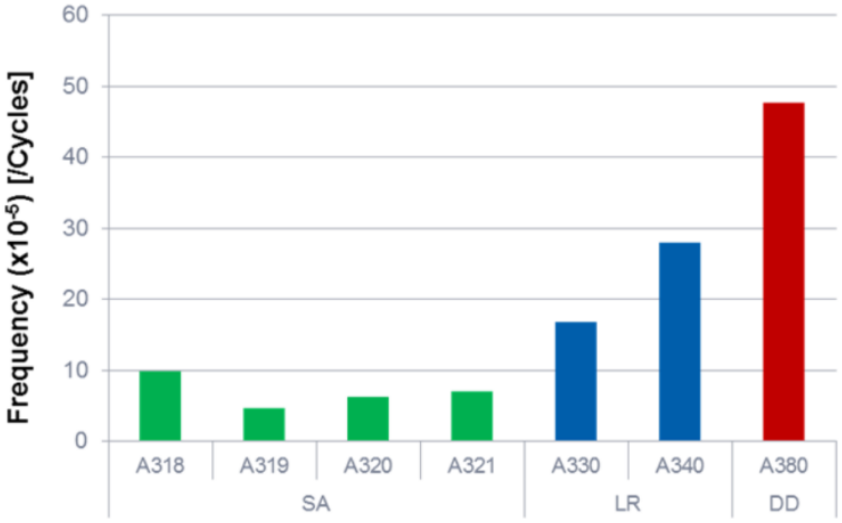

(b)

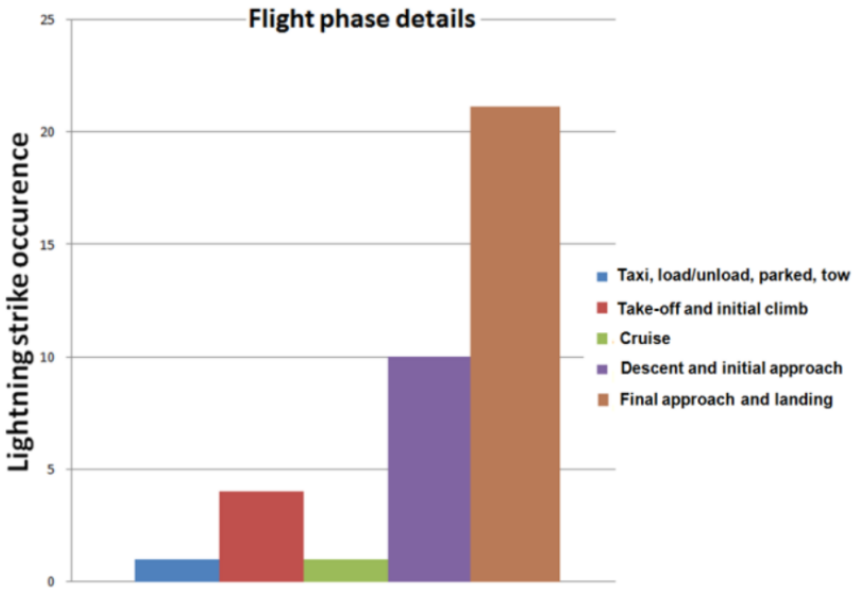

Figure I.8. Data about in service strike. (a) Strike frequency by flight cycles for different type of airlines from the Airbus family from 2008 to 2014 (Fay and Bigand (2015)) SA: single aisle; LG: long range; DD: double deck. (b) Lightning strike occurrence versus flight phases for the Dassault Falcon fleet (F900, F2000 and F7X) from 2003 to 2013 (Roussel et al. (2015)).

Figure I.8*(b)* presents the data of lightning strike occurrence for the different flight phases calculated from 37 registered strikes on the Dassault Falcon fleet (F900, F2000 and F7X) from 2003 to 2013 (Roussel et al. (2015)). Only one event was registered during the cruise phase.

In more than 94% of the cases, the lightning strike occurred during the take-off, descent, initial or final approach and landing.

The works cited above, also reported the distribution of the damages identified after a lightning strike event. The distribution is influenced by the aircraft size/type, but generally the majority of the strikes occur on the fuselage, the nose radome corresponding to almost 70% of the cases, followed by the wings, with the wing tips representing around 60%.

I.2.4 Lightning effects on aircraft

Both attachment and high current phases cause stresses and undesirable effects on the aircraft. The lightning effects to which aircraft are exposed can be divided into direct and indirect effects. Indirect effects are those resulting from the interaction of high electromagnetic fields with electrical/electronic equipment in the aircraft, a phenomenon called EM coupling. As described in section I.2.2, when the lightning strike occurs, a current waveform, composed of many high current peaks, is injected at the entry point. The electric current then circulates over all electrically conducting parts of the structure, on its external surfaces and inside the inner parts, including its electrical system, in order to reach the exit point. This redistribution of the current is a function of the impedances encountered along the various current paths (Parmantier (2012)). Since the current waveform is a transient, the impedances are made up of both a DC component (resistance effect) and time-varying impedance (inductance effect). The indirect effects are beyond the scope of the present work. Interested readers are referred to Refs. (Thottappillil (2002); Punekar and Kandasamy (2011); Parmantier (2012)).

The direct effects of lightning consist of physical damages to structures and external devices, caused by the lightning arc attachment to the fuselage. These effects induce different constraints which can be divided in two main categories; thermal and mechanical constraints.

Thermal constraints are applied both at the direct lightning attachment on the fuselage of the aircraft, and in the other parts of the aircraft in which circulates a significant current. At the attachment point, these constraints can cause erosion, deformation or puncture of the fuselage of the aircraft. In other areas, they can also produce explosions of conductors and induce the formation of hotspots. These constraints have three main origins. The first thermal constraint occurs only in the volume of the body and corresponds to the heat dissipation by the Joule heating. The amount of heat dissipated is all the more important as the material is resistive. Another constraint is the direct heat flux from the arc, which occurs only in the struck surface. This mechanism included the heat flux by conduction, and by electron or ion recombination.

The last heat exchange mechanism is the radiative flux, emitted by the lightning channel (Chemartin (2008)).

Mechanical constraints can lead to breaking, delamination and puncture of the aeronautical material. Similar to the thermal constraints, they are applied at the lightning attachment point or other parts in which circulates a significant current level. They are particularly important during the current peaks (Chemartin et al. (2012)). These constraints have three main origins. The first component of these constraints is the overpressure due to the explosion of the lightning channel, which gives rise to the propagation of a strong shock wave in the radial direction of the arc. The explosion comes from the fast increase in the arc channel temperature in a time interval of a few microseconds. The second component is due the magnetic force induced by the current circulation, which makes a significant contribution to the mechanical constraint in both the arc column and on the material. First of all, the internal pressure of the arc column is reinforced by the concentric magnetic force, a magnetic pinch effect. Also, the current flowing in the structure directly acts as an additional mechanical constraint on the skin, a magnetic pressure effect. Finally, the expansion resulting from the very fast increase in temperature of the material yields an additional contribution to the mechanical stress (ARP5412A (2005); Chemartin et al. (2012)).

In addition to these two main categories, there are also other constraints such as dielectric breaking at the lightning attachment point or sparking at junctions and fasteners.

I.2.5 Composite material challenges

Nowadays, carbon fiber composite (CFC) materials, also referred as carbon fiber reinforced polymer (CFRP), are used in various parts of the aircraft due to their strength and lightness, including wing boxes, fuselage and structural spars. They came to replace metallic materials, massively used on previous generation of aircraft, for the sake of reducing the overall weight and additional fuel savings.

The last airliner programs were both exposed to difficulties for implementing carbon composite structures with account of lightning direct effects. The Boing 787 Dreamliner and the Airbus A350XWB programs employ carbon composite in around 50% weight of the aircraft. The composite materials are used in zones highly exposed to the lightning strike as fuselages and wings. Figure I.9 presents the material distribution of the main components in the Boeing 787 Dreamliner.

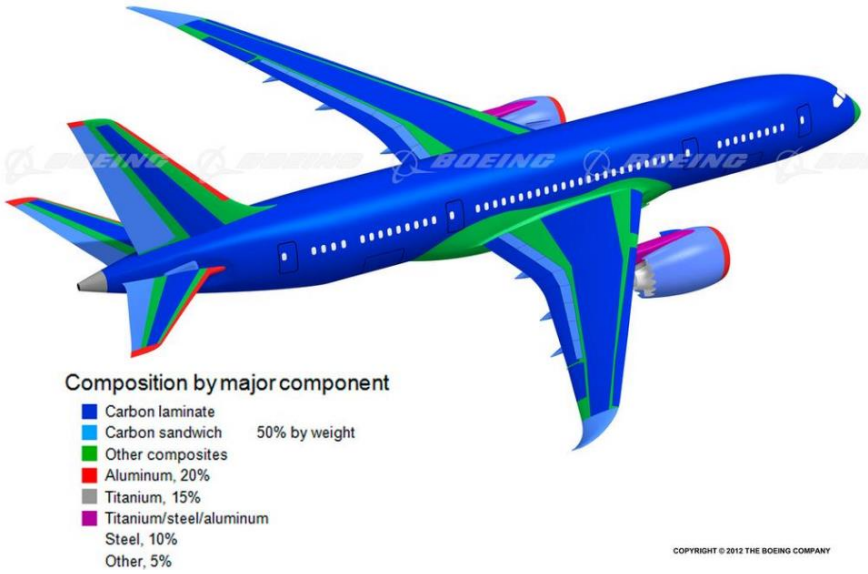

Figure I.9. Boeing 787 Dreamliner material composition (Source: ©Boeing).

The carbon composite most employed in aircraft is the quasi-isotropic laminated composite, which is made of unidirectional multi-layup of carbon plies oriented in different directions in an epoxy matrix. The ply is formed from carbon fiber tows. Typically, each tow is about 3 mm wide strand of continuous fibers. A strand, in its turn, may consist of 12000 individual filaments impregnated with an epoxy resin (Chawla (2012)). Figure I.10 shows a micrograph of the carbon fibers present in a tow and the structure of the multi-layup in a laminated composite with structure $[0°, 90°, -45°, +45°]_S$.

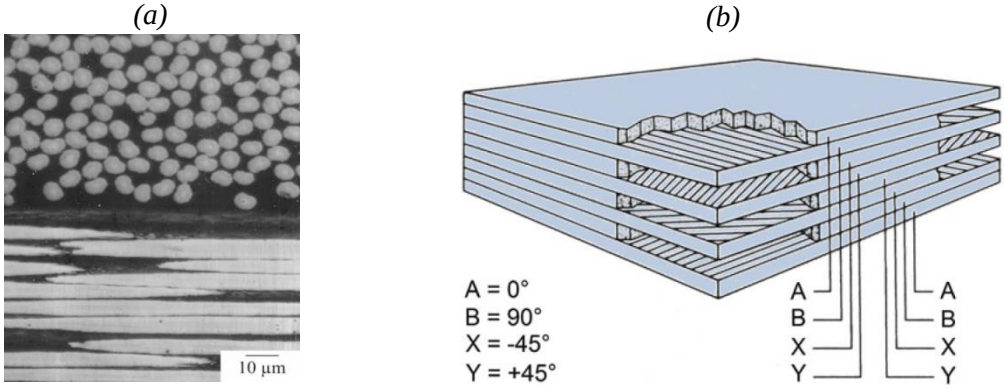

Figure I.10. (a) Laminated composite magnification picture highlighting the carbon fibers of a tow. (b) Layup of plies with different fiber orientations (Chawla (2012)).

The CFRP composites are unable to conduct the high electrical currents and electromagnetic forces sufficiently to prevent structural damage, once their thermal and electrical conductivity are lower than aluminum. The electrical conductivity of a carbon tow is about 60 kS m^{-1} (IM7 fibers, Hecxel), which is very low in comparison to aluminum (37000 kS m^{-1}). In a CFRP,

the electric conductivity highly depends of the direction of the carbon fibers. The electrical conductivities is generally defined by three values: the parallel conductivity, in the direction of fibers, which is in the same order of magnitude than carbon tow conductivity (30 kS m^{-1}), the transverse conductivity, transverse to fibers, but in the same ply (1 S m^{-1}), and the perpendicular conductivity, transverse to fibers, directed between different layers (0.1 S m^{-1}) (Neufeld (2015)). The dependence of the conductivity with the fiber directions may increase locally the resistivity of the material, resulting in an intensification of the thermal constraints.

When lightning currents circulate through these composite structures, the result can be embrittlement, delamination, and/or structural failure (Gou et al. (2010)). Figure I.11 shows an example of the carbon fiber damage at the attachment point after a lightning test.

Figure I.11. Damage of carbon fibers tows at the lightning attachment point (Source: National Institute for Aviation Research (NIAR))

There is a need for lightning strike protection solutions that enable lightning currents and electromagnetic interference forces to flow through the aircraft without inducing major damages. The most severe damage usually occurs at the attachment points of lightning current, where the energy density is the highest. The actual solutions, to enhance the protection on composite parts and reduce or eliminate the damages, are metallic mesh of aluminum or copper, or expanded metal foils bonded to the outer surface of the composite parts. Figure I.12 illustrates the damage after lightning test on a carbon composite sample protected with copper mesh.

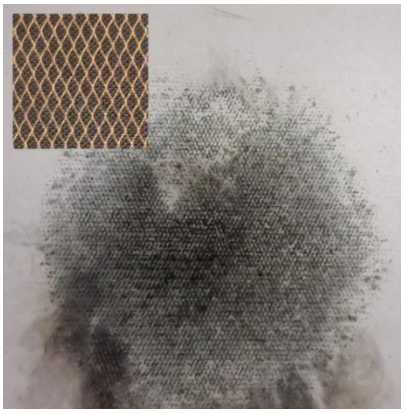

Figure I.12. After test result for a carbon composite sample with copper mesh protection (Source: Morgan-Botti Lightning Laboratory)

Those protections act on one hand to remove a portion of the total current into the composite structure, and on the other hand to help the expansion of the arc root on the structure (McKeeman Brown (2005)). Those both functions decrease the thermal constraints on the CFRP.

Other metallic materials are used besides aluminum and copper, such as nickel and phosphor bronze. However, this additional weight can cause counterbalance of the weight saving conferred by composite materials and will also increase manufacturing costs (Gagné and Therriault (2014)).

I.3 Aircraft lightning protection process

Aircraft are designed to fly regardless of weather conditions. In a context where the risk of a lightning strike is significant, it is essential to consider this risk when designing the aircraft. Therefore, the design stages are based on methods of certification that guarantee the holding of the aircraft to an upper bound lightning strike. Civil certification authorities, such as EASA (European Aviation Safety Agency) and FAA (Federal Aviation Administration), require, through text indicating the basic recommendations, to protect aircraft against catastrophic effects of lightning. Standard committees, such as EUROCAE (European Organization for Civil Aviation Equipment) and SAE (Society of Automotive Engineers), establish guides and normative documents that explain how to achieve these recommendations (Lago (2014)).

We can divide the aircraft lightning protection procedure in three steps. The first group consists of the definition of an idealized lightning environment, mainly a set of current components specifying a standardized current waveform, upper bound to 98% of all measured current

components on ground. The second step is the definition of the lightning strike zones on the aircraft, which are associated to the risk level of lightning strikes and the corresponding current intensities. The final step of the protection process is the direct effect testing on materials, equipment, systems and structures.

I.3.1 Lightning current waveform

Lightning, like any natural phenomenon, is unpredictable in nature. Current levels and waveforms vary considerably among different lightning flashes. In the document SAE Aerospace Recommended Practice ARP5412A (2005), the lightning current waveform is defined by a composition of four current components, named A, B, C and D. This standardized current waveform has been derived to represent the lightning environment, and to give upper bounds of the direct effects of lightning on aircraft. Figure I.13 illustrates the four components of the current waveform with their corresponding maximum current level, time duration, action integral (A^2s) and transferred charge (C). The A- component relates to the first return stroke, and, the D-component, reproduce the subsequent strokes. The B-component is associated to the transition of the current peaks to the continuing current. The C-component reproduces the damages related to the continuous phase. In addition to the current level, the A- and D-components are characterized by their action integral (2×10^6 A^2s and 0.25×10^6 A^2s, respectively), and the B- and C-components are defined by their transferred charge (10 C and 200 C, respectively).

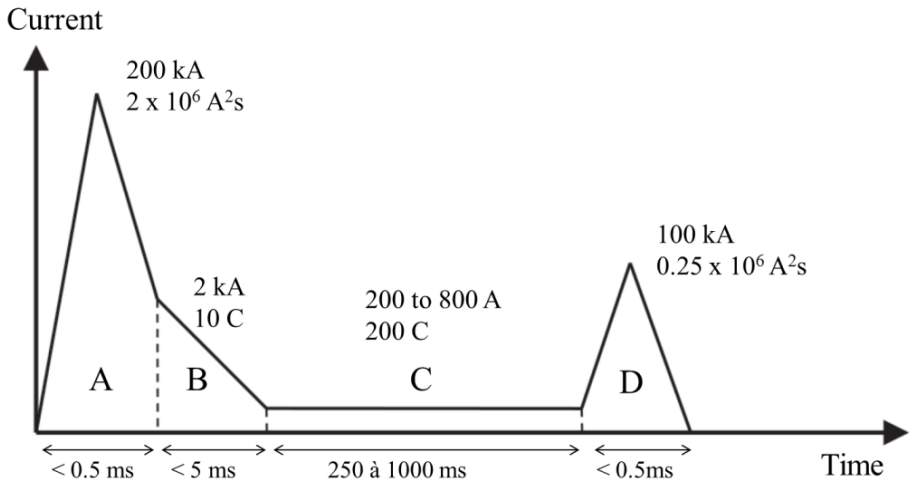

Figure I.13. Standardized lightning current waveforms for lightning direct effect tests (ARP5412A (2005)).

I.3.2 Lightning strike zones

Due to the lightning sweep stroke phenomenon, different locations on an aircraft are exposed to different lightning current components. The dwell times at each attachment point vary according to the nature of the surface, the local geometry, the air flow and the current waveform which could cause reattachment if a current peak occurs (Tholin et al. (2013)). The dwell times recommended in the standards range from 1ms for unpainted metal surfaces to 50ms or more for surfaces covered with "especially thick or high dielectric strength coatings" (ARP5412A (2005)). Following the document SAE ARP5414A (2005), the aircraft is divided into different lightning strike zones which is referred to as *lightning zoning*. In this document, several zones are defined with two labels (a number and a letter) according to their susceptibility to cause attachment or not and to cause sweeping or not, with some additional features. The first label (numbered by 1, 2 and 3) indicates the cause of the presence of the arc: attachment (zone 1), sweeping (zone 2), or neither of them (zone 3). This number is associated to three letters (A, B and C) to describe the ability of the arc to sweep (zone A) or to dwell at the same location (B). Generally, an airliner can be divided into six zones in which different sequences of current components are expected. The defined zones are (ARP5414A (2005); ARP5416A (2005); Sweers et al. (2012)):

- Zone 1A – "First Return Stroke Zone: All areas of the airplane surfaces where a first return is likely during lightning channel attachment with a low expectation of flash hang on". The current sequence associated to these zones is ABC*-components (C*-component is a shorter C-component associated to the dwell time and the surface coating).
- Zone 1B – "First Return Stroke Zone with Long Hang-On: All areas of the airplane surfaces where a first return is likely during lightning channel attachment with a high expectation of flash hang on". Those zones are subjected to the total standardized current sequence (ABCD-components).
- Zone 1C – "Transition Zone for First Return Stroke: All areas of the airplane surfaces where a first return stroke of reduced amplitude is likely during lightning channel attachment with a low expectation of flash hang on". The current sequence associated to this zone is AhBC*-components (Ah-component is a reduced A-component associated to swept leaders at flight altitudes between 1500 and 3000 m).
- Zone 2A – "Swept Stroke Zone: All areas of the airplane surfaces where a first return of reduced amplitude is likely during lightning channel attachment with a low expectation of flash hang on". The current sequence associated to these zones is DBC*-component.

- Zone 2B – “Swept Stroke Zone with Long Hang-On: All areas of the airplane surfaces into which a lightning channel carry subsequent return stroke is likely to be swept with a high expectation of flash hang on”. The current sequence associated to these zones is DBC-component.
- Zone 3 – “Current Conduction Zone (Strike locations other than Zone 1 and Zone 2): Those surfaces not in Zone 1A, 1B, 1C, 2A, or 2B, where any attachment of the lightning channel is unlikely, and those portions of the airplane that lie beneath or between the other zones and/or conduct a substantial amount of electrical current between direct or swept stroke attachment points”.

Figure I.14 shows an example of lightning zoning applied to a commercial aircraft. In general, the extremities of the aircraft as the nose radome, the wing-tips or the engines fronts are classified as susceptible to the ABC*-component of the current waveform. A few zones are susceptible to be impacted to all the lightning current waveform (Zone 1B). Most of the fuselage of the aircraft is classified as ‘Zone 2A’, which corresponds to the DBC*-component.

Lightning zoning tests is a functional step in demonstrating that the aircraft is adequately protected from direct effects of lightning. During these certification tests, there is no characterization of the interaction of the arc attachment point on the material. The main goal is to verify the resistance or not of the material to the applied constraints. From this procedure, the aircraft’s manufacturer designs the materials of each zone, ensuring that they are resistant to the different components of the lightning current waveform.

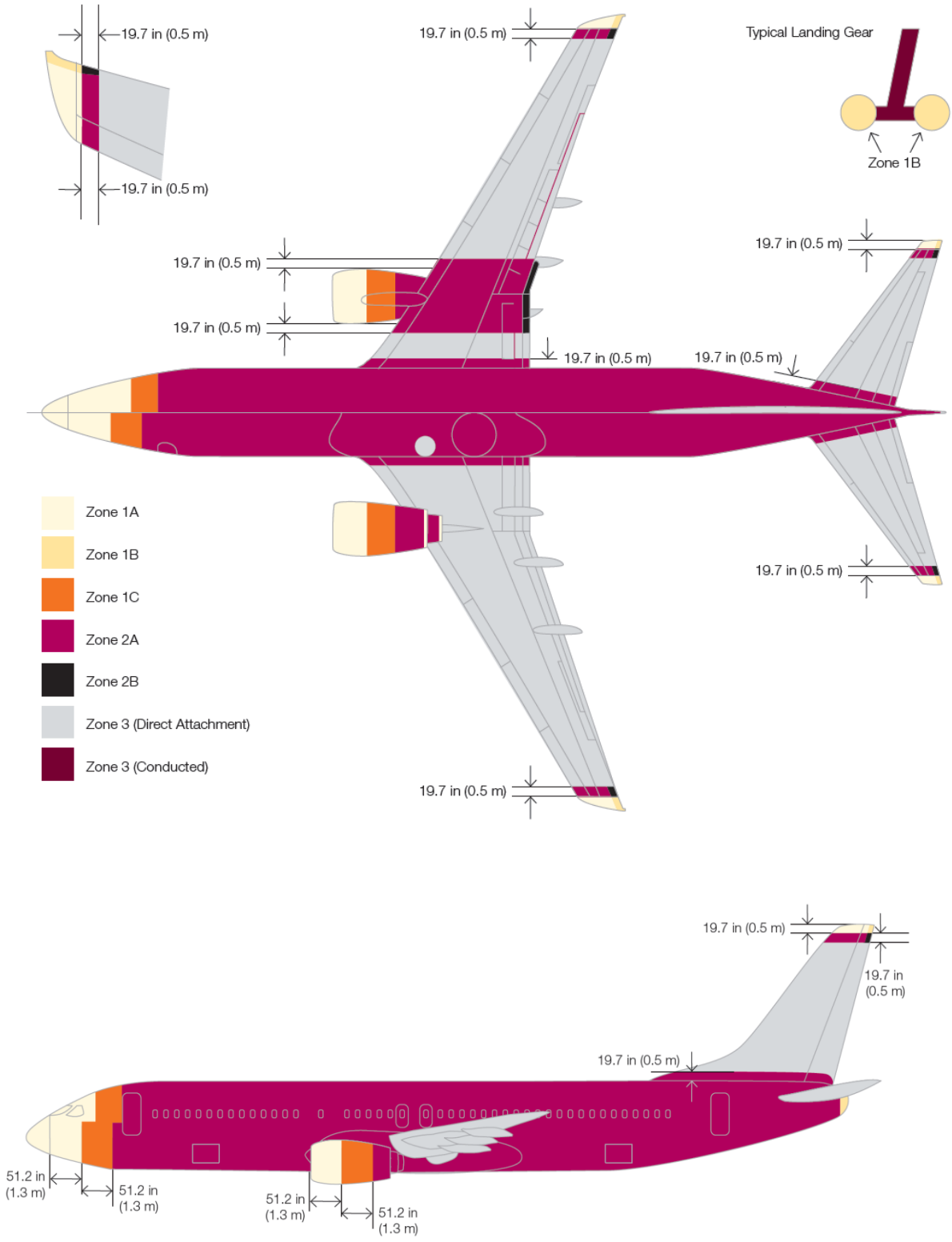

Figure I.14. Example of lightning zoning applied to a Boeing airliner (Sweers et al. (2012)).

I.3.3 High current testing

Direct effects testing, or high current testing, require simulating in laboratory a lightning strike with the idealized current waveform according to the zoning defined previously.

The material under test is subjected to an electrical discharge which follows different criteria imposed by the aeronautics standards, as described in the document SAE ARP 5416A (2005). In the standard certification test procedure, the lightning arc is created between two electrodes. One is formed by the aeronautical object under test. The other, called jet diverter electrode is formed by a tungsten rod on which a dielectric sphere is fixed at its tip.

The work presented in this dissertation is mainly associated with the understanding of direct effects testing.

I.4 Overview of previous studies in lightning arcs

Numerous studies have been performed in the field of lightning arcs. They have as main objectives a better characterization of the arc plasma properties, an accurate description and prediction of the arc evolution, and analyses of the interactions and effects on the materials. The approaches are generally based either on experimental studies, with many limitations due to the experimental conditions and representativeness, or on theoretical studies and modeling, with most of the time a lack of validation. In the following subsections we briefly describe the physical phenomena of lightning arcs and then we present an overview of the main theoretical and experimental works in this field.

I.4.1 Main physical phenomena of lightning arcs

An electric arc is an electric discharge in a gas in which the electric current is strong enough to make the discharge self-sustained. In this regime, the voltage across the column decreases as the current increases, and the discharge exhibits a negative differential resistance ($dV/dI < 0$). In the cases of high pressure arcs in air, with pressure of about 1 bar or higher, the plasma is a single fluid that obeys the Navier Stokes equations, in which electric and magnetic fields acts on the fluid dynamic through the Joule heating and the Laplace forces. Due to the high temperature and pressure, the plasma is expected to be highly collisional, and the assumption of local thermodynamic equilibrium (LTE) is generally applied. Moreover, because of the high temperature of the arc column, radiative transfers may be significant in the energy balance.

Lightning arc is an example of a natural electric arc. A simple physical picture of the lightning arc development can be descripted as follows: after the initiation of the cold discharge (streamer

and leader stages), the current increases quickly in the conductive column because of the high electric field oriented along the channel axis. Due to the finite conductivity of the column, electric power is released to the air plasma by Joule heating. This source power increases the temperature of plasma, which in turn losses a portion of the power by radiative emission. The emitted radiation from the arc core can heat the adjacent gas around the channel, which can promote its radial expansion. The current induced a magnetic field in the azimuthal direction, which gives rise to a magnetic pinch and consequently to an additional overpressure in the channel. Because of these mechanisms, the lightning channel becomes a long electric arc with a length in the order of tens of kilometers.

I.4.2 Modeling and theoretical studies

The theoretical studies and models developed for lightning arcs can be separated according to the arc current phase, i.e., the continuous and the transient components. In most of models presented here, the arc plasma is described as a single fluid with sufficient collisions to reach local thermodynamic equilibrium (LTE).

The earliest theoretical models of the interaction between a lightning arc and a fuselage were focused on the continuous component of the lightning current. These models are based on the magneto-hydrodynamic (MHD) approach, which was previously developed in other fields as circuit breakers, plasma torches, welding, etc. This type of modeling was used initially for simulating stationary arcs in argon by Hsu et al. (1983). Then this category of models has been adapted to the simulation of high current arcs by Delalondre (1990) and Gonzalez (1992). Lago (2004) was one of the first to use a MHD approach to simulate the interaction of lightning arcs with a surface. His model includes the anode in the computational domain to simplify the magnetic boundary conditions.

Chemartin (2008) continued the approach developed by Lago (2004), adding the cathode in the computational domain, and considering unsteady and free moving arcs. The presence of all the electrodes in the computational domain facilitates the definition of the boundary conditions, particularly for electromagnetic quantities (electric potential and magnetic vector potential). This improvement appears to be very interesting in the simulation cases of a lightning swept stroke and the arc reattachment in the aircraft's surface (Chemartin et al. (2011)). A further improvement made by Chemartin (2008) is the definition of boundary conditions suitable for the simulation of infinitely long arc channel. This work allowed the simulation of the tortuosity of a lightning arc channel in a computational domain without spatially periodic electrodes (Chemartin et al. (2009)). Figure I.15 shows an example of the simulation of a lightning arc during the continuous phase, resulting from this MHD approach (Chemartin et al. (2011)).

Solid arrows indicate the plasma jet formed in the cathode arc roots and the dashed circle and arrows illustrate the arc reattachment due to the arc displacement.

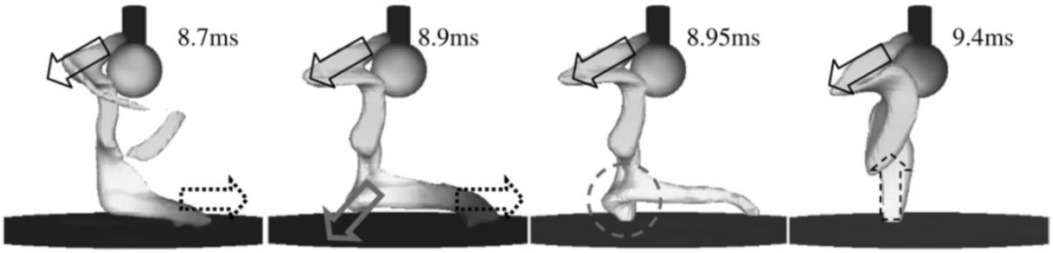

Figure I.15. Simulation of an unsteady continuous arc (400 A) using the MHD approach, considering the electrode effects and the arc reattachment process. The grey region represents an isotherm surface at 8000 K (Chemartin et al. (2011)).

Concerning the transient stages of lightning, the earliest simulations were focused on indirect effects. In general, the Maxwell's equations are solved to determine the current distribution over time on the aircraft's skin, cables or other electrical components (Uman et al. (1975)). Lightning channels are considered as a conductor in which circulates a high current pulse. In these simulations, the arc expansion dynamics and its interaction with the fuselage do not play any role.

For the modeling of lightning channel during a high current pulse (return stroke), there are two main approaches. In the first one, known as circuit approach, the arc channel is modeled as a transmission line whose the distributed elements are described by an electrical circuit based on resistors, inductors and capacitors (Price and Pierce (1977); Little (1978); Baker (1987); Rakov and Uman (1998)). The second approach is based on the gas dynamic equations applied to air plasmas. Plooster (1970) studied cylindrical shock wave theory from a linear source. His work was extended to investigate the evolution of a lightning channel (1D geometry) by gas dynamic modeling (Plooster (1971)). The channel is considered axisymmetric and different thermodynamic quantities are solved within a radius of the channel. The input data is the pulsed current waveform and the results are the evolution over time of arc temperature, pressure and speed distribution. The main assumptions of Plooster's model are: the arc plasma is a continuous medium whose behavior can be modeled by the Navier-Stokes equations; the plasma is at local thermodynamic equilibrium (LTE); the inductive effects are neglected; the arc column is not subjected to Laplace forces; the arc is purely resistive and the electric field is static; radiation modeling is very simplified and the radiative transfer equation is not solved. The pulsed current considered in the Plooster's simulation reached a maximum of 20 kA.

Paxton et al. (1986) completed the model proposed by Plooster (1971) for the same pulsed current levels, improving the calculation of radiative transfer. This improvement is based on two elements. A more complete model of radiative transfer based on the diffusion approximation and absorption coefficients averaged on a few spectral bands. Aleksandrov et al. (2000) employed a resistive MHD model, similar to that proposed by Paxton. The same model of radiative transfer was used, considering absorption coefficients that are averaged on four spectral bands using the Planck mean. They made calculations for a 100 kA current wave with a maximum current rate of 18.2 kA μs^{-1}.

Tanaka (2005) modeled a pulsed arc for low current level (72 A), but the considered time constants are below to those of a lightning arc (peak current of 1 µs). This MHD modeling is carried out assuming chemical non-equilibrium plasma. It takes into account the Laplace force which is often neglected by other authors. Tanaka shows that the Laplace force in this type of pulsed arc is very important and leads to high pressures in the arc channel, which can reach several hundred bars.

Peyrou (2012) studied a free lightning arc during the transient phase, without considering the interaction with the electrodes. He considered an axisymmetric column and developed a MHD model which includes a model for the hydrodynamics, the radiative transfer and the electromagnetism quantities. He studied the D-component of the lightning current waveform, with a current peak level of 100 kA and peak time of 6.4 µs. In the MHD equations, the source term of momentum from Laplace force is taken into account as well as the term source of energy coming from the Joule heating and from the radiative transfer. The radiative transfer equation is solved using the P_1 approximation for the geometrical calculations, combined with a spectral approximation in the absorption coefficients which are averaged on 11 spectral bands using the Rosseland mean. Using the standard current waveform as input (ARP 5416A (2005)), this model gives the evolution over time of the temperature, pressure and velocity distributions. Figure I.16 shows the result profiles obtained for temperature and pressure. In these simulations, the temperature reaches more than 30000 K and exhibits a near constant distribution along the channel radius. The pressure reaches 50 bar at 5 µs after the arc initiation, and its profile presents the combinations of two effects: a parabolic shape near to the arc axis, as a result of the Laplace force and the sharp form in the arc edge due to the shock wave propagation.

Tholin et al. (2015) extended the model proposed by Peyrou (2012), by introducing an electrode into the computation domain to simulate the aeronautical material. To avoid high computation cost, a two-dimensional axi-symmetrical domain was used. They considered the interaction with different aeronautical materials such as aluminum and CRFP composites. They studied the

dynamic of the arc for typical D-component currents, which reach 100 kA at 10 µs. The influence of the material conductivity on the arc root shape was evaluated, showing that a conical shape is formed when the conductivity of the plasma is in the same order of higher than the material conductivity, which occurs roughly for the case of CFRP material.

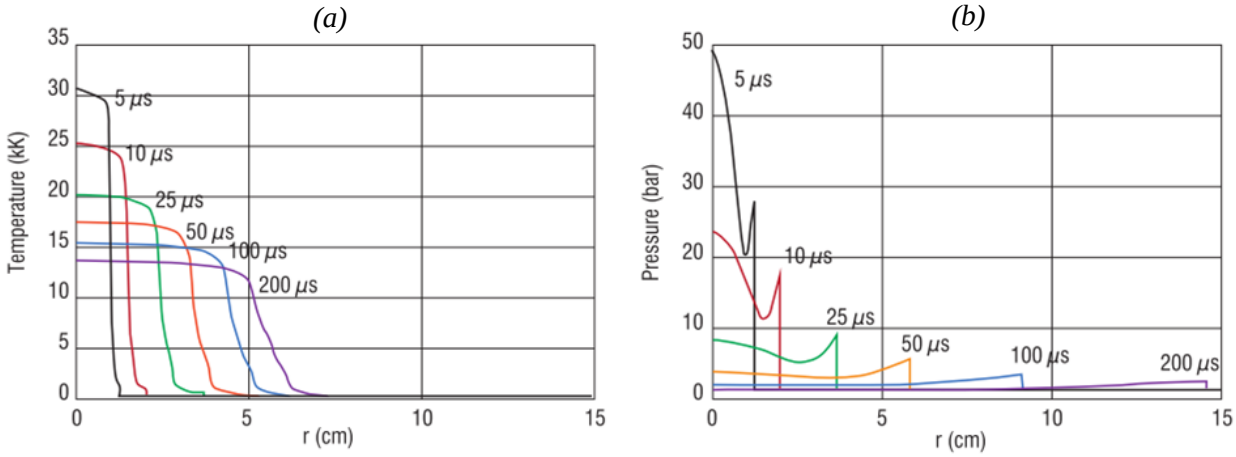

Figure I.16. Temperature (a) and pressure (b) profiles resulting from the MHD code developed by Peyrou (2012). The input is a D-component with current peak of 100 kA and peak time of 6.4 µs.

Villa et al. (2011) proposed a MHD code to describe the pressure field near to the impact point of a lightning strike and to evaluate the dynamic load imposed to the material during the A-component of the standardized current waveform. They performed measurements of the pressure around the impact point by using a transducer-tube apparatus. A three-dimensional fluid dynamics coupled with a one-dimensional code to model the tube is considered. The radiation power loss is modeled by a net radiation coefficient and the radiative heating is neglected. The arc resistivity is approximated using both a fixed resistive model as a function of the arc radius and a variable resistivity model. The calculated pressure evolution over time is compared to measurements at the gauge position and shows good agreement for the pressure peak, which reaches around 70 bar at 5 cm from the arc axis. However, the pressure field inside the arc cannot be directly compared due to a lack of reliable measurements in the arc channel.

Karch et al. (2015) studied mechanical damage of CFRP structures subjected to an arc lightning current waveform with 100 kA peak at 12 µs. They proposed a model for the root radius in the degradation area based on the Braginskii's radius model, which reaches 32 mm at 50 µs. The magnetic pressure that acts in the material is calculated assuming a radial and uniform distribution of the current in CFRP sample. The shock wave induced by the arc is characterized near to the material surface using the self-similar solution and based on the Lin's approach. The calculated wave front reaches 80 mm at 80 µs.

The models and theoretical studies mentioned above, have allowed a huge improvement in the description and understanding of lightning arcs. Nevertheless, a part of these models, mainly those with respect to the transient phase of the lightning, are not completely validated due to a lack of accurate experimental data in the literature for this category of high current arc.

Table I.1 summarizes the mentioned studies, presenting the main characteristics and the associated hypothesis.

Table I.1. Main characteristics of theoretical and modeling studies

Reference	Lightning? Type of current	Regime	Type and geometry	Electro-magnetic	Fluid and plasma	Radiative transfer	Interaction with material
Hsu et al. (1983)	No, continuous	Steady state	MHD, 2D axi-symmetric	Static simplified	Argon, LTE	NEC	Thermal flux
Lago et al. (2004)	Yes, continuous	Slightly transient	MHD, 2D axi-symmetric	Static	Air, LTE	NEC	Thermal flux, vaporization, simplified CFRP
Chemartin et al. (2009)	Yes, continuous	Slightly transient	MHD, 3D	Static	Air, LTE	NEC	Thermal flux, vaporization
Aleksandrov et al. (2000)	Yes, pulsed bi linear	Transient	MHD, 1D axi-symmetric	No	Air, LTE	P1 , 4 bands	No
Peyrou (2012)	Yes, pulsed bi-exponential	Transient	MHD, 1D axi-symmetric	Transient	Air, LTE	P1, 11 bands	No
Tanaka et al. (2005)	No, pulsed bi linear	Transient	MHD, 1D axi-symmetric	Static	Air, with chemical non-equilibrium	NEC with non-CE effect	No
Villa et al. (2011)	Yes, damped exponential cosine	Transient	MHD, 3D	Static simplified	Air, LTE	NEC	No
Karch et al. (2015)	Yes, pulsed bi-exponential	Transient	Analytical analysis	Static simplified	No	No	Real CFRP structure, damaging
Tholin et al. (2015)	Yes, pulsed bi-exponential	Transient	MHD, 2D axi-symmetric	Static	Air, LTE	P1, 11 bands	Simplified CFRP

I.4.3 Experimental studies

There are many experimental studies in the field of lightning strike to aircraft that involve the measurement of current distribution, electrical and magnetic fields, etc. (Moreau et al. (1992); Lalande et al. (1999); Uman and Rakov (2003); Laroche et al. (2012)). The main objectives of these previous studies were the determination of lightning current waveforms and a better understanding of the lightning initiation phenomenon and of the swept stroke process. However, no comprehensive experimental studies have been conducted to investigate the physical properties of the lightning arc and the plasma channel itself.

In the field of natural lightning strike to grounded structures, the plasma channel was widely studied between the 1960s to the 1970s to understand the physical processes and to characterize the phenomenon. Due to high intense radiation emitted by the lightning channel, optical emission spectroscopy (OES) was frequently used as diagnostic method to characterize the plasma.

Zhivlyuk and Mandel'shtam (1961) performed time-integrated OES measurements of singly ionized nitrogen and oxygen lines (N II and O II). They employed the Planck radiation law and assume an optically thick channel at the center of some N II and O II lines to obtain the channel temperature. They report temperatures in the range of 14000 K to 31000 K, with an average of 21000 K from the analysis of 4 different lightning flashes. Prueitt (1963) analyzed individual lightning strokes using slitless spectra (spectra recorded with a slitless spectrometer). He obtained temperature measurements from the ratio of N II multiplets under three main assumptions; the plasma channel is at local thermodynamic equilibrium (LTE), the plasma is optically thin to the lines of interest and the plasma properties are uniform in the radial direction and along the lightning channel (ranging from several meters to a few kilometers). He found a temperature ranging from 24200 K to 28400 K. These spectra and temperature results were then used by Uman et al. (1964) to investigate electron density and pressure of the lightning channel near maximum temperature. They estimated the amount of atomic nitrogen and oxygen, and singly ionized nitrogen from their corresponding line-intensity measurements (N I, O I and N II) and considering a temperature of 24000 K. Based on the thermodynamic properties of dry air at high temperature calculated by Gilmore (1955), they estimated the electron density to about 4.3×10^{18} cm^{-3} and pressure to around 18 bar.

Orville (1968a, 1968b) performed the first time-resolved OES measurements of a lightning return stroke. Using a slitless spectrograph with a high-speed streaking camera, he performed measurements with a time resolution of 5 µs. The plasma state hypotheses of the lightning channel were the same done by previous authors and cited above. The temperature was obtained

using the intensity ratio of N II multiples and the electron density by broadening measurements of H-alpha line. He reported a peak temperature of 36000 K in the first 5 µs, and then an average temperature of 20000 K between 20 to 25 µs. The electron density was estimated to around 10^{18} cm^{-3} in the first microsecond, and then falling to 10^{17} cm^{-3} after 30 µs. The accuracy of these density measurements was estimated to 50%. Krider (1973) extended the analyses done by Orville using time-resolved spectra of atomic and singly ionized nitrogen and oxygen lines (N I, O I, N II and O II) for temperature and electron density measurements, and the hydrogen Balmer-alpha line for electron density estimation. He reported an average temperature of 28400 K at 10 µs, which falls to around 10000 K after 50 µs. Electron density and pressure were estimated, respectively, to around 10^{18} cm^{-3} and 8 bar in the first microseconds.

Even they are quite old, the studies cited above provide understanding and information on the plasma channel properties in a lightning stroke. However, with regard to the utilization of these experimental data for comparisons and validations of theoretical models of lightning channel, we can mention two main drawbacks. Firstly, the reliable information of the current waveforms is not available, which prevents the inputs and boundary conditions for the simulation codes. Secondly, the lack of a space-resolved measurement makes it impossible to accurately analyze the radial evolution of the physical quantities of the plasma channel, as electrical conductivity, temperature, density, pressure, etc.

More recent experimental studies on natural lightning strikes have also estimated the channel temperature and electron density by OES measurements under optically thin hypothesis and by using some well-known diagnostic methods cited above. Cen et al. (2011) found maximum temperature around 29000 K and estimated the current peak from the measured radiated electric field, which reaches 27.5 kA. Mu et al. (2016) report temperature and electron density at the first 110 µs, which reach, respectively, 27700 K and 4.2×10^{18} cm^{-3}.

In others fields of high current electric arcs, as welding arc and circuit breakers, experimental characterization of the arc plasma properties is made, mainly, via optical diagnostics. In what follows, we present an overview of recent studies performed using high-speed imaging and OES measurements as diagnostic methods.

Valensi et al. (2010) reported temperature, electron density and metal concentration in a plasma of metal inert gas welding arc, with a dc current of 330 A. High-speed imaging was used to characterize the plasma shape and an interferential filter was used to evaluate the metal vapor repartition. The electron density was estimated by Stark broadening measurement of iron and argon lines and was around 10^{17} cm^{-3}. The temperature reached 12500 K and is determined by Boltzmann plot method of iron lines. Ma et al. (2011) performed time-resolved filtered

spectrometer measurements for plasma temperature determination in a pulsed tungsten-inert-gas welding arc with a peak current of 200 A and a pulse frequency of 5 Hz. The temperature was estimated using an argon line and the Fowler-Milne method. It reached approximately 22000 K near to the arc axis, and decreased to around 10000 K at 3 mm from this position.

Eichhoff et al. (2012) studied a switching arc in a model circuit breaker with a current peak of 5.6 kA and a peak time of 5.2 ms (half-cycle of a sinusoidal current with frequency of 50 Hz). The arc was in a carbon dioxide atmosphere and is led through polytetrafluorethylene (PTFE) nozzles. The plasma was characterized by measurement of absolute line intensities of atomic fluorine and ionized carbon lines and assuming the plasma to be optically thin to these lines. At the current peak, the temperature reached 20000 K at the arc axis and decreased to around 14000 K in at 12 mm from this position.

Ratovoson et al. (2014) performed an investigation of a transient arc, which can occur during the separation of electric contacts between pantograph and catenary in railway electric traction system. The current reached 1 kA with a variable time constant of 24 to 41 ms. Space- and time-resolved OES measurements were employed to estimate temperature and electron density under plasma optically thin hypothesis, and high-speed imaging was used to assess the plasma distribution. Temperature was deduced from the Boltzmann plot method of ionized nitrogen lines and reached approximately 15000 K. Electron density reached 2×10^{17} cm^{-3} and was estimated from the Stark broadening of the hydrogen Balmer-alpha line and from the Saha's law applied to neutral and ionized nitrogen.

These works cited above employed well-known spectroscopic plasma diagnostics for the temperature and electron density determination, as for instance the Boltzmann plot method and the Stark broadening of the hydrogen Balmer-alpha line or of others atomic and ionic lines. However, all these methods require the optically thin plasma hypothesis and, for reliable results, we have to use well-isolated and resolved lines. Moreover, even for the cases of pulsed arcs, these studies deal with lower levels of current peak and growth rate of current compared to those found in lightning arcs.

Table I.2 summarizes the mentioned studies, with the associated hypothesis, the current and measurement characteristics and the employed diagnostic methods.

Table I.2. Main characteristics of experimental studies

Reference	Lightning?	Current origin and type	Space- and time-resolved?	Assumptions and method
Zhivlyuk and Mandel'shtam (1961)	Yes	Natural, peak	No	Optically thick channel, Planck radiation law
Uman et al. (1964) Prueitt (1963)	Yes	Natural, peak	No	Optically thin channel; Boltzmann plot method + Stark broadening
Orville (1968a, 1968b) Krider (1973)	Yes	Natural, peak	Time resolved, (5 µs)	Optically thin channel; Boltzmann plot method + Stark broadening
Cen et al. (2011)	Yes	Natural, peak	No	Optically thin channel; Boltzmann plot method
Mu et al. (2016)	Yes	Natural, peak	Time-resolved, (110 µs)	Optically thin channel; Boltzmann plot method + Stark broadening
Valensi et al. (2010)	No, welding with argon	Controlled, 330A DC	Time- and space-resolved (340 µs with 10 µm or 200 µs with 25 µm)	Optically thin channel; Boltzmann plot method + Stark broadening
Ma et al. (2011)	No, welding	Controlled, repetitive 200A peak,	Time- and space-resolved (1 ms with 80 µm)	Optically thin channel; Fowler-Milne method
Eichhoff et al. (2012)	No, switch gear with CO	Controlled, 5.6kA peak	Time- and space-resolved (~0.2 ms with ~ 0.36 mm)	Optically thin channel; Absolute line intensities + Stark broadening
Ratovoson et al. (2014)	No, pantograph	Controlled, 1kA peak	Time- and space-resolved (1 ms with ~ 10 µm and 0.25 ms with ~ 20 µm)	Optically thin channel; Boltzmann plot method + Stark broadening or Saha's law

I.5 Research objectives

The previous literature overview shows that there is a significant number of models and simulations codes which were developed to describe and predict the behavior of lightning arcs in an aeronautical context. These simulation codes are of great interest for the optimization of materials protections and could also help aircraft manufacturers to reduce time and cost by avoiding the need to perform numerous lightning tests for certification. Nevertheless they have not been completely validated by experimental measurements due the lack of physical data in the literature. To answer this need, the present study consists of developing methods and experimental diagnostics allowing to obtain physical quantities of a lightning arc plasma and of the interaction between the plasma and an aeronautic material, in order to build a database for comparison and model validation. First, we investigate the free arc channel created between two electrodes during the high current phase. Then, the interaction between this high current arc and aeronautical materials is considered, and different physical properties of this interaction are determined.

The physical properties investigated in the present work can be classified in three main categories. First, we study the macroscopic properties of the plasma, as the evolution of the conductive arc radius, and the shock wave induced by the arc expansion. Second, we characterize the electrical properties of the arc, as the time-varying impedance and the electrical conductivity of the plasma. Finally, we investigate the intensive thermodynamic properties as temperature, electron density and pressure distribution within the arc channel. All these quantities are directly comparable to the results of simulation codes and will be a valuable source of data for model development.

Another important challenge of this work is to develop a methodology for arc characterization that could be used on real aeronautical structures, particularly painted and protected CFRP thin skin used for aircraft wing box and fuselage.

As mentioned in the introduction of the dissertation, the objectives of the present study are to provide answers to important questions, which can be summarized as follows:

- How is the evolution over time of the lightning arc? What is its size and shape? Is there an influence of the current level? Is there a strong shock wave induced by the arc expansion? What are the characteristics of this wave?
- What are the arc electrical characteristics? How the conductivity varies with time? What electrical energy does the lightning arc absorb?

- What are the temperatures and pressures distribution of the arc column? How they change with time and with the arc current?
- Are there some differences between a free arc column and an arc interacting with aeronautical materials? How do the arc properties change when applied to different materials and surface coatings?

Chapter II.

Experimental setup, diagnostics and characterization methods

In this chapter, we describe the experimental tools used to achieve the objectives of this work. We present the lightning current generator utilized to create the transient lightning arcs. Furthermore, we introduce the employed electrical and optical diagnostics, both for the arc column and for the material under test, and also their main characteristics and limitations.

II.1 Experimental setup

In this section, the current generator, utilized to create the transient lightning arc studied in this work, is briefly described. Two different configurations of the electrodes are also presented. These configurations allow us to study either the free arc column or the arc-material interaction.

II.1.1 Current generator

To reproduce the arc lightning plasma in laboratory we use the GRIFON generator (*Générateur de Recherche sur l'Impact du Foudroiement de l'ONera*). The discharge is produced in accordance with the criteria imposed by the aeronautics standards, described in the document SAE ARP 5416A (2005). The shape of the high current pulsed arc studied in this work is the D-component of the lightning wave sequence. As described in Chapter I (section I.3), this component corresponds to the subsequent lightning return strokes that can arise during the continuous phase. In terms of aircraft zoning, this wave is associated with the fuselage parts of the aircraft (see chapter I, Figure I.13).

To generate this waveform, the current generator is formed by four capacitors of 52 µF each, connected in parallel, which discharge through a series of ballast resistors. These resistors are separated in two branches and their value can be adjusted to obtain different waveform shapes. The equivalent resistance used in this work is 193 mΩ. The initial voltage of capacitors can also be adjusted from 14 to 40 kV to provide different types of current waveforms. Figure II.1 presents a picture of the current generator, highlighting the main components.

The capacitors are charged with negative or positive high voltage power supply. A spark gap is used to switch on the circuit once the capacitors voltage reaches the target voltage.

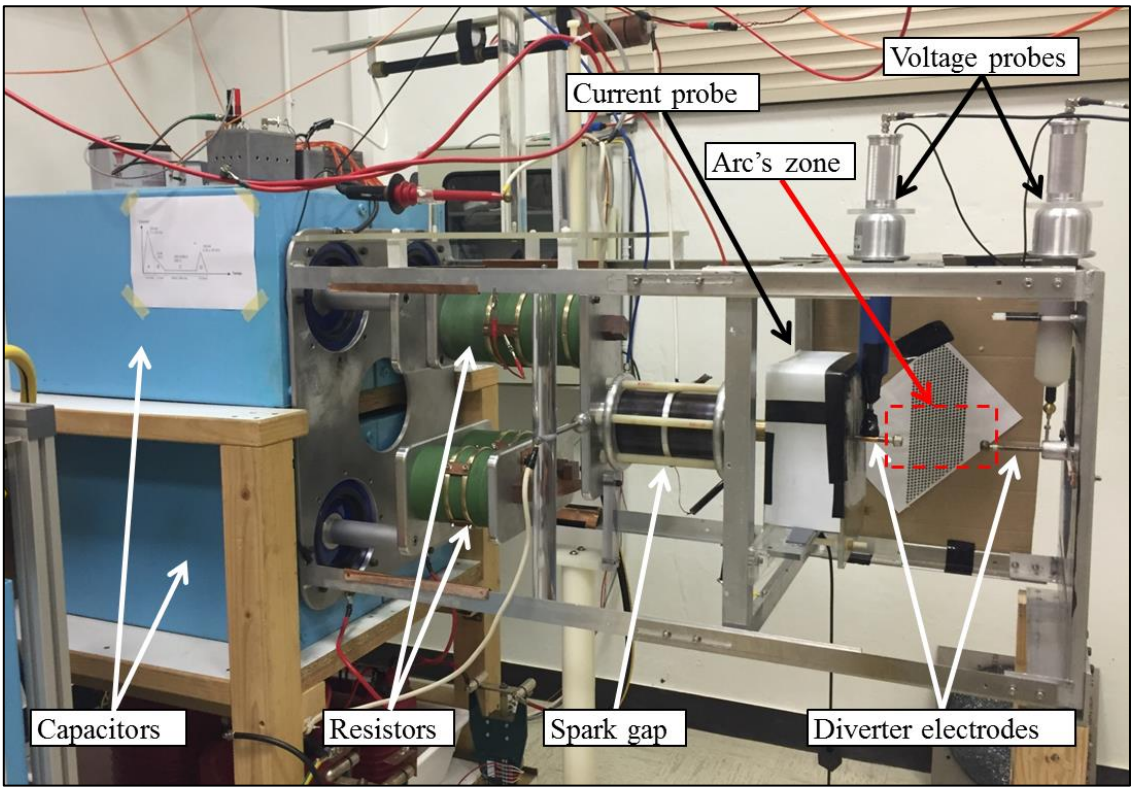

Figure II.1. GRIFON current generator.

During the capacitors discharge, an inductive component appears from the self-inductance of the structure. To minimize this undesired inductance, which limits the growth rate of current, the generator is designed in an approximated coaxial structure. The current flows in the discharge located at the central axis of the structure and returns toward the capacitors by four symmetric aluminum bars. In a simplified way, the generator can be seen as an RLC discharge circuit. The coaxial structure is grounded via a 1 kΩ resistor.

The test zone is located at the end of the coaxial structures. The length of this zone can be adjusted according to the test to be performed and the instrumentation to use. This set-up can received different kinds of objects to be tested, for instance panels and flat structures, fastening assemblies, cables, tubes and bars or electrical systems.

II.1.2 Electrodes configuration

The arc is created between two electrodes. In a standard certification test procedure, one is formed by the object under test, generally a flat structure of hundred millimeters side. The other, called jet diverter electrode is formed by a tungsten rod on which a dielectric sphere is fixed at its tip. This technique allows, on the one hand, to avoid the formation of a jet of plasma directed from the electrode to the sample, such as in a welding arc configuration. On the other hand, it avoids the appearance of a shock wave directed toward the sample surface that would produce additional mechanical stress.

In addition to this standard certification configuration, we adapted the electrodes to obtain a second setup. The panel was replaced by another jet diverter, to obtain two electrodes with an identical form. This yields a symmetric configuration, which helps the evolution of the arc column in a cylindrical plasma channel. Moreover, this configuration allows us to analyze mainly the free air plasma produced by the current flow, thereby, avoiding major effect from the electrodes. The distance between the two dielectric spheres can be adjusted from 60 mm to 180 mm to investigate the electrical properties of the arc channel, and is used in Chapter IV. In Chapter III and V this distance is fixed to 120 mm. In this work, the second setup will be denominated *diverter-diverter* configuration, in contrast to the first one, which will be named as *diverter-panel* configuration.

Figure II.2 illustrates the two electrodes configurations utilized in this work. The *diverter-diverter* configuration is used to study the plasma of the free arc channel. The *diverter-panel* configuration is employed for the characterization of the arc attachment point and the interaction between the plasma and the aeronautical material. This last configuration is used in Chapter VI with the distance *diverter-panel* fixed to 60 mm.

In order to reduce the working voltage, the arc is ignited with a thin conductive wire with diameter of tens of micrometers. For the *diverter-diverter* configuration, the ignition wire is fixed on the electrodes at the junction between the tungsten rod and the dielectric sphere and it is strained, passing outside the sphere. For the *diverter-panel* configuration, the ignition wire is fixed at the center of the square panel and on the jet diverter electrode at the junction between the tungsten rod and the dielectric sphere. For every shot, this filament is rigorously aligned and fixed at the same location, to ensure repeatability of the experiment. We present in chapter 3 a brief comparison of the effects of 12 µm metal wire and a thinner carbon wire.

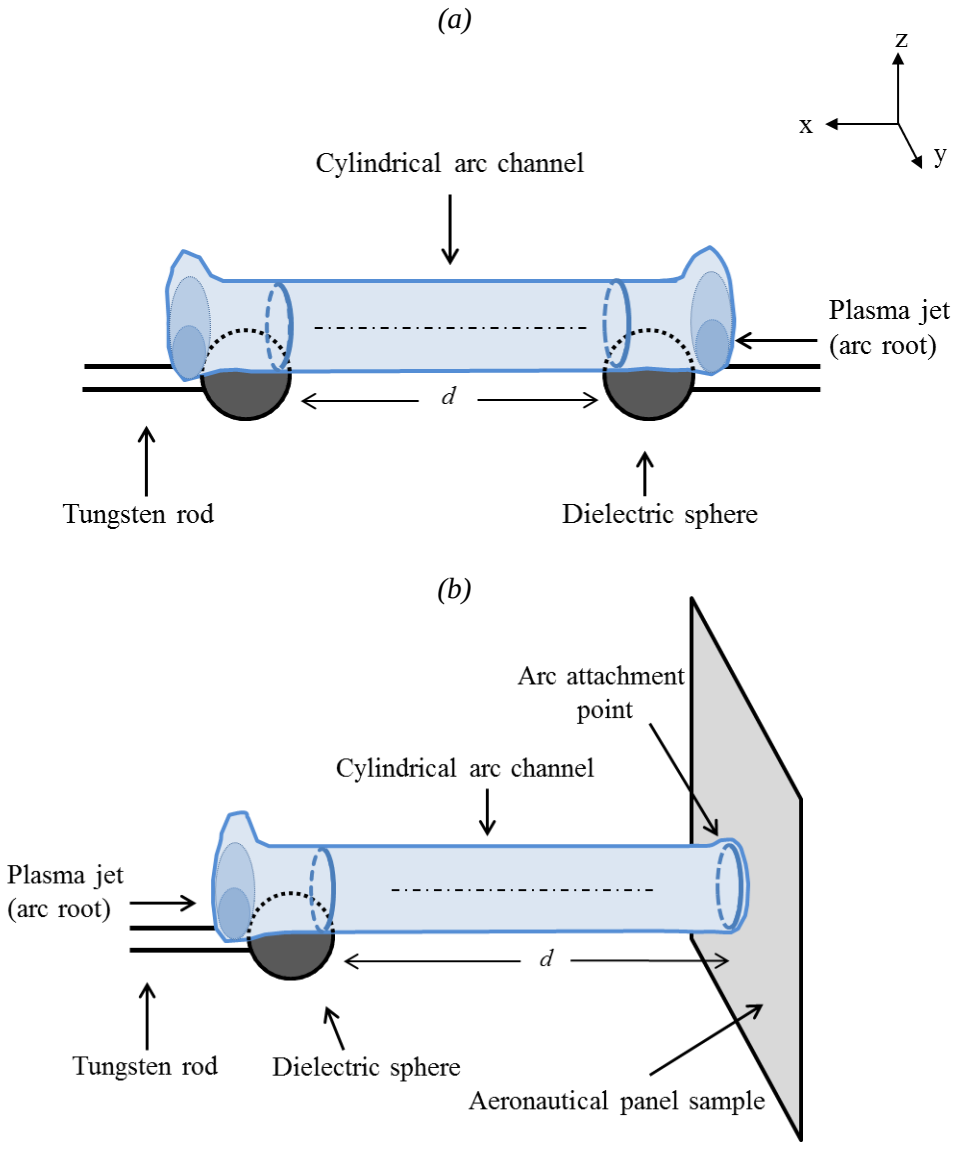

Figure II.2. Electrodes configuration. (a) diverter-diverter. (b) diverter-panel.

II.2 Electrical diagnostics

The current measurements are realized using a current monitor Pearson 1423, which has a sensitivity of 0.001 V A^{-1} with 1% precision and a bandwidth of 1.2 MHz. The current is measured on the tungsten rod of the high voltage side (see Figure II.1). To avoid any problem of voltage floating, the two voltage probes are referred to the ground and a differential measurement is made to acquire the arc voltage. The voltage is measured by using two high voltage probes North Star PVM-1 which can measure a maximum pulsed voltage of 60 kV and have a bandwidth of 80 MHz and accuracy better than 3%.

Since the generator is not an ideal current source, the current measurement is compulsory. Moreover, in arc modeling, the main input of simulations codes is the current waveform. This quantity drives all others physical properties in the arc plasma, as temperature, pressure and velocity distributions. Therefore, to build a solid experimental database, the generator was adapted to produce different current waveforms, including standard components (ARP5412A (2005)).

The generator is able to deliver D- and A_h- component, but is not able to deliver an A-component. The main electric characteristics of the standards waveforms are summarized in table II.1.

Table II.1. Electrical characteristics of the standard waveforms.

	A	**A_h**	**D**	**D (GRIFON)**
Current peak (kA)	200±10%	150±10%	100±10%	100±5%
Action integral (kJ Ω^{-1})	2000±10%	800±20%	250±20%	270±10%
Rise time (µs)	<50	<37.5	<25	7
Max time to 1% of peak value (µs)	500	500	500	304

The action integral is the integral of square of the current, expressed in A^2 s or J Ω^{-1}. The thermal energy dissipated on the objected under test is given by the product of the action integral and the resistance of the object. The rise time is defined in this standard by the time between 10 and 90% of peak amplitude, assuming a monotonic rise of the current before the time of peak. The maximum time to reach 1% of the peak value, during the decreasing phase, is

used to constraint the action integral to be dissipated in a maximum time. The right column presents statistics on GRIFON generator, compiled with hundreds of shot on different type of test objects. The generator delivers a D-component is accordance to the standards, with a relatively fast rise time and a high action integral.

The parametric study is then performed for five peak levels ranging from 10 kA to 100 kA. These current are scaled D-components of the standard lightning sequence. The arc's voltage and current are measured over time for the five current peak levels. Figure II.3 shows the averaged current waveforms delivered by the generator and the standard deviation for the 100 kA peak computed for 20 shots performed with a 120 mm long *diverter-diverter* configuration. A similar repeatability was found for over more than 50 tests and the standard deviation remains always lower than 0.3 kA.

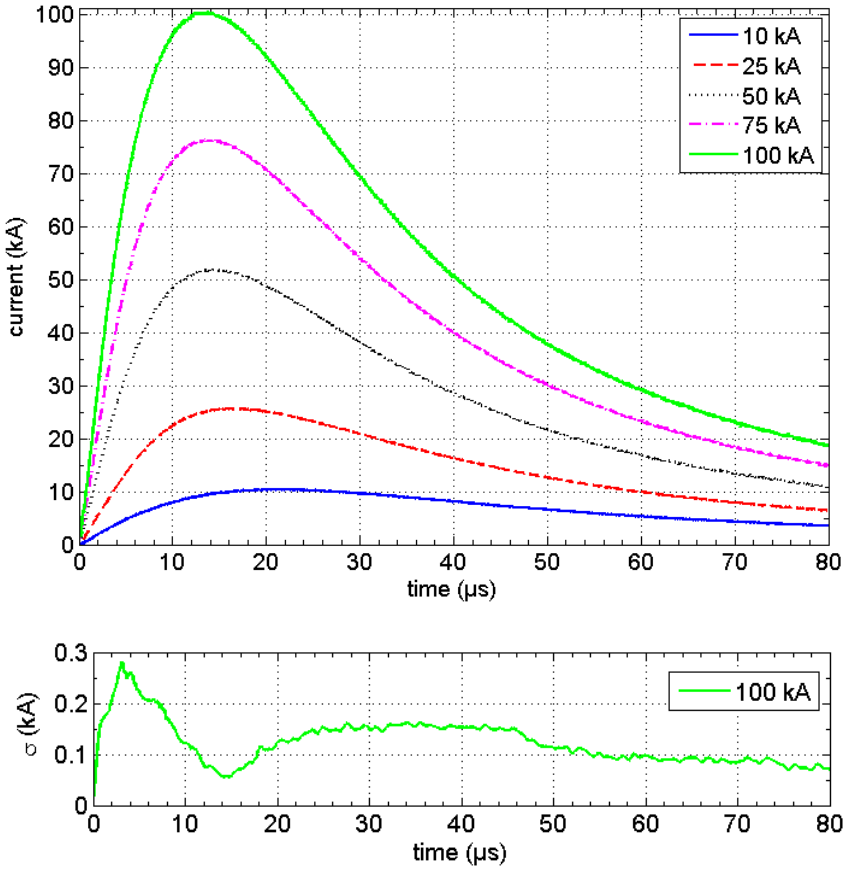

Figure II.3. Average of the measured current waveform produced with the experimental setup. On bottom part the standard deviation for the 100 kA peak level calculated using 20 shots.

Four main parameters drive the current waveforms; the charging voltage of the capacitors, the generator electrical components (capacitors and ballast resistors), the geometry of the structure, and the test object (including the arc). The generator characteristics were kept constant during

the experiments. The charging voltage was the only modified parameter to achieve the different levels of current, which causes a slight deformation in the waveform. The time to reach the current peak is slightly shifted, changing from 21.3 µs in the case of 10 kA to 13.5 µs for 100 kA. These deviations can be also viewed as a variation of the arc impedance for the different current peak levels. Chapter IV is dedicated to the study and discussion of the electrical behavior of the arc plasma.

II.3 Optical diagnostics of the arc column

The high current and high power density in the electric arc prevents the use of intrusive diagnostics. Consequently, non-intrusive approaches, as optical diagnostics, are better suited. Among different methods, we have chosen to use three techniques; high-speed imaging, background-oriented schlieren, and optical emission spectroscopy. All these techniques are described in the following subsections. Figure II.4 shows a picture taken from the arc position which illustrates a few optical diagnostics that observe the arc.

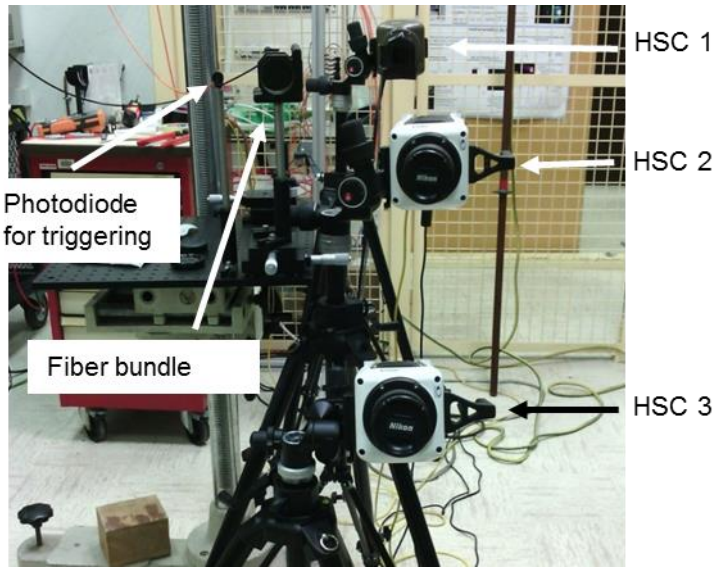

Figure II.4. A few optical diagnostic viewed from the arc position.

II.3.1 High-speed imaging

Arc plasmas in ambient air are generally highly luminous and suitable for observation and characterization by fast imaging. Qualitative information can be observed, as the presence of an unstable and chaotic behavior in the electric discharge beyond a few hundred of microseconds. Also, high speed imaging allows us to obtain quantitative information, such as light intensity

profiles during the first microseconds of the arc lifetime. In this work, these light intensity profiles are used to determine the arc channel shape and the luminous channel radius over time.

The three high speed cameras (HSC) employed in this work are Phantom V711 from Vision Research, which have a CMOS sensor of 1280 × 800 pixels with a pixel size of 20 µm. The HSC can work up to 1.0 Mfps at reduced resolution of 128 × 16 pixels and allows us to set the exposure time to a minimum of 300 ns. Figure II.5 shows a picture of the arc channel taken with a resolution of 256 × 96 pixels, which imposes a maximum frame rate of 200 kfps, and an example of luminous intensity profile of the central region of the arc column. Using this setup configuration, we can evaluate characteristics lengths of arc column as its shape and the luminous arc radius by applying different criteria, which will be presented and discussed in the next chapter. Also this allows us to evaluate the time after which a turbulent and chaotic behavior takes place and then the axisymmetric assumption for the arc channel is no longer valid.

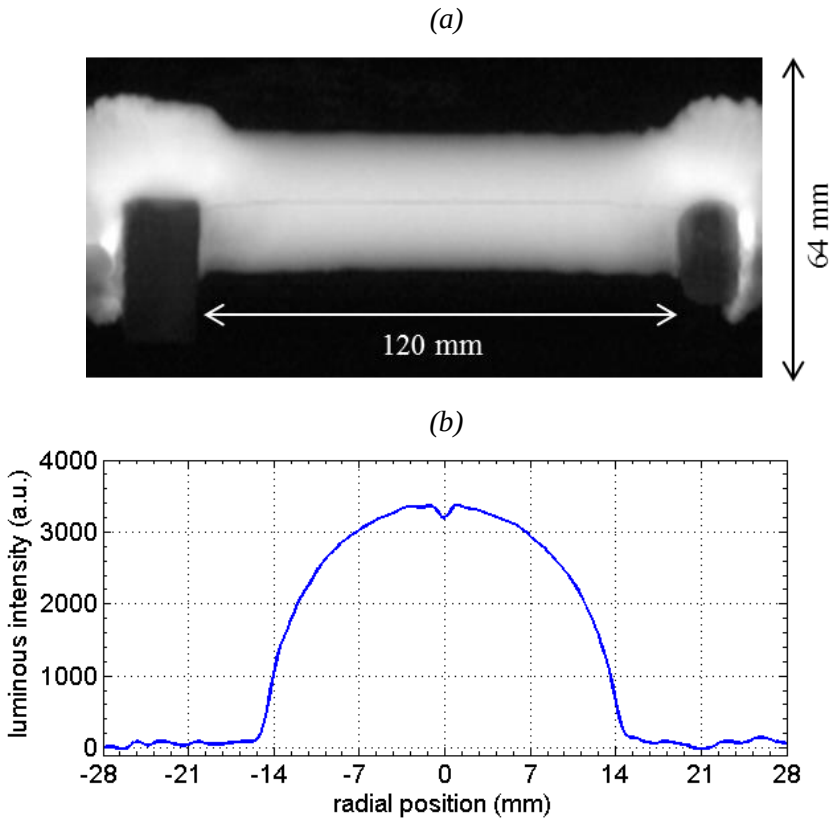

Figure II.5. (a) Picture of the arc in the diverter-diverter configuration for a 100 kA peak waveform at 14 µs after ignition (resolution: 256 × 96 pixels; scale: 0.67 mm/pixel;exposure time: 300 ns). (b) Light intensity distribution along the radial direction at mid-distance between the dielectric spheres (saturation: 4095 a.u.).

II.3.2 Background-oriented Schlieren

The fast increase of the temperature in the arc channel leads to the propagation of a strong shock wave in the radial direction of the arc. This shock wave exhibits a strong discontinuity of the mass density which makes possible the use of schlieren techniques. This technique is a well-known method to visualize density gradients in compressible media. It is based on the refraction of light crossing a media with variable refractive index (Settles (2001)). Among different schlieren methods, the background-oriented schlieren (BOS) was selected due to the high luminous intensity of the arc plasma. This method allows refractive matters to be visualized by their distortion of a patterned background (Settles (2001); Hargather and Settles (2010)). In this work, BOS is employed to assess the position and velocity of the wave front over the time, and also, the mass density distribution inside the shock wave.

The BOS camera can be positioned in the axial direction of the column arc, as illustrated by the camera 'HSC axis direction' in the diagram of Figure II.6. This configuration allows us to analyze the cylindrical form of the shock wave and its radial propagation around the arc channel. Also, the BOS camera can be placed in a perpendicular direction to the discharge axis, at the same point of view of the light intensity measurements camera. The cameras can be positioned at two or three meters from the column axis, to allow different measurement resolutions. The background is located 30 cm behind the column axis. To ensure a parallel collection of the light issued from the background, the focusing is done at mid-distance between the background and arc column, and the minimum aperture size (f/22) is employed to increase the deep of field.

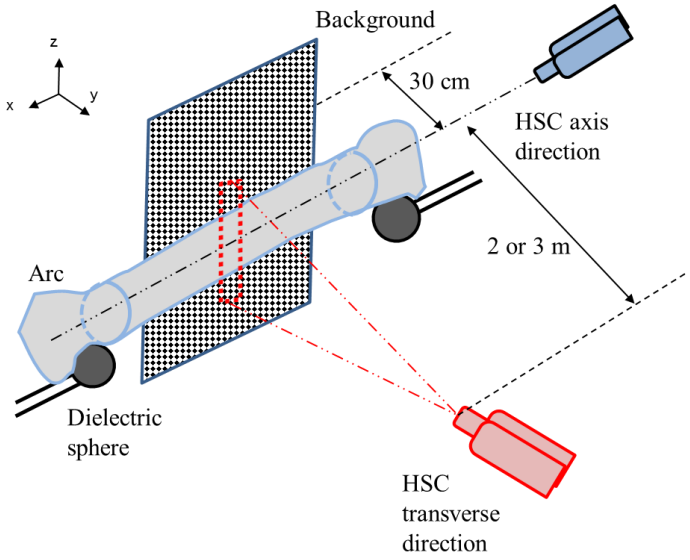

Figure II.6. Schematic diagram of the BOS setup and the two directions utilized to characterize the shock wave.

Figure II.7 shows some pictures of the shock wave propagation taken from this position. The images are purposely saturated in the arc channel to allow the collection of enough light from the background and therefore are not used for the luminous radius analysis.

Generally to improve the image correlation in the BOS method, the background is formed by a black surface with a random speckle pattern on white paint. This type of pattern is used in this work for qualitative analysis. To perform a quantitative study, we choose to work with a background formed by a black/white square mesh, similar to a checkerboard, due to the limited number of pixels in our pictures. We can identify the position of wave front by the detection of the changing patterns of the background squares. For the detection purposes, we used the difference between the image to be analyzed and a reference image, taken without arc. In the next chapter, the processing and correlation image criteria will be discussed in details.

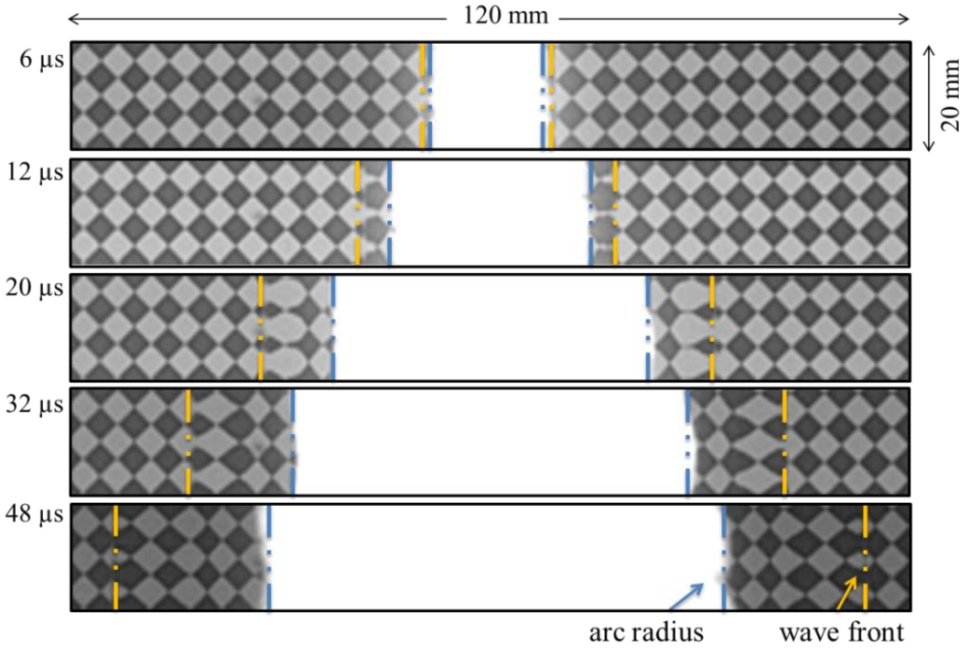

Figure II.7. Pictures of the luminous central arc region and shock wave evolution for the 100 kA peak.

II.3.3 Optical emission spectroscopy

Optical emission spectroscopy (OES) is commonly used as diagnostic method to characterize arc plasmas, due to high intense radiation emitted by the arc. In this work, OES is used to perform a time- and space-resolved study of the intensive thermodynamic properties of the lightning arc channel as the temperature, the electron density and the pressure distribution.

A direct collection of the light toward the spectrometer's entrance slit is not possible due to the intense electromagnetic noise emanated from the current generator. Therefore, the spectrometer

is located in another room and an optical fiber bundle with 16 fibers and 20 m length is used. The fibers have a diameter of 250 µm, and are positioned in a line array with a spacing of 500 µm between two fiber centers.

An optical system is used for imaging a transverse plane of the arc channel at the entrance of the fiber bundle. The optical system is formed by two achromatic lenses optimized in the visible range (400 nm to 700 nm), with a focal length of 750 mm for the lens L_1 and 400 mm for the lens L_2, to allow more flexibility in the magnification factor, and with a diameter of 50.8 mm. As illustrated in Figure II.8, a different point inside the arc channel is imaged in each fiber. The distance between the arc and the first lens is 1.5 m, which is long enough compared to the arc size. The ratio between the diameter of the lenses and the arc-lens distance leads to a very small solid angle for the collected cones, of approximately 0.0036 steradians. Also, the depth of field was verified by analyzing the spot of a laser beam undergoing the reverse optical path. This presented a clear spot at the channel axis and around 10 cm after and before this position. These factors support the assumption of a collection of parallel and narrow chords of the light emitted inside the discharge, which will be considered thereafter in the present work.

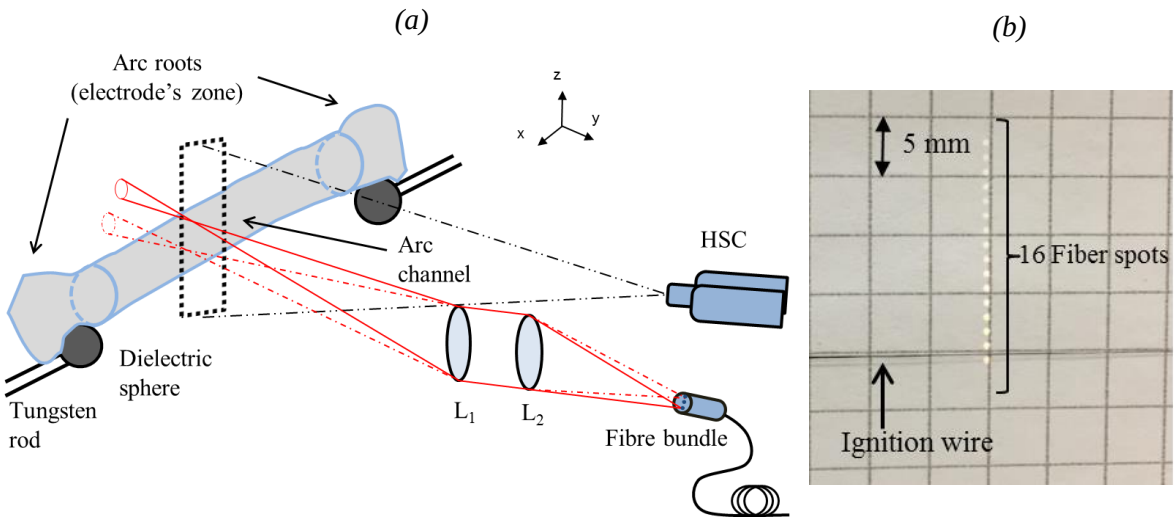

Figure II.8. (a) Optical system for OES measurements. (b) Fiber spots collected by the optical system for an asymmetrical bundle configuration.

The spacing between two collected chords can be adjusted between 1.2 mm to 2 mm. The spatial resolution, deduced from the spot size of a laser beam, can also be adjusted between 1.2 mm to 2 mm. The fiber bundle can be translated in the radial direction to allow the collection of light from only one half of the arc. It is used centered, when both sides of the column profile can be captured with the best spatial resolution (1.2 mm by fiber). For arc diameters that exceed 20 mm the bundle is moved to get light from only one half of the column.

The spectrometer used is an ACTON SP-2750 with 750 mm focal length, which is mounted with two gratings of 300 grooves mm^{-1} and 600 grooves mm^{-1}, both blazed at 500 nm. Using an entrance slit aperture of 20 µm, the gratings yield a measured slit function with full width at half maximum (FWHM) of 0.166 nm and 0.083 nm, respectively. This slit function is measured using a HeNe laser line (632.816 nm). The FWHM is assessed by an adjusting of the measured line by a Voigt function, which is the result of the convolution between a Gaussian and Lorentzian function. Figure II.9 shows the measured slit functions and their correspondent Voigt fit.

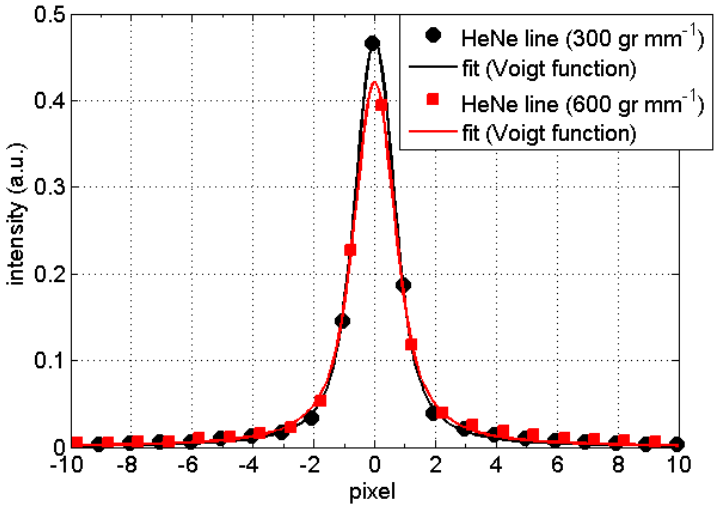

Figure II.9. Measured HeNe line (632.816 nm) used for slit function determination. For the gratings of 300 grooves mm^{-1} and 600 grooves mm^{-1}, one pixel corresponds to 0.104 nm and 0.05 nm, respectively.

The detection is realized with an intensified CCD camera PI-MAX 2 Roper Scientific (512 × 512 pixels of 13 μm^2), controlled by a ST-133 camera controller. The acquired spectra were calibrated in relative intensity for each fiber using a DH-2000-CAL Deuterium Tungsten-Halogen Calibration Light Source from Ocean Optics.

Figure II.10 shows an example of calibrated spectra recorded with this diagnostic setup. As one moves from the arc edge to the center, the different collected spectra shows a significant variation in the continuum emission.

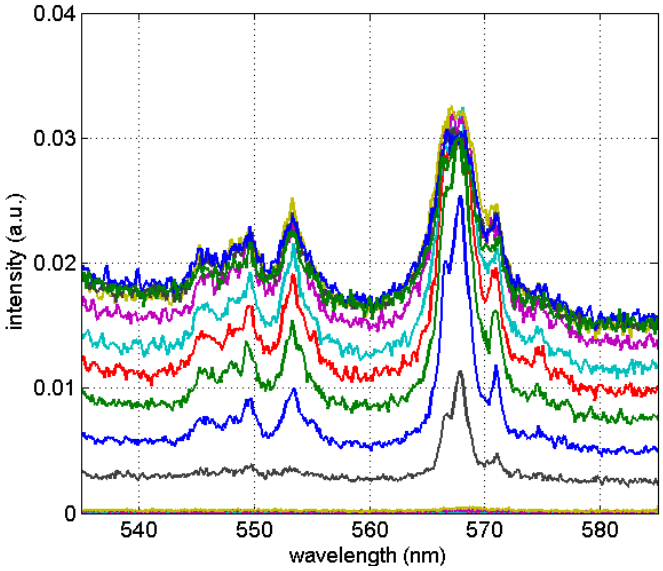

Figure II.10. Example of spectra collected by the diagnostic setup at different position inside the channel arc. Experimental parameters: current peak = 100 kA; time = 9 µs; exposure time = 200 ns.

The positions covered by the 16 collected chords are adjusted to ensure that at least one chord is located outside the arc. Therefore, the farthest (from the arc center) collected chord shows no intensity in the visible spectral range. This configuration allows us to precisely determine the first chord that crosses the arc channel, but also to validate the parallel and narrow light collection assumption gives by the optical system.

To perform time-resolved OES measurement, we need to synchronize the arc with the spectra acquisition. The ICCD camera gate is synchronized with the arc current triggering by a photodiode Thorlabs SM05PD1A (13 mm^2 of active area and 10 ns of rise/fall time) which observes the arc channel at the same point of view as the optical system (at mid-distance between the electrodes). Figure II.11 shows three signals; the voltage obtained from the photodiode, the normalized current of the arc and the ICCD camera gate. The voltage value chosen as threshold criterion to trigger the camera gate is 0.3 V, which is approximately in the middle of the rising edge of the photodiode signal. This value corresponds to 5% of the current peak, which is 0.5 µs after the current initiation. This delay is taken into account to set the pulses of the camera controller. The jitter in the synchronization system is estimated to 0.1 µs and was determined by systematic recording of the three signals in the same oscilloscope.

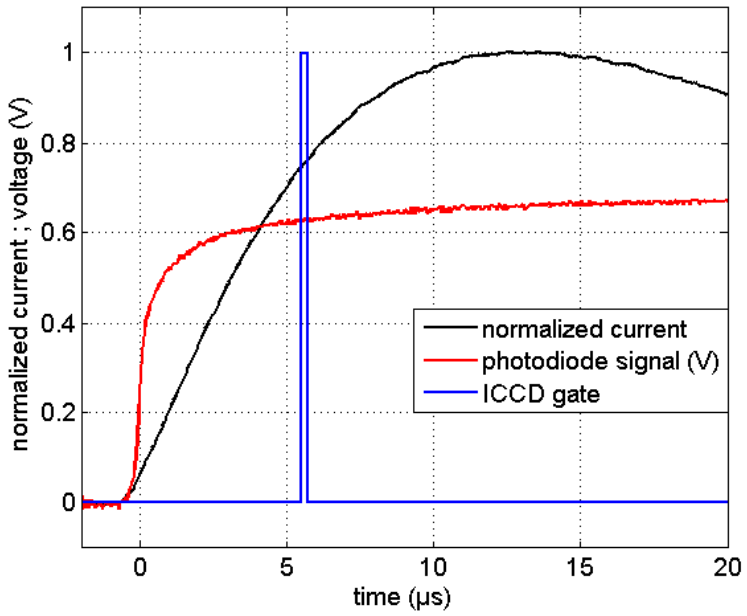

Figure II.11. Synchronization between the current waveform and the spectra acquisition. In this example, the gate is opened 6 µs after the current initiation and has a width of 200 ns.

II.4 Optical diagnostics of the material under test

Intrusive diagnostics of the material under test are also not suitable, because of the arc constraint and the undesirable effects that could be caused by the sensors. Consequently, two optical diagnostics were used. The infrared thermography was used to evaluate the thermal constraint, and the deflection measurement was used to evaluate the mechanical constraint. These techniques are described in the following subsections.

II.4.1 Infrared thermography

Heat flux due to the arc/panel interaction can be investigated by infrared thermography (IRT) measurement in the rear face of the panel under test.

The measurements are performed with an infrared (IR) camera Optris PI160, which has an uncooled detector of 160 × 120 pixels of 25 µm^2. The spectral range of the detector is from 7.5 µm to 13 µm and the acquisition frame rate is 120 Hz. The camera is mounted with a telephoto lens, which has a field of view of 6° × 5° and a focal length of 35.5 mm. The rear face of all studied panels is painted with a matte black aerosol paint to ensure the same emissivity. The calibration is performed by applying an experimental curve. This experimental reference curve is obtained by heating the panel with an external source (in the range of 30 to 260 °C) and

then measuring the surface temperature with both the IR camera and an high accuracy platinum resistance thermometer probe (PT100, 0.2 mm diameter), which is fixed at the rear panel surface. The experimental calibration curve and the setup for calibration are presented in appendix A. The obtained temperature ratio between IR camera and PT100 measurements is 0.996, which shows that the paint emissivity is very close to 1.

The camera is positioned in the axial direction of the arc channel and observes the rear face of the panel at 0.5 m or 1.2 m from it. The area monitored by the camera is a rectangle that can be adjusted to 50 × 37.5 mm^2 or 124.8 × 93.6 mm^2, centered at panel center. Figure II.12 shows an example of a surface temperature obtained with the diagnostic setup and temperature profiles for different times.

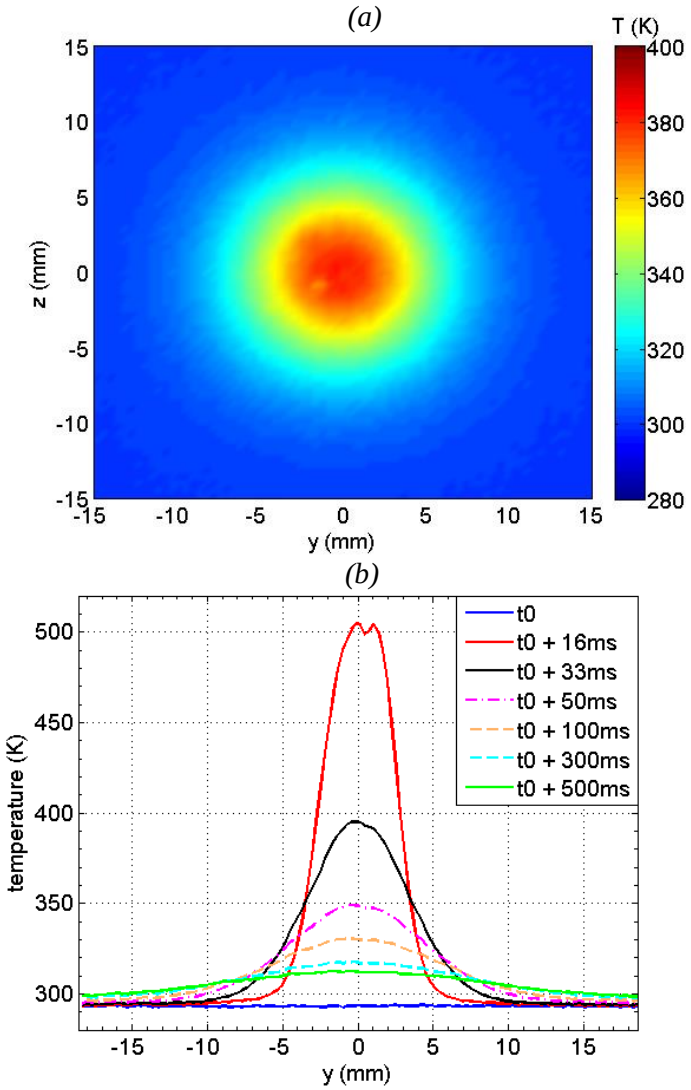

Figure II.12. (a) Surface temperature in the rear face of an aluminum panel of 1 mm thickness with paint of 100 µm at 33 ms after the trigger. (b) Temperature profiles for z = 0 at different times (scale: 0.31 mm/pixel; current peak: 100 kA).

II.4.2 Deflection measurement

Deflection and plastic deformation are expected in the panels under test due to the mechanical constraints that act on the arc attachment point. Two different methods were used to evaluate this displacement over time and position.

II.4.2.1 Stereo-digital image correlation

The stereo-digital image correlation (Stereo-DIC) is a common tool to perform deflection measurement over the surface of an object. It is an optical technique capable of performing full-field shape, displacement and strain measurements on length scales ranging from microns to meters with a time resolution up to nanoseconds (Genovese et al. (2013)).

This technique can be described as follows: a series of image pairs captured from two different points of view of the object are used to locate and track a given set of surface points during motion and/or deformation. To correlate the two stereo-views, DIC requires the object surface to be provided with a random pattern of dark and bright features. This allows finding the best match between corresponding points in the two images by comparing the local grey scale distribution of square pixel subsets on the basis of the normalized cross correlation coefficient.

Therefore, the rear face of the panel is visualized to obtain the motion of the panel over time after the lightning arc impact in the front face. In this work, the two points of view are taken and recorded using only one high-speed camera and a plane mirror. This adaptation avoids the need of multiple cameras synchronization, as well as it saves a HSC that can be used in other diagnostic techniques. Figure II.13 shows the setup for Stereo-DIC measurements and an example of a picture recorded by the HSC.

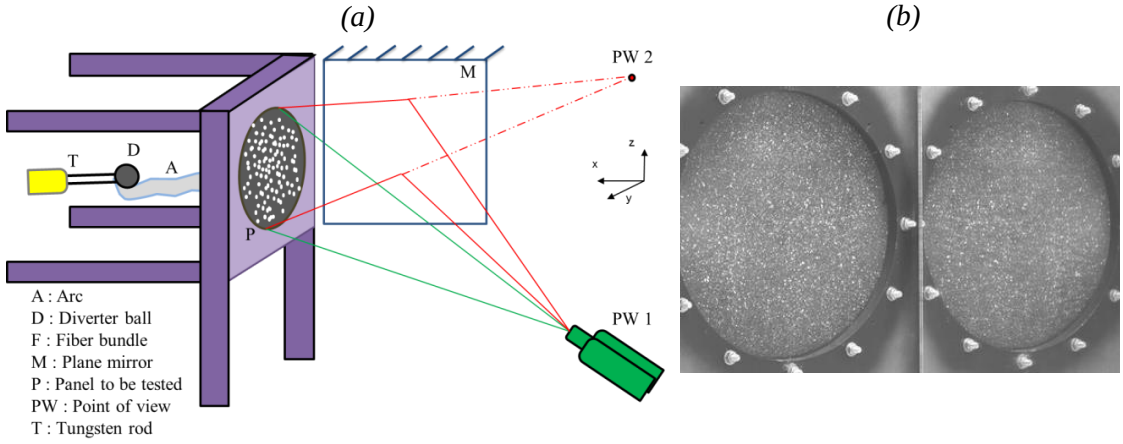

Figure II.13. (a) Setup for Stereo-DIC measurement. (b) Example of two points of view taken using only one HSC and a plane mirror (resolution: 800 × 500 pixels; scale: 0.75 mm/pixel).

The rear face of the panel is painted in black with a random speckle pattern in white paint, in order to improve the image correlation method. The image processing is performed using a dense window-based algorithm, named FOLKI (Le Besnerais et al. (2009)). This stereo-DIC processing tool was developed at ONERA and is based on the Lucas-Kanade algorithm (Le Besnerais and Champagnat (2005)). FOLKI allows the reconstruction of each point in the panel surface, which provides the deflection of the total surface over time. The calibration of the system is performed with a test card, used to calculate the characteristics of the two points of view (translation, rotation and full field view). The scene is lighted with two high power blocks of LEDs in order to get a low integration time. The frame rate used for this measurement is 16 kfps and the exposure time is set to 62 µs. This adjustment is a compromise for having both a good deflection assessment during the first millisecond and several oscillations of the panel. Figure II.14 shows a few examples of the surface deflection reconstruction of the rear face of panel, which allows us to evaluate the deflection of the total surface over time.

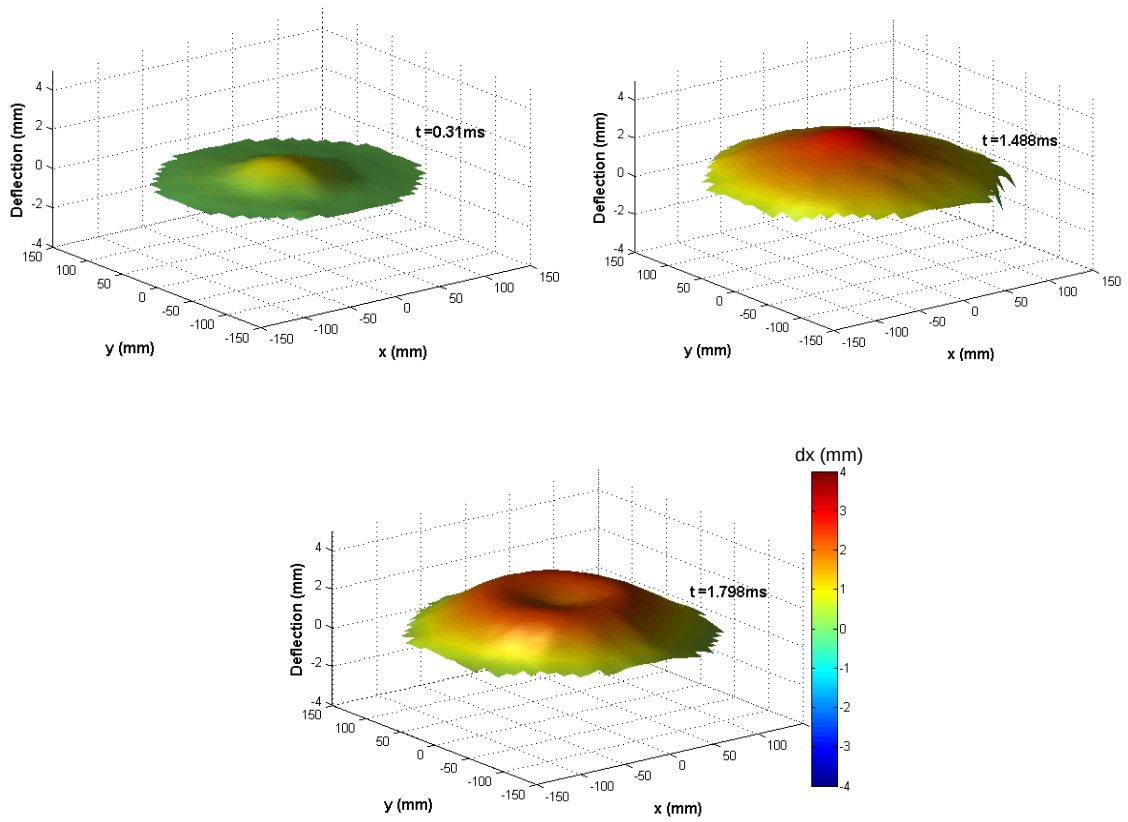

Figure II.14. Examples of deflection reconstruction using the algorithm FOLKI for a 100 kA current peak waveform.

II.4.2.2 Fast direct deflection measurement

In order to evaluate the deflection of one particular point, a direct visualization using only one point of view can be employed. Therefore, to analyze the displacement of the center of the panel

with a high frame rate, we used one HSC at its maximum speed acquisition, which corresponds to a frame frequency of 1 Mfps with a resolution of 128 × 16 pixels. To optimize the spatial resolution, the camera was mounted with a telephoto lens Nikon AF Micro-Nikkor, 200 mm of focal length, and was positioned at 88 cm from the panel center. The exposure time was set to 0.6 µs, and the two high-power LEDs are used to brighten the area of interest. To assess the precise position, a line crossing the panel center is marked in the rear face, which reflects the light from the LEDs and gives sufficient signal to the HSC. To ensure the accuracy of the measurements, a second camera with a similar setup is positioned to observe the displacement of the generator structure.

Figure II.15*(a)* illustrates the diagnostic setup. The HSC observes the panel center from a diagonal direction, with an important angle (~65°) to the arc axis. The setup covers a deflection of 10 mm along the *x*-axis. Figure II.15*(b)* shows an example of the deflection measurements done for the case of painted aluminum panel subjected to an arc of 100 kA peak. The origin of the reference frame in figure II.15*(b)* is set at the intersection between the arc axis and the material rear surface.

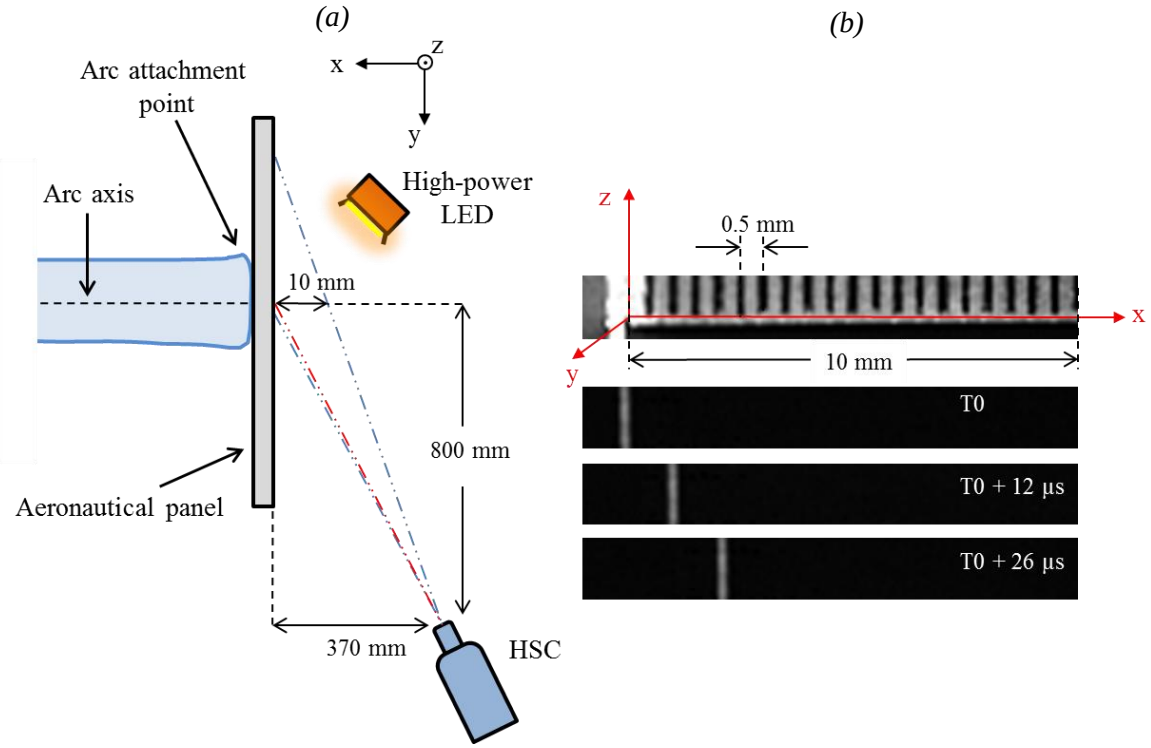

Figure II.15. (a) Top-view of the diagnostic setup for fast direct deflection measurements. (b) Pictures taken using the camera setup of 128 × 16 pixels to the scale settings and an example of deflection measurement for a 100 kA peak current waveform applied to a painted aluminum panel.

Chapter III.
Hydrodynamic characterization of the free lightning arc channel during the high current phase

In this chapter, we investigate the hydrodynamic properties of the free arc channel. This characterization includes the study of several quantities as the evolution over time of the channel arc shape and the luminous arc radius, the propagation of the shock wave induced by the arc expansion and the mass density distribution inside the shock wave.

Two optical diagnostics presented in Chapter II are used for this characterization; the high-speed imaging and the background-oriented Schlieren. To produce the free arc channel and to avoid any major effects from the electrodes, the setup used is the *diverter-diverter* configuration.

III.1 Shape characterization of the arc channel

III.1.1 Ignition wire effect

To start the electric discharge in an air gap with a length in order of ten centimeters, we need to employ some techniques to reduce the breakdown voltage. The usual method is a thin wire to create an initial electrical connection between the two electrodes. We first analyze the influence of this ignition wire in the development of the channel shape.

Metallic wires, typically made of copper or aluminum, are typically utilized for plasma ignition in long arcs. First tests were performed with a copper alloy wire of tens of μm. After record a few videos from different shots, we noticed that the channel exhibits an axial inhomogeneity along plasma column, and a chaotic behavior takes place after a few microseconds. Figure III.1*(a)* shows some pictures of the column at different instants. One possible explanation for this inhomogeneity and instability is the following: when the current level growths, the thin wire is evaporated and gives place to the discharge in air. However, this evaporation is non-uniform, and different amount of copper is projected into the plasma in distinct positions along the column. The wire may be not perfectly cylindrical, which could cause this phenomenon. This copper contamination appears to substantially modify the emitted light intensity of the plasma channel, as highlighted in the two last pictures of figure III.1*(a)*, which prevents the study of the lightning arc itself.

We also performed some test with thin carbon filaments taken from a carbon fiber tow. The results are completely different from what was obtained with copper. The plasma channel develops in a cylindrical and homogenous column around the ignition wire for times lasting to several tens of microseconds. The emitted light is also less important than the previous case. Figure III.1 presents pictures of the columns evolutions for both cases taken at the same instants. Comparing the results of the two wires, we can conclude that the use of carbon wires give more appropriate arc columns for characterization purpose. First, because the arc is more homogenous, and second because the quantity of material inserted into the arc column is less significant than the case of copper wire. The total radius of the carbon tow used for arc ignition is indeed apparently less important than the metal wire, and it is not completely fused during the arc phase (sometimes it is undamaged or partially damaged).

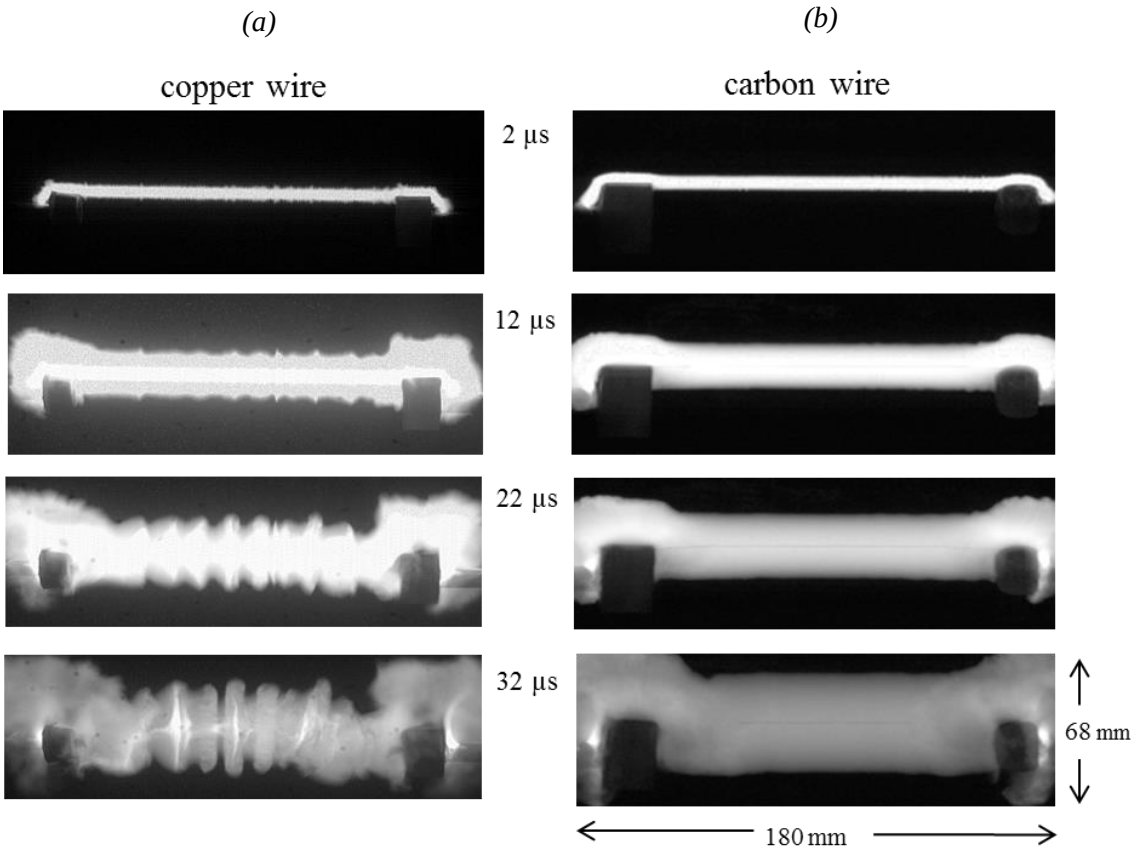

Figure III.1. Comparisons of the development of the arc column using two different ignition wire. (a) Copper wire. (b) Carbon wire. Experimental parameters - resolution: 256 × 96 pixels; scale: 0.70 mm/pixel; exposure time: 300 ns; current peak: 100 kA.

The physics of the ignition with the carbon wire is not completely understood. Most of the wire seems to remain solid during the first 50 µs and can be observed in the pictures at the column axis during those times. It is unclear if there is some amount of carbon evaporated, which makes possible the breakdown triggering or, if a surface discharge takes places around the wire. Using optical emission spectroscopy, we analyzed collected emission spectra in the range of 431.5 to 585 nm. In this spectral range, intense carbon multiplets are expected, as for instance those centered at 493.205 nm, 505.217 nm and 538.033 for C I or at 514.516 nm and 566.246 nm for C II. Nevertheless, no lines were detected at these positions, and then the influence of the ignition wire in the arc plasma was neglected.

In any case, the study of the arc initiation is beyond the scope of the present work. The main objective of the use of a thin wire is to create repeatable and homogeneous arc columns, not or minimally influenced by the ignition technique, to allow then the study of the air plasma properties.

III.1.2 Axisymmetric channel hypothesis

Following the analysis of the ignition wire effects, we observed that the arc initiates around the ignition wire and develops as a cylindrical column. This behavior lasts up for many tens of microseconds until to be disturbed by a turbulent motion that comes from the electrodes (a boundary effect due to a finite channel length). This axisymmetric shape is very useful regarding arc characterization. Firstly, it allows us to define a column radius and a symmetric distribution for all others plasma properties. Secondly, MHD arc models that deal with the high current phase are generally one-dimensional models and have as main assumption an infinite and axisymmetric column. Therefore, producing and characterizing a symmetrical arc column will provide experimental data which are directly comparable with models and results of simulation codes.

To validate the axisymmetric hypothesis, two high speed cameras were used. Both cameras were positioned to observe the discharge at the same transverse plane but in different azimuthal positions. Figure III.2 illustrates the camera setup. Due to the return aluminum bars of the generator structure, we are not able to create an angle of exactly 90° between the cameras and the column axis. However, an angle of 67° was achieved, which allows a suitable visualization from different points of view.

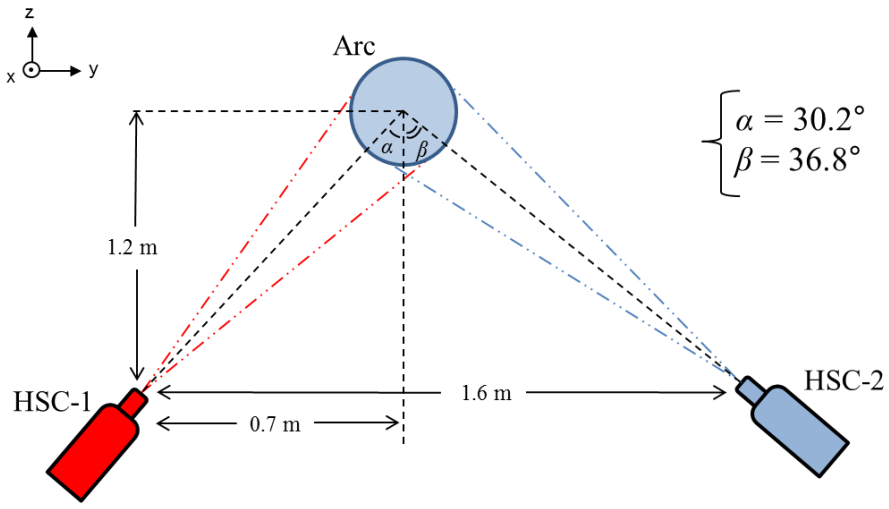

Figure III.2. Schematic diagram for different azimuthal position collection.

Nearly identical light intensity profiles were found in both azimuthal positions as depicted in figure III.3. These profiles are normalized to put in evidence the shape obtained from each camera and to avoid comparison of the absolute light intensity due to the lack of absolute intensity calibration and the utilization of different neutral filters and distances from the arc for each HSC.

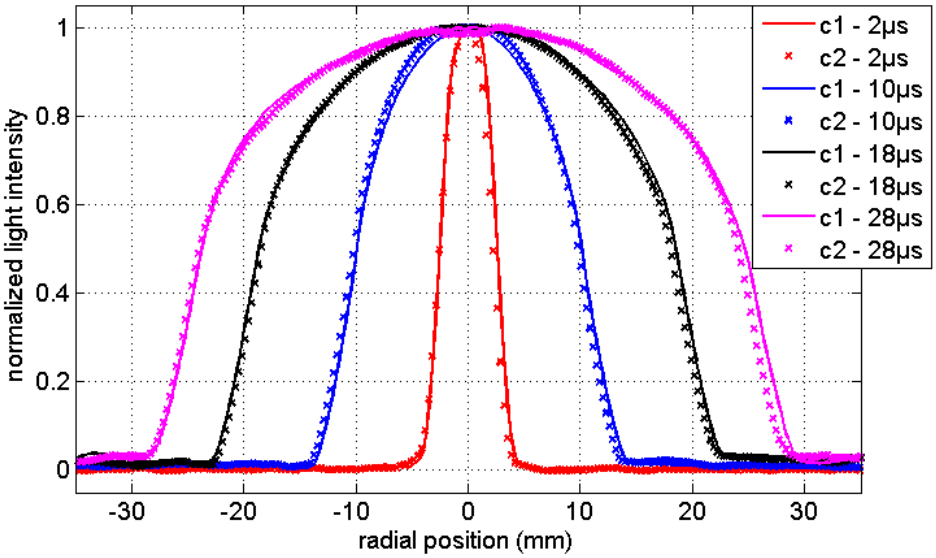

Figure III.3. Light intensity distribution obtained from different azimuthal positions.

The time when the axisymmetric assumption is no longer valid, and the turbulent and chaotic behavior takes place, varies for each current peak. For the arc column with a length of 120 mm (distance between the diverters), this time is about 50 µs for 100 kA and increases as the current peak decreases. For the 10 kA the symmetrical column last up to 80 µs. For a column length of 160 mm, the column is still cylindrical at 120 µs.

III.1.3 Channel radius criteria

We assume that the emitted light is a good criterion to evaluate the shape of the plasma. As a result, we evaluate the conductive radius of the arc from the apparent luminous radius taken from the HSC. In order to define the radius based on the intensity profile measurements, two criteria were tested. The first one was to find the position of maximum rate of change of the intensity with radius for each profile. The second was to use a threshold of 20% of the maximum intensity of all images from a shot. Both criteria lead to approximately the same results, with a maximum difference of 0.8 mm, which corresponds to less than 3 pixels in the best camera resolution (0.29 mm/pixel). Figure III.4 shows two light intensity profile with the modulus of their respective derivatives and illustrate the two criteria.

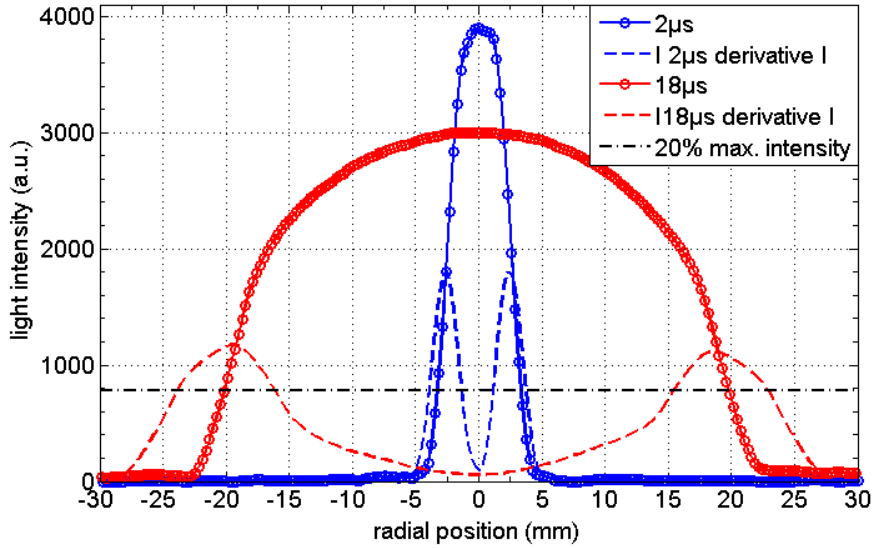

Figure III.4. Criteria for luminous radius determination. Experimental parameters - resolution: 256 × 32 pixels; scale: 0.29 mm/pixel; exposure time: 300 ns; saturation: 4095 a.u..

III.1.4 Luminous radius measurements and expansion velocity

The shape analysis and the axisymmetric validation were done with a spatial resolution (the scale factor given in pixel/mm) that allows the visualization of the total arc channel (see figure III.1). To evaluate the arc radius evolution, we focus our attention on a part of the column at mid-distance between the electrodes, in the most cylindrical zone over the arc length. A resolution of 256 × 32 pixels is then used to improve the frame rate, and the camera is positioned to cover 75 mm in the arc transverse direction, which leads to a scale factor of 0.29 mm/pixel. Figure III.5 shows a set of pictures of the column acquired with this camera setup.

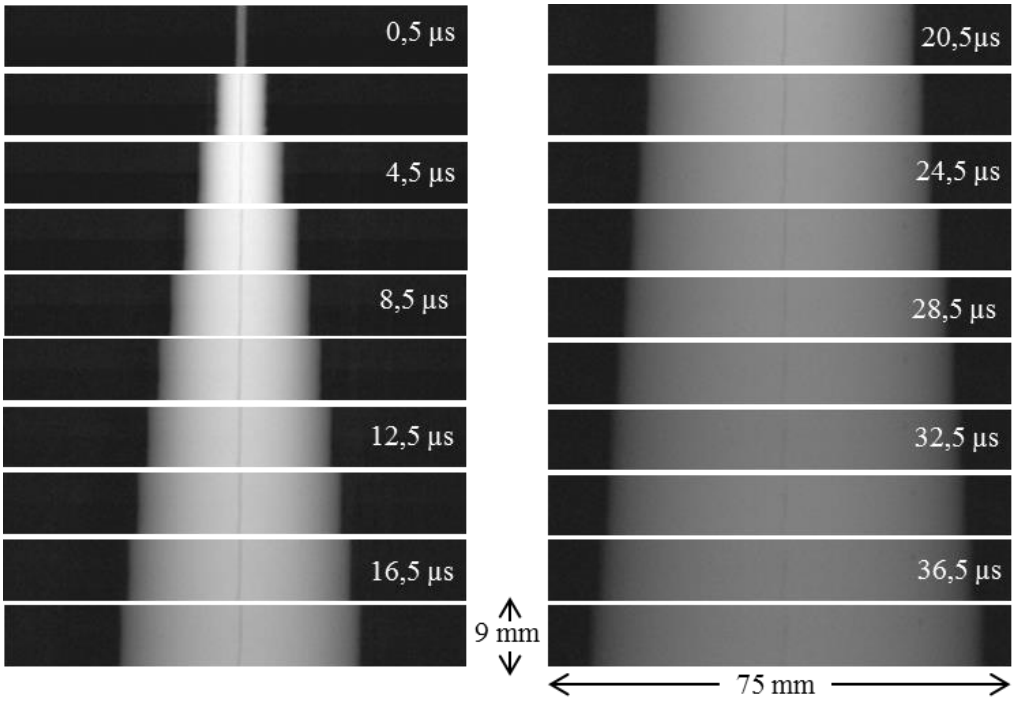

Figure III.5. Pictures of the column expansion during the first 38.5 µs. Experimental parameters – current peak: 100 kA; resolution: 256 × 32 pixels; scale: 0.29 mm/pixel; exposure time: 300 ns.

Along the column axis (*x*-axis in our notation), 32 transverse positions are taken in each picture. The two criteria for radius determination are applied separately for each *x* position and then an average radius is obtained. The procedure is repeated for different shots, which leads to a mean value and a standard deviation for the arc radius. A total of around 50 shots are made for the 100 kA peak, and 10 shots for the others current levels. For each current peak, the radius is estimated during the period when the axisymmetric assumption is adequate. In the present work, the total uncertainty, ε_{total}, in the radius estimation, is calculated for each time as:

$$\varepsilon_{total} = \sqrt{\varepsilon_{statistical}^2 + \varepsilon_{criteria}^2 + \varepsilon_{instrumental}^2} \qquad \text{(III.1)}$$

where $\varepsilon_{statistical}$ is the error obtained from the standard deviation of different shots and transverse positions, $\varepsilon_{criteria}$ is the difference between the results from the two criteria and $\varepsilon_{instrumental}$ is the scale factor, i.e., the length corresponding to one pixel of the camera. The average of the total uncertainty, for the different times and current peaks, is 1.15 mm. Figure III.6 shows the results for the five current peaks with the error bars calculated using equation (III.1).

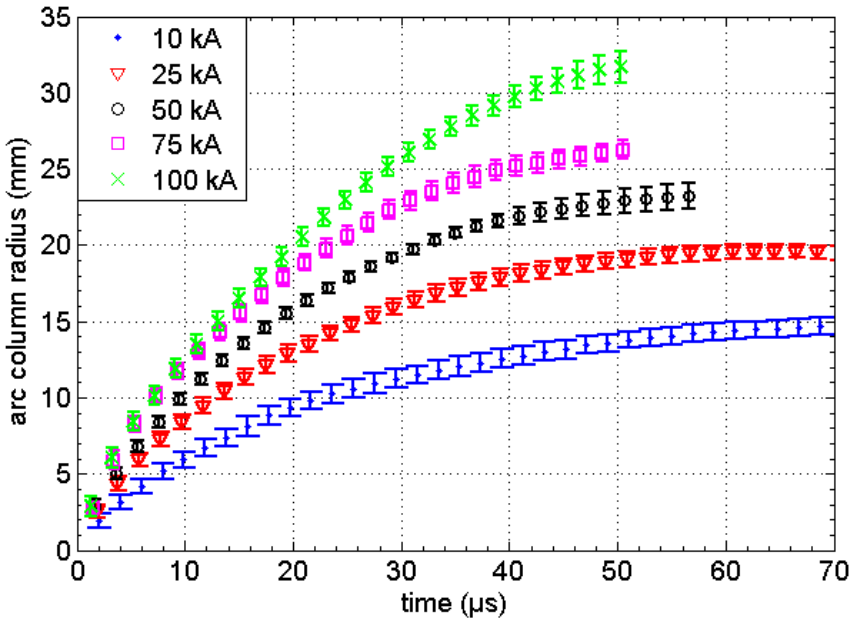

Figure III.6. Luminous arc radius for different current peaks.

The arc column radius reaches 32 mm for the 100 kA peak at 50 µs and 15 mm for 10 kA at 70 µs. The radius evolution has a similar shape for all current peaks. This shape seems to follow a time root square law. The effect of the current peak on the arc radius is monotonic, i.e., the radius increases with the current peak. A quasi-linear dependence was observed for current peaks higher than 25 kA and for times greater than 20 µs. Figure III.7 presents the plot for the column radius versus the current peak for a few instants.

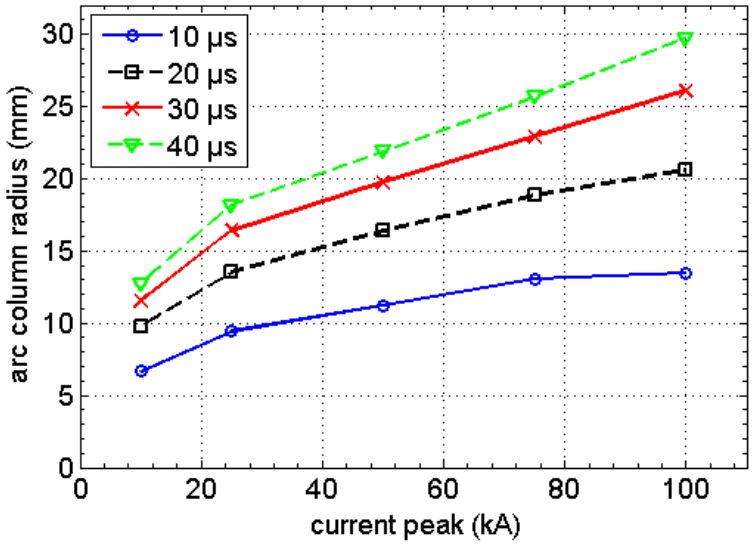

Figure III.7. Arc column radius versus the current peak for different times.

From the radius, we can deduce the expansion velocity of the arc column with a time derivation. Figure III.8 shows this velocity. For the 100 kA current peak, the velocity at 2 µs is close to 2 km s^{-1} and is certainly higher just after the arc ignition. This initial velocity falls to around 0.75 km s^{-1} for 10 kA.

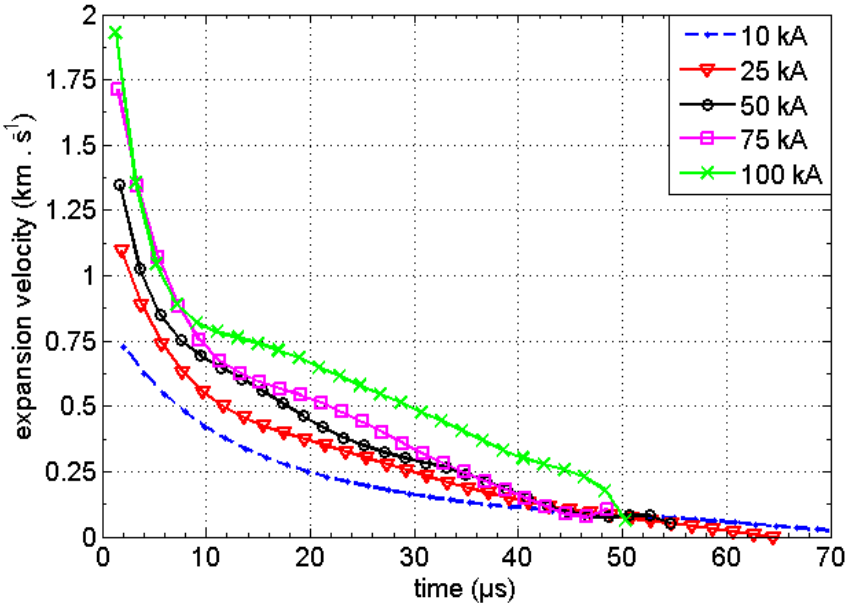

Figure III.8. Expansion velocity for different current peaks.

We can notice a specific feature on velocities for the two highest current arcs (75 and 100 kA) between 10 to 50 µs. The velocities seem to be increased by an additional effect, associated with a bump-component added in the curve. This effect is not well understood.

III.2 Shock wave characterization

Before the arc ignition, the initial air density is that for standard temperature and pressure. However, after ignition, the rapid transfer of a large amount of energy into the small volume of the arc channel rises its temperature and tends to make it expand. This fast expansion, which can reach more than 2 km s^{-1} as deduced in section III.1, gives rise to a strong shock wave in the radial direction of the column. This shock wave exhibits a high gradient of the mass density at the wave front, which modifies the local refractive index, making possible its characterization by schlieren techniques. Due the high light intensity emitted by the arc, the background-oriented schlieren (BOS) method is used to study this shock wave. In this section, we start by analyzing the shock wave geometry and then the wave front position and the propagation velocity are

estimated. Finally, the last part of this section is devoted to the development of a model of the light deflection inside the shock wave to estimate the mass density behind the wave front.

III.2.1 Shock wave geometry

In a first approach, the BOS method is used for a qualitative analysis of the shock wave, which allows us to investigate its geometry. Analytical theories of shock waves (Taylor (1950a); Sakurai (1954); Lin (1954); Sedov (1959)) and experimental investigations of electrical discharges (Freeman and Craggs (1969); Xu et al. (2011); Castera (2015)) demonstrate that a fast energy release in a linear channel will induce a cylindrical shock wave.

To verify the geometry of the shock wave created by the arc studied in the present work, the BOS camera was positioned in the axial direction of the arc column. The random speckle pattern is used in this part once we look for a qualitative analysis. Figure III.9 illustrates a few pictures taken from this position. The set of pictures confirms the expected cylindrical form of the shock wave and its radial propagation from the column axis.

III.2.2 Wave front trajectory and propagation velocity

To follow the wave front evolution accurately, the BOS camera is positioned in a perpendicular direction to the arc column, with the same setup of the column radius measurement camera, i.e., a resolution of 256 × 32 pixels, observing a part of the column at mid-distance between the electrodes. Figure III.10*(a)* shows some pictures of the shock wave propagation taken with this position setup. The images are purposely saturated in the arc channel to allow the collection of enough light from the background.

We can identify the position of the wave front by the detection of the changing patterns of the background squares. For the detection purposes, we used the difference between the image to be analyzed and a reference image, taken without arc. We defined the intensity variation as the root mean square value of all the pixels in the same horizontal position (each column of a picture). The region of the arc channel, which is saturated, does not contribute to the detection and its value is set to zero. Figure III.10*(b)* shows the intensity variation for the five presented pictures. Starting from the farthest position from the center, for each side of the axis, we search for the first intensity variation higher than a threshold level of 40% of the maximum intensity variation in each picture. The position corresponding to the found intensity is defined as that of the wave front.

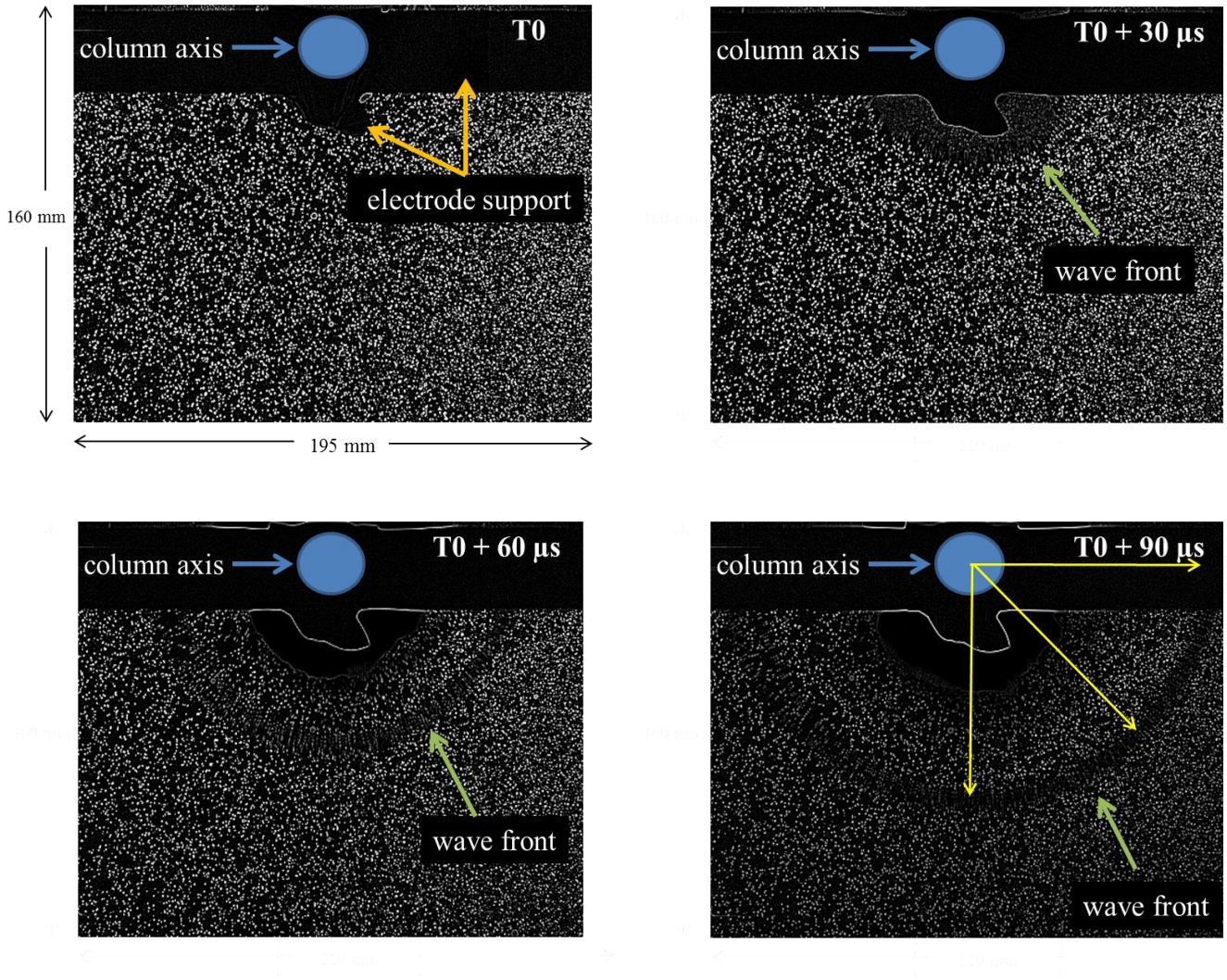

Figure III.9. Pictures the shock wave evolution obtained with the BOS camera in the axial direction of the column for the 100 kA current peak.

Two HSC are used and positioned at different distances from the arc (2 m and 3 m) to cover a larger range of measurements. The nearest camera observes a transverse area of 120 × 20 mm^2 as the pictures presented in figure III.10*(a)*. The light collection in that camera is optimized, by using neutral filters and by adjusting the aperture size, to evaluate the detachment between the wave front and the arc column. The farthest camera observes an area of 160 × 26.7 mm^2 and is configured to collect enough light for wave front detection up to 140 µs.

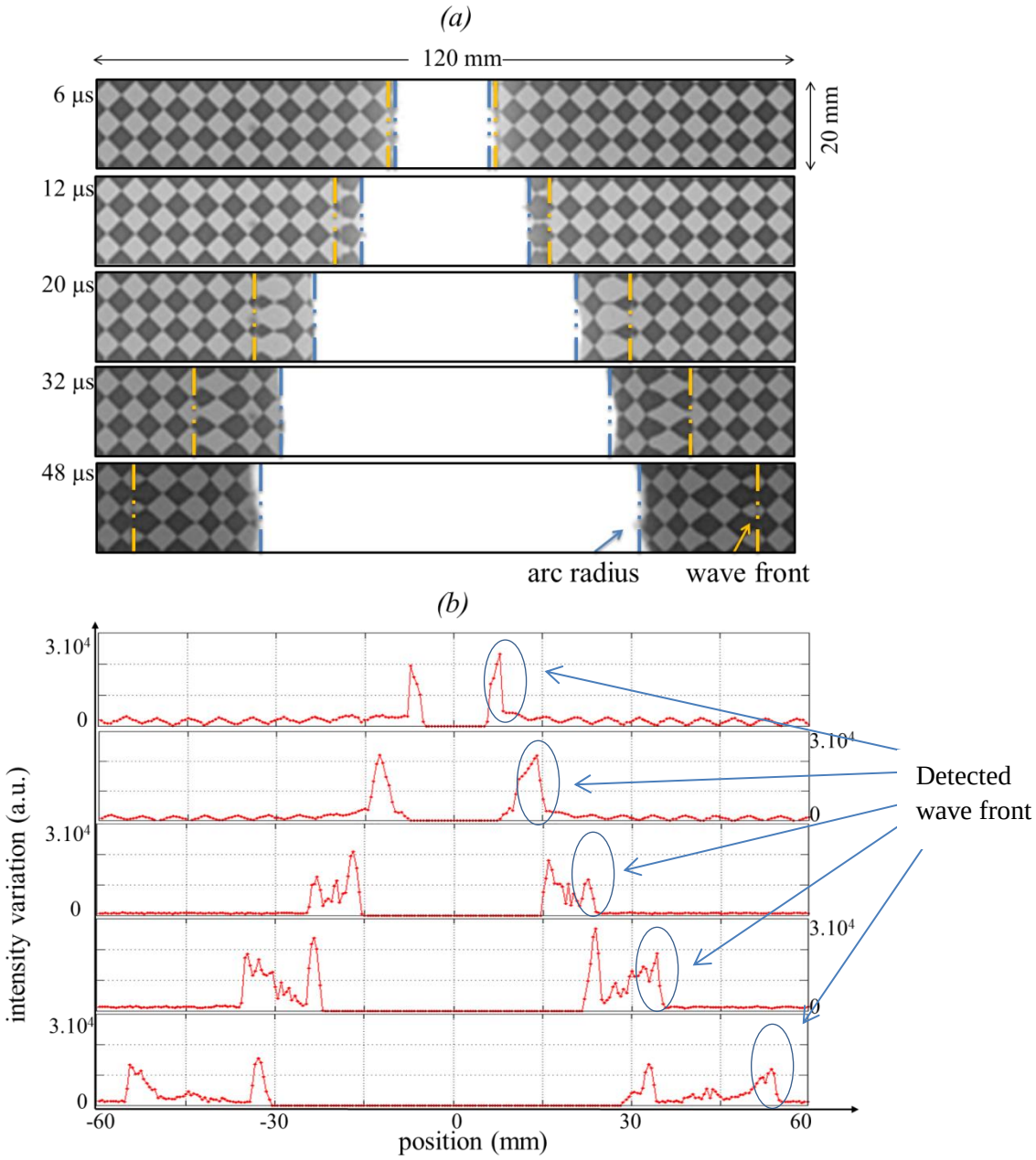

Figure III.10. (a) Pictures of the luminous central arc region and the shock wave evolution for the 100 kA peak. (b) Plot of the variation of the background schlieren intensity used to identify the wave front.

Figure III.11*(a)* shows the average measurement of the wave front position for the five current peak levels over 30 shots and presents also a fit by a power law function. The measurements over different shots give a very good repeatability and the wave front detection from the two HSC shows a good overlapping. The statistical and the instrumental error on the measurements were calculated as for the arc radius measurement (equation III.1). The maximum total

uncertainty found for all current levels was 1.55 mm. Figure III.11*(b)* shows the shock wave velocity deduced from the position measurements.

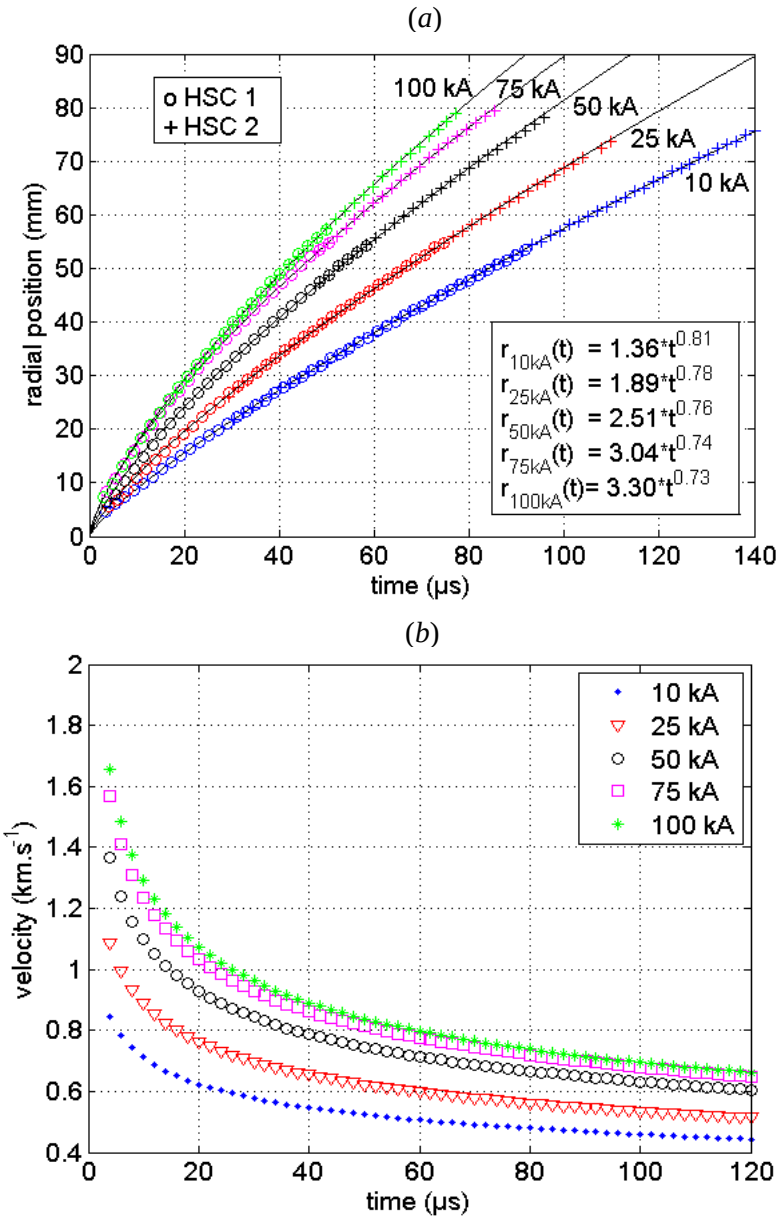

Figure III.11. (a) Shock wave position measured by the HSC 1 at 2 m and the HSC 2 at 3 m from the arc column and (b) the shock wave velocity.

Analyzing the results obtained from the curves shown in figure III.11(*a*) and comparing to the channel radius evolution of figure III.6, we can see that the time of detachment between the channel plasma arc and the shock wave is near 6 µs. While the arc channel radius increases approximately as square root function of time, the shock wave propagates faster in an almost linear shape with a speed of 1.6 km s^{-1} at the detachment time for the case of 100 kA.

We can see from the power law function fits that as the current peak increases, the power exponent decreases. This behavior is in accordance with the description given by Freeman (1968) concerning shock wave propagation with variable energy deposition. With the increase of the current peak, the growth rate at time $t = 0$ is also increased and consequently, there is a faster energy deposition in the plasma channel. In the limit case of a cylindrical strong shock wave with instantaneous energy deposition the power exponent tends to 0.5 (Lin (1954); Vlases and Jones (1966); Freeman (1968)).

III.2.3 Study of mass density distribution inside the shock wave

In this section, we develop a model of the light deflection inside the shock wave. This model allows us to estimate the mass density profile behind the wave front taking into account the deformation of the patterned background recorded during the determination of the shock wave position, described in the previous section. The mass density profile is useful for comparisons with the results of numerical simulation of high current arcs and model development. Furthermore, the estimated mass density is compared to the Rankine-Hugoniot relations, which are derived from the measured shock wave velocity presented in Figure III.8. This comparison completes and highlights all the results obtained from the BOS measurements.

Let us consider the shock wave already detached and far from the plasma column. Looking in the radial direction, from the outside to the discharge axis, we expect that the mass density has a fast increase at the wave front, passing from ρ_0 to ρ_{MAX} and then gradually decreases toward the plasma until reaching a value $\rho_{MIN.}$ This minimum value reached by the mass density must be smaller than ρ_0 to respect the mass conservation in the transverse section of the shock wave. As a first approach, we used linear shapes varying from ρ_{MIN} to ρ_{MAX} and then from ρ_{MAX} to ρ_0 as illustrated in figure III.12*(a)*. This choice is based on the simulations of the radial expansion of a lightning arc described by Aleksandrov et al. (2000) that deals with a pulsed current waveform of a return stroke similar to the present work, which reaches 100 kA at 5.5 µs. They obtained, for the cylindrical shock wave, a wave front velocity around 1.4 km s^{-1} at 5µs, which is in good agreement with our results. Their results of mass density distribution behind the wave front show a quasi-linear shape.

In figure III.12*(a)*, R is the position of the wave front, r_{ARC} is the arc radius, δ is an adjustable parameter which characterizes the density profile slope and ε is the shock wave thickness. The value of the shock wave thickness is of the order of a few mean free paths and was fixed at 0.2 µm in the simulations (Zel'dovich and Raizer (2002)).

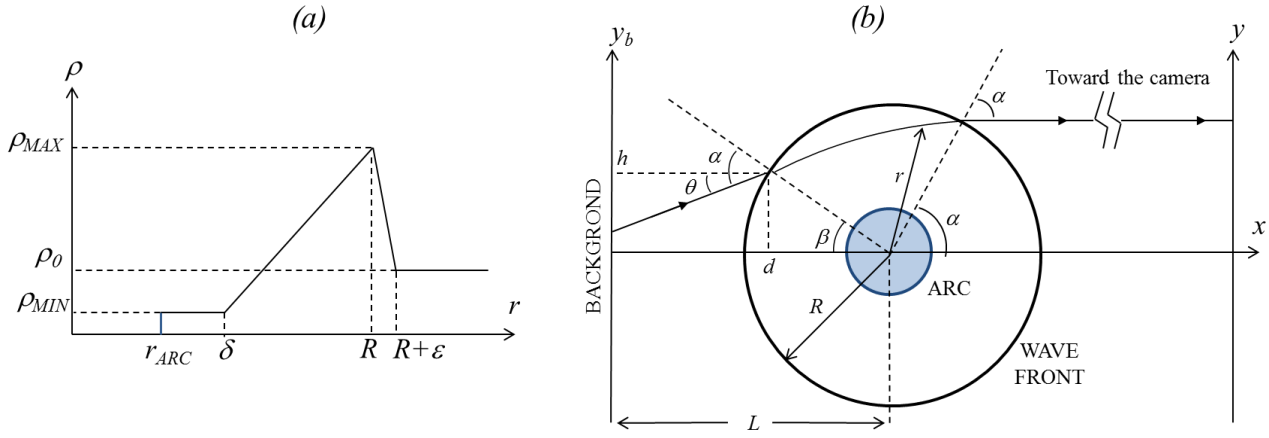

Figure III.12. (a) Schematic mass density profile inside the shock wave. (b) Light deflection through the shock wave.

We used the Gladstone-Dale relation to link the mass density ρ to the refractive index n, by the proportional expression $(n - 1) = K\rho$, where K is the coefficient of refractivity, which is a function of the gas composition and of the wavelength (Anderson (1967); Boudaoud and Lamerini (2015); Stoller et al. (2015)). The shocked gas is formed by N_2 and O_2, which are non-polar molecules and consequently, their refractivity coefficient are independent of the temperature if that one remains lower than 2000 K and the chemical composition does not change (Anderson (1967); Stoller et al. (2015)). For air at standard conditions, K can be supposed relatively constant and equal to 0.23 $cm^3\ g^{-1}$ on the response range of the optical system (400 nm to 800 nm) (Hargather and Settles (2010)). Consequently, the proportionality between the refractive index and the density is a valid assumption in the present case.

The camera which looks to the background is configured to improve the collection of parallel rays. This enhancement is possible by working with the minimum aperture size (f/22) and by positioning the camera far from the arc (3 m). The distance was selected to be a good compromise between the pixel resolution and the parallel hypothesis. The used scale factor was 0.4 mm/pixel.

Figure III.12*(b)* illustrates the deflection of the light inside the cylinder formed by the shock wave. We consider only the trajectories that pass outside of the channel arc. The deflection of the light collected by the camera after passing through the shock wave is taken into account based on the method described by Marcuse (1979). This yields to the deflection of the parallel incoming rays that cross a radial variable refractive index $n(r)$. In this work, we consider the reverse trajectory, i.e., the rays that are parallel after crossing over the shock wave must have a

slope at the entering point which can be deduced from the light ray equation and can be written as:

$$\frac{\mathrm{d}y}{\mathrm{d}x} = \frac{2}{n_0}\int_y^R \frac{\partial n}{\partial r}\frac{y}{\sqrt{r^2 - y^2}}\mathrm{d}r \qquad \text{(III.2)}$$

where x and y are the coordinates of a transverse plane with an origin coincident with the camera center, R is the position of the wave front, n_0 is the refractive index of the ambient gas. The three angles α, β and θ shown in figure III.12*(b)* can be calculated by basic geometry as follows (Acosta et al. (2005)):

$$\sin(\alpha) = \frac{y}{R} \;\; ; \;\; \sin(\beta) = \frac{h}{R} \;\; ; \;\; \tan(\theta) = \frac{\mathrm{d}y}{\mathrm{d}x} \;\; ; \;\; \alpha = \beta + \theta \qquad \text{(III.3)}$$

where d and h are the coordinates of the entering point with the origin at the background plane. In the frame of reference of figure 12*(b)*, the correspondence between the camera plane y and the background plane y_b can then be written as:

$$y_b(y) = R\sin(\alpha - \theta) - \frac{2yd}{n_0}\int_y^R \frac{\partial n}{\partial r}\frac{\mathrm{d}r}{\sqrt{r^2 - y^2}} \qquad \text{(III.4)}$$

Using the density profile illustrated in figure III.12, equation (III.4) becomes:

$$y_b(y) = R\sin(\alpha - \theta) - \frac{2yd}{n_0}\left[\frac{n_{MAX} - n_{MIN}}{\delta}\int_y^R \frac{\mathrm{d}r}{\sqrt{r^2 - y^2}} - \frac{n_{MAX} - n_0}{\varepsilon}\int_R^{R+\varepsilon} \frac{\mathrm{d}r}{\sqrt{r^2 - y^2}}\right] \qquad \text{(III.5)}$$

Under the assumption of a collimated light collected by the camera, equation (III.5) gives for each transverse plane the correspondence between the light issued from the background and the pixel of the camera as a function of the three parameters n_{MAX}, n_{MIN} and δ.

A simulated deformation can be created using a reference image taken without the arc. The three profile parameters are then optimized for each frame by a minimization method which has as criterion the image correlation coefficient. The correlation coefficient C of two matrices of pixels A and B can be written as:

$$C = \frac{\sum_m \sum_n (A_{mn} - \bar{A})(B_{mn} - \bar{B})}{\sqrt{\sum_m \sum_n (A_{mn} - \bar{A})^2 \sum_m \sum_n (B_{mn} - \bar{B})^2}} \qquad \text{(III.6)}$$

where A_{mn} and B_{mn} are terms of the matrices and $\bar{A}$ and $\bar{B}$ are their respective matrix mean values. Two identical images will result in a correlation coefficient equal to 1.The set of parameters that maximizes the correlation coefficient is defined as the minimization result.

Figure III.13 shows an example of a simulated and a measured deformation using this method. Due to the cylindrical symmetry of the shock wave, the refractive index gradient is exclusively transverse. Therefore, the lines of black squares that compose the background are shifted to increase the deformation level in each image, which improves the accuracy of the correlation. With this changing, the maximum correlation coefficient found using equation (III.6) increased from 0.88 to 0.94.

The minimization allows us to estimate the mass density profile inside the shock wave over time. This determination is possible from the time when the shock wave is completely detached from the arc, i.e., the distance between the wave front position and the column arc radius are at least in the order of 10 mm. This distance allows the acquisition of a deformation image large enough to apply the correlation criteria.

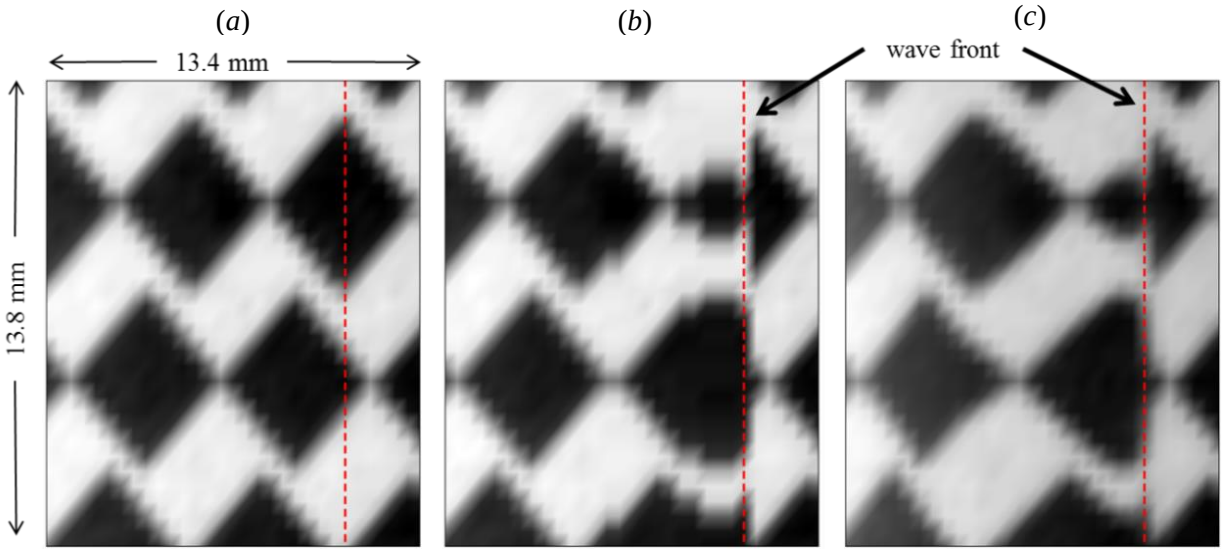

Figure III.13. Example of image reconstruction from a mass density profile. (a) Reference image; (b) Simulated image; (c) Measured image.

The profiles obtained from this minimization method are then compared with the boundary conditions at the wave front, called the Rankine-Hugoniot (R-H) relations, which are derived from the expressions for conservation of mass, momentum and energy across the wave front (Needham (2010)). Under the assumption of an ideal gas and a locally planar shock wave, the expression for the ratio ρ_{MAX}/ρ_0 depends only of the adiabatic index γ and the Mach number M, and can be writen as (Candel (2001)):

$$\frac{\rho_{MAX}}{\rho_0} = \frac{(\gamma+1)M^2}{2+(\gamma-1)M^2} \tag{III.7}$$

From equation (III.7) we can obtain the mass density at the wave front by considering the adiabatic index of air constant and equal to 1.4 and by using the propagation velocity of the wave front v_s deduced in section III.2.2 (see figure III.11). The Mach number is calculated considering a value of 343.15 m s^{-1} for the speed of sound in ambient air c_0, with local temperature T_0 equal to 293 K, and can be expressed by:

$$M = \frac{v_s}{c_0} = \frac{v_s}{\sqrt{\gamma r_{spec} T_0}} \tag{III.8}$$

where r_{spec} is the specific gas constant, and is taken for dry air equal to 287.06 J kg^{-1} K^{-1}.

Density profiles and ρ_{MAX} calculated from the Rankine-Hugoniot relation are plotted in figure III.14. Generally, the mass densities at the wave front are in good agreement with the ρ_{MAX} obtained using our light deflection and correlation method. For 10 kA, 50 kA and 100 kA the results are very close in the first microseconds (44 µs, 38 µs and 32 µs, respectively). After this time, there is a slight divergence between the values as the density decreases. For 25 kA, ρ_{MAX} is slightly overestimated by our method in the first 36 µs and then the results seem to converge.

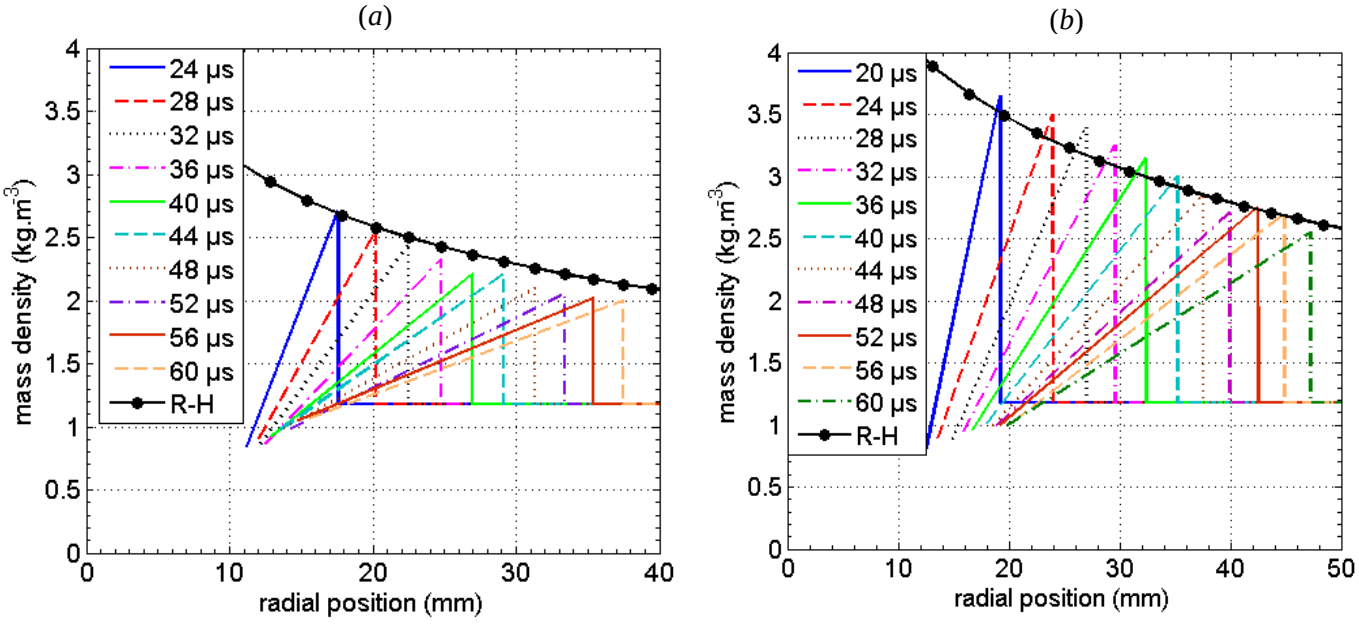

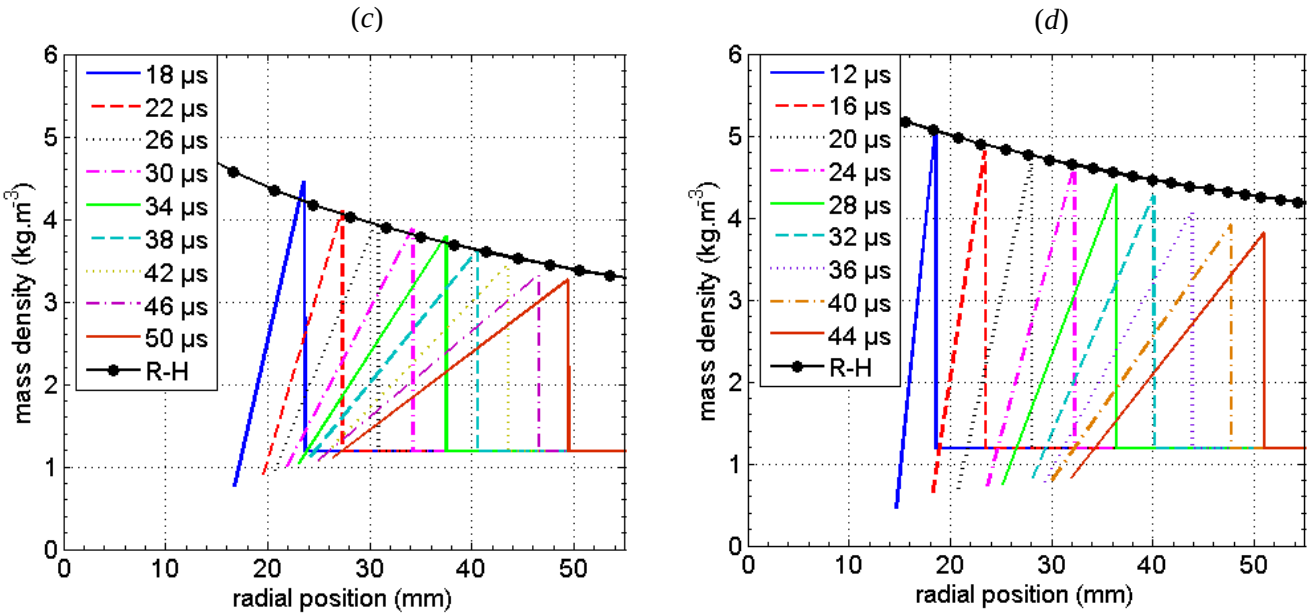

Figure III.14. Mass density profile and comparison with R-H relation for: (a) 10 kA; (b) 25 kA; (c) 50 kA; (d) 100 kA.

Three main reasons can explain the differences. The method is based on the degree of deformation of the image. Then as the density gradient becomes lower, the level of deformation is also reduced and consequently it is more difficult to achieve an image correlation with high accuracy. The second reason relates to the profile hypotheses. As the extension of the shock wave (i.e. the parameter δ in figure III.12*(a)*) increases, the assumption of a linear profile may not be enough to model the variation from ρ_{MAX} to ρ_{MIN}. Finally, the required conditions for the application of the Rankine-Hugoniot relations may not be totally respected in this case, which could lead to certain divergence. Nevertheless, the difference between the curves remains smaller than 10% up to 60 µs, which shows that the developed method leads to good results and reinforce the reliability of the shock wave characterization by the BOS method.

III.3 Conclusion

High speed imaging has allowed us to assess the temporal dynamics and the spatial shape of the arc. The measurements of the characteristic lengths, as the shock wave and the arc channel radii, have been made over time up to 140 µs. The diameter of the arc reaches 6.4 cm at 50 µs for the case of 100 kA. The shock wave detaches from the arc column around 6 µs. It expands at about 0.8 km s^{-1} at the beginning of the arc for 10 kA, and is twice faster for 100 kA.

A model of light deflection based on the Background-Oriented Schlieren measurements and the Gladstone-Dale relation was developed to estimate the mass density profile inside the shock wave. The results are in good agreement with Rankine-Hugoniot relations using the measured shock wave velocity but the assumption of a linear profile is less accurate for lower density values.

The results presented in this chapter will serve as a reference for part of an experimental database for lightning arcs. They were the subject of a paper in a conference proceeding (Sousa Martins et al. (2015b)) and were published as a research paper by IOP Publishing in *Journal of Physics D: Applied Physics* (Sousa Martins et al. (2016a)).

In the next chapter we will focus our attention on the electrical properties of the free arc channel. The arc column radius obtained here will be useful to develop an electrical model for the channel, and also to estimate the electrical conductivity of the plasma.

Chapter IV.
Electrical characterization of the free lightning arc channel during the high current phase

In this chapter we investigate the electrical properties of the lightning arc. An electrical model for the arc is developed, which allows us to determine the time depending impedance of the arc column and the estimation of other useful characteristics.

The geometry and the evolution over time of the arc shape, determined by using high-speed imaging and presented in the previous chapter, are used in the development of the electrical model. Therefore, the same experimental setup used for the hydrodynamic characterization is kept in this chapter. From this electrical approach, the total arc resistance and the average electrical conductivity of the arc column are estimated for times lasting up to 50 µs. The electrical power and energy dissipated inside the arc column by Joule effect is also evaluated.

Finally, a parametric study on the arc length is performed, which allows us to assess the linear column resistance, and to provide an accurate evaluation of the electrical conductivity of the plasma inside the column, as well as and the electrical energy loss per meter in the column. These quantities are directly comparable to the results of simulation codes and are of great interest for model development.

IV.1 Electrical model for the arc channel

The electrical measurements are used for the development of a simplified electrical model. Aiming to an electrical description, numerous works in the literature have proposed and analyzed the arc channel as a time depending resistance (Weizel and Rompe (1947); Vlastos (1969); Vlastos (1972); Larigaldie (1987); Elias and Castera (2013); Castera and Elias (2014)). In the present work, due to the length of the arc and also to the coaxial structure of the current generator, an inductive component in the channel must to be taken into account. Therefore, the arc channel is modelled here as an impedance varying with time, formed by a series circuit composed of an inductor and a resistance. A potential redistribution around the channel would lead to capacitive currents. We consider that these currents are negligible, due to the geometry of the generator and the frequencies involved in the current waveform.

Figure IV.1 shows the equivalent electric circuit for the current generator with two variable components, L_{ARC} and R_{ARC}, to model the arc channel. The generator components (R, L and C) are constants during all the experiments. The position of the voltage and current probes are also illustrated. To avoid any problem of voltage floating, the two voltage probes are referred to the ground and a differential measurement is made to acquire the arc voltage. The probes are directly connected to the tungsten rod of the electrodes. The current is measured on the first electrode (high voltage side) as illustrated in figure IV.1.

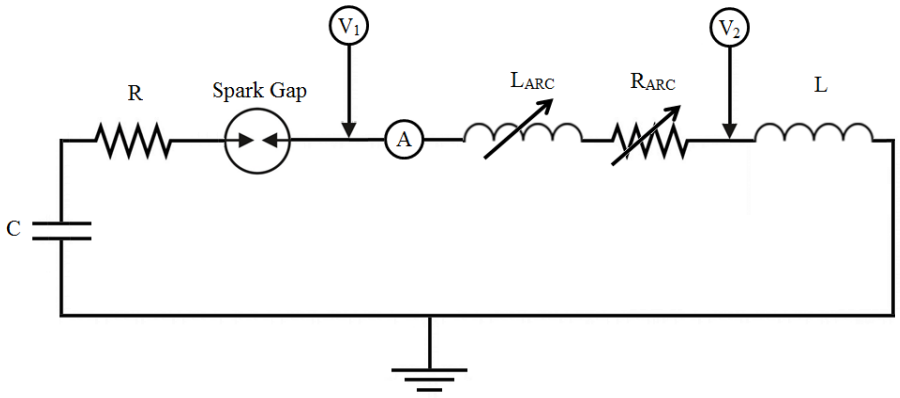

Figure IV.1. Equivalent electric circuit of the lightning current generator with variable components L_{ARC} and R_{ARC} and the probes V_1 and V_2 for voltage measurements and A for current measurements.

IV.1.1 Electrical measurements

An example of the measured voltages V_1 and V_2, the difference $V_1 - V_2$, and the current measurement I, for the case of the 100 kA current peak level, is shown in figure IV.2. We can

see that the cathode voltage (V_2) has a low level compared to the anode voltage (V_1). The voltage V_2 becomes negative close to the current peak, which suggests that this voltage is caused by the inductive characteristic of the structure. Nevertheless, this differential measurement is useful for an accurate determination of the effective arc voltage.

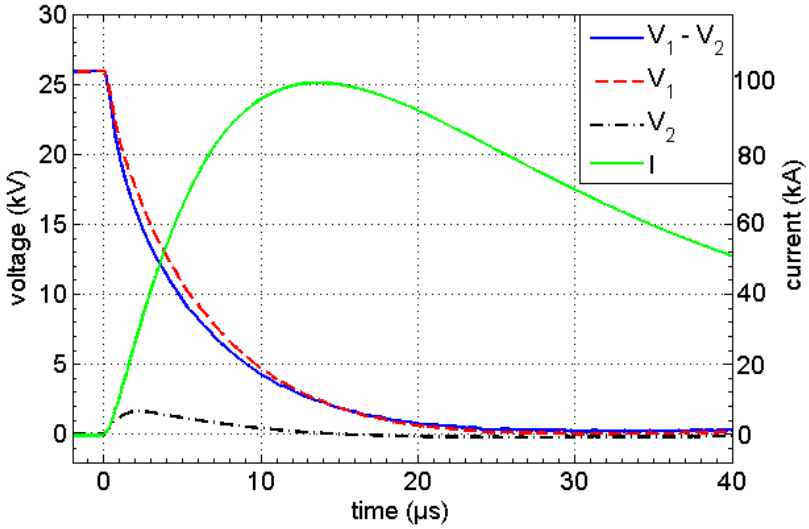

Figure IV.2. Example of voltage measurements by probes V_1 and V_2 and current measurements I by the probe A for the 100 kA peak.

Figure IV.3 illustrates the arc voltage evolution for the five current levels. The voltage level at the arc ignition ($t = 0$) increases as the current peak increases, which is expected once the initial charging voltage was the variable parameter chosen to produce the desired current waveform. Then, the arc voltage falls approximately one order of magnitude in the first ten microseconds as the current in the arc starts to increase. When analyzing these voltage curves in a semi-logarithmic scale an interesting behavior can be noticed. In the first 14 µs, which corresponds to the period when the current increases until reaches its peak, the negative voltage slope ($-dV/dt$) increases as the current peak level increases. From this time, the arc voltage for the 10 kA peak decreases continuously, while the voltage for the other cases decreases until reaching a steady level. This steady level decreases as the current peak increases, changing from 770 V for the 25 kA peak to 440 V for the 100 kA peak.

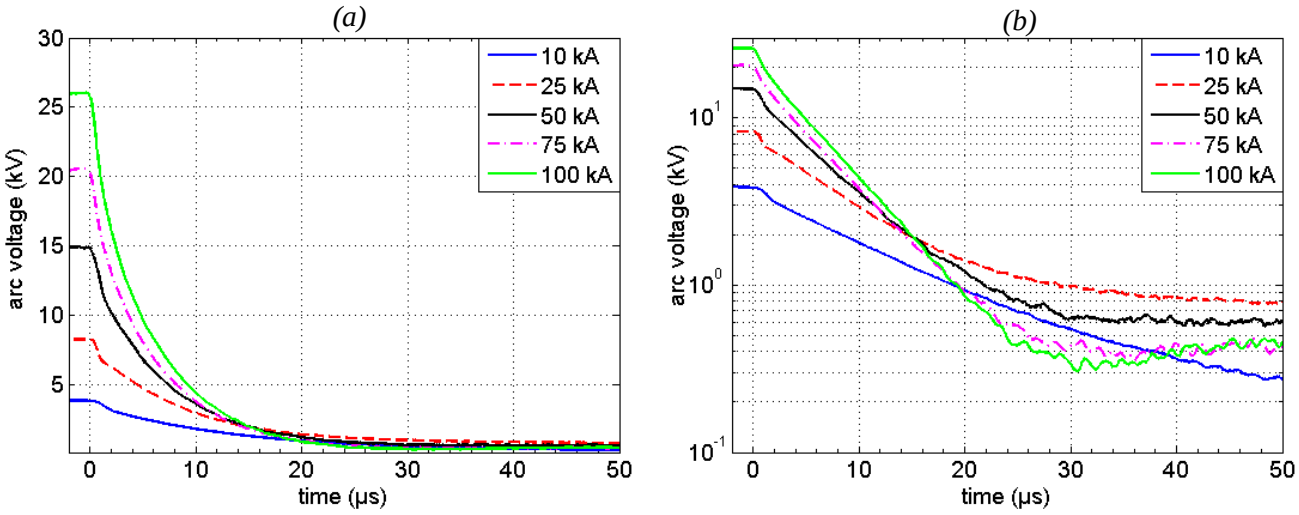

Figure IV.3. (a) Arc voltage for the five levels of current peak.
(b) Arc voltage in semi-logarithmic scale.

IV.1.2 Arc inductance

To establish the model, a few hypotheses are made on the geometry of the problem. The evolution over time of the arc column radius obtained in Chapter III is used to take into account the geometric dependence of the inductor in the electrical model. Based on the generator structure geometry, the arc inductance is approximated by an air coaxial channel. The current flows in the arc at central structure axis and returns around the arc column via the four aluminum bars. Because of the cylindrical symmetry, we assumed that the magnetic field $\boldsymbol{B}$ has only an azimuthal component B_φ. Applying the Ampere's circuital law inside the arc column and in the region between the column and the return aluminum bars, the total arc inductance is deduced as a function of only geometric terms and can be written as (Cheng (1989)):

$$L_{ARC} = \frac{\mathrm{d}\Lambda}{\mathrm{d}i} = \frac{\mu_0}{2\pi}\left(\frac{1}{4} + \ln\frac{r_S}{r_{ARC}}\right) l_{ARC} \qquad \text{(IV.1)}$$

where Λ is the total magnetic flux linkage, i is the arc current, μ_0 is the vacuum permeability, r_S is the equivalent radius of the generator structure, which corresponds to the distance between the arc and the aluminum bars for the current return and is equal to 300 mm, r_{ARC} is the arc radius and l_{ARC} is the arc column length. In this first approach, the air gap between the two diverters is fixed to 120 mm, and the arc length is then set to this same value. Figure IV.4 presents the evolution over time of the arc inductance for the five levels of current peak. All inductances start around 0.2 µH and then decrease approximately by a factor of 2.5, as a result

of the arc radius expansion. At 50 µs the arc inductance is equal to 0.089 µH for the 10 kA, and 0.068 µH for the 100 kA.

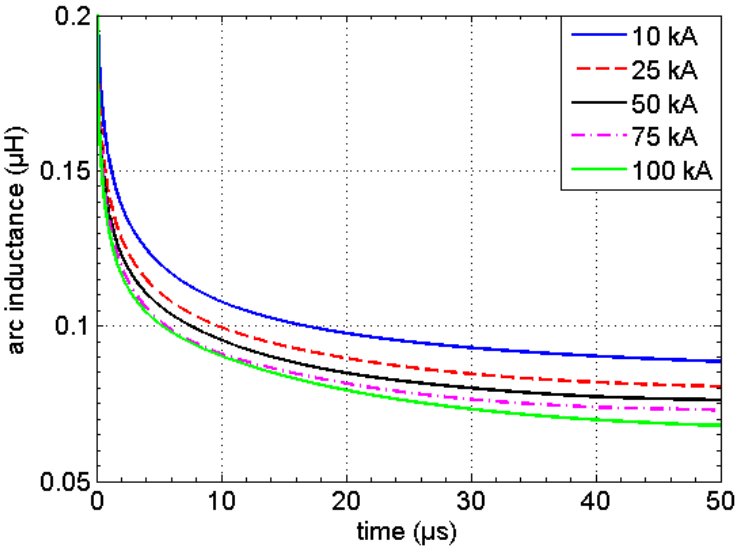

Figure IV.4. Arc inductance evolution for the five levels of current peak (the arc column length is fixed to 120 mm).

IV.1.3 Total arc resistance

Following the diagram shown in figure IV.1, the circuit equation for the voltage and current measurements can be written as:

$$V_1 - V_2 = \frac{\mathrm{d}(L_{ARC}\, i)}{\mathrm{d}t} + R_{ARC}\, i \tag{IV.2}$$

where V_1 and V_2 are the measured voltages, and i is the measured current. Equation (IV.2) is then solved for the total arc resistance R_{ARC} in each time step t_n, using an explicit forward Euler scheme, which is written as:

$$R_{ARC}(t_n) = \frac{1}{i(t_n)}\left\{[V_1(t_n) - V_2(t_n)] - L_{ARC}(t_n)\,\frac{[i(t_{n+1}) - i(t_n)]}{dt} - i(t_n)\frac{[L_{ARC}(t_{n+1}) - L_{ARC}(t_n)]}{dt}\right\} \tag{IV.3}$$

where dt is the time step of the measurements and is equal to 10 ns. The first term in the right hand side of equation (IV.2) corresponds, in the maximum case, to around 16% of the second term. Then, the use of L_{ARC} in the electrical model can be seen as a correction factor in the determination of the arc resistance and its geometrical approximations have low impact on the

result. The results for the evolution over time of arc resistance for the five current levels are plotted on figure IV.5.

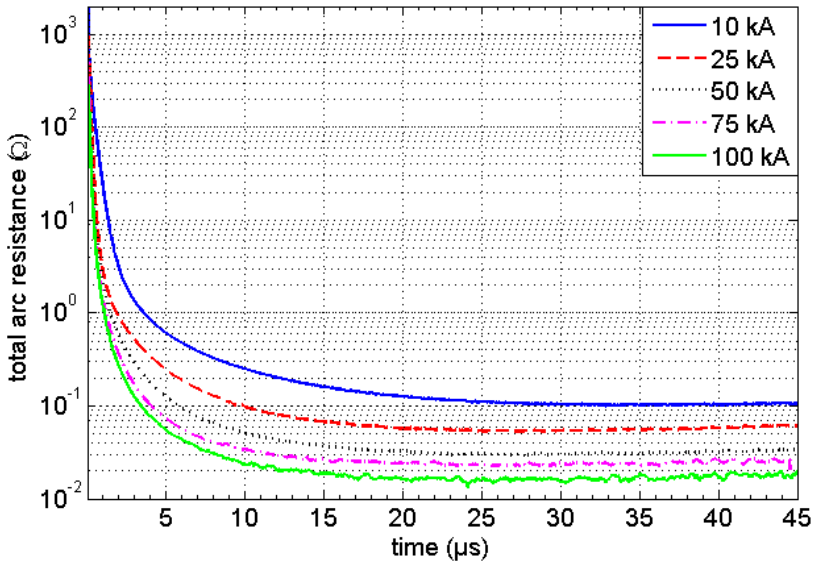

Figure IV.5. Evolution over time of the total arc resistance for all current levels.

The arc resistance starts around 1 kΩ for all current levels, which roughly corresponds to the value of the ignition wire. Then it decreases quickly in the first three microseconds and reaches values lower than 1 Ω. As the current peak increases, the arc resistance decreases more rapidly and monotonically. The resistance seems to have an asymptotic value, which is inversely proportional to the current peak and reaches approximately 20 mΩ for the case of 100 kA and100 mΩ for 10 kA.

IV.1.4 Estimation of the electrical conductivity from the total arc resistance

The electrical conductivity of the arc channel, σ_{ARC}, can be estimated by using the total arc resistance combined with the arc radius. For this estimation, we considered a homogeneous distribution of the electrical conductivity in the radial direction and along the arc channel. This assumption leads to a simple relationship between σ_{ARC}, R_{ARC} and r_{ARC}, which can be written as:

$$\sigma_{ARC} = \frac{1}{R_{ARC}} \frac{l_{ARC}}{\pi {r_{ARC}}^2} \tag{IV.4}$$

Figure IV.6 shows the electrical conductivity obtained by applying equation (IV.4) with the total arc resistance presented in figure IV.5.

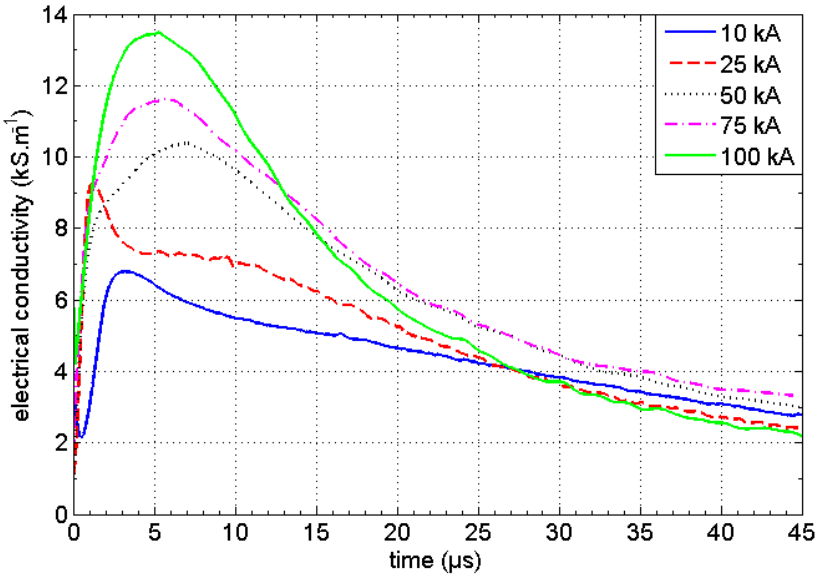

Figure IV.6. Electrical conductivity of the arc channel obtained from the total arc resistance (arc column length fixed to 120 mm).

The electrical conductivity is proportional to the inverse square of the arc radius and is strongly dependent on this parameter. The values in the first microseconds must be analyzed with carefulness, because the radius measurement in this time interval is less accurate. The shape of the electrical conductivity curves is different for each current level, but globally the electrical conductivity increases to a peak value and then decreases. The peak value is reached around 2µs for 10 kA and 25 kA and around 5 µs for the other cases. These times are lower than the current peak time for all wave currents. In general, the electrical conductivity peak increases with the increase of the current peak. It reaches 6900 $S.m^{-1}$ for 10 kA and 13700 $S.m^{-1}$ for 100 kA. Table IV.1 summarizes these main results.

Table IV.1. Maximum electrical conductivity and peak time for the five current levels using the total arc resistance.

Current peak (kA)	10	25	50	75	100
Maximum σ_{ARC} (kS m^{-1})	6.9	9.2	10.4	11.6	13.7
σ_{ARC} peak time (µs)	3.14	1.32	6.83	5.52	5.26

Note that in the present approach, the estimated electrical conductivity is averaged over radial and axial direction and does not take into account boundary effects due to the electrodes. In the next section, those effects will be considered and analyzed.

IV.2 Arc column resistance

The total arc resistance, estimated in the previous section, is composed by the arc column resistance and probably some additional resistance caused by the electrodes and the region near to the arc root, where the channel shape assumes a non-cylindrical form. To study those boundary effects and to be able to separate the different resistance components, a parametric study is conducted, where the arc length is varied.

The total arc resistance of the electric model R_{ARC} is assumed to be the sum of a first term proportional to the length of the arc column, and a constant term (a non-length dependent term), modeling the electrode effects. Therefore, the resistance equation can be written as:

$$R_{ARC} = r_{col}\, l_{ARC} + R_{elec} \tag{IV.5}$$

where r_{col} is the linear column resistance, expressed in $\Omega\ m^{-1}$, l_{ARC} is the arc length and R_{elec} is called in the present work the electrode resistance, which takes into account the boundary effects. The assumption that the column resistance is proportional to the arc length is based on the column voltage fall (V_{col}) modeling, which often assumes a proportionality relationship between V_{col} and the arc length (Valensi et al. (2016)).

The parametric study is performed considering three lengths between the diverters; 60mm, 120mm, and 180mm. The experimental parameters (ignition wire, current waveform, probes and electrodes …) are the same for the three lengths. For each arc length, the total arc resistance is obtained by using equation (IV.3) and following the same procedure descripted in section IV.1.3. Figure IV.7 presents R_{ARC} calculated for different arc lengths. As expected, the resistance increases as the arc column is elongated and seems to be a linear function of the arc length.

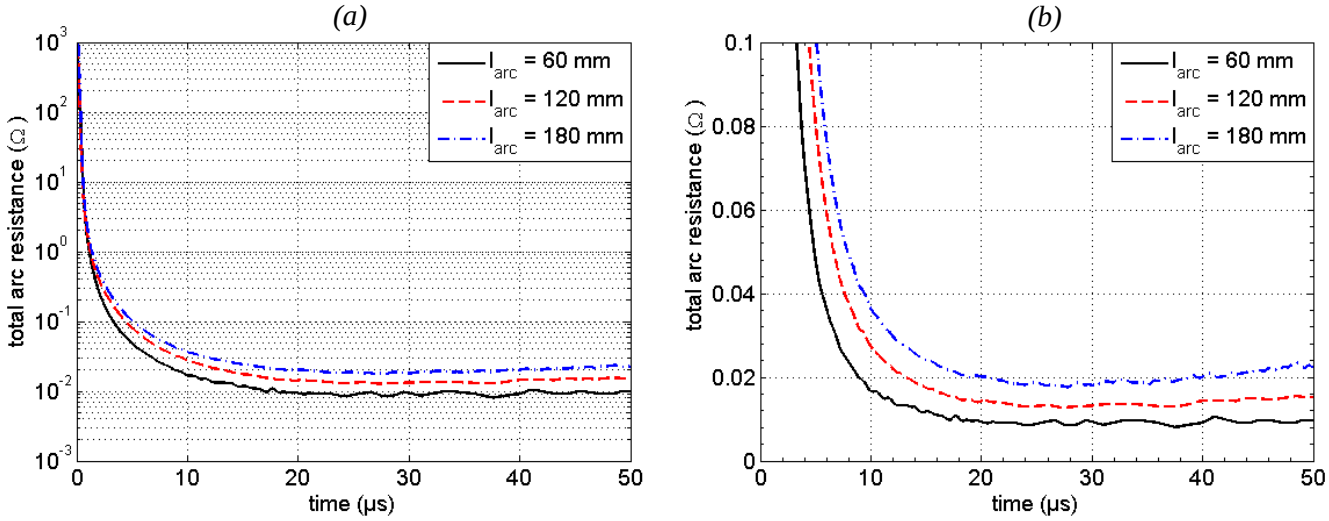

Figure IV.7. (a) Example of total arc resistance for three arc lengths, for the case of 100 kA peak. (b) Plot in linear scale to highlight the linearity of the arc resistance as a function of the arc length.

With the different values of total arc resistance, a linear regression is applied for each time step, which allows us to estimate the parameters of r_{col} and R_{elec} in equation (IV.5). Figure IV.8 shows an example of this linear adjustment at 15 µs for the current of 100 kA peak, and also the root mean square error (RMSE) over time.

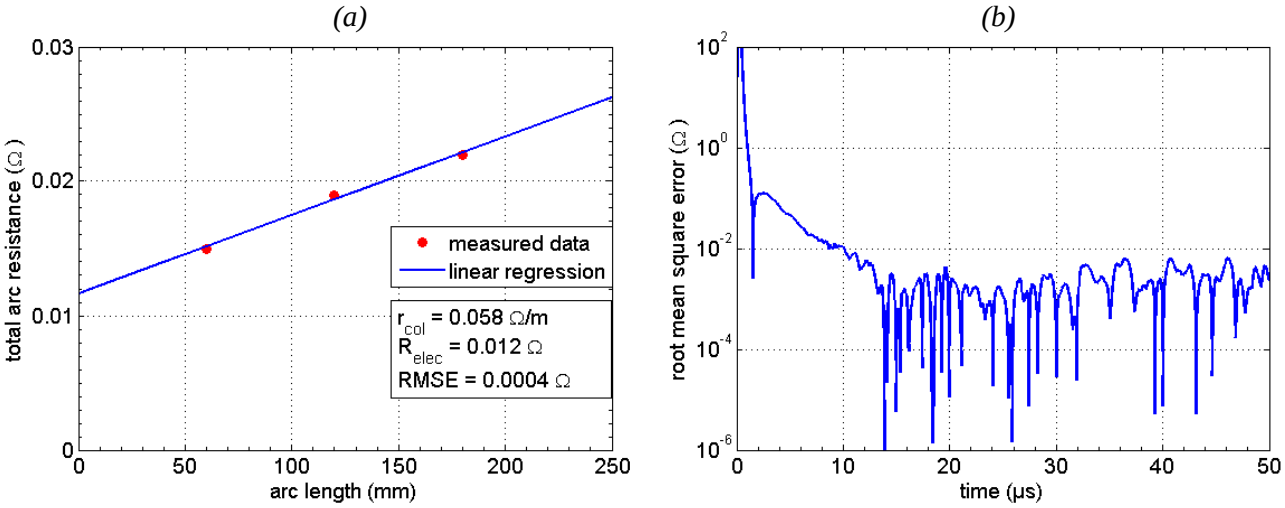

Figure IV.8. Example of (a) linear regression for the 100 kA peak at 15 µs and (b) the root mean square error (RMSE).

In the first microsecond, when the total resistance is yet in the order of hundreds of ohms, the resistance value is affected by the initial resistance of the ignition wire. In those times, the linear fit is not satisfactory, which leads to RMSE of the same order of magnitude as the resistances. Therefore, the estimation of the arc column resistance and the electrode resistance is only

performed when the RMSE is, at least, one order of magnitude lower than the column resistance.

Figure IV.9 shows the results of arc column resistance and electrodes resistance obtained for three levels of current peak. As for the case of the total arc resistance, both the column and the electrode resistance decrease approximately three orders of magnitude in the first microseconds. As the current peak increases, the column resistance decreases more rapidly and reaches lower steady values. This steady value is reached approximately at 18 µs and is around 0.05 Ω m^{-1} for 100 kA, and 0.2 Ω m^{-1} for 25 kA. The electrode resistance reached a steady value earlier than the column resistance, and this time decreases as the current peak increases. It is around 3 µs for the 100 kA peak. However, after this rapid reduction, the values of the electrode resistance converge to approximately 0.01 Ω for the three levels of current. In the composition of the total resistance, the electrode resistance has a significant contribution. Its value corresponds to around 25% for the 25 kA peak, and can reach 50% for the 100 kA peak.

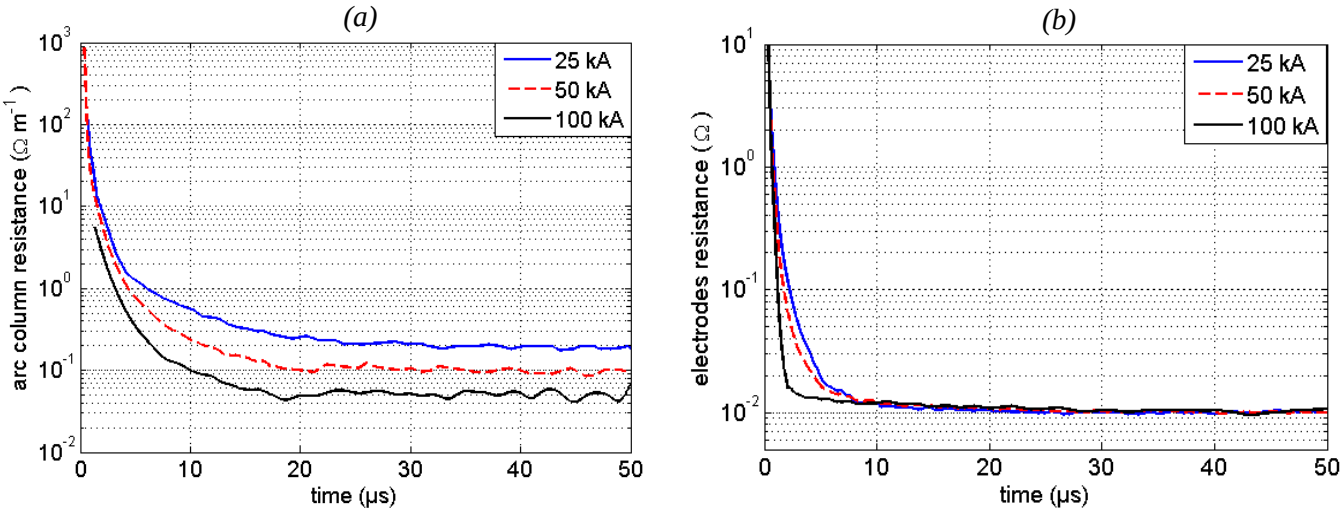

Figure IV.9. (a) Arc column resistance and (b) electrodes resistance obtained from linear regressions of each time step and using different arc lengths.

IV.2.1 Estimation of the electrical conductivity from the arc column resistance

The electrical conductivity of the arc column can be estimated with more accuracy by employing the arc column resistance instead of the total arc resistance. For this estimation, we considered a homogeneous distribution of the electrical conductivity in the radial direction of the column, however in this approach, the boundary effects due to the electrodes are taken into account. Equation (IV.4) is then applied, replacing $R_{ARC}/\ l_{ARC}$ by r_{col}. Figure IV.10 shows the obtained electrical conductivity and also the previous results obtained from the total arc resistance.

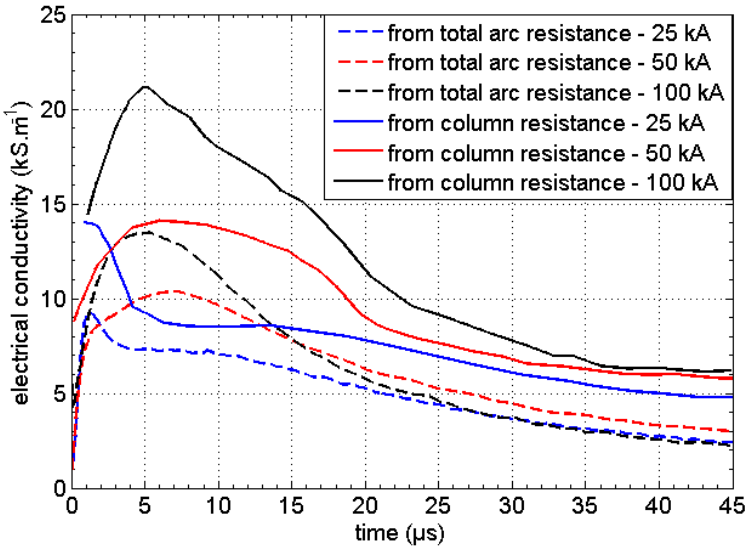

Figure IV.10. Electrical conductivity of the arc column obtained from the column resistance and from the total arc resistance.

In general, for each current level, the electrical conductivity curves have a similar shape regardless the applied method. This similarity is expected once the steady value of the electrode resistance is reached very quickly, in just a few microseconds, and then the shape of the total and the column resistance curves remain also similar. The electrical conductivity reaches 21100 S m^{-1} for the 100 kA, which is 54% higher than the previous estimation. Table IV.2 summarizes the comparison of the maximum and the peak time values for the three current peak levels.

Table IV.2. Comparisons of the maximum electrical conductivity and σ_{ARC} peak time using the total arc resistance and the arc column resistance.

Current peak (kA)	25	50	100
Maximum σ_{ARC} from r_{col} (kS m^{-1})	13.9	14.1	21.1
σ_{ARC} peak time from r_{col} (µs)	2.15	6.37	5.21

It is interesting to note that the maximum conductivity increases with the current, with a fast rise below 50kA. Moreover, the conductivity reaches the maximum before the time of the current peak, when the current density is highest. We can also point out that the conductivity peak time is greater for the 50kA arc than for 25 or 100kA.

The results are in agreement with other studies in the field of high intensity transient arcs such as the investigation of the electrical conductivity of a lightning return stroke reported by

Uman (1964). He obtained an average integrated value over the channel of 18000 S m^{-1} with an uncertainty of 30%. However this study has no accurate measurements of the current waveform.

IV.2.2 Estimation of the electrical power of the arc column

From the arc column resistance we can obtain a precise estimation of the power and energy dissipated inside the arc by Joule effect. The power P_J is calculated over time by the relation: $P_J(t) = r_{col}(t)\, i(t)^2$. The accumulated energy at an instant t is then calculated by the time integral of this power, from the arc initiation: $E_J(t) = \int_0^t P_J(t)dt$. Figure IV.11 shows the obtained results.

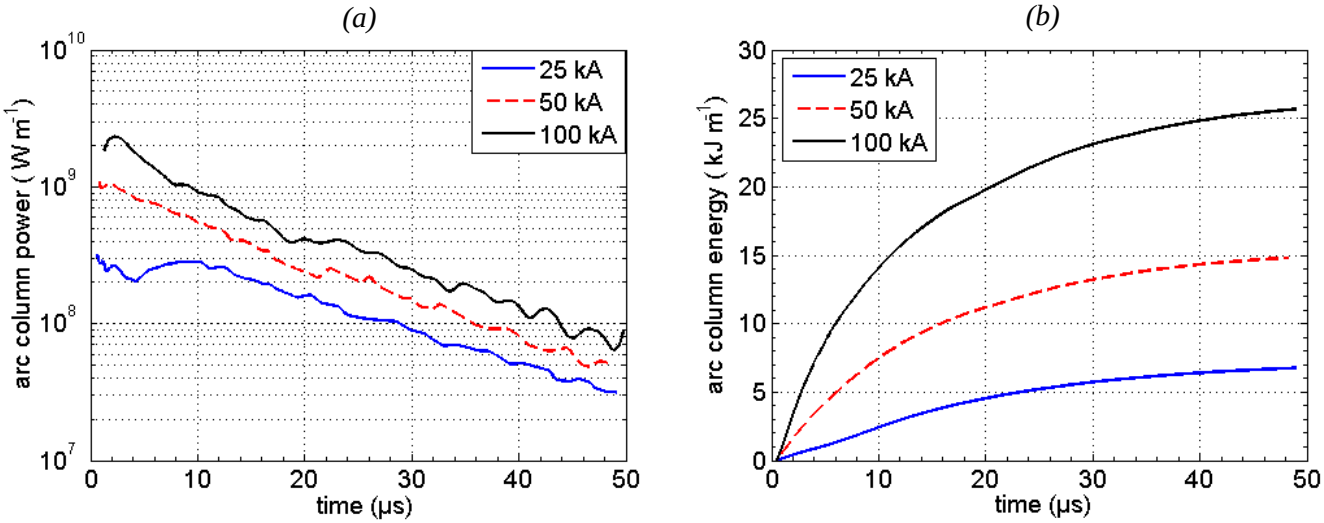

Figure IV.11. Power (a) and accumulated energy (b) dissipated per length inside the arc column by Joule effect.

For the cases of 50 and 100 kA peak, the power reaches its maximum at a very early stage of the arc, at around 2 µs, and then decreases in an approximately exponential function of time. For the 25 kA, the power shows an irregular behavior in the first ten microseconds, having a local minimum at 4 µs. The reason for this result may be related to a less accuracy of the column resistance estimation in the arc initiation, or due to the different current growth rate between the three waveforms. Nevertheless, after 10 µs, the power for 25 kA has a decreasing over time similar to the other two current peaks. It reaches values of around 2.3 GW m^{-1} for the 100 kA peak, and 1 GW m^{-1} for 50 kA. For the three peak levels, the power decreases one decade in approximately 35 µs. At 49 µs, the accumulated energy dissipated in the arc column reaches 6.7 kJ m^{-1} for 25 kA and 25.7 kJ m^{-1} for 100 kA. The energy is proportional to the current peak but there is no a linear relation between them. Due to the decreasing phase of the current waveform, the energy curves seems to tends to a roughly steady-state at 50 µs.

IV.3 Conclusion

In this chapter we performed an electrical characterization of the free arc channel. An electrical model for the arc channel was developed, which assumes the arc column as a time-dependent impedance. The geometry and the evolution over time of the arc shape were used in the model development. This model allowed us to determine the inductance and the resistance of the arc from the electrical measurements, as the arc voltage and current, for the five current waveforms. The characterization was done for times lasting up to 50 µs, when axisymmetric assumption was valid.

A parametric study on the arc length was done, to take into account the boundary effect due to the electrodes and to assess the different components that constitute the total arc resistance. The total and the linear column resistance decrease with the increase of the current peak and reach a steady value, after a few microseconds. This value ranges from $0.05\ \Omega\ m^{-1}$ to $0.2\ \Omega\ m^{-1}$ for the column.

The electrical conductivity, calculated assuming a homogenous radial distribution in the column, reaches a peak value of $21100\ S\ m^{-1}$ for 100 kA and $14100\ S\ m^{-1}$ for 50 kA. The conductivity peak is around 6 µs which is about 8 µs earlier than the current peak. The shape of the conductivity varies for the different current peaks and is highly dependent on the arc radius.

The electrical power and energy dissipated inside the column by Joule effect are estimated from the column resistance. For the 100 kA peak, the power reaches $2.3\ GW\ m^{-1}$ at 2 µs and the cumulated energy reaches $25.7\ kJ\ m^{-1}$ at 49 µs.

The results obtained in this chapter are directly comparable to the results of simulation codes and are of great interest for model development. A part of this electrical study was published, together with the hydrodynamic characterization presented in Chapter III, as a research paper by IOP Publishing in *Journal of Physics D: Applied Physics* (Sousa Martins et al. (2016a)).

In the next chapter we will focus our attention on the intensive thermodynamic properties of the free arc channel. This characterization will include the determination of temperature, electron density and pressure distribution within the arc column. Based on these quantities, the electrical conductivity in the arc column can also be deduced and then compared to the results obtained in this chapter.

Chapter V.

Temperature, electron density and pressure profile determination of the free lightning arc during the high current phase using optical emission spectroscopy

In this chapter, we investigate the intensive thermodynamic properties of the lightning arc. Optical emission spectroscopy is employed to assess space- and time-resolved properties that

include temperature, electron density and pressure of the arc column. The free arc column is produced using the experimental setup with the *diverter-diverter* electrode configuration, as was the case in the two previous chapters.

Ionic lines of nitrogen and oxygen are used to determine radial profiles of temperature and electron density of the column over time from 2 µs to 36 µs. A combination of 192 N II and O II lines is considered in the calculation of the bound-bound contribution of the absorption coefficient of the plasma column. Calculations of the optical thickness are performed and showed that self-absorption of those ionic lines in the arc column is significant. Therefore, well-known diagnostic methods, which need optically thin assumption, are inadequate in this case. Then, to obtain temperature and electron density profiles, the radiative transfer equation is solved across the arc column considering the channel formed by uniform concentric layers.

The pressure inside the channel is estimated using the determined temperature and electron density distribution and the air plasma composition at local thermodynamic equilibrium. These results are utilized to estimate the electrical conductivity of the arc column, in order to compare to the results obtained in the previous chapter from the electrical measurements.

V.1 Theory and procedure

V.1.1 Sensitivity study and selection of the spectral lines

To perform a quantitative characterization via optical emission spectroscopy, we started to analyze and define the most suitable spectral zones. We selected the spectral lines to be studied, from the species present in air plasmas, according to their sensitivity to the temperature. Following the previous works on lightning strokes (Zhivlyuk and Mandel'shtam (1961); Prueitt (1963); Uman (1964); Orville (1966b); Uman (1969); Krider (1973)), the expected range of temperature for the arc column is from 20000 K to 35000 K. Therefore, we searched in the spectral range of our optical system (400 nm to 700 nm) the lines with significant intensity variation for these range of temperature.

The HTGR EM2C spectroscopic database is used to analyze the sensitivity to the temperature of the lines present in that spectral range. This is an exhaustive and accurate spectroscopic database which was developed in previous studies (Chauveau (2001); Chauveau et al. (2002); Chauveau et al. (2003)) for radiative transfer in air plasmas. It provides the absorption coefficient for air plasmas (78.46% N_2 – 21.05% O_2 – 0.49% Ar) calculated under local thermodynamic and chemical equilibrium assumptions for a large temperature range. The database was extended for pressures ranging from 0.1 bar to 150 bar and temperatures ranging

from 300 K to 35000 K, in a spectral bandwidth between 50 nm to 10 µm (Kahhali et al. (2010); Peyrou et al. (2012)). All emission processes associated with bound-bound, bound-free and free-free transitions that may intervene in these temperature and pressure ranges were taken into account. Overall, eighteen species, composed of atoms, ions and molecules were considered (Chauveau et al. (2003); Kahhali et al. (2010); Peyrou et al. (2012)).

For a given pressure, we calculate the derivative of the absorption coefficient κ, with respect to the temperature $d\kappa/dT$, for each wavelength. The derivative $d\kappa/dT$ is weighted by its corresponding κ, to emphasize the spectral zones having a high intensity variation and with a significant absorption coefficient. The modulus of this product is taken, and a base-10 logarithm is applied to put in evidence the different orders of magnitude present in this calculation. An example of a contour plot of the logarithm of this product is shown in figure V.1. The red contours are several orders of magnitude higher than the most areas in the plot, which highlights the sensitivity of those zones. The three zones presenting the highest intensity variation with temperature are those centered at 463 nm, 500 nm and 568 nm, which correspond to nitrogen ionic lines. These N II multiplets show an excellent sensitivity for temperatures ranging from 20000 K to 30000 K and are the most convenient choice to be studied.

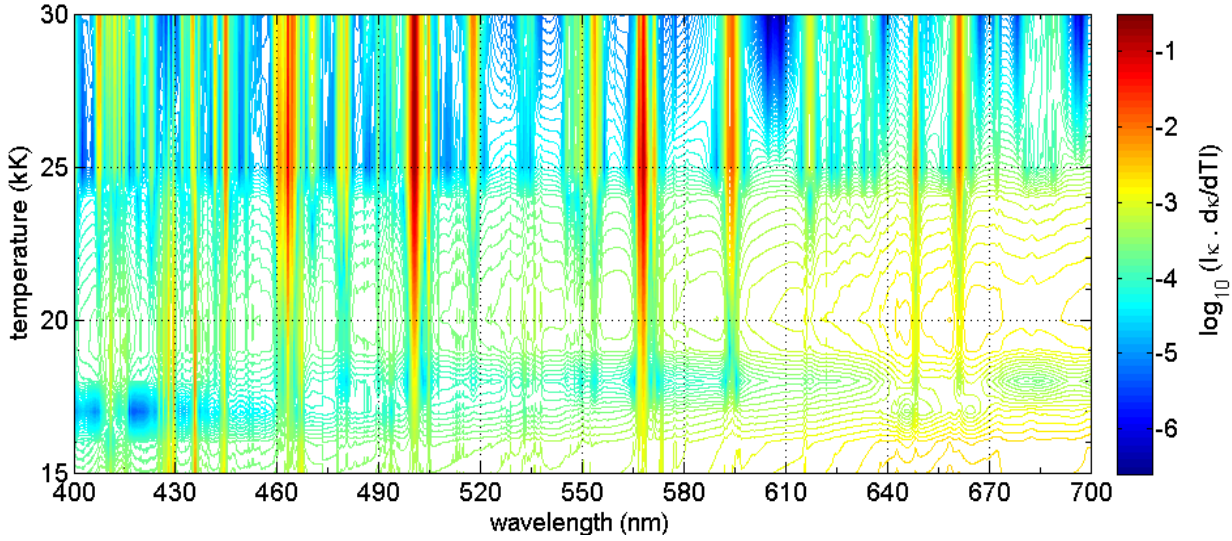

Figure V.1. Contour plot of $\log_{10}(|\kappa.d\kappa/dT|)$ calculated with a fixed pressure of 15 bar.

By using the grating of 300 grooves mm^{-1}, we were able to record a spectral window of approximately 53.5 nm by shot. Consequently, to ensure the continuity of the spectral windows and to cover the three chosen N II multiplets, we selected three continuous spectral windows with the first starting at 431.5 nm and the last ending at 585 nm (window I: 431.5 to 485 nm; window II: 481.5 to 535 nm; window III: 531.5 to 585 nm).

We can find 192 lines of O II and N II for this spectral range from the NIST database (Kramida and al. (2015)) when setting the minimum Einstein emission coefficient to 10^6 s^{-1}. Figure V.2 shows a plot of line positions, weighted by their corresponding degeneracy and Einstein emission coefficient. It will be shown in section V.2 that these ionic lines can be well identified in the arc spectra.

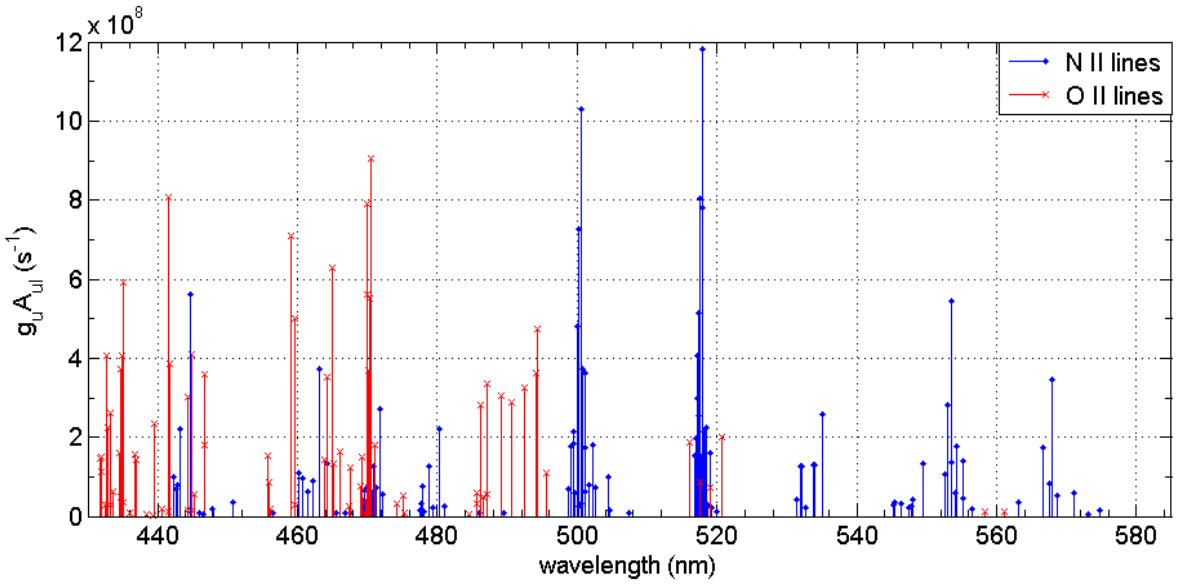

Figure V.2. Nitrogen and oxygen ionic lines in the spectral range 431.5 nm to 585 nm, weighted by their corresponding degeneracy and Einstein emission coefficient.

V.1.2 Absorption coefficient and optical thickness

In the order to select an adapted spectroscopic diagnostic method to be applied for the column characterization, we need to verify the hypothesis that must be adopted about the optical thickness τ of the plasma.

As described in Chapter II, the optical setup of the OES measurements is optimized to collect parallel and narrow chords of the light emitted inside the arc column. We estimated and analyzed the optical thickness of a collected chord by calculating the absorption coefficient of the selected spectral lines and by using the arc radius evolution presented in Chapter III.

The column radius r_{ARC} allows us to determine the lengths of each chord that crosses the column. The chord length l_c, for each collected line-of-sight, can be expressed as a function of its distance from the column axis d by the relation, $l_c = 2(r_{ARC}^2 - d^2)^{1/2}$. The radius ranges from a few millimeters to more than three centimeters, for the case of the 100 kA current peak, which led to lengths of the chords in the order of, or higher than, the centimeter. Figure V.3 shows an example of the evolution of the chord length for the 100 kA, calculated for a few

times. It can be seen that even in the beginning of the arc, as for instance at 3 µs, the chord crossing the column center reaches a length of 12 mm.

In the following subsections, we present the assumptions and the procedure used to calculate the absorption coefficient of the chosen ionic lines.

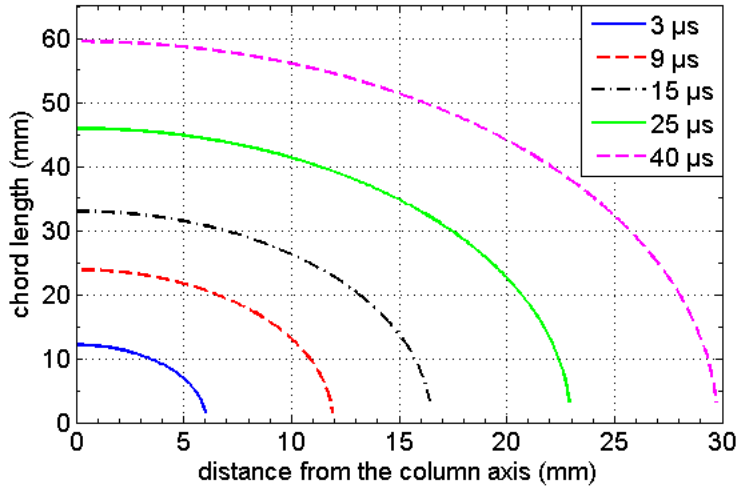

Figure V.3. Example of chord lengths that cross the column as a function of the distance from the column axis, calculated for 100 kA peak.

V.1.2.1 LTE assumption and absorption coefficient formula

The free arc column studied in the present work is assumed to be at the local thermodynamic equilibrium (LTE). The LTE assumption requires two main conditions; the electrons have to follow Maxwellian velocity distribution and the atoms and ions have to be populated according to Maxwell-Boltzmann statistics at the same temperature as electrons. In high-density plasmas, the collisional effects are dominant when compared to radiative effects. Consequently, the high rate of electron's collisions leads to the thermalization of the plasma (Griem (1997)). This is often the case of air plasma in electrical arcs, mainly far from the electrodes (Gleizes et al. (2005)).

By considering the LTE assumption and using the Kirchhoff's law, the absorption coefficient, for bound-bound transitions of atomic species, can be obtained from the ratio of the emission coefficient η to the Planck function I^0. The resulting expression is a function of the temperature T and the electron density N_e and can be written as:

$$\kappa(\lambda, T, N_e) = \frac{\eta(\lambda, T, N_e)}{I^0(\lambda, T)} = \frac{\lambda^5\left(e^{hc/\lambda kT} - 1\right)}{2hc^2} \sum_{line} \frac{hc}{4\pi}\left(\frac{g_u A_{ul}}{\lambda_{line}}\right) \frac{N_o(T, N_e)}{Q(T)} e^{-\frac{E_u}{kT}} f(\lambda - \lambda_{line}, T, N_e \tag{V.1}$$

where h and k are respectively Planck and Boltzmann constants, c is the speed of light, E_u and g_u are respectively the energy and the degeneracy of the upper transition level, A_{ul} is the Einstein emission coefficient for the transition from the upper (u) to the lower (l) level, N_o is the total population of the radiating species, Q is its internal partition function, λ_{line} and f are the central wavelength and the spectral line shape of the transition.

For each transition, the spectroscopic constants in equation (V.1), as E_u, g_u, A_{ul} and λ_{line} were taken from the NIST database (Kramida and al. (2015)). The assumptions and calculations for the internal partition functions, the total populations of the species and the spectral line shape are described in the following subsections.

V.1.2.2 Internal partition function

The internal partition functions are calculated using the energy levels and the degeneracies from the available data in NIST energy levels, which is considered to be complete enough for this calculation (Deron (2003); Chauveau et al. (2003)). In general, the expression for Q can be written as:

$$Q(T) = \sum_i g_i e^{-E_i/kT} \tag{V.2}$$

where the sum is taken over all energy levels i until reaching the ionization level of the corresponding species, in the electrostatic conditions of the plasma mixture. Figure V.4 shows the evolution with the temperature of the partition functions for N II and OII. Also, the calculated partition functions are compared to the results obtained by Deron (2003), which take into account lowering of the ionization potential due to Coulombian interactions (Debye-Huckel effect). The maximum differences between the two methods are 0.2% for $Q_{N\,II}$ and 3% for $Q_{O\,II}$. Therefore, we assume that the partition functions, calculated using equation (V.2) and the energy levels listed by NIST, are sufficiently accurate for the purposes of the present work.

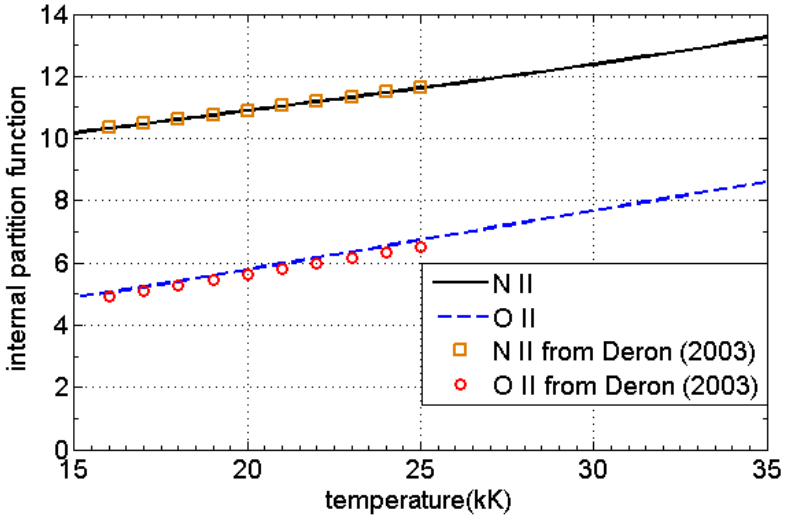

Figure V.4. Comparison of the evolution with temperature of the internal partition functions to the results of Deron (2003).

V.1.2.3 Total population of the radiating species

To obtain the total population of each studied species we use the LTE air plasma composition model, developed in Refs. (Deron (2003); Chauveau et al. (2003)), which assumes chemical equilibrium and atmospheric pressure. This composition model was extended for pressures ranging from 0.1 bar to 150 bar, by Peyrou et al. (2012). Briefly, the population densities are obtained by solving a set of 19 equations corresponding to the conservation of nuclei (N (78.46%), O (21.05%) and Ar (0.49%)), to three Guldberg–Waage dissociation reactions (N_2, O_2, and NO), 11 Saha ionization reactions and the electrical neutrality and perfect gas state equations (Peyrou et al. (2012)).

Generally, in this kind of database, the total populations of the species are given as functions of the temperature T and the pressure P. Then, for each T, the bijective correspondence between P and N_e allows us to link the three variables T, P, and N_e. Figure V.5 shows an example of the population densities calculated at 15 bar.

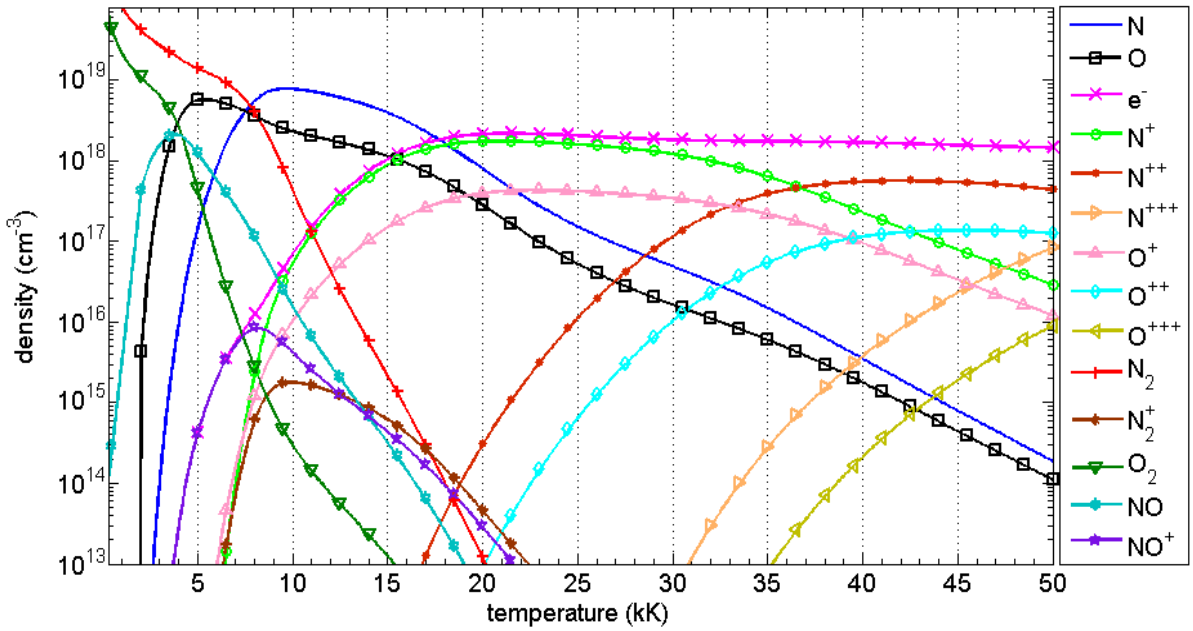

Figure V.5. Population densities of LTE air plasma composition calculation at 15 bar (Argon not shown).

V.1.2.4 Spectral line shape and broadening mechanisms

Several broadening mechanisms may affect the spectral line shape. Generally, they can be classified into three types; natural broadening, thermal Doppler broadening and collisional broadening (Griem (1974); Griem (1997)). Natural broadening is related to the finite lifetime of the excited level. This line broadening is in the order of 10^{-4} nm and is neglected in the present work. The Doppler broadening is due to thermal motion of the radiation emitters and the corresponding width is proportional to the square root of the ratio between the temperature and the emitter mass. This mechanism leads to a Gaussian distribution of the spectral line emission. Collisional effects are caused by the interaction between the radiation emitters and others particles present in the medium. In turn, they may be separated in three broadening components; resonance, van der Waals and Stark effects. The collisional mechanisms produce a Lorentzian distribution for the line shape. For a complete description of the different broadening mechanisms, the interested reader is referred to Griem (1974).

For the considered ionic lines, the Doppler broadening calculated at 40000 K reaches a half width at half maximum (HWHM) of approximately 0.01 nm. The expected electron density for the lightning arc is above 10^{18} cm^{-3}, which leads to a Stark broadening with HWHM at least 20 times higher than the Doppler contribution. Therefore, the Doppler broadening can be neglected when compared to collisional broadenings, and the spectral line shape f is approximated by a Lorentzian profile. The resonance and van der Waals broadenings are approximately

proportional to the density of neutral perturbers (Griem (1974); Griem (1997); Djurovic and Konjevic (2009)), and then, for those ionic lines in such range of electron density, they can be neglected when compared to the Stark contribution, which is due to collisions with charged particles (Griem (1974); Milosavljevic (1998)). Finally, the Stark broadening can be assumed as the major contributor to line broadening. The line shape *f* can be written as:

$$f(\lambda, T, N_e) = \frac{1}{\pi} \frac{\gamma}{\gamma^2 + (\lambda - \lambda_{line})^2} \tag{V.3}$$

where γ is the Stark HWHM. For the considered ionic lines, the Stark broadening coefficient is assumed proportional to the electron density and is slightly dependent on the temperature (Griem (1974); Griem (1997); Konjevic et al. (2002)).

The Stark HWHM, as a function of the electron density and the temperature, is obtained from linear extrapolation in the tables of experimental data compiled by Konjevic et al. (2002). For the transitions that are listed by NIST but the Stark parameters are not present in Konjevic tables, we applied the average parameter value of the same multiplet of the transition. Stark parameters, Einstein emission coefficients, degeneracies and energy levels, used for each line, are listed in appendix B.

V.1.2.5 Optical thickness estimation

In the expected range of temperature and electron density and by considering the hypotheses cited above, the absorption coefficient given by equation (V.1) becomes completely defined by the two parameters *T* and N_e. Figure V.6 presents the calculation of the absorption coefficient of the N II and O II lines for a few representative values of temperature and electron density. In figure V.6*(a)* the temperature is fixed at 30000 K and the electron density is varied from 1×10^{18} cm^{-3} to 5×10^{18} cm^{-3}. In figure V.6*(b)* the electron density is fixed at 3×10^{18} cm^{-3} and the temperature is varied from 25000 K to 35000 K.

From the examples shown in figure V.6, the absorption coefficient of the central regions of the main multiplets can reach values in the order of 10 cm^{-1}. The optical thickness, given by the product $\tau = \kappa\, l_c$, can then reach values around 10 for a chord length of 10 mm.

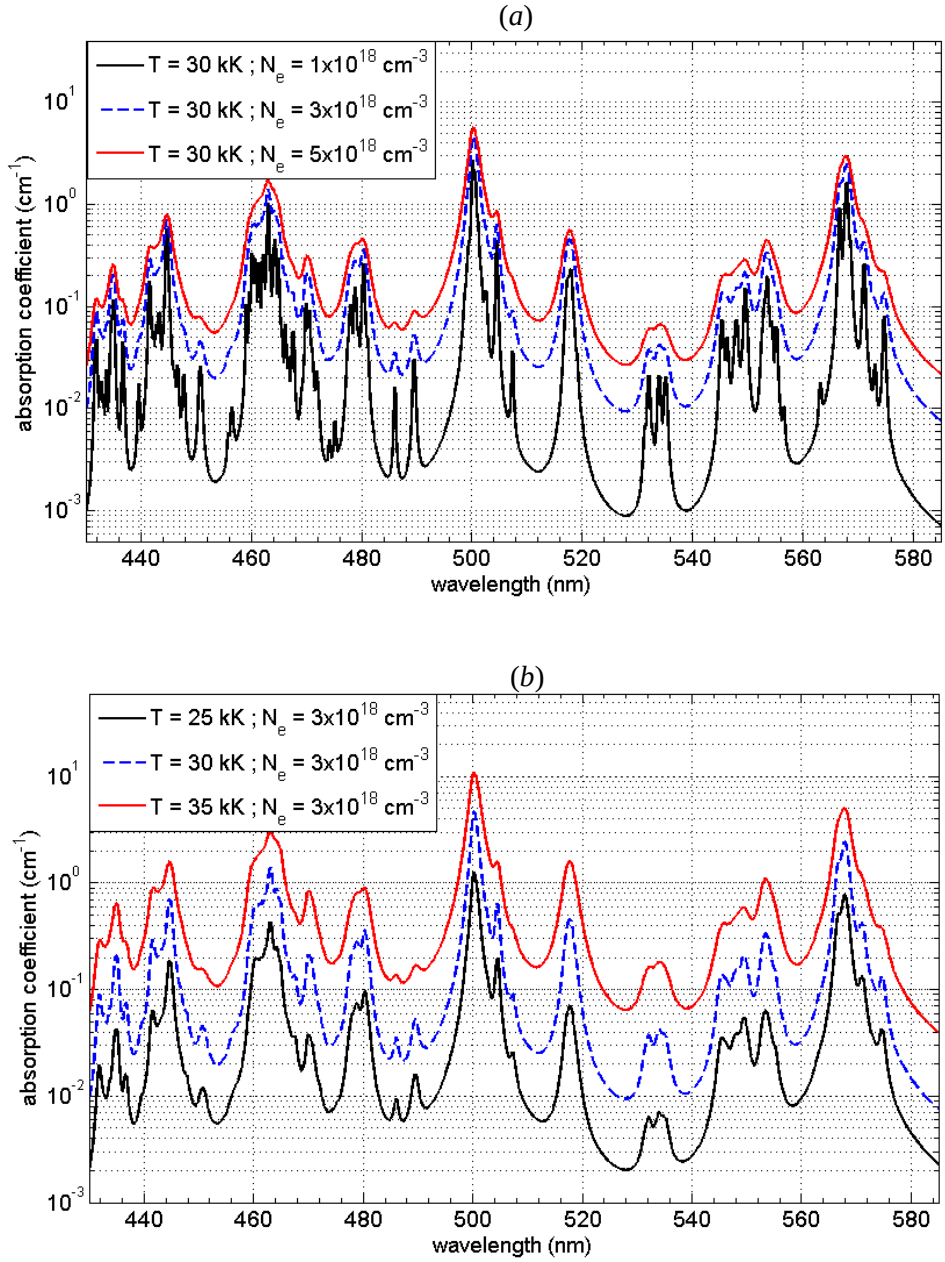

Figure V.6. Absorption coefficient calculated from equation (V.1) for different values of T and N_e. (a) Variation with electron density. (b) Variation with temperature.

In general, for the application of the optically thin hypothesis, the accepted upper limit for τ is 0.2 (Uman and Orville (1965)). Consequently, this assumption cannot be adopted for the lightning column and then the vast majority of the well-known plasma diagnostic methods, as the Boltzmann plot and the Stark broadening measurements, cannot be directly applied. In the next section, an alternative method to characterize the plasma under non-optically thin assumption is developed based on the resolution of the radiative transfer equation.

V.1.3 Radiative transfer equation

The radiative transfer equation allows us to take into account the self-absorption phenomenon for the ionic lines studied in this work. The axisymmetric hypothesis for the arc column during the first 50 µs was demonstrated by high-speed imaging in Chapter III. We consider, therefore, the arc channel as a combination of concentric isothermal-isobaric layers as illustrated in figure V.7. Each layer is defined by a constant temperature T and electron density N_e.

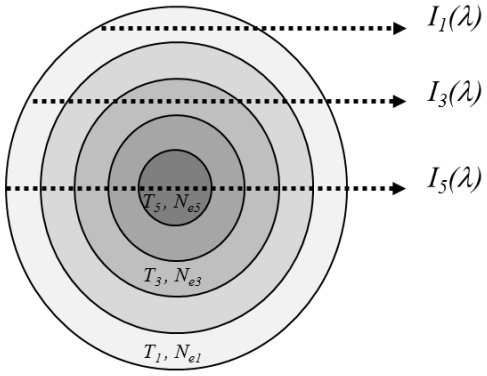

Figure V.7. Schematic for the chords that cross the arc channel in discretized homogeneous layers. Each layer i has a constant temperature T_i and electron density N_{ei}.

The radiation intensity $I_m(\lambda)$ collected from each line-of-sight m can be written from the optical energy balance between absorption and emission processes along the chord (Griem (1997)). Neglecting the scattering phenomenon and any transverse gradient inside each collected chord, the radiative transfer equation can be put in a simple form and $I_m(\lambda)$ can be written as:

$$I_m(\lambda) = \sum_{i=1}^{i=2m-1} I^0_{\lambda\,i}(1 - e^{-\kappa_{\lambda_i} x_i}) e^{-\sum_{j=i+1}^{j=2m-1} \kappa_{\lambda_j} x_j} \qquad \text{(V.4)}$$

where m is the chord number, starting from the farthest position from the arc channel center until the chord that crosses the central layer (the channel axis), i is the column inside the layers crossed by the chord, x is the column length and κ_λ is the absorption coefficient, formed by adding the bound-bound contribution and the continuum contribution. The first summation is taken over all columns crossed by the chord. The second summation, inside the exponential, represents the absorption of the layers ahead the column i, and is taken from $i+1$ until the channel edge. Note that in the RTE context, the word *column* refers to the continuous zone crossed by a chord inside a given layer with a length x, in opposition to the term *arc column* which refers to the cylindrical region of the arc channel with a length l_{ARC}.

For each chord and wavelength, the radiation intensity I_m, modeled by equation (V.4), is only a function of the absorption coefficient κ_λ and the column length x. The lengths are calculated from the total chord length (figure V.3) and by considering the layer thickness as the distance between two adjacent chords (1.2 mm for the highest resolution and 2 mm for the lowest). The general form for the *nth* column lengths x_n as a function of the distance d_m of the *mth* collected chord to the arc axis can be written as:

$$\begin{bmatrix} x_1 \\ x_2 \\ \vdots \\ x_{n-1} \\ x_n \end{bmatrix} = \begin{bmatrix} \sqrt{R_1^2 - d_m^2} - \sqrt{R_2^2 - d_m^2} \\ \sqrt{R_2^2 - d_m^2} - \sqrt{R_3^2 - d_m^2} \\ \vdots \\ \sqrt{R_{n-1}^2 - d_m^2} - \sqrt{R_n^2 - d_m^2} \\ \sqrt{R_n^2 - d_m^2} \end{bmatrix} \quad \text{, with:} \quad \begin{bmatrix} R_1 \\ R_2 \\ \vdots \\ R_{n-1} \\ R_n \end{bmatrix} = \begin{bmatrix} r_{ARC} \\ (d_1 + d_2)/2 \\ \vdots \\ (d_{n-2} + d_{n-1})/2 \\ (d_{n-1} + d_n)/2 \end{bmatrix} \tag{V.5}$$

where R_n is the radius of the *nth* layer. The total number of columns crossed by the *mth* chord is equal to *2m-1*. Due to the symmetry, the length terms with index *i* and *2m-i* are identical. Therefore, the index *n* varies from 1 to *m*, with *n* = *m* being the crossed layer closest to the arc axis.

The total absorption coefficient is calculated from equation (V.1) added to a linear term, $A\lambda + B$, to model the continuum contribution. A calculated spectrum is obtained by a convolution of the radiative intensity of equation (V.4) and the spectrometer slit function (see Chapter II).

The procedure applied to obtain the profiles of temperature and electron density from the resolution of the RTE can be briefly described as follows: starting from the farthest chord that crosses just one layer, the calculated spectrum is compared to the measured one by applying a least-square procedure with four fit parameters *T*, N_e, *A* and *B*. Then the set of fit parameters is fixed for the first layer and we proceed systematically for the next chord until reaching the central chord. This procedure can be seen as a simple Abel inversion for non-optically thin media, avoiding the use of spatial derivatives, and then, more suited for our limited number of optical fibers.

At the first microseconds, the arc channel radius is still small, with a value of 4.2 mm at 2 µs. Therefore, even with the highest spatial resolution, only a few fibers collect significant light at these first instants, which leads to a discretization of the arc channel in a small number of layers. The worst case get with this setup is four layers to describe the arc channel at 2 µs. Using theoretical distribution for temperature and electron density, we performed a sensitivity analysis of the results obtained by the present method, for those cases of limited number of layers.

Calculations were carried out using Gaussian profiles, with the half width at half maximum (HWHM) corresponding to the channel radius. The difference between the real value at the center of a layer (T_{theo}) and the average value obtained by our discretized procedure (T_{avg}) were evaluated at different times from the ratio T_{theo}/T_{avg}. For the case of four layers and with values of T and N_e at the axis channel of 40 kK and 5×10^{18} cm^{-3}, respectively, the maximum difference takes place in the first external layer and decreases in the internal layers as one moves toward the channel axis. The maximum difference reaches 10.6% for the temperature and 15.2% for the electron density. As expected, these differences decrease as the number of discretized layers increases. At 4 µs, the maximum difference decreases to 8.7% for T and 13.8% for N_e, and at 14 µs it falls to 5.9% and 9.8%, respectively. Consequently, although the maximum error takes place in the channel edge, the results obtained by that procedure must be taken with care when the number of layers is small.

V.1.4 Hydrogen Balmer-alpha line

Hydrogen Balmer-alpha line (Hα) is observed in the spectra of the lightning arc. Atomic hydrogen is probably originated from the molecular dissociation of water vapor present in the laboratory room. In the previous studies of the lightning strike, it was reported the presence of Hα around 20 µs after the lightning initiation (Orville (1966a); Orville (1966b); Uman (1966); Krider (1973)). In these works, the Hα line was used for electron density measurements under an optically thin hypothesis.

In the present work, we were not able to perform a complete analysis of the optical thickness of the Hα line as was done in section V.1.2, due to the lack of knowledge of the total amount of hydrogen in the room for the duration of the experiment. Therefore, we choose to analyze the Stark broadening of Hα line assuming the plasma as optically thin and we discussed in section V.2.2 the consequences of this hypothesis.

There are many studies of the Stark broadening of hydrogen lines due to their major interest in astrophysical problems and also in plasma diagnostics (Griem (1964); Griem (1997)). We can mention, for instance, the work of Stehlé and Hutcheon (1999), which is based on the Model Microfield Method (MMM) approach and gives extensive tabulations for the total line profile, from the line center to the far wings, as a function of electron density and temperature. In the present work, we chose to focus only on the measurement of the full-width at half maximum (FWHM) of the Hα line, to avoid any inaccuracy that could appears in the line profile measurement, caused by neighboring emission transitions.

To obtain the electron density from the FWHM Stark width of Hα line, we applied the relation developed by Kepple and Griem (1968), which is based on an impact theory for electron collisions and a quasi-static approximation for the ion collisions. This relation was recently compared to experimental FWHM measurements for densities above 10^{18} cm^{-3} and showed a very good agreement (Griem et al. (2005)). The expression for the electron density in cm^{-3} can be written as:

$$N_e = \left(\frac{w_s \times 10^{18}}{2.5\alpha_{1/2}} \right)^{3/2} \tag{V.6}$$

where w_s is the FWHM Stark width in meters and $\alpha_{1/2}$ is the reduced semi-half-width which is tabulated in Ref. (Griem (1974)) as a function of the electron density and temperature.

The FWHM Doppler broadening of the Hα line is lower than 0.09 nm for temperatures below 35000 K and is neglected when compared to the measured FWHM, which ranges from 4 nm to 11 nm. Therefore, all the broadening of the line shape is considered to be due to the Stark effect. The measured and calculated spectra are compared using a least-square method, with w_s as the fit parameter. The Hα line is fitted by a Lorentz function, given by equation (V.3), convolved to the spectrometer slit function. For each measured w_s, we performed an iterative interpolation in the tables to find the appropriate value of $\alpha_{1/2}$.

V.1.5 Error estimations

To estimate the errors that arise in the determination of temperature and electron density presented above and to evaluate the sensitivity of the results, three approaches were considered. The first one is derived from the mathematical analysis of the least-squares method applied to nonlinear equations. This approach was proposed by Burrell (1990) and considers the derivatives of the χ^2 and the objective function, to obtain an expression for the standard deviation in the fit parameters. The second method, supposes a linear relationship between the parameter errors (δT and δN_e) and the residual function of the fit. This relationship can be written as a function of the deviation of T and N_e from the fit results. A criterion for the parameter errors can be obtained from the maximum value reached by that relationship. Finally, the last approach is based on the study of the residual fit function, and how this function is modified as T and N_e vary around the fit result.

The mathematical approach led to errors higher than 100% in some cases, and the criterion of the second one is not achievable in all cases. Therefore, the two first methods are not used

thereafter, and the last approach was chosen to evaluate the parameter errors and is detailed below.

The residual fit function represents the root mean square error (RMSE) between the measured spectrum, I^{meas} and the calculated one, I^{calc}. The set of fit parameters is determined from the least-square procedure by a minimization of this function which can be defined as:

$$R(T, N_e) = \left[\sum_{\lambda=\lambda_i}^{\lambda_f} \left(I_\lambda^{meas} - I_\lambda^{calc}(T, N_e) \right)^2 \right]^{1/2} \quad \text{(V.7)}$$

where λ_i and λ_f are respectively, the initial and the final wavelengths in the spectrum. A rough estimation of the error bars in the fit procedure is defined here as the distance between the fit value and the parameter values that leads the residual function to a factor two of the minimum residual, R_{FIT}. Figure V.8 shows the evolution of the residual function with two parameters, T and N_e, and illustrates the procedure to estimate the error bars shown in section V.2.

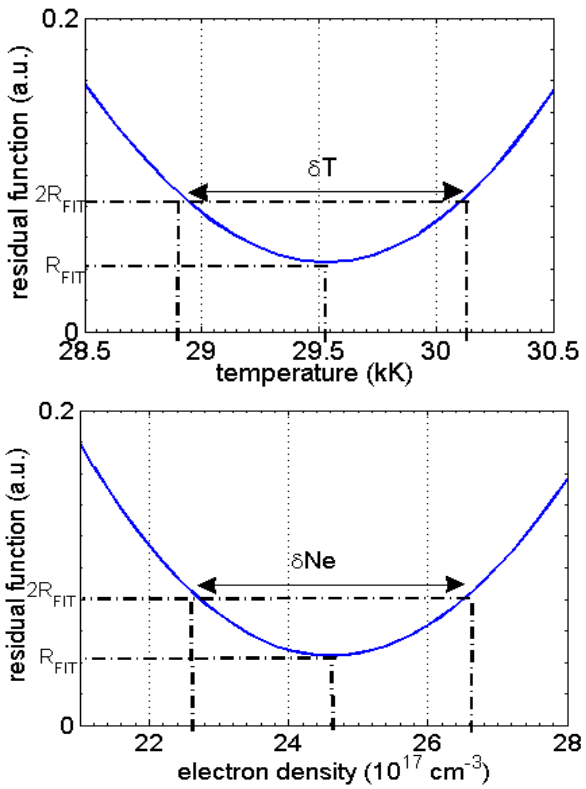

Figure V.8. Examples of variation of the residual fit (equation (V.7)) as a function of two parameters and the criterion for the error bar estimations.

This criterion for the estimation of the error bars has the advantage to help the characterization of the parameter's sensitivity. A peaked curve for the residual function will lead to small values for the error bars and represents a good sensitivity for the fit. Conversely, a shallow curve will

result in large error bars and represents a poor sensitivity (Babou et al. (2008)). In addition to the above criterion, results from different spectral windows give another idea on the dispersion of the measured quantities and are also discussed in section V.2.

V.2 Results and discussion

In this section we present and discuss the results of temperature, electron density and pressure profiles obtained using the procedures described in section V.1. First, we introduce the results obtained from the RTE solution using the N II and O II lines and a comparison of the properties for different current levels. Then, we present the results obtained from the exploitation of Hα line and we discuss the partial intensity emission from each layer, in order to check that the central region also contributes to the measured emission. Finally, we present the electrical conductivity profiles calculated from temperature and pressure distributions and we compare them to the results obtained in the Chapter IV from electrical characterization.

V.2.1 Temperature, electron density and pressure distributions from N II and O II lines

As presented in section V.1.1, we investigate the spectral range from 431.5 nm to 585 nm, which must be recorded in three different shots due to the spectrometer setup. In this range, 192 lines of O II and N II are listed in the NIST database with an Einstein emission coefficient higher than 10^6 s^{-1}. Figure V.9 shows an example of the overlapping of the collected spectra from the three spectral windows after the relative intensity calibration.

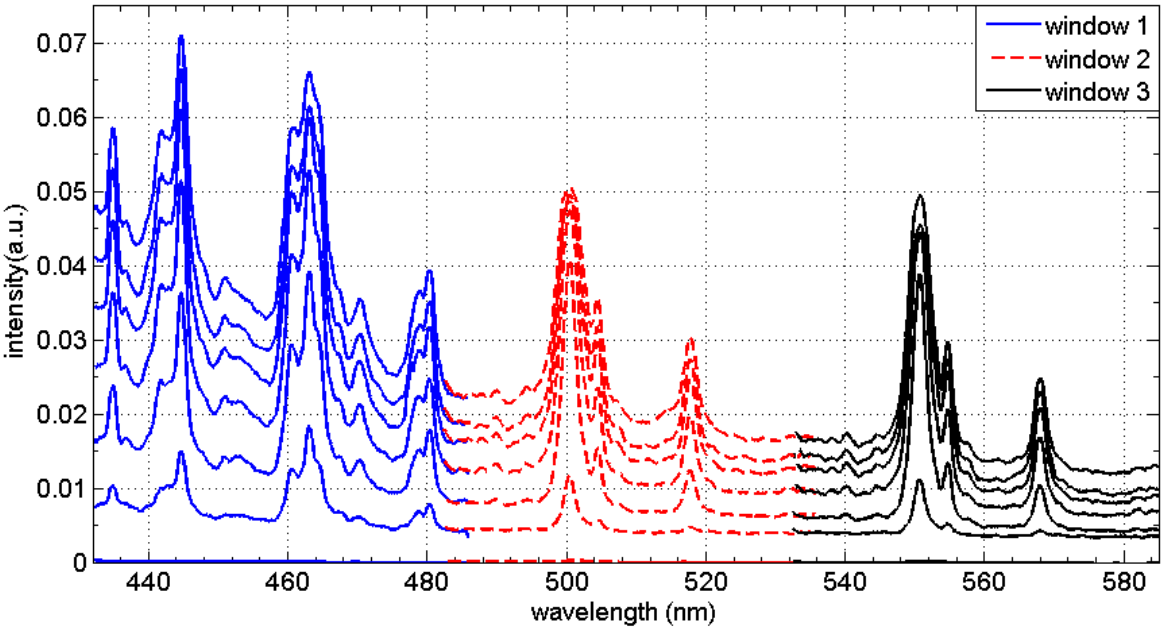

Figure V.9. Example of the overlapping of the collected spectra from the three spectral windows after relative intensity calibration.
Experimental parameters: peak of current = 100 kA; time = 14 µs; chord positions from the central arc: 11 mm, 8.3 mm, 5.7 mm, 4.4 mm, 3.1 mm 1.8 mm; exposure time = 200 ns.

Figure V.10 shows an example of the normalized spectra collected for three spectral windows. The fitted spectra are also plotted with the position of the ionic. The majority of the expected N II and O II lines can be easily identified in the spectra. Also, despite the fact that some carbon evaporation of the ignition wire is certainly present in the arc plasma, we would expected intense carbon multiplets in the studied spectral range, as for instance those centered at 493.205 nm, 505.217 nm and 538.033 for C I or at 514.516 nm and 566.246 nm for C II. Nevertheless, no lines were detected at these positions, and then the influence of the ignition wire in the plasma was not considered.

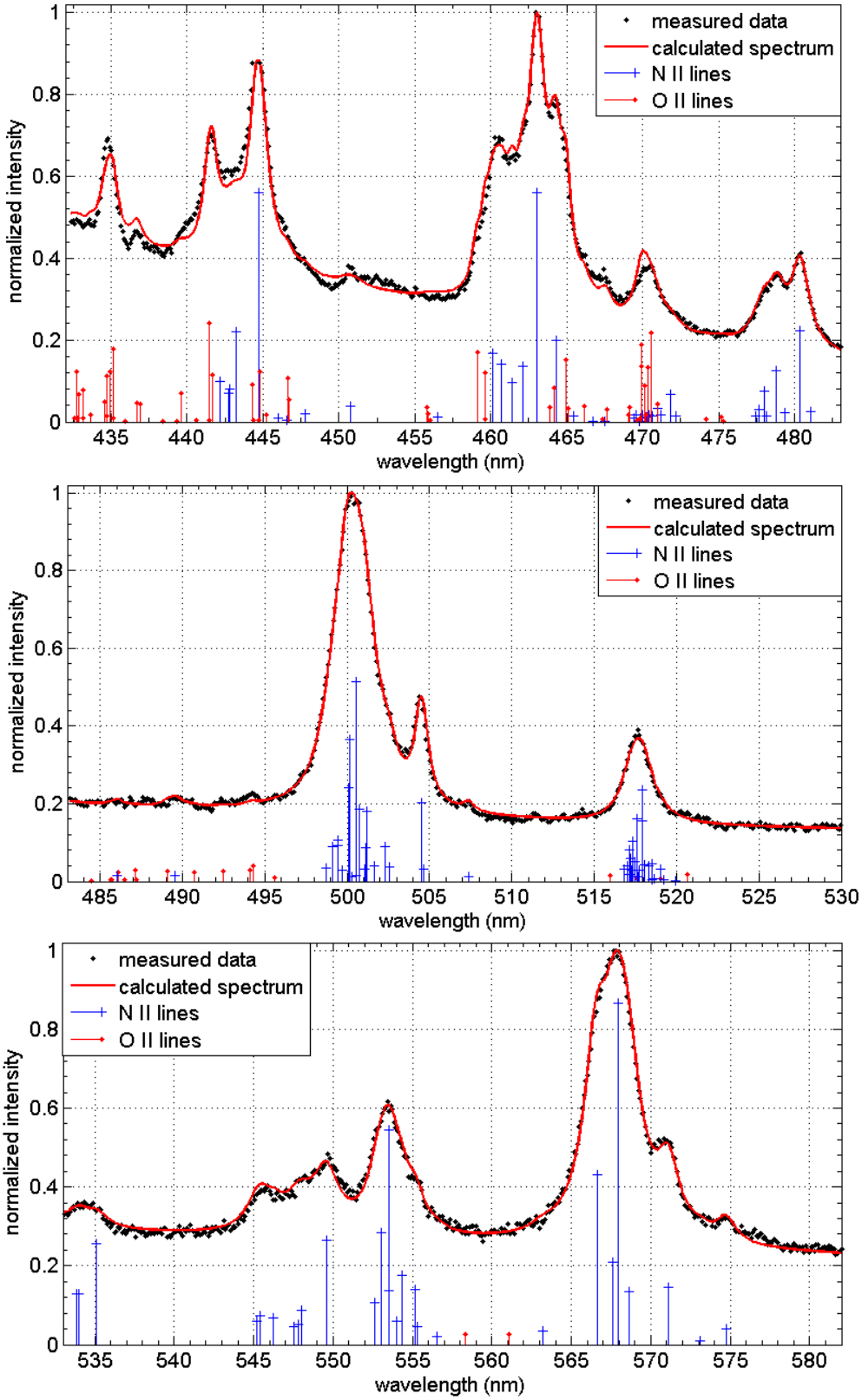

Figure V.10. Examples of measured and calculated spectra for the three spectral windows. Experimental parameters: peak of current = 100 kA; time = 6 μs; chord position from the central arc = 3.6 mm; exposure time = 200 ns.

V.2.1.1 Results for the 100 kA current peak

Solving the RTE for each collected spectrum as described in section V.1.3, we can obtain the radial distribution of temperature and electron density. The profiles for the current peak of 100 kA and for the three spectral windows are presented separately in figure V.11. In order to analyze the dynamics of arc properties, different instants are acquired, ranging from 2 µs to 36 µs, which cover the rise and the decrease phase of the current waveform. It was shown in Chapter III that the axisymmetric assumption of the arc column is valid at least until 50 µs. However, the intensity of the N II and O II lines becomes very weak after 40 µs preventing their exploitation. For each profile of T and N_e presented in figure V.11, the farthest radial position is set to the standard ambient temperature (298.15 K) for T and zero for N_e, since no intensity was detected at these positions in the studied spectral range. Also, in accordance with the column radius evolution, these positions are located outside the arc channel. For the two firsts chords at 36 µs, located at 25.7 mm and 27.8 mm, line intensities were very weak. Therefore, for this instant, the first chord used was that located at 23.7 mm from channel center and these two positions are left empty.

Temperature and electron density determination is performed from the outside to the inside of the arc channel, i.e., from the chord that crosses just one layer until the chord that crosses all layers. Consequently, the increase of the number of the crossed layers reduces the sensitivity of the emitted intensity to the searched parameters, and then the uncertainty of the results increases as one moves toward the channel center. The uncertainty, according to the chosen criterion, is lower than 12% for the temperature and reaches 30% for the electron density. This significant value for δN_e results from the criterion adopted for uncertainty estimation. The variation of N_e affects directly the broadening of the lines, which in turn lead to a slight modification of the residual function. This implies that high values of δN_e are required to reach a significant difference between the measured and calculated spectra and achieve the criterion described in section V.1.5.

Generally, the three spectral windows lead to similar results, even if the spectral lines that compose each window have different characteristics. The first window (431.5 nm to 485 nm) is characterized by a significant mixing of ionic nitrogen and oxygen lines, with a total of 96 considered transitions. The good agreement between the measured and the calculated spectra in this zone indicates a good thermal and chemical equilibrium for the species. The second window (481.5 nm to 535 nm) has a majority of N II lines and their upper energy level cover a very broad range, ranging from 20.9 eV to 30.3 eV. This significant energy gap leads to spectra with high sensitivity to temperature, which improves the measurement method.

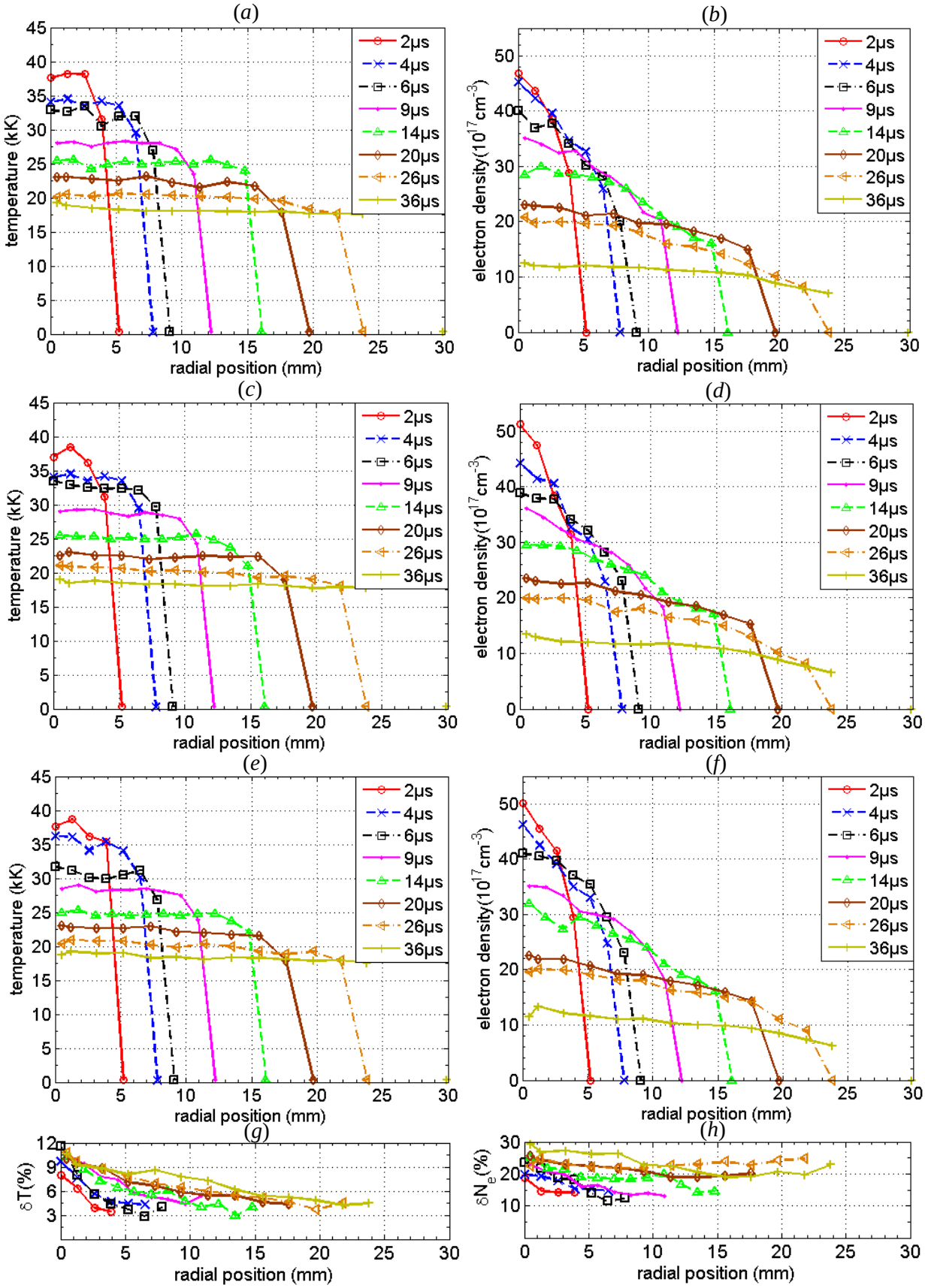

Figure V.11. Temperature and electron density profiles for the 100 kA current peak from the three spectral windows; (a-b) 431.5 nm to 485 nm; (c-d) 481.5 nm to 535 nm; (e-f) 531.5 nm to 585 nm; (g-h) maximum percentage uncertainty according to the criterion of section V.1.5.

The last spectral window (531.5 nm to 585 nm) is similar to the second one, with a majority of N II lines and an upper energy level ranging from 20.6 eV to 30.3 eV. The number of N II lines is smaller than in the others zones, but the multiplets are well separated, which allows a better resolution of the line groups, enhancing the sensitivity of the method.

Figure V.12 shows the average radial distribution of temperature and electron density calculated using the results obtained from the three spectral windows. For this figure, the error bars are calculated using the dispersions of the three values and is lower than the estimations obtained from the residual criterion described in section V.1.5. The dispersions are around 5% for the temperature and 12% for the electron density, which shows a good consistency of the results.

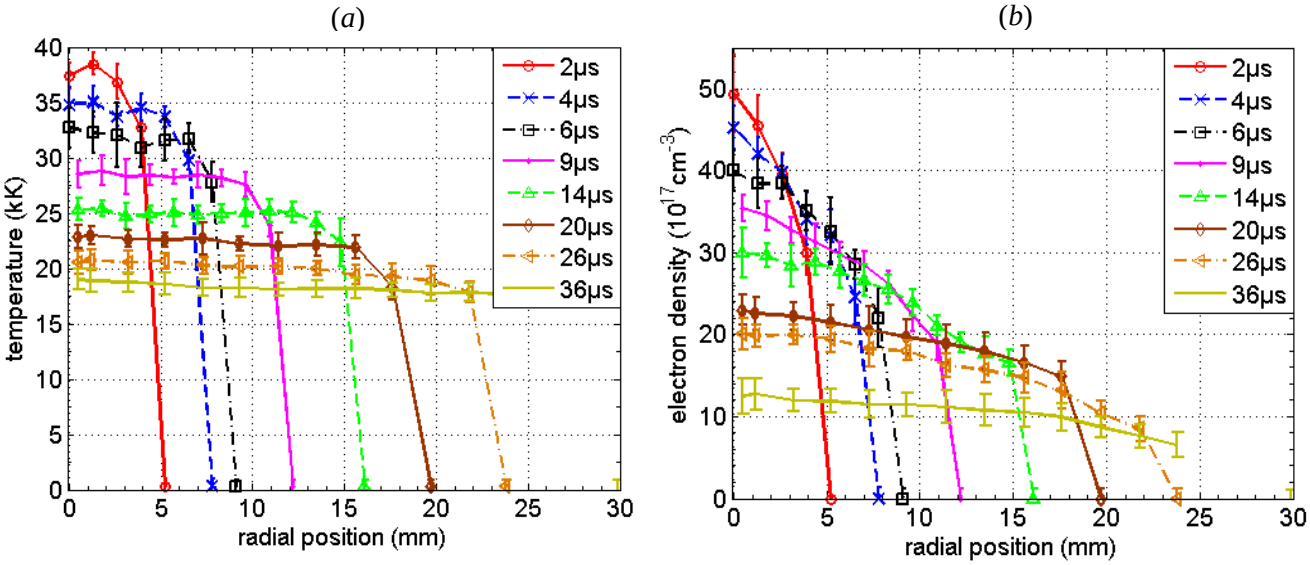

Figure V.12. Average radial distributions of temperature and electron density calculated from the profiles of the three spectral windows for the 100 kA peak current; error bars indicate here the dispersion of the three results.

In the column center, the temperature and the electron density reach, respectively, 37400 K and 4.9×10^{18} cm^{-3} at 2 µs, when the current is in the high growth phase and its value is 29 kA. At the current peak, the temperature decreases to 25300 K and the electron density to 3×10^{18} cm^{-3}. In general, the temperature remains relatively constant in the inner region of the channel and shows a sharp gradient on the edge. The electron density decreases with the radial position and takes approximately a parabolic shape. At 36 µs the current drops to 57 kA and the channel radius reaches around 28 mm. At this time, the temperature decreases to 19200 K and the electron density is around 10^{18} cm^{-3}. Table V.1 summarizes the average results obtained at the column center.

Note that as discussed in section V.3.3, the results for the first microseconds are obtained by a discretisation of the arc channel in just a few layers due to the small size of the channel radius and a limited spatial resolution. For those instants, the accuracy of the results is affected by possible gradients in the radial distributions. However, despite the result at 2 µs, the measured radial distributions (figures V.11 and V.12) present a roughly flat shape, which leads to small errors compared to those obtained using Gaussian profiles.

Table V.1. Current, column radius, temperature and electron density at the column center over time for the 100 kA current waveform.

Time (µs)	**Current (kA)**	**Column radius (mm)**	**Temperature (kK)**	**Electron density (10^{17} cm^{-3})**
2 µs	29.06	4.2	37.4	49.3
4 µs	56.32	7.0	34.8	45.2
6 µs	75.90	9.2	32.7	40.1
9 µs	92.92	11.8	28.5	35.4
14 µs	100.07	15.7	25.3	29.9
20 µs	91.83	20.0	22.8	23.0
26 µs	78.28	23.7	20.5	20.1
36 µs	57.23	28.4	19.2	12.5

The pressure inside the channel can be estimated from the results presented in figure V.12. As described in section V.1.2.3, from the LTE air plasma composition, the pressure can be deduced for each pair of temperature and electron density. Figure V.13 shows the pressure calculated using the average results obtained from the three spectral windows. For these radial distributions, the first position outside the arc channel, where no intensity was detected by OES measurements, was not set to the standard ambient pressure. This choice is made because a deviation from the ambient pressure is expected in this region due to the shockwave generated by the arc expansion (see Chapter III). The pressure reaches 45 bar at the channel center and decreases to 8 bar at 36 µs. As the temperature is approximately constant inside the channel, the pressure profiles have similar shapes as the electron density, decreasing with the increase of radial position. The uncertainties shown in figure V.13 are directly estimated from the

combination of δT and δN_e and from plasma composition tables. In the channel center this uncertainty reaches about 20% in the first microseconds and 32% at 36 µs.

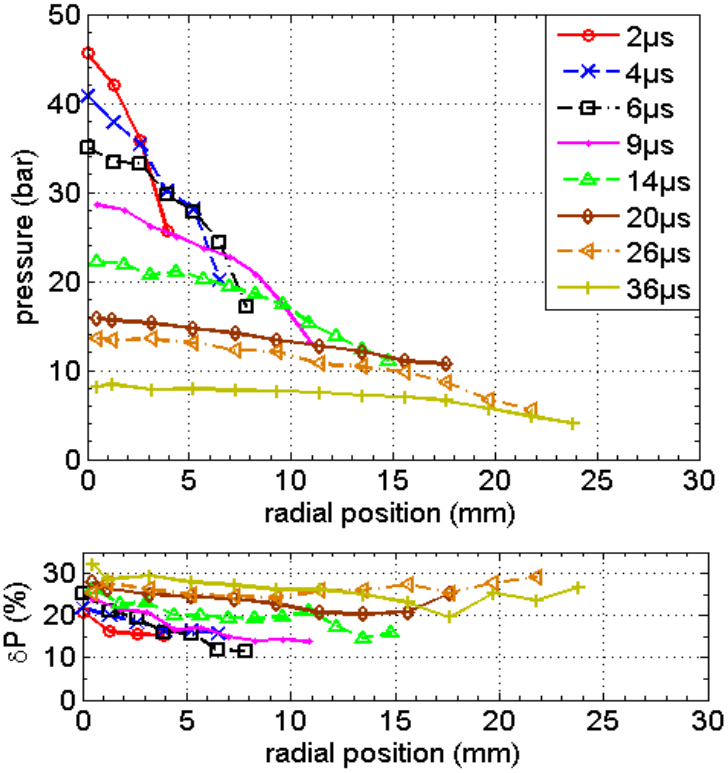

Figure V.13. Pressure profile for the 100 kA current peak, calculated from the average values of temperature and electron density, and the percentage uncertainty.

V.2.1.2 Results for different current peak values

A comparison between temperature and electron density profiles for the four levels of current peak is shown in figure V.14. The parametric study is performed for two instants, 6 µs and 9 µs. For the two lower current peak levels (10 kA and 25 kA), the line broadening are less important and therefore the 600 grooves mm^{-1} grating was used to improve the spectral resolution. In general, the shapes of the profiles are similar for all current peaks, with a quasi-constant temperature inside the arc channel and a decreasing electron density along the radial direction. However, the temperature profile for 10 kA and 25 kA at 6 µs seems to decrease along the channel radius, changing from 22000 K to 19000 K for 10 kA and from 25000 K to 20000 K for 25 kA. Nevertheless, the arc radius for these waveforms at 6 µs is small, with a value around 6 mm. Then the spatial resolution of the measurements is reduced and the gradients in the profiles should be analyzed with care. The temperature increases by about 10000 K when the current peak increases from 10 kA to 100 kA, which corresponds approximately to a factor 1.5. The variations of the electron density with the current peak are more remarkable; it is

approximately twice higher between 25 kA and 50 kA and increases by a factor of more than 6 when the current peak changes from 10 kA to 100 kA.

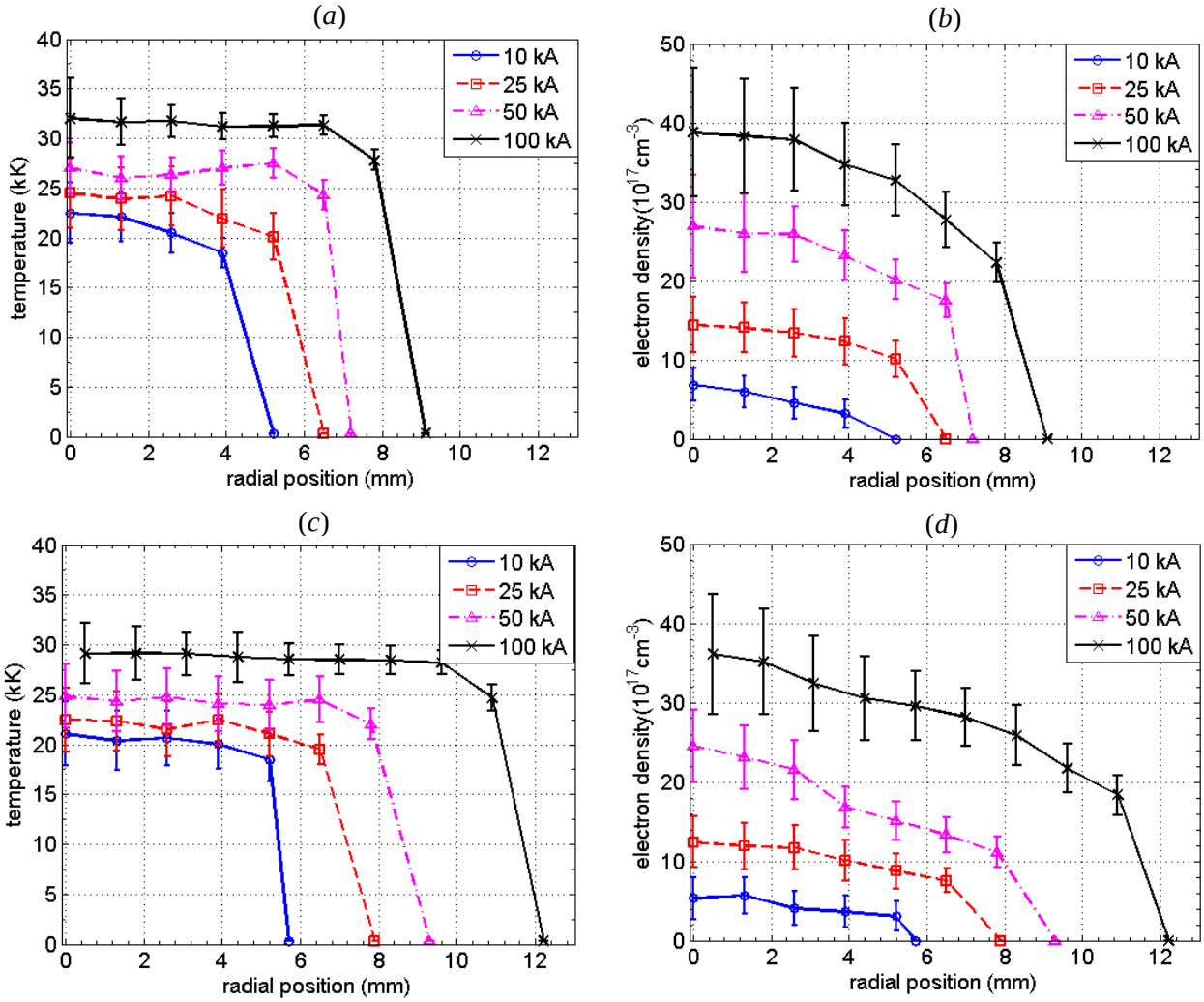

Figure V.14. Profiles of T and N_e for four levels of current peak; (a-b) 6 µs (c-d) 9 µs.

The present results are in fair agreement with the time-resolved study of a natural lightning return stroke performed by Orville (1966b). He found an average peak temperature of 31000 K, with a maximum of 36000 K in the first 5 µs. The temperature decreased to around 20000 K after 20 µs. The electron density was around 10^{18} cm^{-3} in the first microseconds and then decreased to around 10^{17} cm^{-3} after 30 µs, which is lower than the present results. However, the current measurements were not available and all the analysis was done assuming an optically thin plasma and the properties constant in the channel cross section. As highlighted in the results shown in figure V.14, the current level has a significant impact on the electron density, and then a low current waveform could explain the differences.

V.2.2 Electron density from Hα line

At 100 kA current peak, the Hα line had low intensity and was barely distinguished for times before 14 µs. From 20 µs the line was intense and well isolated from the emission lines of other species, allowing its exploitation by the method described in section V.1.4. Figure V.15 shows the spectra recorded at the central chords for a few times from 20 µs, with the corresponding fit by a Lorentzian function (equation (V.3)) applying a least-square method as fit criterion. In figure V.15, they are plotted with their respectively relative intensity, to put in evidence the intensity variation over time.

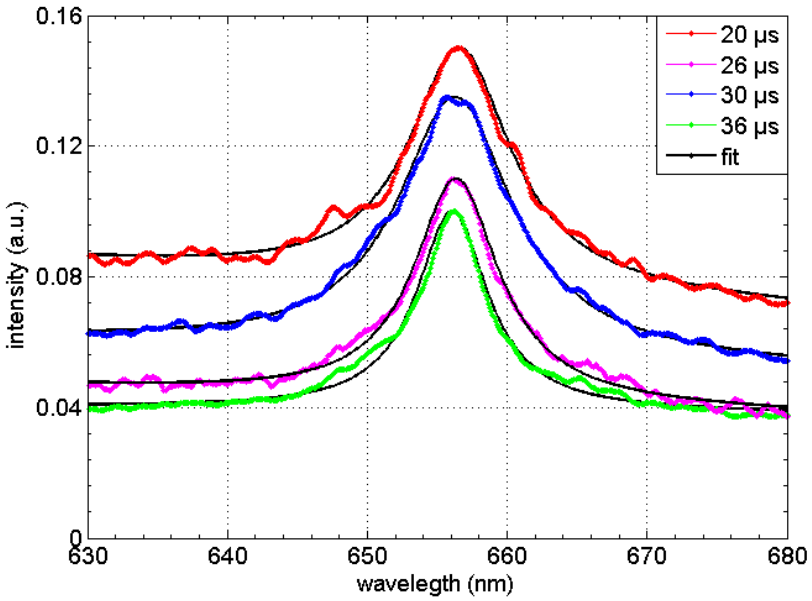

Figure V.15. Examples of collected spectra of Hα line at the central chord and the corresponding fit. Current waveform of 100 kA peak.

To estimate the electron density from 20 µs using the Hα line, we assumed a homogenous arc column. The central chord is used to obtain the Stark FWHM and then N_e is deduced using equation (V.6). In order to perform comparisons of this estimated electron density ($N_{e_{H\alpha}}$) with those obtain from the N II and O II lines ($N_{e_{RTE}}$), a radial average is performed in the data presented in figure V.11(*b*), using the relation:

$$\overline{N_e}_{RTE}(t) = \frac{1}{\pi r_{arc}^2} \int_0^{r_{arc}} 2\pi r N_e(t,r)_{RTE} dr \qquad \text{(V.8)}$$

where $\overline{N_e}_{RTE}$ is the radial average of the electronic density for each time t . Table V.2 presents the results obtained from the Hα FWHM measurements for times ranging from 20 µs to 36 µs, and from the ionic lines using equation (V.8). The electron density from Hα line reaches 3.37 ×

10^{18} cm^{-3} at 20 µs, which is twice higher than the result from ionic lines. As the electron density decreases, the differences between the results of the two methods also decrease. At 36 µs, $N_{e_{H\alpha}}$ is around 44% higher than $\overline{N_{e_{RTE}}}$. The significant differences can be explained by the assumption of optically thin plasma. As explained in section V.1.4, we were not able to perform an accurate calculation of the absorption coefficient of the Hα line, and then the optically thin plasma hypothesis was adopted. Nevertheless, comparing the relative intensity of Hα with the nearest N II multiplet utilized in this work (at 568 nm) and considering the absorption coefficient of N II estimated at 20 µs, we can expect a significant optical thickness at the central wavelength of the Hα line, with a value around 1.75. The broadening of a Lorentz line calculated in a medium with such optical thickness leads to an overestimation of the FWHM of the order of 50%. Considering this overestimation, the electron density obtained from both methods show some agreement, given, at least, results in the same order of magnitude.

Table V.2. Comparisons of electron density obtained from the exploitation of Hα line ($N_{e_{H\alpha}}$) and N II and O II line ($\overline{N_{e_{RTE}}}$), for the 100 kA current waveform.

Time (µs)	**Electron density (10^{17} cm^{-3}) from Hα line ($N_{e_{H\alpha}}$)**	**Electron density (10^{17} cm^{-3}) from N II and O II line ($\overline{N_{e_{RTE}}}$)**
20 µs	33.74	16.95
23 µs	28.77	-
26 µs	24.05	12.35
30 µs	18.90	-
33 µs	15.11	-
36 µs	12.29	8.55

V.2.3 Partial emission intensity of layers

As previously discussed, the studied lightning arcs cannot be considered as optically thin. The aim of this section is to show the contribution of the inner layers to emission and to check that reliable information can be extracted from these regions.

We use the radial distribution presented in figure V.11 to calculate the partial intensities that compose the total intensity collected for a given line-of-sight. The partial contribution of the cylindrical layer *i* corresponds to the terms of index *i* and *2m – i* inside the main summation in equation (V.4). It represents the emission of the cylindrical layer, reduced by the absorption of all following layers. Figure V.16 shows the obtained spectrum of each layer for the chord that crosses the channel center. As an example, these partial spectra are calculated at two instants with significant optical thickness, 6 µs and 9 µs and for the 100 kA current peak waveform. The spectra of the central layer are highly broadened and highly absorbed at the central region of the main multiplets (500 nm and 569 nm). However, figure V.16 highlights the fact that even with significant optical thickness, there is a certain amount of light that escapes from the channel center allowing the investigation of this position. In the composition of the total spectrum, the intensity level of the central layer is similar to the intensity of the other layers and has an important contribution in the far wings of the main multiplets.

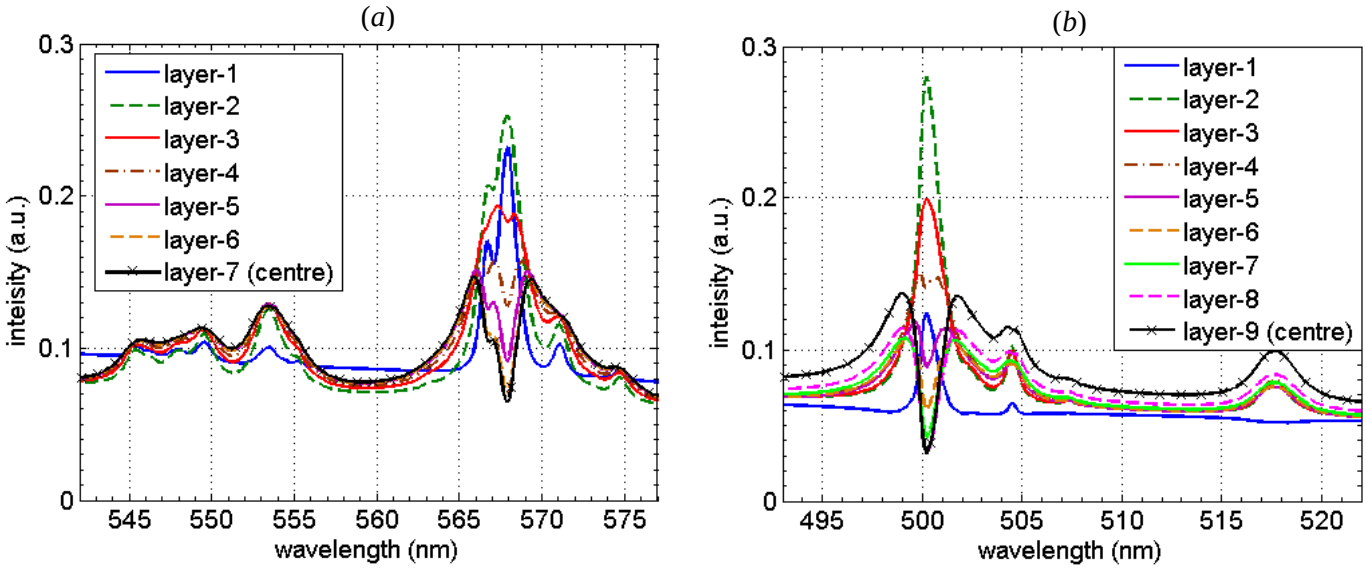

Figure V.16. Emission spectra from each layer for a chord that traverses the channel center; (a) 6 µs. (b) 9 µs.

V.2.4 Electrical conductivity

The electrical conductivity of the arc channel can be estimated from the results of temperature and pressure profiles. Using the tables of thermodynamic and transport properties of equilibrium air plasmas calculated by D'Angola et al. (2008) the profiles of electrical conductivity can be deduced from each pair of *T* and *P*. Figure V.17(*a*) shows the results for the 100 kA current peak level. The conductivity error $\delta\sigma$ can be estimated by combining the errors obtain in section V.2.1 for *T* and *P*. Its evolution is shown below the graph and ranges from 18% to 38%.

Figure V.17(*b*) shows a comparison of the radial average conductivity over the column cross section (calculated with an identical relation of equation (V.8), replacing $N_e(t,r)_{RTE}$ for $\sigma(t,r)$), obtained from the present *T* and *P* profiles, and the results obtained from the electrical measurements presented in Chapter IV.

In general, the evolution over time of the average electrical conductivity exhibits a similar shape when derived from the two different methods. However, in the first 5 microseconds, the conductivities derived from arc resistance are increasing, while those using OES analysis decrease monotonically since 2 µs. This fact may be explained by the accuracy of the column radius in the first microseconds. As discussed in Chapter IV, the electrical conductivity is considered proportional to r_{ARC}^{-2} which is a measure with less accuracy in the beginning of the arc.

The results derived from the estimation of *T* and *P* are higher than those obtain from electrical measurements. It is approximately 73% higher when compared to the results from the total arc resistance at 4 µs. Nevertheless, the total resistance, as discussed in Chapter IV, does not take into account boundary effects due to the electrodes and then overestimates the column resistance and underestimates the electrical conductivity of the column cross section. This emphasizes the interest to have a space-resolved measurement using OES measurements which is less sensitive to electrode effects and can focus only on the channel central cross section.

Compared to the results derived from the column resistance, the two methods present a good agreement. The results from *T* and *P* lead to an electrical conductivity 9.1% higher at 6 µs. The differences increase with time, and reach a deviation of around 50% at 36µs. These differences are of the same order of magnitude of the estimated errors for OES analysis. This agreement reinforces the consistency of the results obtained in both electrical characterization, performed in Chapter IV, and temperature and pressure determination, done in this chapter.

(*a*)

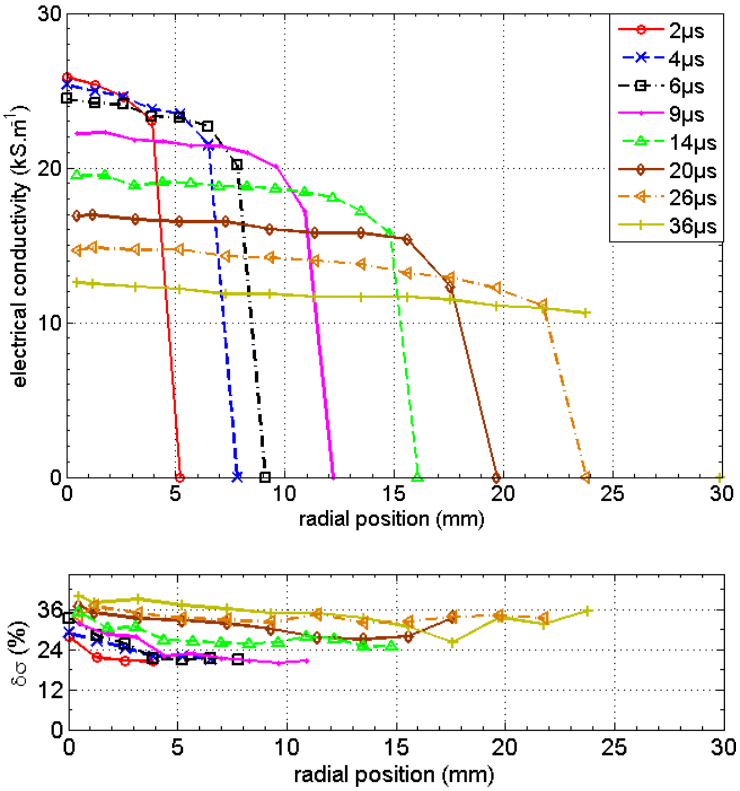

(*b*)

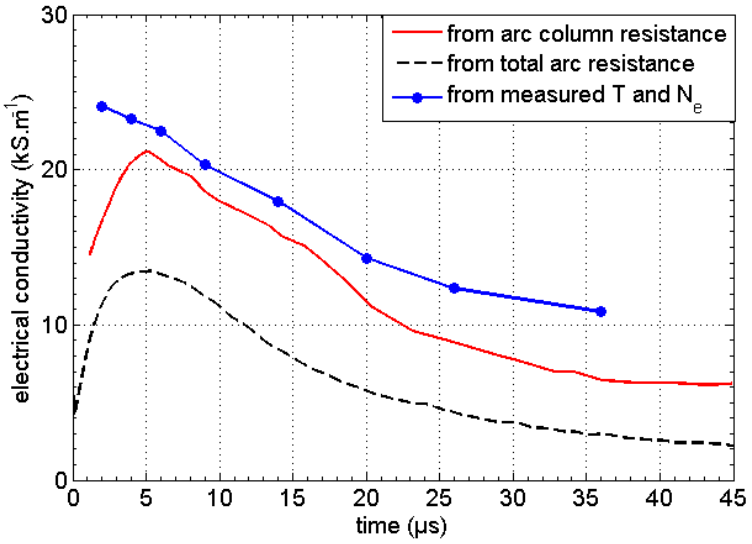

Figure V.17. (a) Electrical conductivity profile for the 100 kA current peak level. (b) Comparison of the radial average values over the cross section estimated from T and P, and from electrical measurements.

V.3 Conclusion

In this chapter we performed an investigation of the intensive thermodynamic properties of a free arc channel using OES. A study of the sensitivity to the temperature of nitrogen and oxygen ion line intensities was performed. More than 190 lines were used to estimate the optical thickness of the arc channel. This allows the determination of the arc properties in a non-optically thin medium by solving the radiative transfer equation and assuming the arc channel as a combination of concentric layers.

The radial profiles of temperature, electron density and pressure were determined for the 100 kA current peak over time up to 36μs. The temperature is approximately constant inside the arc channel, and the electron density and the pressure show roughly a parabolic shape along the radial direction. In the channel center, the temperature and the electron density reach, respectively, 37400 K and 4.9×10^{18} cm^{-3} at 2 μs. The pressure reaches 45 bar with an accuracy estimated at 20%.

A comparison between results for four current peak levels, ranging from 10 kA to 100 kA was performed for two instants. The temperature seems to have a moderate dependence on the current level, but the electron density shows a significant sensitivity to the current, increasing by a factor of more than 6 when the current changes from 10 kA to 100 kA.

Stark broadening of Hα line was measured from 20 μs to 36 μs at 100 kA current peak, and the resulting electron densities were compared to the RTE method. In the first microseconds after 20 μs, significant differences are found, but the overestimation of the electron density derived from the Hα line can be explained by a significant optical thickness of this line.

Based on the obtained radial distribution of temperature and pressure, the electrical conductivity in the column cross section is calculated and compared to the results derived from electrical measurements. The results from the determined *T* and *P* are higher than those from the column resistance. Nevertheless, the differences are within the estimated error of the measurements, which reinforces the consistency of the considered methods and the achieved results.

The results presented in this chapter will serve to complete a database for simulation codes for this category of pulsed arcs, and will be very useful for model development and for the validations of computational tools. They were recently published as a research paper by IOP Publishing in *Journal of Physics D: Applied Physics* (Sousa Martins et al. (2016b)).

After a large investigation of the free arc channel performed in the three previous chapters, we will now focus our attention on the interaction between the high current arc and aeronautical materials. In the next chapter, the physical properties of this interaction as temporal dynamics, spatial shape, shockwave propagation, heat flux and internal pressure are studied for different material and surface coatings. This characterization will allow us to evaluate the similarities and differences between the free arc column and the arc attachment point.

Chapter VI.
Characterization of the interaction between the transient lightning arc and aeronautical materials

In this chapter, we investigate the interaction between the high current arc and aeronautical materials. Different materials and surface coatings are analyzed, and many physical properties and constraints of this interaction are studied, which includes; the temporal dynamics and spatial shape of the arc roots, the shock wave propagation near to the attachment point and the thermo-mechanical constraints imposed by the arc on the material.

The arc is produced using the experimental setup with the *deviator-panel* electrode configuration, in contrast to the previous chapters. Here, we focus our attention in the 100 kA peak current waveform. The characterization allows us to evaluate the influence of different

materials and surface coatings on the plasma evolution and then compare and analyze the similarities and differences between the free arc column and the arc attachment point.

VI.1 Aeronautical materials

The samples studied in this work are separated in two sets. Each category is made of one different material employed in aeronautical industry; aluminum and carbon fiber reinforced polymer (CFRP) composite, often simply called carbon fiber composite. The samples are square panels of 400 × 400 mm^2 with thickness of 2 mm for the CFRP composite and varying from 1 to 1.6 mm for the aluminum. The panels are clamped at the generator structure by a circular mounting with a diameter of 380 mm. In the following, we briefly present the characteristics of each material.

VI.1.1 Aluminum panels

The aluminum panels used in this work are made of the alloy Al 2024-T3. They are composed of 95% Al, 4% Cu and 1% Mg (AMS (2016)). Generally, for aeronautical purposes, the material has to be coated by paint, which includes primers, enamels and acrylic lacquers, and other kinds of protection layers. In order to analyze the influence of the surface coating, painted aluminum panels are also studied. Three thicknesses of paint are investigated, with value of 100 µm 300 µm and 500 µm with an accuracy of 5 µm. The paint layer follows standard aeronautical paint employed in aerospace industry and is made of two primer layers and a finish layer. The first primer layer (P99, PPG Aerospace) is a chromate wash primer designed for the protection of aircraft exteriors, with good adhesion to a variety of light alloys. The second primer layer (PAC33, PPG Aerospace) is corrosion inhibitive, polyurethane primer modified with epoxy resin. The polyurethane finish (PU66, PPG Aerospace) provides decorative color, chemical and environmental resistance, with resistance to Skydrol fluids, hydraulic fluids and corrosion.

VI.1.2 Carbon fiber composite panels

The CFRP composite panels are provided by the Material and Structure branch of ONERA. The composite material is a T700-M21, which is made of carbon fibers (T700, Toray Carbon Fibers America) inside a thermosetting resin made of epoxy M21 (Hexcel). The CFRP panel is formed with a quasi-isotropic multi-layup with a cell structure made of eight plies with orientations respectively of 45°, 90°, -45°, 0°, 0°, -45°, 90° and 45°. This layup structure is normally represented by the notation $[45°, 90°, -45°, 0°]_S$. Figure VI.1 illustrates the orientation and the

order of the ply of a unit cell. The dry ply is placed manually to form the layup. The resin is applied to the hand layup and is cured at a temperature of 177 °C and a pressure of 7 bars. The mass density of the CFRP panel at 300 K is 1538 kg m^{-3}.

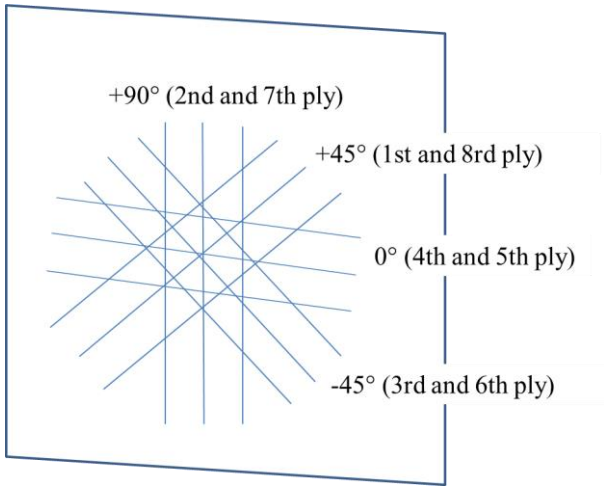

Figure VI.1. Example of a unit cell structure in a multi-layup CFRP panel.

VI.2 Shape characterization of the arc roots

As for the case of the arc channel characterization done in Chapter III, we started to investigate the shape of the arc roots by high speed imaging, to assess their symmetry and their radius evolution. In this work, we define *arc root* as the disc in contact between the arc and the material, and *arc root zone* as the region within the arc extending from the material surface until 1 mm from it. To focus on this zone, the HSC are positioned to observe regions close to the material surface, as described below.

VI.2.1 High speed camera positions

Since the area of interest is in the vicinity of the material, both the radius measurement and BOS cameras were placed in a perpendicular direction to the arc channel axis, having a grazing angle with the material surface. Figure VI.2 presents the schematic diagram of the arc attachment point and shows the viewed area by each camera.

A third HSC is positioned with some angle to the material surface and is configured to observe the total arc channel with both electrodes. Figure VI.3 shows an example of a picture taken from this position for the cases of unpainted and painted aluminum panels, which allows us to observe the electrode's configuration and the column formed in the central region.

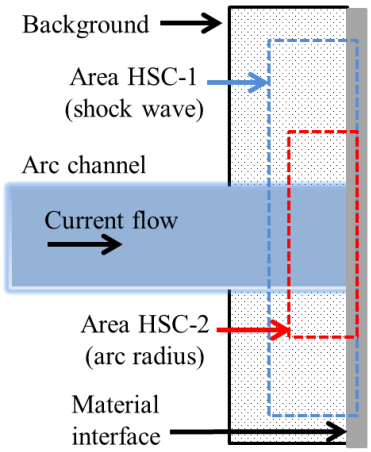

Figure VI.2. Side view of the arc attachment point. Area of collection for the two high speed cameras (HSC).

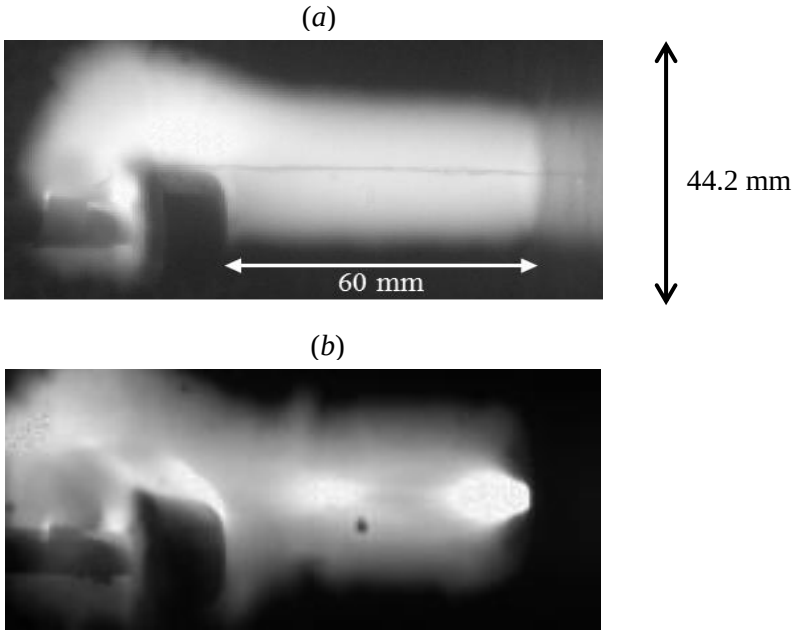

Figure VI.3. Example of arc picture taken at 15 µs after the current triggering for the 100 kA peak waveform applied to unpainted aluminum (a) and painted aluminum (b). The jet diverter electrode is located on the left-hand side and the panel is on the right-hand side (resolution: 256 × 96 pixels; scale:0.46 mm/pixel; exposure time: 0.3 µs; frame rate: 200 kfps)

We can see than the structures of the arcs are different in both cases. While the arc column seems to be homogeneous in term of shape and luminous emission for the unpainted material, the arc reaches more complex structure in the presence of paint. An important emission of light is observed at the initial attachment point, as can be observed in the case of continuous current lightning arc (Chemartin (2011)). This point is discussed in the next sections.

VI.2.2 Arc root characterization for aluminum panels

For both unpainted and painted aluminum panels, the arc root develops around the ignition wire, in the radial direction and exhibits an axisymmetric shape, as for the case of the arc column. Figure VI.4 shows a few pictures of the arc root evolution over time for the case of an unpainted aluminum panel. It can be seen that the arc root seems to continuously increase, with a smaller velocity than the rest of the arc column. This leads to parabolic shape of the plasma column in the axial direction.

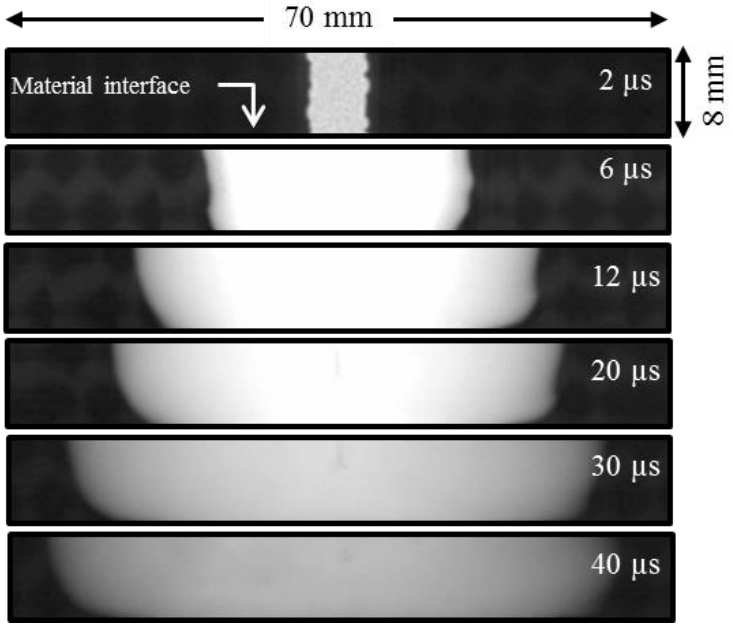

Figure VI.4. Pictures of the arc root zone over time applied to an unpainted aluminum panel. The material surface is located at the bottom of each picture.

For painted aluminum, this slower increase of the arc root is also noticed, however an additional effect is observed after several microseconds. An abrupt reduction of the visible arc root radius takes place during the expansion phase of the arc column. Figure VI.5 illustrates a few pictures of the arc root zone for the case of 300 µm painted aluminum. It can be observed that in the first microseconds the arc root expands following the expansion of the column. Then, as the paint is removed from the surface, the arc root seems to be concentrated in the area without paint, forming an intense plasma jet, which has a radius slightly decreasing over time. In the example of figure VI.5, the first instant where the ejected paint fragments are clearly detected is at 12 µs.

The criteria used for radius measurements from the radial luminous profiles are the same developed and described in Chapter III (section III.1.3). The radial profiles are analyzed between 0.75 to 1.25 mm from the material surface, which includes three rows of pixels in a picture. Generally, using aluminum panels, the arc root radius has a similar shape during the

first 18 µs, for the different panels and paint thickness, following the evolution of the free arc column.

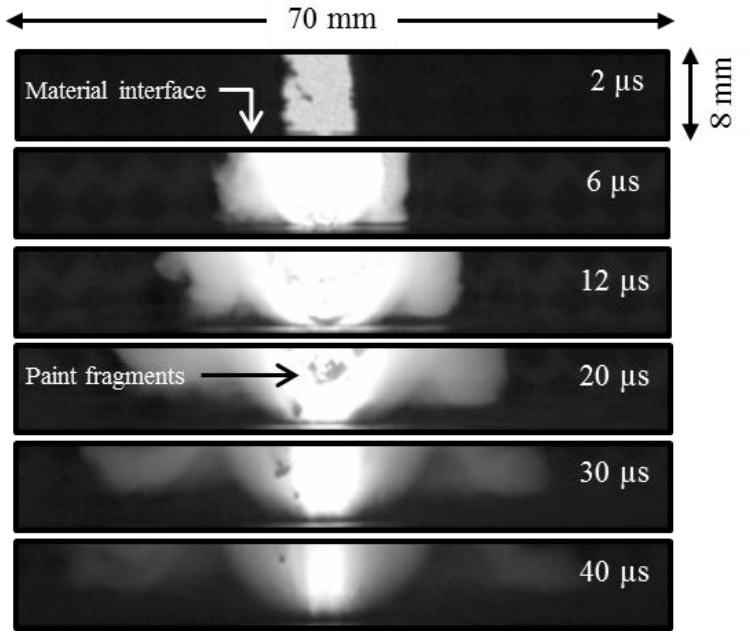

Figure VI.5. Pictures of the arc root zone over time applied to a 300 µm painted aluminum panel.

In the case of unpainted aluminum, we can observe, after 18 µs, a slower expansion of the visible arc roots than the column expansion. It can be noticed that the change in the aluminum thickness from 1.0 mm to 1.6 mm does not play a significant role in this expansion. Figure VI.6 shows the results for different panels.

Concerning the painted panels, the abrupt reduction of the visible arc root expansion mentioned above is clearly highlighted. As the paint thickness increases, the time for this rapid decreasing is shifted, changing from 20 µs for the 100 µm paint to 38 µs for the 500 µm paint. Therefore, the maximum apparent radius reached by the arc root after the fall also increases with the paint thickness. If we compare this apparent radius at 20 µs (about 16 mm) to the radius of the punctured paint, observed after the test (about 3 mm, see section VI.4), we point out a large discrepancy. Because the electric current cannot flows across the insulating paint layer, we assume that the visible arc root radius measured with the HSC overestimates the real one. The intense light coming from the arc avoids an accurate estimation of this radius.

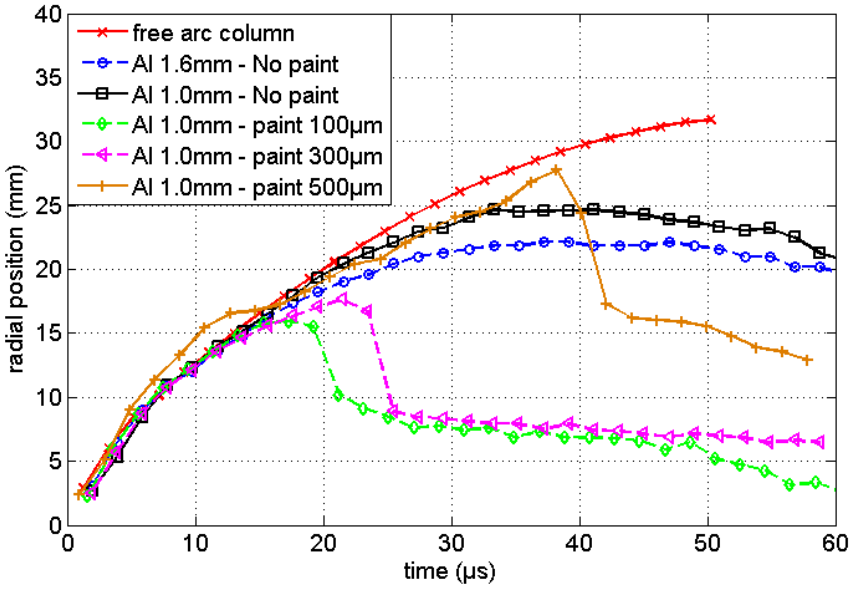

Figure VI.6. Evolution of the visible arc root radius for aluminum panels and the radius of a free arc column.

This intense light comes from the constriction of the current streamlines in the small surface where the paint is vaporized, as illustrated in figure VI.7. This effect would cause a high light emission in the arc root, and the formation of a plasma jet in the attachment point, which can be seen in the pictures of figure VI.5. It is also believed that in the case of the 500 µm painted panel, the formation of the multiple spots after the test over a large zone prevent the arc radius estimation for longer durations.

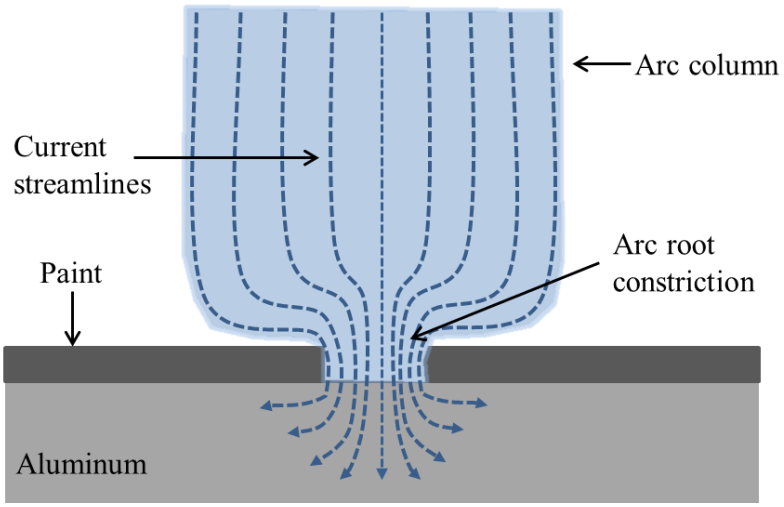

Figure VI.7. Illustration of the current streamlines constriction in paint aluminum panels.

VI.2.3 Arc root characterization for carbon fiber composite panels

For the case of CFRP panels, the arc root evolution presents a significant difference compared with the case of aluminum panels. As described in section VI.1.2, the layup structure of the CFRP results in a unidirectional ply in the material surface, which is expected to play an important role in the arc root structure, because of the orthotropic surface conductivity. For that reason, to assess the behavior and characteristics of the arc root shape in this case, two HSC are positioned to observe the attachment point at different azimuthal positions, as the setup employed in Chapter III, section III.1.2. Figure VI.8 shows the camera setup position.

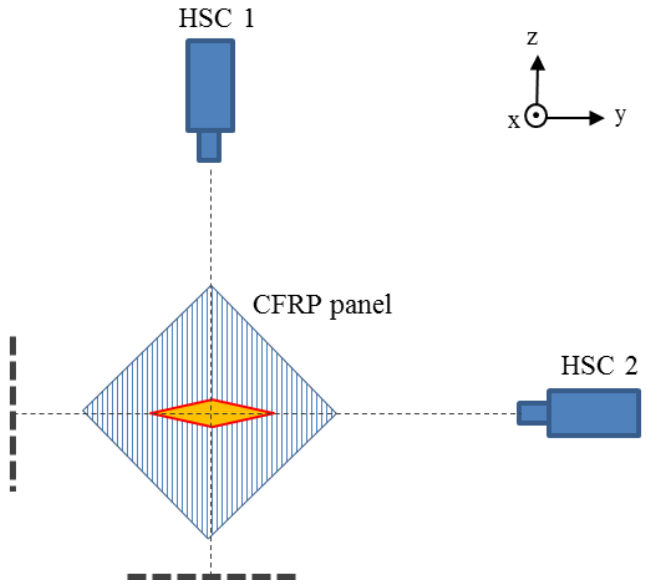

Figure VI.8. Schematic diagram of the different camera positions.

The first camera has the optical axis parallel to the surface ply orientation and, therefore, observes the radial evolution transverse to the ply. The second camera is positioned in the perpendicular direction to the first one, observing then the radial evolution along the surface ply. Figure VI.9 illustrates a set of pictures taken from these two positions. To optimize the acquisition in both directions, a different scale factor is set for each camera.

In the direction along the surface ply, the visible arc root expands with approximately the same velocity as the arc column. The fluid dynamic is apparently more instable than the case of unpainted aluminum. In the transverse direction, however, a different shape is formed. The region closest to material surface expands faster than the arc column, producing an arc root with a roughly conical profile. Also, at the point of intersection between the column and the root region, the channel becomes narrower than the rest of the column, as though a constriction effect occurred in the plasma.

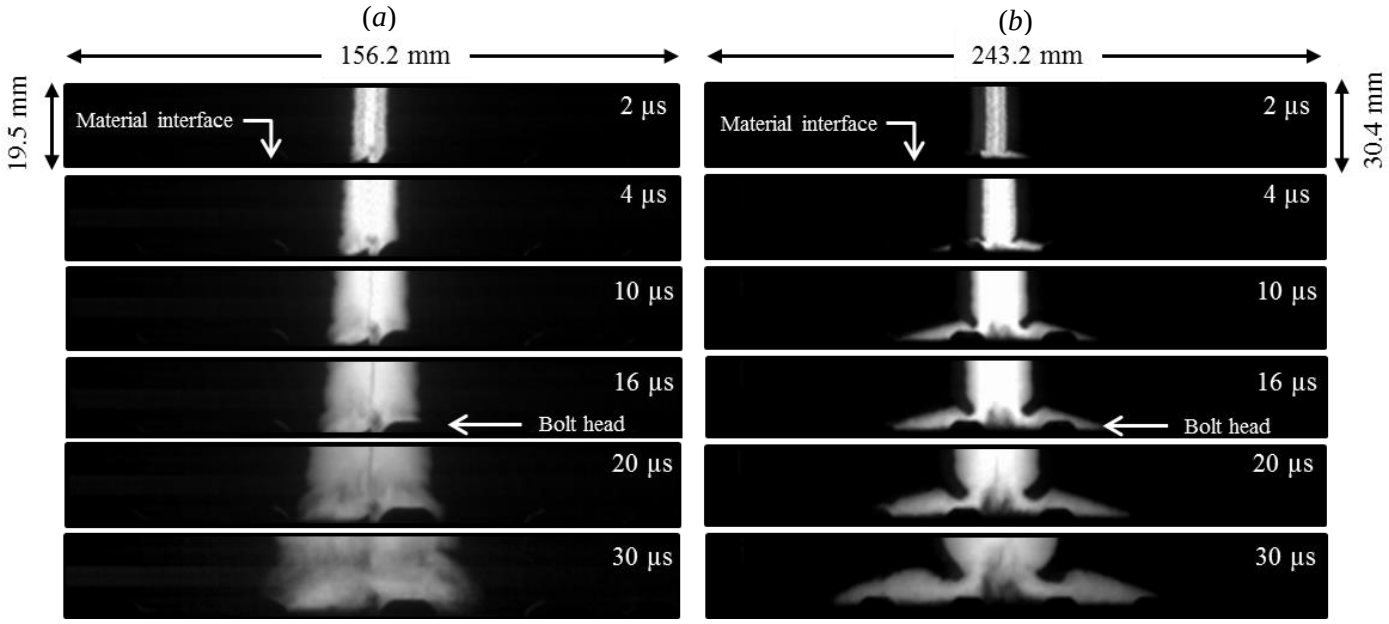

Figure VI.9. Pictures of the arc root evolution over time applied to a carbon fiber composite panel. (a) Camera axis perpendicular to the surface ply orientation (resolution: 256 × 32 pixels; scale: 0.61 mm/pixel; exposure time: 0.3 µs). (b) Camera axis parallel to the surface ply orientation (resolution: 256 × 32 pixels; scale: 0.95 mm/pixel; exposure time: 0.3 µs).

To put in evidence the shape taken by the arc root, another point of view, having an oblique angle to the material surface, is also assessed and is recorded with the third HSC. Figure VI.10 presents an example of a few pictures taken from this position. The origin of the reference frame is set at the intersection between the arc column axis and the material surface. The arc column axis is oriented along the *x*-axis and the panel is in the *yz* plane, with the surface ply oriented along the *z*-axis. From this position, it is very clear that the difference in the expansion velocity along the parallel and transverse directions of surface ply has a significant impact on the root shape symmetry. Therefore, the axisymmetric hypothesis, verified for all other cases studied until now, is no longer valid. Instead, an approximately diamond form is observed.

We evaluate the radial evolution of the visible arc root in the parallel and transverse direction to the surface ply orientation. As for the case of aluminum panels, the radial profiles are analyzed between 0.75 to 1.25 mm from the material surface regions Despite the fact that no axisymmetric form is verified, we employ the term *radius* to describe the distance between the root axis and the edge, since for both direction, some symmetry is found in each side of the axis.

In the parallel direction, the root radius has a similar shape as the column evolution, being slightly faster in the first 30 µs. However, the expansion stops around 30 mm at 36 µs, while the column radius stops in 32 mm at 50 µs.

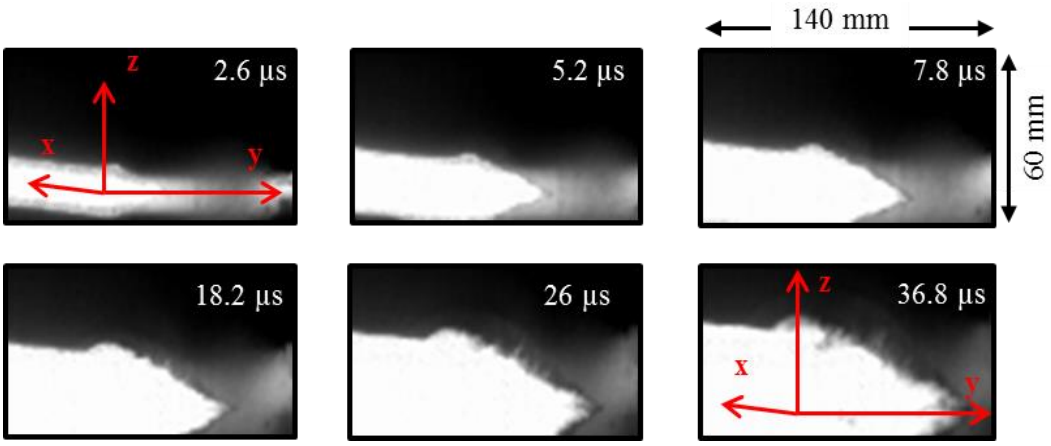

Figure VI.10. Pictures of the arc taken from an oblique angle to the material surface, to put in evidence the shape of the arc roots. The arc column axis oriented along the x-axis and the composite panel is in the plane yz, with the surface ply along the z-axis.

In the transverse direction, the radius expansion is approximately three times faster than in the parallel direction. The arc root radius reaches 42 mm at 10 µs, corresponding to an average velocity of 4.2 km s^{-1}, while the average column velocity is 1.2 km s^{-1}. At 36 µs, the radius reaches 87 mm, which is the limit of our measurement window, but it still has a significant expansion velocity of 1.0 km s^{-1}. Figure VI.11 shows the evolution of the radius and velocity expansion for both directions and also for the free arc column.

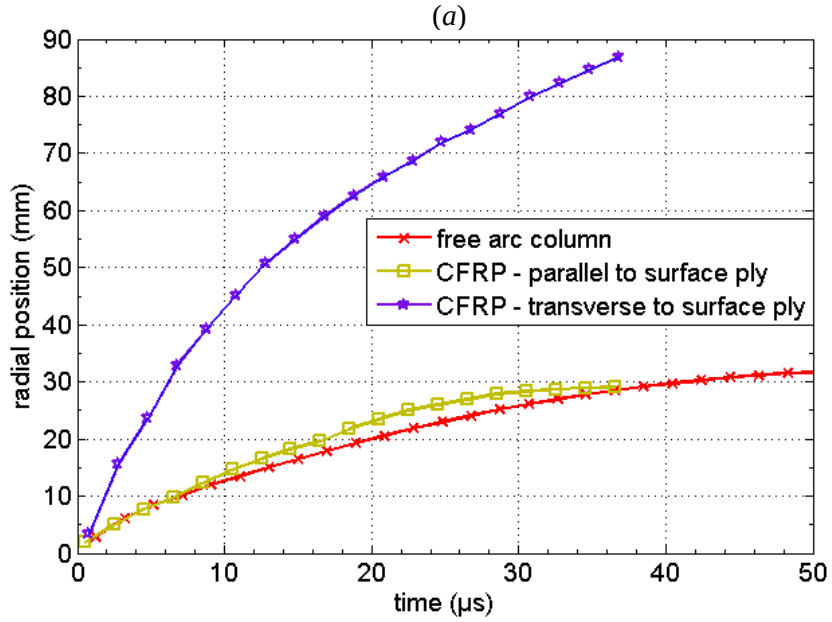

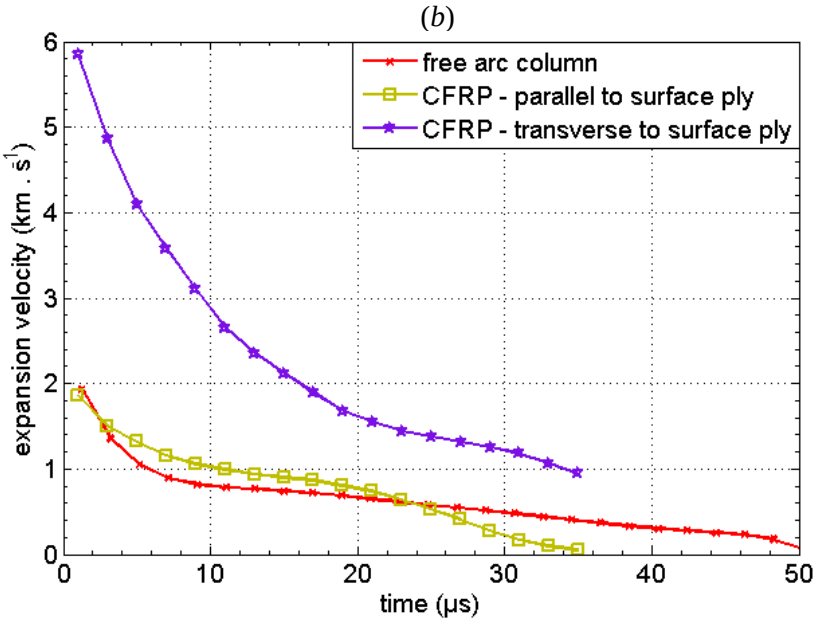

Figure VI.11. Radius (a) and expansion velocity (b) in both direction of a CFRP panel.

VI.3 Shock wave characterization near to the attachment point

To characterize the shock wave propagation near to the material surface and to follow the wave front evolution, we used the BOS method described and employed in Chapter III to study the shock wave induced by the free arc column. The BOS camera was placed in a perpendicular direction to the discharge axis, at the same point of view of the light intensity measurements camera (see figure VI.1). As described in Chapter III, we identify the wave front position by the changing in the patterns of the background squares, using the reference image taken without arc. Figure VI.12 shows some pictures of the shock wave propagation when the arc is applied to an unpainted and painted aluminum panel.

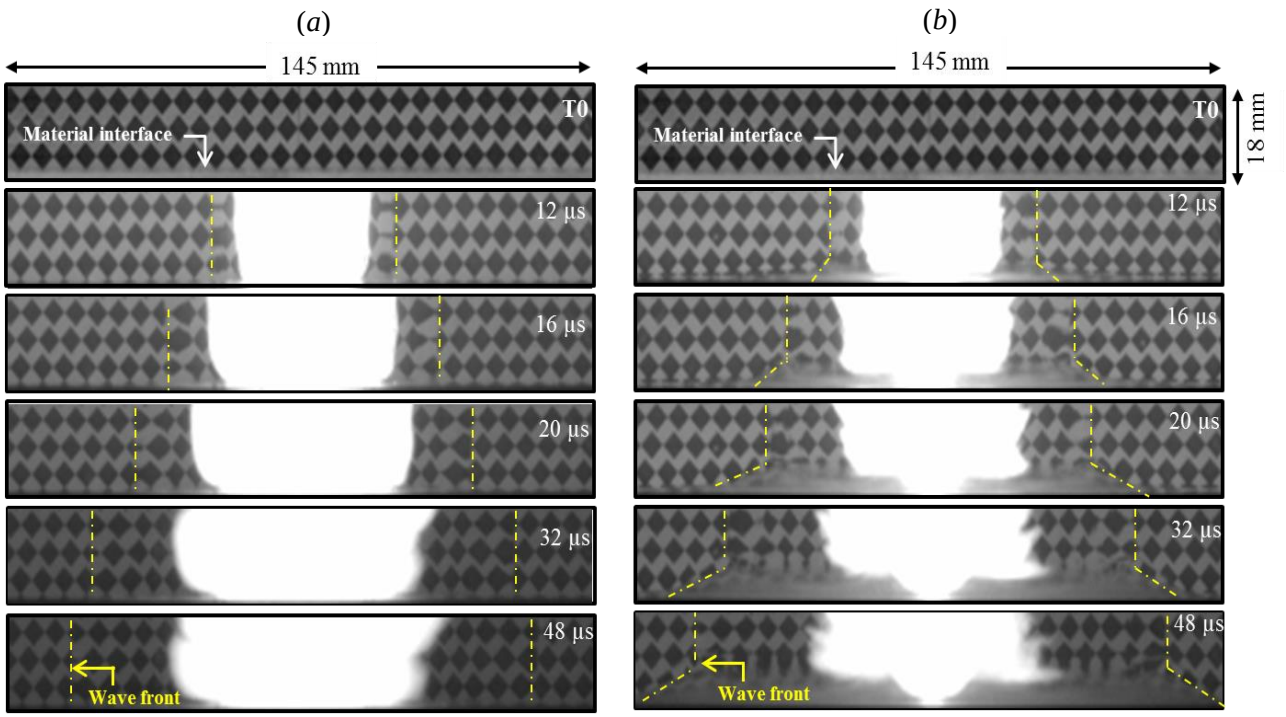

Figure VI.12. Pictures of the shock wave propagation for the case of (a) unpainted and (b) painted aluminum panels.

For the cases of the unpainted panels, the shock wave is transverse to the arc channel and has a cylindrical shape, which is very similar to those induced by free arc columns. Nevertheless, for painted panels, the observed shock wave keeps a symmetrical shape, but is distinguished by a larger radius at the interface with the material. It is believed that this shape comes from an additional shock wave superimposed on the main cylindrical shock, which appears from the arc attachment point.

This shock seems to propagate in the oblique direction, starting from the material surface, as can be seen in figure VI.12*(b)*. Due to the quasi-spherical shape of the wave front, this second shock wave could be interpreted as the result of a punctual energy deposition on the arc root, which seems to be more significant for the case of painted surfaces than compared to unpainted ones. Figure VI.13 shows an illustration for the two shock waves.

Figure VI.14*(a)* shows the average measurement of the wave front position of the cylindrical shock wave, for the different material and paint thicknesses. The measurements over different shots give a very good repeatability. The maximum difference found was 1.3 mm, by using three shots for each type of panel

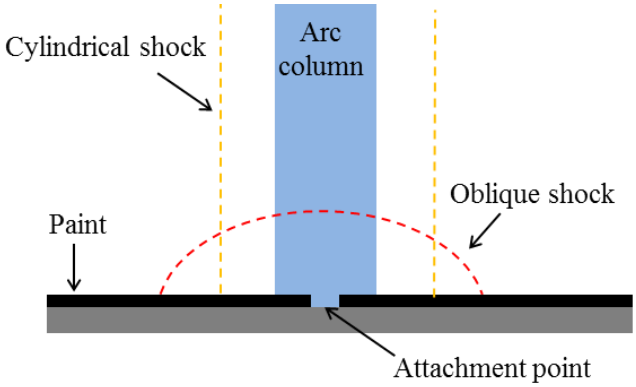

Figure VI.13. Illustration of the two shock waves for the case of painted aluminum panels.

. Comparing the results obtained from the curves shown in figure VI.14*(a)* to the arc root radius of figure VI.6, we can see that the time of detachment between the plasma and the shock wave is near 6 µs for all tested materials, as for the free arc channel. While the arc channel radius increases approximately as square root function of time, the shock wave associated with painted panels propagates faster in an almost linear shape. The results of the wave front position for unpainted panels have a very good agreement with those of shock waves generated by a free arc channel. However, the cylindrical component of shock waves induced using painted panels propagates faster, and reaches 70 mm at 56 µs, while for the free arc column this radius is reached at 65 µs. An interpretation for this fast expansion of the cylindrical shock observed with painted panels is that the spherical shock, coming from the constricted arc root, propagates with a fast speed inside the arc column, which increases the internal pressure of the arc, and consequently increases the velocity of the cylindrical shock.

Figure VI.14*(b)* shows the comparison between the position of the cylindrical and the oblique shock wave. The oblique component was measured at 1 mm from the material surface. This oblique wave propagates around 20% faster than the cylindrical component. At 46 µs, they reach 70 mm and 60 mm respectively.

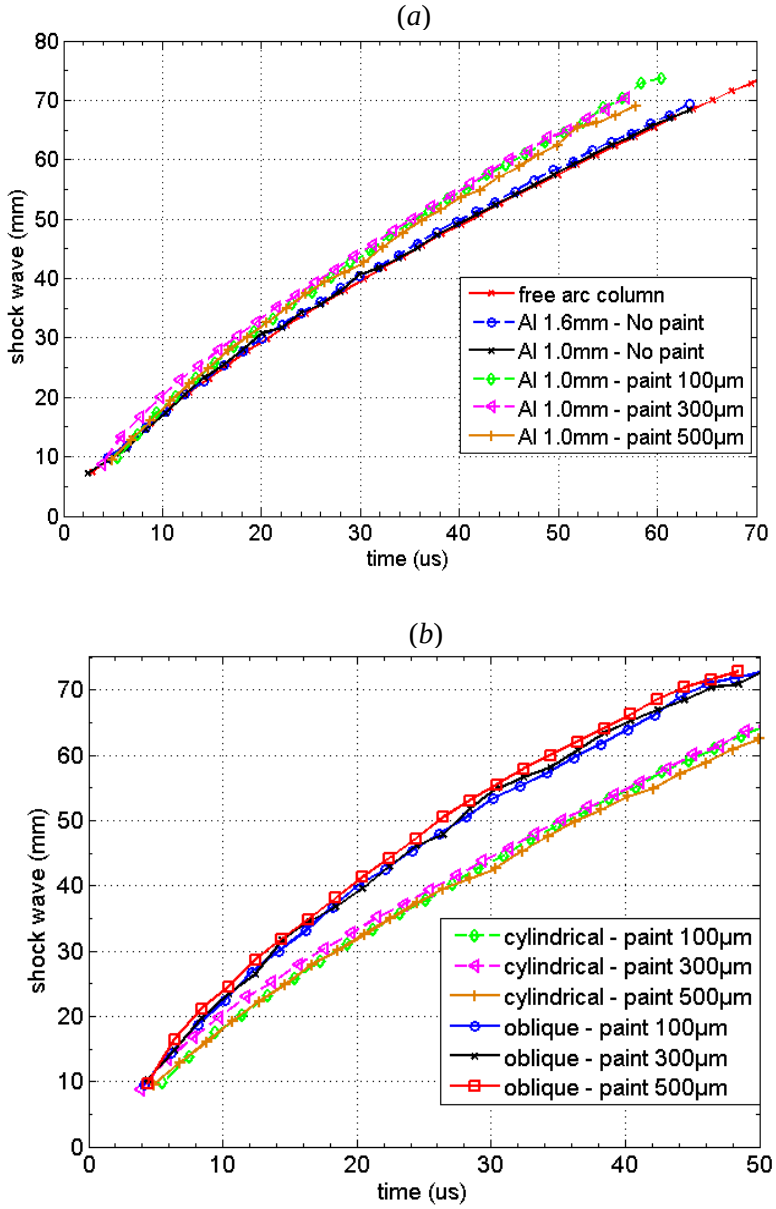

Figure VI.14. Shock wave position for different paint thicknesses. (a) Comparison of the cylindrical shock wave for all aluminum panels and the free arc column. (b) Comparison of the cylindrical and oblique shock wave for painted panels.

For the CFRP panels, the shock wave propagation is measured in the parallel and transverse direction of the surface ply, as the case done for the root radius measurements. In the parallel direction, the shock wave is always perpendicular to the panel, even in the region very closes to the material surface, showing a similar behavior than the case of unpainted aluminum. The wave front propagation is slightly faster than the free arc column.

In the transverse direction, the wave front is also evaluated at 1 mm from the material surface. As presented before, the arc root has a conical shape and a high expansion velocity of around 6 km s^{-1} at the arc ignition. The detachment between the wave front and the plasma occurs later than for all other studied cases. The first detectable instant was at 18 µs. For the previous instants, we consider that the wave front is at the same position of the arc root radius. At the detachment time, the expansion velocity is approximately 1.7 km s^{-1}. This velocity is similar to that found in the detachment time for the others cases. Figure VI.15 shows the curves for the shock wave position along both directions, the corresponding arc root radius, and also, the result obtained for shock wave induced by the free arc column.

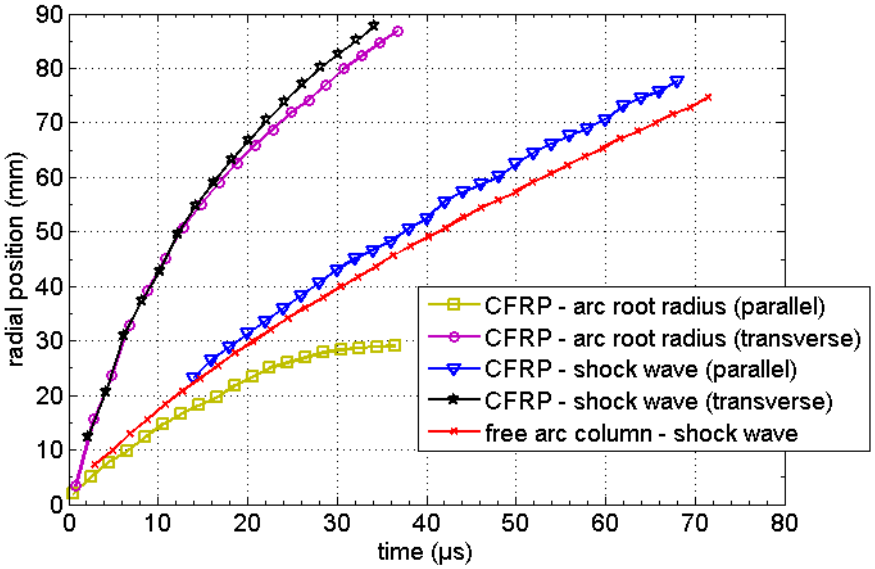

Figure VI.15. Shock wave position and arc root radius for the CFRP panel in the parallel and transverse direction to the surface ply.

VI.4 Examination of the panel surface damage

The evaluation of the panel surface after the lightning arc can improve and confirm a few characteristics of the arc/material interaction.

Figure VI.16 presents the surface panel for the aluminum cases. Generally, the damaged areas exhibit a roughly circular form for both painted and unpainted panels. For the painted panels, the visible damage takes the form of a zone in which the paint layers are missing, and the aluminum seems to be solidified after the cooling phase. For the 100 µm paint, the damage has a diameter of approximately 5 mm and shows some irregularities in the radial direction. The 300 µm paint panel presents a similar damage, with a diameter of around 6 mm, however the

puncture is quite axisymmetric. For the 500 µm paint, the area where the paint was destroyed is much larger than the others paint thicknesses, reaching a diameter of 30 mm. Inside the damage area, the first layers of paint (primaries) seem to be quite undamaged, except in the center, in a disc of 6 mm in diameter, and in numerous other spots disposed in a circular form. The unpainted panel presents a darker color in the area that interacts with the arc roots, and has a diameter of about 30 mm. Because of the surface irregularities, it seems that the aluminum was solidified after the cooling phase.

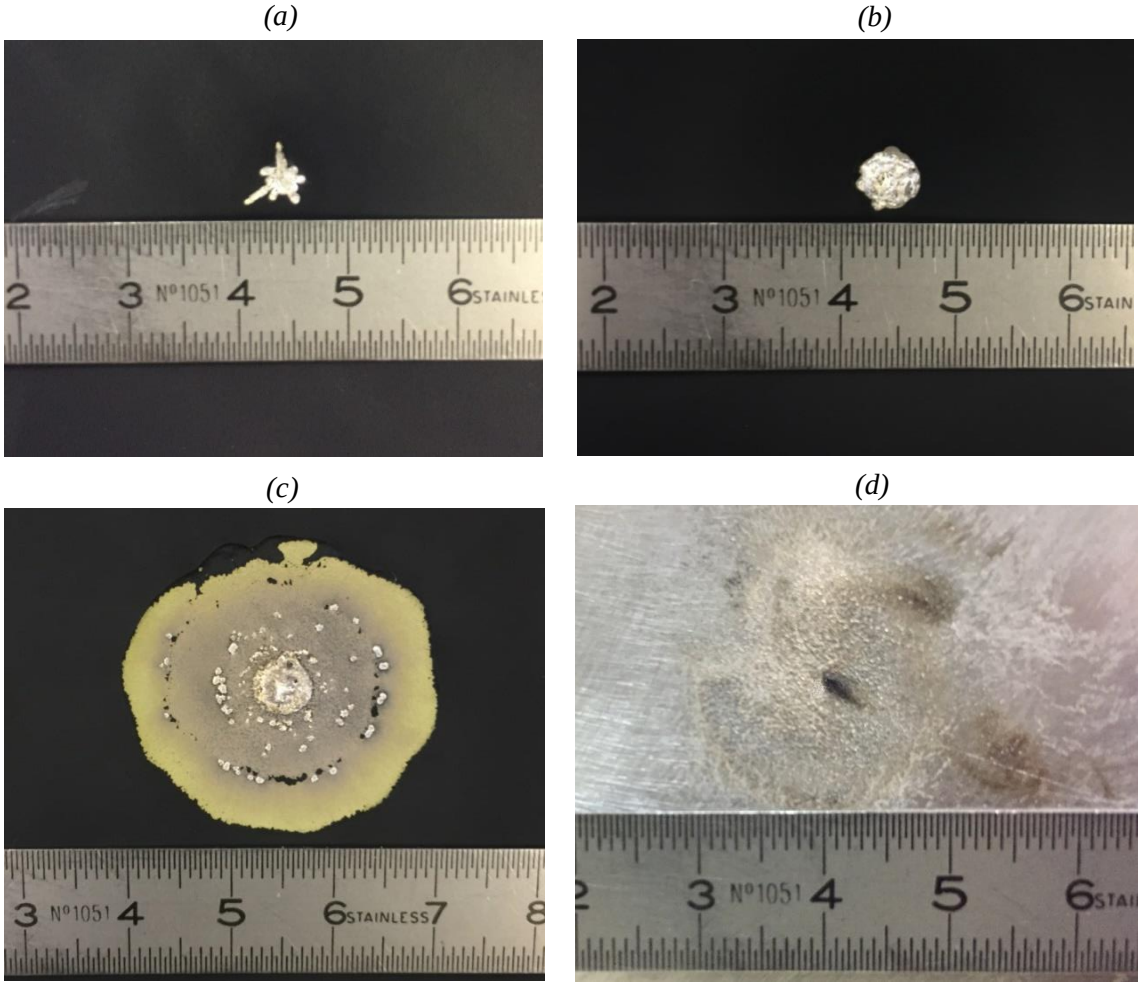

Figure VI.16. Some pictures of the damage in the aluminum panels after the direct lightning arc test. (a) 100 µm. (b) 300 µm. (c) 500 µm. (d) unpainted.

For painted aluminum with 1 mm thickness, the panel shows a plastic deformation at the attachment point. Figure VI.17 shows the rear face of the panel, which put in evidence the deformation at the panel center. This deformation was observed only for the 1 mm panel

thickness. In section VI.6 we analyze in more details the mechanical constraints and the associated deflection for different materials.

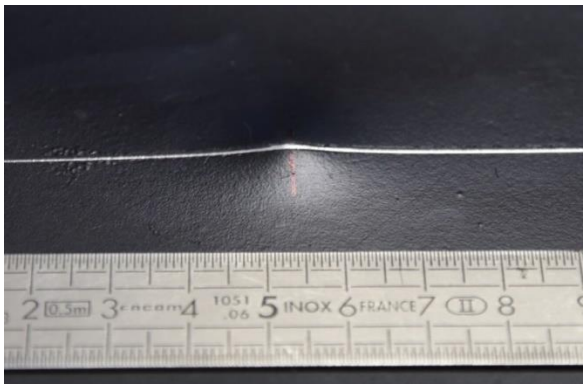

Figure VI.17. View of the rear face of the panel, highlighting the plastic deformation for the 1 mm aluminum 100 µm paint, after the application of a 100 kA current waveform.

Figure VI.18 shows the damage in CFRP panels. We can see clearly the delamination of the surface and even in some internal ply. The delamination reaches a length of about 80 mm along the fibers and 25 mm in the transverse direction. The damage area has an opposite shape to that obtained in section VI.2 for the arc root, which reaches 80 mm in the transverse direction and only 30 mm along the surface ply. This indicates that the delamination is mainly favored by the orientation of the surface ply.

(a) *(b)*

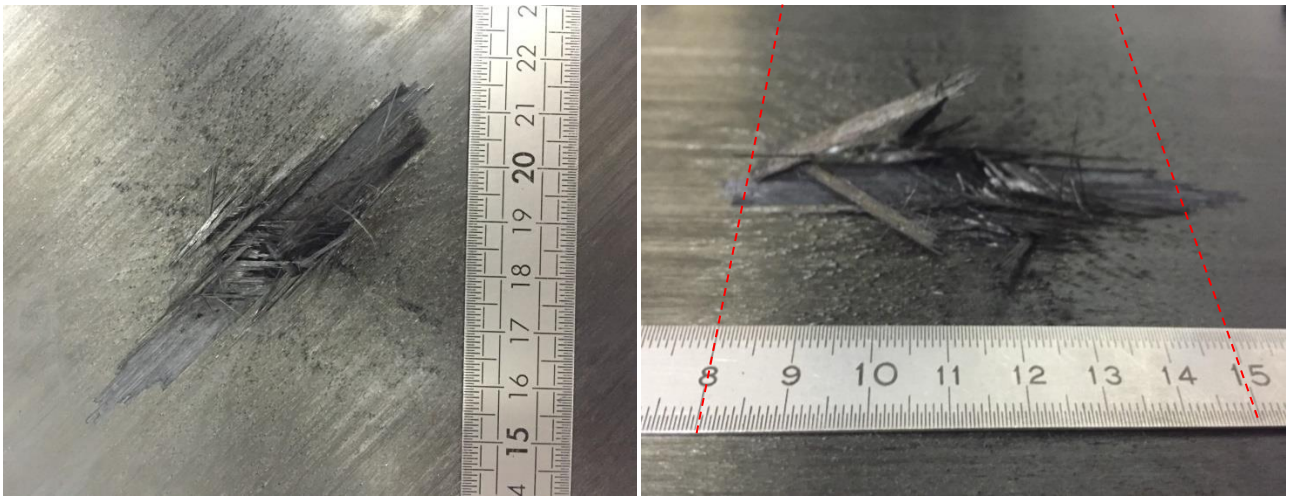

Figure VI.18. Damage in CFRP panel after the direct lightning arc test.

We can also notice that a huge number of spots are arranged around the damaged zone, especially in the transverse direction. These spots could be associated to the fast transverse expansion of the arc presented in the previous section.

VI.5 Evaluation of the thermal constraint

The arc imposes thermal constraints to the material, which cause a significant increase of the panel temperature. In this section we briefly discuss the main mechanisms of heat transfer between the arc and the material and in the phase after the arc lifetime. Also, we present the rear surface temperature measurements done using infrared thermography (IRT).

VI.5.1 Heat transfer between the arc and the material

During the arc lifetime, which corresponds to approximately 100 µs, the energy exchange source in the interaction between the arc and the material can be separated into two groups; (*i*) the incident heat flux vector $\vec{q}$ (W m^{-2}), which occurs at the arc-material interface with the normal $\vec{n}$ oriented outward the material, and (*ii*) the volumetric power P (W m^{-3}) released within the material.

We can consider that the heat flux vector is the combination of four mechanisms; the electric flux $\vec{q}_{elec}$ due to the electrical current that flows at the interface, the radiative flux $\vec{q}_{rad}$ resulting from the emission and absorption balance between the arc channel and the panel surface, the evaporative flux $\vec{q}_{evap}$ due to the evaporation of the material and, finally, the convective flux $\vec{q}_{conv}$. Therefore, the thermal flux balance at the interface, during the arc lifetime, can be written as:

$$-\lambda_{mat}\vec{\nabla}T.\vec{n} = \vec{q}_{elec} + \vec{q}_{rad} + \vec{q}_{conv} - \vec{q}_{evap} \quad \text{(VI.1)}$$

where λ_{mat} is the thermal conductivity of the material (121 W m^{-1} K^{-1} for the Al 2024-T3 alloy (AMS (2016)) and 0.95 W m^{-1} K^{-1} for the CFRP composite in the direction parallel to the normal $\vec{n}$ (Neufeld (2015)). Figure VI.19 illustrates the fluxes at the interface arc-material.

The volumetric power dissipated in the material is a result of the Joule heating due the current circulation. Taking into account all the mechanisms mentioned above, the heat diffusion equation within the material can be written as:

$$\rho C_p \frac{d}{dt}T = \lambda\nabla^2 T + P_{Joule} \quad \text{(VI.2)}$$

where ρ is the mass density and C_p is specific heat of the material (respectively 2780 kg m^{-3} and 875 J kg^{-1} K^{-1} for the Al 2024-T3 alloy (AMS (2016)), and 1538 kg m^{-3} and 1160 J kg^{-1} K^{-1} for the CFRP composite at 300 K (Neufeld (2015))).

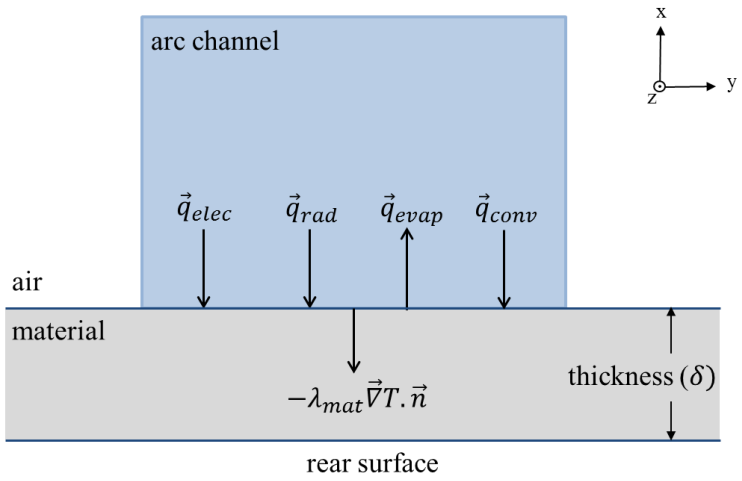

Figure VI.19. Diagram of the energy balance at the arc-material interface.

After the arc lifetime, we can mention three mechanisms to account for the cooling of the panel; the thermal diffusion in radial and transverse direction, the thermal radiation and the natural convection.

VI.5.2 Rear surface temperature measurements

The measurements of the surface temperature in the rear face of the panel are performed using the infrared thermography (IRT). The acquisition rate of the camera is limited to 120 Hz, and then the first measurement occurs only at 8.33 ms after the arc ignition, which is very late in comparison with the duration of the current injection. Therefore, at the first temperature measurement, the cooling phase is already taking place. This low temporal resolution prevents a precise analysis of the incident heat flux using the rear surface temperature measurements. Therefore, in the following paragraphs, we present the measured temperature and its evolution over time for the different materials and surface coatings, for the purpose of providing additional information for the understanding of the thermal constraint.

Figure VI.20 shows the maximum temperature measured over time for different materials and surface coatings. The initial temperature for all panels is approximately 295 K. The highest temperatures are reached in the painted aluminum panels. It reaches 523 K for the 100 µm paint, which corresponds to a variation of 228 K. The unpainted aluminum panel reaches 407 K for the 1 mm thickness and 361 K for 1.6 mm. The maximum temperature of the CFRP panel reaches 356 K.

In any case, even the arc occurring only in the first hundreds of microseconds, the temperature reaches its maximum between 15 to 30 ms. This time difference is related to the temporal diffusion of the temperature across the panel thickness. This value is in accordance with theoretical time constant τ for transverse conduction across a thickness δ, given by $\tau = \delta^2 \rho C_p / \lambda$,. Using the appropriate constants for each material, we obtain 20.1 ms for 1 mm thickness aluminum and 7.5 s for CFRP panel.

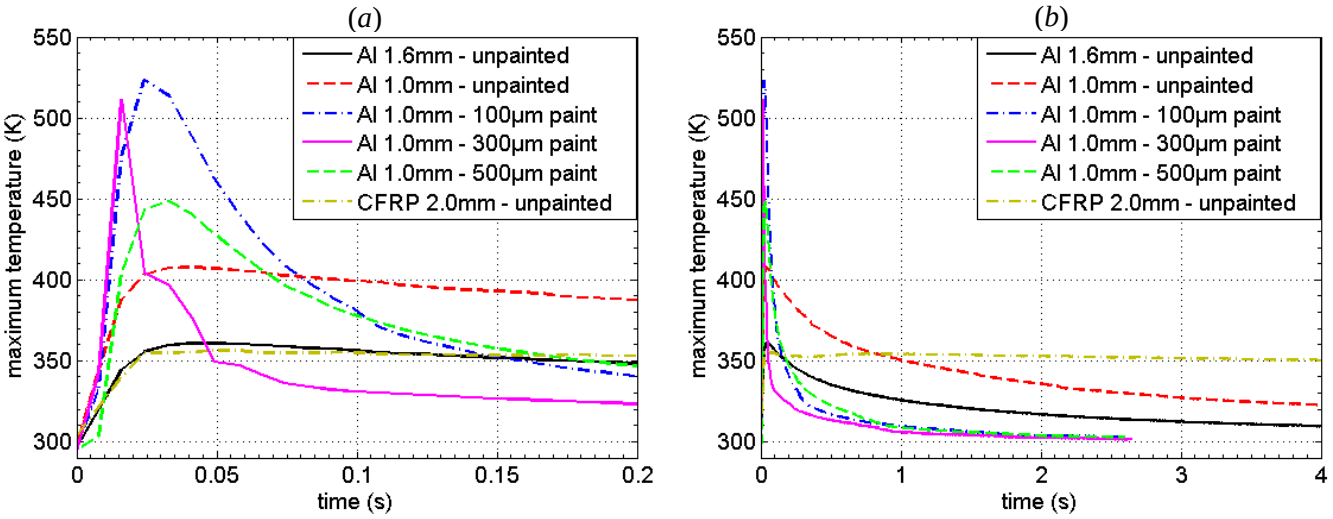

Figure VI.20. Maximum temperature in the rear face of the different panels. Detail in the first 200 ms (a) and the evolution during 4 s (b).

However, the time constants of temperature fall, defined here as the times when the temperature falls to the half maximum, are very different for one panel to another. They range from 50 ms for the 100 µm painted aluminum to 800 ms for the unpainted 1.6 mm thickness aluminum. For the CFRP panel, this time constant is much higher than the aluminum cases, with a value around 15 s.

The temperature profile over panel surface is axisymmetrical for the case of aluminum. Figure VI.21 shows an example of radial profiles at several times, for painted and unpainted panels.

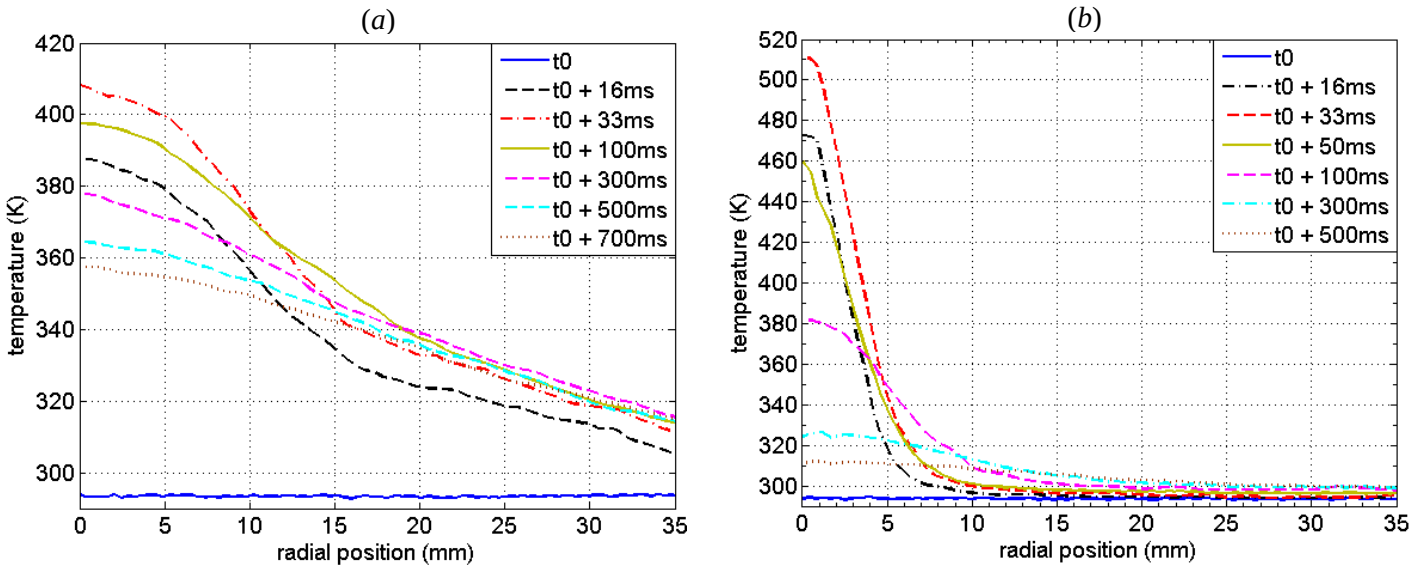

Figure VI.21. Radial profiles of temperature of aluminum panels with 1 mm thickness. (a) Unpainted panel. (b) 100 µm painted panel.

To characterize the evolution of these profiles over time, we calculated the half width at half maximum (HWHM) for all aluminum panels. Figure VI.22 shows the results of HWHM. We can see that the temperature distribution on unpainted panels has a larger half width than the case of painted panels. In other words, the heating of the panel is more constricted in the presence of paint. These HWHM at the first measured time are in accordance with the arc root radii of the damaged area discussed in section VI.6 (see figure VI.16).

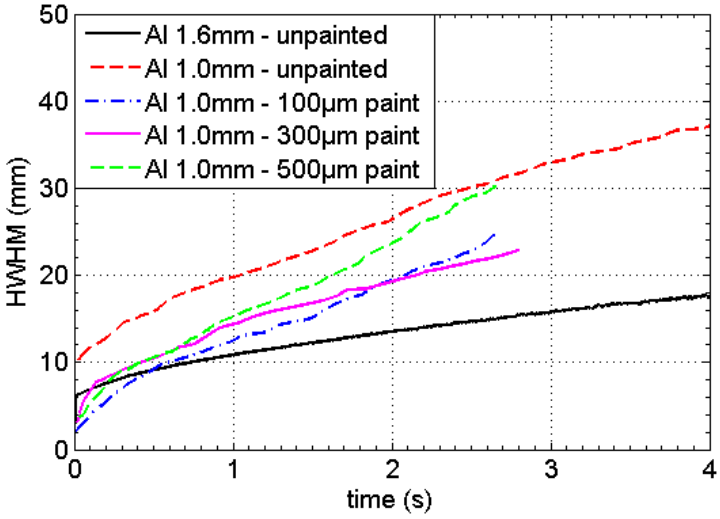

Figure VI.22. Half width at half maximum (HWHM) for the temperature profile in the panel surface.

For the CFRP panels, the surface temperature distributions are different from those of the aluminum case. They have no radial symmetry and show an important rise of temperature far from the attachment point for times greater than 1 s, while the temperature at the center remains almost constant. Figure VI.23 shows the temperature mapping for the CFRP panels at a few times, and the plots of distribution in the horizontal and vertical direction. We can notice the asymmetrical diffusion of the temperature, which is closely related to the layup disposition of the carbon ply in different orientations. These different ply orientations lead to an anisotropic thermal conductivity in the CFRP panels (Neufeld (2015)).

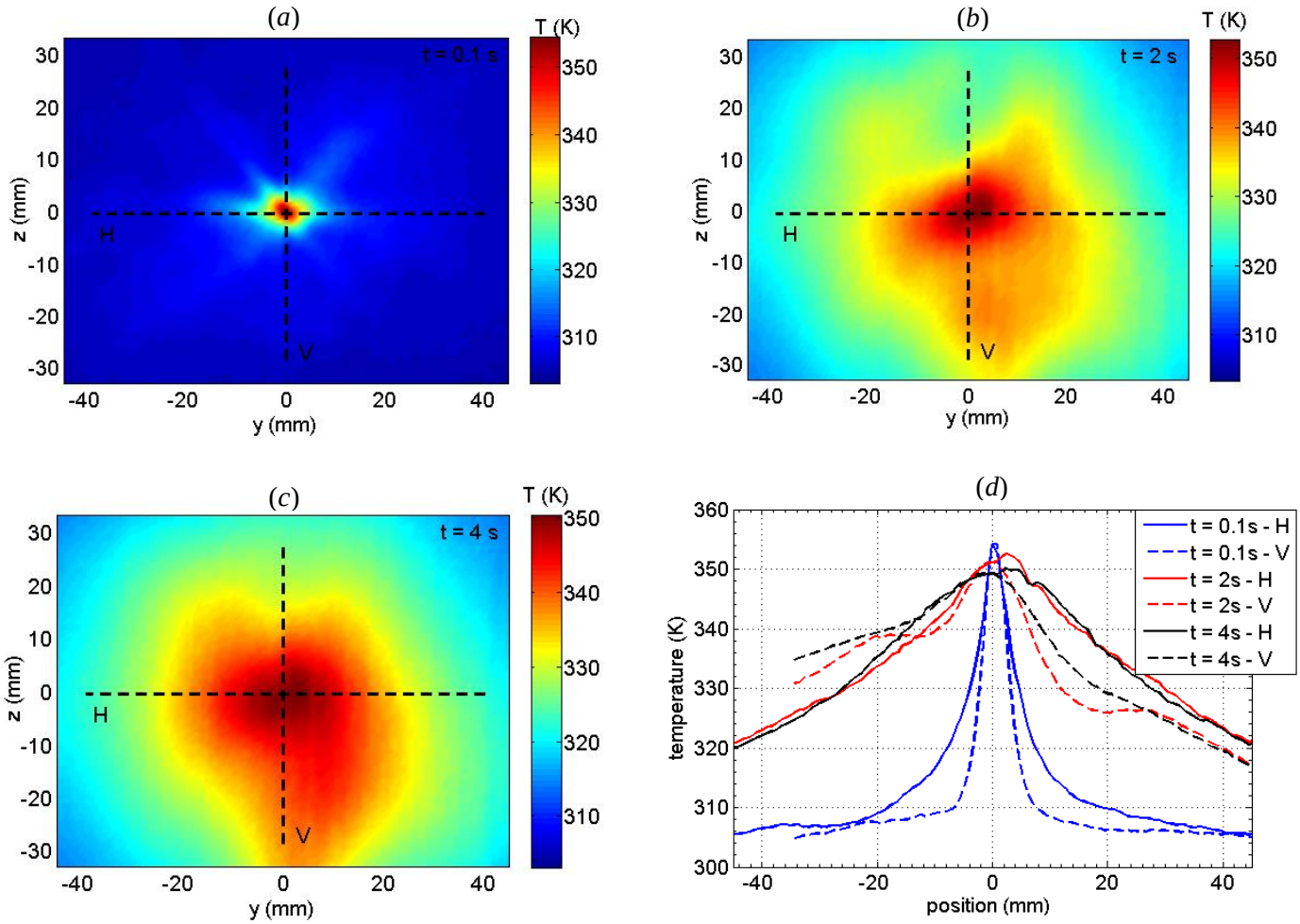

Figure VI.23. Mapping of temperature in the CFRP panel. (a) 0.1 s. (b) 2 s. (c) 4 s. (d) distribution for the horizontal (H) and vertical (V) lines which cross the panel center.

VI.6 Evaluation of the mechanical constraint

The arc root applies a force in the panel oriented along the arc axis that induces mechanical constraints in the material. To evaluate those mechanical constraints we perform deflection measurements using two techniques; Stereo-digital image correlation (Stereo-DIC) and fast direct deflection measurements.

VI.6.1 Stereo-DIC measurements

Stereo-DIC is used to assess the mapping deflection in the entire panel. Figure VI.24 shows an example of the deflection profile for a horizontal line crossing the panel center (along *y*-axis). The circular mounting of 380 mm diameter, that clamp the square panels, defines the boundary conditions and leads to a problem of a deflection in a circular panel clamped at its edges. The profiles show approximately an axisymmetric shape, which is also related to the symmetrical arc root shape in the first microseconds. In both panels, it can be seen that the main vibration mode is superimposed to secondary modes.

From the deflection profiles, we can obtain the deflection of the panel center over time. Figure VI.25 shows this center deflection for different materials. Generally, the center deflection follows a damped sine wave where harmonic vibrations modes of higher frequency are superimposed. The frequency of the main mode is approximately 140 Hz for the unpainted aluminum and is closely the same for painted aluminum and CFRP panel, with a value of 200 Hz.

(*a*)

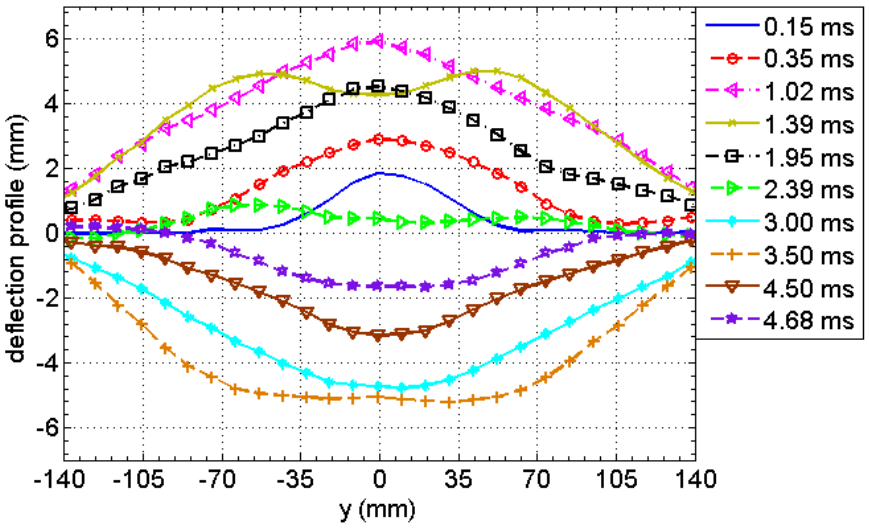

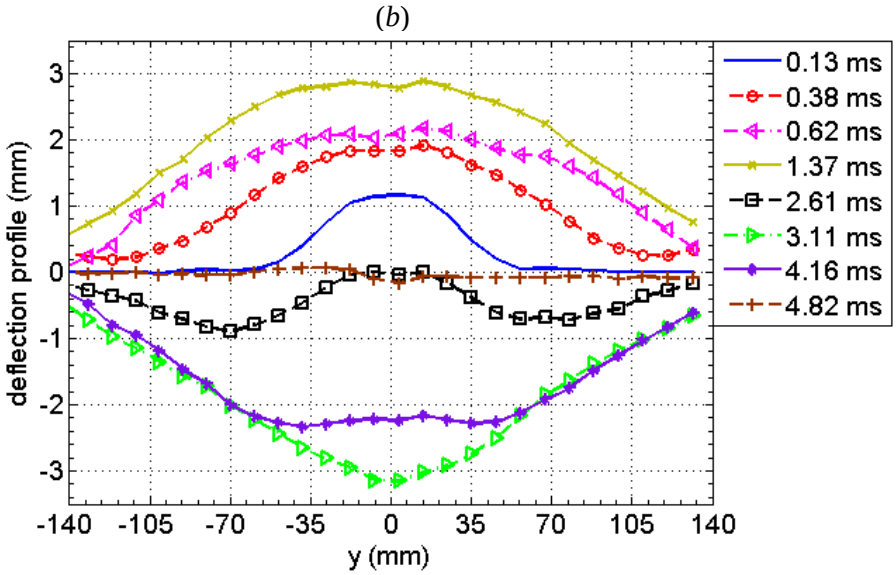

Figure VI.24. Example of deflection profile along y-axis. (a) 1.0 mm aluminum panel with 100 µm paint. (b) 2.0 mm CFRP panel.

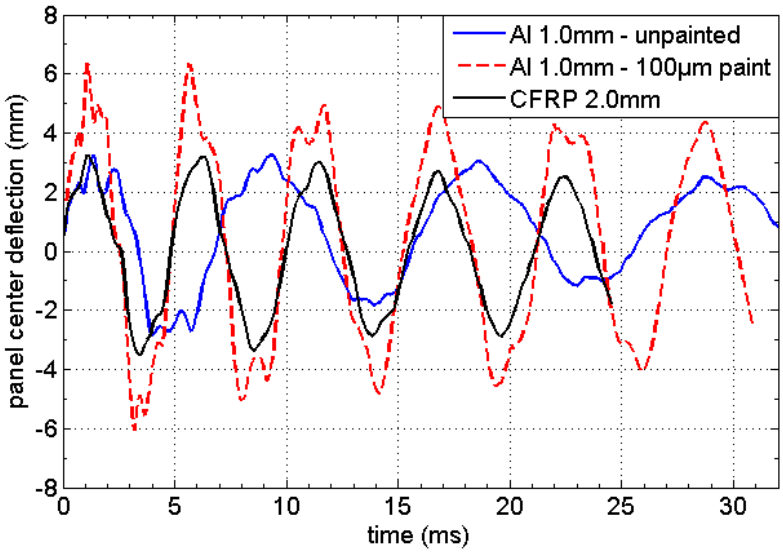

Figure VI.25. Deflection of the panel center over time for different materials.

We can notice that the curves reach their maximum at approximately 1ms, which is larger than the duration of the mechanical action caused by the current (100 µs). This means that the deflection at the panel center continues to increase without arc. This phenomenon could be explained by the mechanical inertia of the panel after the initial acceleration. We can also notice that the maximal amplitudes slightly decrease for the first oscillations.

The maximal amplitude is about 6.1 mm for a painted panel, while it is about 3.1mm for an unpainted one. It seems that the constraint applied on the material is lower on an unpainted

aluminum panel. In the same way, the maximal amplitude on CFRP is about 3.1 mm, which is similar to unpainted panel, while the thickness is twice and the modulus of elasticity is more important. The mechanical constraint applied on the CFRP panel is probably more important than on aluminum.

While the maximal positive and negative deflections are similar for both unpainted panel (Aluminum and CFRP), an offset seems to be applied on the deflection curve for the painted panel. The first positive maximal deflection is 3.2 mm and the negative is about 2.9 mm. This unbalance increases with time, with a deflection of 3 mm at 18 ms and 1 mm at 23 ms. The difference is explained by the plastic deformation of the panel, which is observed after the shot (see figure VI.17).

Stereo-DIC gives some interesting information on the mechanical constraint applied on the panel. Nevertheless, as described in Chapter II, to obtain the stereo-DIC in the total surface of the panel, we need to set a resolution of 800 × 500 pixels for the HSC. This resolution setup limits the maximum frame rate to 16 kfps, which correspond to a time step of 62.5 µs. This measurement rate enables us to assess important information about the panel dynamics, allowing the analysis of the internal mechanical constraints in the material. Nevertheless, it is not fast enough to evaluate the applied arc pressure, which is significant only in the first 30 µs.

VI.6.2 Fast direct deflection measurements

To study the force that acts on the panel, we used the direct visualization of the center deflection, using the maximum frame rate of the HSC, which corresponds to a time step of 1 µs. The results are combined with theoretical relationships to evaluate the overpressure applied on the panel during the arc phase. For that, we present in this section some fundamental relations for thin plates. Then, we propose a numerical procedure to treat the fast direct deflection measurements.

Figure VI.26 shows the measurements obtained for 3 different aluminum panels; one unpainted panel of 1 mm thickness and two 100 µm painted with both 1.0 mm and 1.6 mm. The diagnostic setup for the fast direct deflection measurement is described in Chapter II.

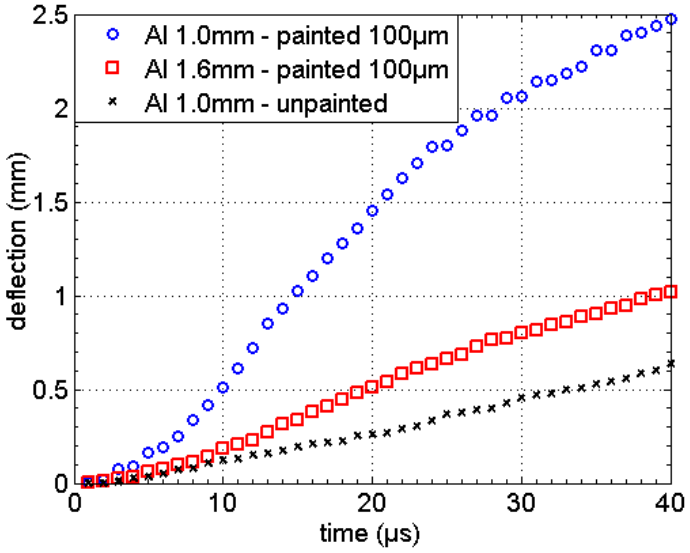

Figure VI.26. Measurements of the deflection at the panel center.

To correlate the deflection measurement with the pressure applied on the panel by the arc root, we employ a particular analysis derived from the Kirchhoff-Love plate theory. In a stationary case, the deflection in a thin plate located in the plane *yz*, clamped at its edges and submitted to a transverse load *p(y,z)* (N m^{-2}) oriented along the *x*-axis obeys the equation (Timoshenko (1959)):

$$D\nabla^2\nabla^2 w(y,z) = p(y,z) \tag{VI.3}$$

where *w(y,z)* is the deflection distribution and *D* is the flexural rigidity of the plate, which is a function of the modulus of elasticity *E*, the Poisson's ratio *v* and the plate thickness δ, and can be expressed as:

$$D = \frac{E\delta^3}{12(1-\nu^2)} \tag{VI.4}$$

For the aluminum panel used in this work (alloy Al 2024-T3), the flexural rigidity for 1 and 1.6 mm thickness are, respectively, 0.0068 and 0.028 GPa m^3.

For a circular plate (or clamped by a circular mount as the case of the present work) with an axially symmetrical load *p(r)* applied to the plate, the resulting deflection distribution will be also axisymmetric. For the case of a time-dependent load *p(r,t)* applied to the plate, equation (VI.3) must be modified to include the inertia of the plate, and can be written, in cylindrical coordinates, as (Ventsel and Krauthammer (2001)):

$$D\frac{1}{\mathrm{r}}\frac{d}{dr}\left\{r\frac{d}{dr}\left[\frac{1}{r}\frac{d}{dr}\left(r\frac{d}{dr}w(r,t)\right)\right]\right\} = p(r,t) - \rho\delta\frac{\partial^2}{\partial t^2}w(r,t) \quad \text{(VI.5)}$$

In this work, the load *p(r,t)* can be seen as the pressure applied in the panel by the arc root. Therefore, we can evaluate this arc pressure by using equation (VI.5) with some hypotheses. In a first approach, we estimate the influence of the term on the left-hand side of equation (VI.5) by a simplification in the deflection distribution. In the axisymmetric hypothesis, the deflection shape function, at a particular time t_p, can be approximated to the first order by (Ventsel and Krauthammer (2001)):

$$w(r) = C(R^2 - r^2)^2 \quad \text{(VI.6)}$$

where *C* is a constant varying over time and *R* is the equivalent radius of the panel, equal to 190 mm. With the deflection at the panel center *w(0)*, we can express, for each instant, this constant by $C = w(0)/R^4$. The left-hand side term of equation (VI.5) becomes then $64Dw(0)/R^4$, which is equal to 0.637 mbar for a deflection of 1 mm and for the panel with 1 mm thickness. Even considering an equivalent radius smaller for the deflection distribution, as suggested by first radial profile in figure VI.24*(a)*, this term remains small. For instance, using *R* = 10 mm, for a deflection of 1 mm, the term is equal to 0.43 bar. Therefore, this term can be neglected and equation (VI.5) is reduced to a relation similar to the Newton's second law, which can be written as:

$$p(0,t) = \rho\delta\frac{\partial^2}{\partial t^2}w(0,t) \quad \text{(VI.7)}$$

As expressed by equation (VI.7), the pressure applied at the panel center, can be directly deduced from the second derivative of the deflection, which represents its acceleration. Nevertheless, the measurements presented in figure VI.26 have a low spatial resolution (85 µm), and during the first 10 µs, when the displacement is lower than 500 µm and the pressure is expected to reach its peak, the deflection is not sufficiently sampled. We attempted to use approximations for the derivatives of *w(0,t)* by finite differences, and even using high truncation errors, as for example $O(h^{12})$, the resulting acceleration is extremely noisy and leads to inconsistent values of the pressure.

To avoid the derivative calculations, we suggest a different approach. We propose a candidate analytical function for the pressure $p(0,t)$, and then we analyze if the resulting expression for $w(0,t)$ is suitable to describe the measured deflection. To choose an analytical equation for the pressure, we look for a function which satisfies some conditions; (*i*) the overpressure before the

arc initiation is equal to zero, (*ii*) the function must increase until reaching a peak value and then (*iii*) it should decreases to zero, once the arc ends after a hundred microseconds. We selected, as a first approach, a sum of two exponential functions with coefficients P_1 and P_2 , and time constants τ_1 and τ_2, which can be written as:

$$p(0,t) = P_1 e^{-\frac{t}{\tau_1}} + P_2 e^{-\frac{t}{\tau_2}} \tag{VI.8}$$

By applying an initial overpressure equal to zero, the coefficients of equation (VI.8) must satisfy $P_1 = -P_2$.

To obtain an analytical expression for the deflection center, equation (VI.8) is integrated two times, with two initial conditions; at the arc initiation (*i*) there is not deflection of the panel (*w(0) = 0*), and (*ii*) the panel is at rest (*w'(0) = 0*). Therefore, the resulting expression for the deflection can be written as:

$$w(0,t) = \frac{P_1}{\rho\delta}\left[\tau_1^2 e^{-\frac{t}{\tau_1}} - \tau_2^2 e^{-\frac{t}{\tau_2}} + (\tau_1 - \tau_2)t + (\tau_2^2 - \tau_1^2)\right] \tag{VI.9}$$

Equation (VI.9) described the deflection at the panel center as a function of three parameters, P_1, τ_1 and τ_2. Using this equation, the calculated deflection is then compared to the measured one by applying a least-square procedure with those three fit parameters. Figure VI.27 shows the obtained results.

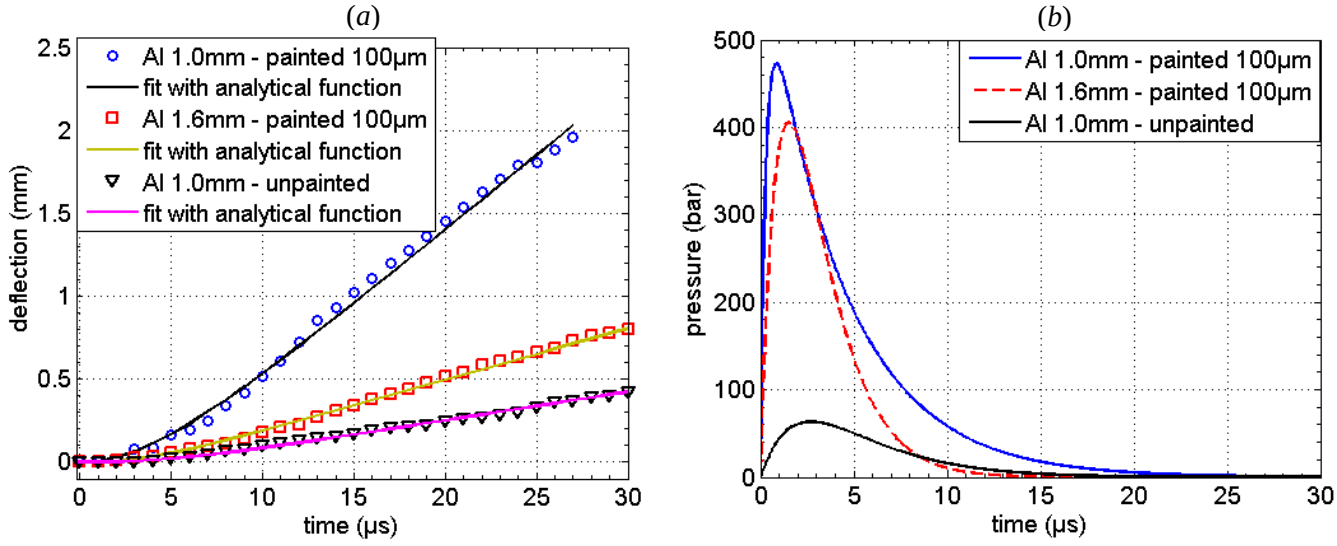

Figure VI.27. (a) Measured and calculated deflection, using the analytical function derived from a bi-exponential pressure (equation (VI.10)). (b) Pressure obtained from the three fit parameters.

The measured deflection is well described by the analytical function in the first 30 µs. For painted panels, the obtained pressure reaches very high values, with a peak value in the first 2 µs, reaching approximately 475 bar for the 1 mm panel and 405 bar for 1.6 mm. These high values could be expected for the case of painted material, once the small conductive area leads to a very high current density, and consequently the formation of the plasma jet (as described in section VI.2), that may increase the pressure at this point. Even if the two painted panels have the same paint thickness, the obtained curves are not identical. Two possible explanations for this difference are: the slightly plastic deformation that occurs for the 1 mm panel at the impact point and which is not present in the 1.6 mm panel (see figure VI.17), or a worst sampling of the deflection measured for the 1.6 mm panel.

For the unpainted panel, the pressure reaches a maximum of 63 bar at 2.6 µs. In these panels, as discussed in section VI.2, the behavior of the arc root is similar to the arc column, i.e., the arc root expands radially without a significant effect of current streamlines constriction and neither the formation of the plasma jet, as was observed for painted panels. Therefore, the unpainted case seems to be more suitable to comparisons with the pressure obtained by OES measurements in Chapter 5. At 2 µs, the pressure is equal to 60 bar, which is 33 % higher than the pressure, at the same instant, obtained in the arc column center (45 bar). Considering all assumptions and uncertainties related to both methods, the agreement is fairly remarkable.

Note that the accuracy of the deflection measurements, both spatially and temporally, is limited. The results of this section should be taken with care. The most important outcome that we can mention is the original diagnostic and procedure that were developed to assess the mechanical constraints imposed by the arc root in the panel.

VI.7 Conclusion

In this chapter, we performed an investigation of the interaction between the high current arc and aeronautical materials. Several properties of this interaction are characterized and evaluated for different material and surface coatings.

High speed imaging allowed us to assess the temporal dynamics and the spatial form of the arc roots. For the case of aluminum panels, the presence of the material reduces the arc root radius, when compared to the evolution of a free arc column. The paint impacts the arc root evolution, causing an important reduction of its radius. The maximum root radius is also influenced by the paint thickness. In CFRP panels, the arc root is highly influenced by the orientation of the

surface carbon ply. In the transverse direction to the surface ply, the arc root reaches more than 90 mm and has an initial expansion velocity of approximately 6 km s^{-1}.

For unpainted aluminum panels, the shock wave close to the surface materials is cylindrical and its evolution is identical to that induced by a free arc channel. For painted panels, the shock wave spreads faster and gives rise to an additional quasi-spherical wave front, which is centered at the arc root. In CFRP panels, the shock wave follows the shape of the arc root in each surface ply orientation. It has an oblique propagation in the transverse direction to the surface ply. In the parallel direction, the wave front is the perpendicular to the panel surface.

Examination of the panel surface after shot shows that the damage areas are roughly axisymmetric and small for the case of painted panels, with a diameter in the order of 6 mm for both 100 µm and 300 µm paint. For the 500 µm paint, the area where the paint was destroyed is much larger than for the other paint thicknesses, reaching a diameter of 30 mm. Significant delamination occurs for CFRP panel, with a damage that can reach 80 mm and which is very dependent on the surface ply orientation.

Thermal constraints imposed by the arc on the material are discussed and rear surface temperature measurements are performed using the IRT. Painted aluminum reaches a temperature variation of more than 200 K, which decreases with a time constant in the order of 100 ms, while the CFRP panels reaches a variation of 55 K with time constant of around 15 s.

Mechanical constraints are analyzed by deflection measurements. Different vibration modes are observed in the panel deflection. The deflection at the panel center reaches 6.1 mm for painted aluminum and around 3.1 mm for unpainted and CFRP panels. The maximum deflection is reached at approximately 1 ms. By the fast direct measurement of the deflection at the panel center, we evaluate the pressure that acts at this point. At the first 30 µs, the displacement is in the order of 2 mm for 1 mm aluminum with 100 µm paint and 0.5 mm for unpainted panel. Applying the thin plate deflection equation with a few simplifications and assuming a bi-exponential expression as candidate for the pressure, we obtained estimations for the pressure at the arc root axis. For the painted case, the pressure reaches 475 bar at 1 µs, and for unpainted panel, it reaches 63 bar at 2.6 µs. Compared to results of the arc column pressure, obtained in Chapter V by OES measurement, the results show a reasonable agreement.

The results and analyses presented in this chapter give new experimental data and insights for the interaction between a lightning arc and aeronautical materials and will be very useful for comparison and model validation. A part of these results are the subject of a paper in a conference proceeding (Sousa Martins et al. (2016c)).

Conclusion

The modern aircraft industry faces two major challenges: to improve fuel efficiency and to reduce greenhouse gases; objectives that can be achieved by a significant use of carbon fiber composite in many parts of the aircraft, as wing boxes and fuselage, provoking a substantial contribution to the weight reduction. However, new materials require particular attention for lightning protection solutions, due to their low thermal and electrical conductivity, which lead to an increase in the thermo-mechanical constraints. An accurate understanding of the physical quantities of the lightning arcs, as well as models and computational tools to predict the behavior of these arcs, are essential for aircraft manufacturers. This knowledge serves as the basis for the optimization of aeronautics protections and in time and cost reduction by avoiding the need to perform numerous and costly lightning tests for certification.

Nevertheless, experimental data of laboratory lightning arcs, used for lightning protection development, were not initially available in the literature. Aiming to answer the scientific need, we have developed methods and experimental diagnostics to obtain physical properties of lightning arcs and the interaction between the arcs and aeronautical materials.

In arc modeling, the main input of simulation codes is the current waveform. This quantity drives all others physical properties in the arc plasma, as energy, temperature, pressure, and velocity distributions. Therefore, to build a solid experimental database, we used an electric current generator, which was adapted to produce different current waveforms. The parametric study was performed for five peak levels ranging from 10 kA to 100 kA, with a peak time around 15 µs.

The results obtained in this dissertation allowed us to provide the responses to the fundamental questions raised in the introduction:

- How is the evolution over time of the lightning arc? What is its size and shape? Is there an influence of the current level? Is there a strong shock wave induced by the arc expansion? What are the characteristics of this wave?

High-speed imaging has allowed us to assess the temporal dynamics and the spatial shape of the arc. The measurements of the characteristic lengths, as the shock wave and the arc channel radius, have been made over time up to 140 µs. The diameter of the arc reaches 6.4 cm at 50 µs for the case of 100 kA. The shock wave detaches from the arc column around 6 µs. It expands at about 0.8 km s^{-1} at the beginning of the arc for 10 kA and is twice faster for 100 kA.

A model of light deflection based on the Background-Oriented Schlieren measurements and the Gladstone-Dale relation was developed to estimate mass density profile of the shock wave. The results are in accordance with Rankine-Hugoniot relations using the measured shock wave velocity, but the assumption of a linear profile is less accurate for lower density values.

- What are the arc electrical characteristics? How the conductivity varies with time? What electrical energy is absorbed by the lightning arc?

We performed an electrical characterization of the free arc channel. An electrical model for the arc channel was developed, which assumes the arc column as a time dependent impedance. The geometry and the evolution over time of the arc shape were used in the model development. This model allowed us to determine the inductance and the resistance of the arc from the electrical measurements, as the arc voltage and current, for the five current waveforms. The characterization was done during times lasting up to 50 µs when the axisymmetric assumption was validated.

A parametric study on the arc length was done, to take into account the boundary effect due to the electrodes and to assess the different components that constitute the total arc resistance. The total and the linear column resistance decrease with the increase of the current peak, and reach a steady value, after a few microseconds. This value ranges from 0.05 $\Omega\,m^{-1}$ to 0.2 $\Omega\,m^{-1}$ for the arc column.

The electrical conductivity, calculated assuming a homogenous radial distribution in the column, reaches a peak value of 21100 $S\,m^{-1}$ for 100 kA and 14100 $S\,m^{-1}$ for 50 kA. The conductivity peak is around 6 µs which is about 8 µs earlier than the current peak. The shape of the conductivity varies for the different current peaks and is highly dependent on the arc radius. The electrical power and energy dissipated inside the column by Joule effect are estimated from the column resistance. For the 100 kA peak, the electrical power reaches 2.3 $GW\,m^{-1}$ at 2 µs and the cumulated energy reaches 25.7 $kJ\,m^{-1}$ at 49 µs.

- What are the temperature and pressure distributions of the arc column? How do they change with time and with the arc current?

An investigation of the intensive thermodynamic properties of a free arc channel using optical emission spectroscopy was performed. A study of the sensitivity to the temperature of nitrogen and oxygen line intensities was done. More than 190 ionic lines were used to calculate the absorption coefficient and the optical thickness of the arc channel. The absorption coefficient allowed the determination of the arc properties in a non-optically thin medium by solving the radiative transfer equation and assuming the arc channel as a combination of concentric layers.

The radial profiles of temperature, electron density, and pressure were determined for the 100 kA current peak over time up to 36 µs. The temperature is approximately constant inside the arc channel, and the electron density and the pressure show roughly a parabolic shape along the radial direction. In the channel center, the temperature and the electron density reach, respectively, 37400 K and 4.9×10^{18} cm^{-3} at 2 µs. The pressure reaches 45 bar with an accuracy estimated at 20%.

A comparison of the results for four current peak levels, ranging from 10 kA to 100 kA was performed at two instants. The temperature seems to have a moderate dependence on the current level, but the electron density shows a significant sensitivity to the current, increasing by a factor of more than 6 when the current changes from 10 kA to 100 kA.

Stark broadening of Hα line was measured from 20 µs to 36 µs at 100 kA current peak, and the resulting electron densities were compared to the RTE method. In the first microseconds after 20 µs, significant differences were found, but the overestimation of the electron density derived from the Hα line can be explained by a significant optical thickness of this line.

Based on the obtained radial distribution of temperature and pressure, the electrical conductivity in the column cross section is calculated and compared to the results derived from electrical measurements. The results from the determined temperatures and pressures are higher than those from the column resistance. Nevertheless, the differences are within the estimated error of the measurements, which reinforces the consistency of the considered methods and the achieved results.

- Are there some differences between a free arc column and an arc interacting with aeronautical materials? How do the arc properties change when applied to different materials and surface coatings?

We performed an investigation of the interaction between the high current arc and aeronautical materials. Several properties of this interaction were characterized and evaluated for different material and surface coatings. High-speed imaging allowed us to assess the temporal dynamics and the spatial form of the arc roots. For the case of aluminum panels, the presence of the material reduces the arc root radius, when compared to the evolution of a free arc column. The paint impacts the arc root evolution, causing a significant reduction in the visible root radius, after a few tens of microseconds. The maximum visible root radius is also influenced by the paint thickness. In carbon fiber reinforced polymer (CFRP) panels, the arc root is highly influenced by the orientation of the surface carbon ply. In the transverse direction to the surface

ply, the visible arc root reaches more than 90 mm and has an initial expansion velocity of approximately 6 km s^{-1}.

For unpainted aluminum panels, the shock wave close to the surface materials is cylindrical and its evolution is identical to that induced by a free arc channel. For painted panels, the shock wave spreads faster and gives rises to an additional quasi-spherical wave front, which is centered at the arc root. In CFRP panels, the shock wave follows the shape of the arc root in each surface ply orientation. It has an oblique propagation in the transverse direction to the surface ply. In the parallel direction, the wave front is the perpendicular to the panel surface.

Examination of the panel surface after shot shows that the damage areas are roughly axisymmetric and small for the case of painted panel, with a diameter in the order of 6 mm for 100 and 300 µm paint. For the 500 µm paint, the area where the paint was destroyed is much wider than for the other paint thicknesses, reaching a diameter of 30 mm. Significant delamination occurs for CFRP panel, with a damage that can reach 80 mm and which is very dependent on the surface ply orientation.

Thermal constraints imposed by the arc on the material are discussed and the rear surface temperature is measured using the infrared thermography (IRT). Painted aluminum reaches a temperature variation of more than 200 K, which then decreases with a time constant in the order of 100 ms, while the CFRP panels reaches a variation of 55 K with time constant of around 15 s.

Mechanical constraints are analyzed by deflection measurements. Different vibration modes are observed in the panel deflection. The deflection at the panel center reaches 6.1 mm for painted aluminum and around 3.1 mm for unpainted and CFRP panels. The maximum deflection is reached at approximately 1 ms. By the fast direct measurement of the center deflection, we evaluate the pressure that acts at this point. At the first 30 µs, the displacement is in the order of 2 mm for 1 mm aluminum with 100 µm paint and 0.5 mm for unpainted panel. Applying the thin plate deflection equation with a few simplifications and assuming a bi-exponential expression for the pressure, we obtained estimations for the pressure at the arc root axis. For the painted case, the pressure reaches 475 bar at 1 µs, and for unpainted panel, it reaches 63 bar at 2.6 µs. Compared to results of the arc column pressure, obtained by OES measurement, the results show a reasonable agreement.

The results presented in this dissertation will serve as a reference for part of an experimental database for lightning arcs. They are the subject of three papers in conference proceedings (Sousa Martins et al. (2015a); Sousa Martins et al. (2015b); Sousa Martins et al. (2016c))

and two research papers published by IOP Publishing in *Journal of Physics D: Applied Physics* (Sousa Martins et al. (2016a); Sousa Martins et al. (2016b)).

For further studies, an improvement of the diagnostics related to the interaction arc/material can be considered. First, we advise for the application of some spectroscopic method in the arc roots, to assess the temperature and pressure in this region. A major difficulty for this measurement is the contamination of the plasma by the material and paint evaporation, as well as the no axisymmetric shape of the arc root for some materials. Furthermore, using the results of IRT measurements of the rear face of the panel, a complete model for the evaluation of the incident heat flux could be developed, which should take into account the thermal diffusion in transverse and radial directions of the material, and also the radiative and convective loss. Moreover, we can mention the need for an improvement of the spatial resolution of fast deflection measurements (in the order of a few micrometers). This enhancement would allow a more accurate investigation of the evolution over time of the pressure applied by the arc during the transient phase.

References

Acosta, E., Vazquez, D., Garner, L. and Smith, G. (2005). Tomographic method for measurement of the gradient refractive index of the crystalline lens. I. The spherical fish lens. *J. Opt. Soc. Am. A,* **22,** 424-33

Aleksandrov, N. L., Bazelyan, E. M. and Shneider, M. N. (2000). Effect of continuous current during pauses between successive strokes on the decay of the lightning channel. *Plasma Phys. Rep.,* **26,** 893-01

American Meteorological Society (2012). *Meteorology Glossary*. (ver. 25 April 2012) Available: http://glossary.ametsoc.org/wiki/Hydrometeor. [2016, May 27]

ASM Aerospace Specification Metals, Inc. (2016). *Aluminum 2024-T3*. (ver. 9.2016) Available: http://asm.matweb.com/search/SpecificMaterial.asp?bassnum=MA2024T3. [2016, June 10]

Babou, Y., Rivière, Ph., Perrin, M.-Y. and Soufiani, A. (2008). Spectroscopic study of microwave plasmas of CO2 and CO2-N2 mixtures at atmospheric pressure. *Plasma Sources Sci. Technol.,* **17,** 045010

Baker, L. (1987). Return-stroke transmission line model. *Electromagnetics*, **7**, 229-40

Becerra, M. (2008). *On The Attachment of Lightning Flashes to Grounded Structures*. Ph. D. thesis, Uppsala University

Bazelyan, E. M. and Raizer, Y. P. (2000). *Lightning physics and lightning protections.* (London: Institute of physics publishing)

Boccippio, D. J., Cummins, K. L., Chiristian, H. J. and Goodman, S. J. (2001). Combined satellite and surface based estimation of the intracloud-cloud-to-ground lightning ratio over the continental United States. *Mon. Weather Rev.*, **129**, 108–122

Burrell, K. H. (1990). Error analysis for parameters determined in nonlinear least-squares fits. *Am. J. Phys.*, **58**, 160-5

Candel, S. (2001). *Mécanique des fluides.* (Paris: Dunod)

Castellani, A., Bondiou-Clergerie, A., Lalande, Ph., Bonamy, A. and Gallimberti, I. (1998). Laboratory study of the bi-leader process from an electrically floating conductor – Part 1: General results. *IEE Proc. Sci. Meas. Technol.*, **145** 185–192

Castera, P. and Elias, P. Q. (2014). Resistance Models Applied to the Return Stroke Phase of Negative Pulsed Surface Discharges in Air. *IEEE Transactions on Plasma Science*, **42,** 1922-33

Castera, P. (2015). *Energy coupling mechanisms in pulsed surface discharges for flow control*. Ph. D. thesis, Ecole Centrale Paris

Cen, J., Yuan, P., Qu, H. and Zhang, T. (2011). Analysis on the spectra and synchronous radiated electric field observation of cloud-to-ground lightning discharge plasma. *J. Plasma Phys.*, **18**, 113506

Chauveau, S. (2001). *Constitution de bases de données spectroscopiques relatives à un plasma d ' air . Application au calcul de transferts radiatifs.* Ph. D. thesis, Ecole Centrale Paris

Chauveau, S., Perrin, M.-Y., Rivière, Ph. and Soufiani, A. (2002). Contributions of diatomic molecular electronic systems to heated air radiation. *J. Quant. Spectrosc. Radiat. Transfer*, **72,** 503–30

Chauveau, S., Perrin, M.-Y., Rivière, Ph. and Soufiani, A. (2003). Radiative transfer in LTE air plasmas for temperatures up to 15000K. *J. Quant. Spectrosc. Radiat. Transfer*, **77,** 113–30

Chawla, K. K. (2012). *Composite Materials*. 3nd edition, (New York: Springer Science+Business Media)

Chemartin, L. (2008). *Modélisation des arcs électriques dans le contexte du Foudroiement des aéronefs*. Ph. D. thesis, Université de Rouen

Chemartin, L., Lalande, Ph., Montreuil, E., Delalondre, C., Chéron, B. G. and Lago, F. (2009). Three dimensional simulation of a DC free burning arc. Application to lightning physics. *Atmo. Res.*, 91, 371-80

Chemartin, L., Lalande, P., Delalondre, C., Chéron, B. and Lago, F. (2011). Modelling and simulation of unsteady dc electric arcs and their interaction with electrodes. *J. Phys. D: Appl. Phys.*, **44**, 194003

Chemartin, L., Lalande, Ph., Peyou, B., Chazottes, A., Elias, P. Q., Delalondre, C., Cheron, B. G. and Lago, F. (2012). Direct effects of lightning on aircraft structure: Analysis of the thermal, electrical and mechanical constraints. *Journal AerospaceLab,* **5**, AL05-09

Cheng, D. K. (1989). *Field and waves electromagnetics.* (New York: Addison Wesley)

Christian, H.J., Blakeslee, R.J. and Goodman, S.J. (1992). Lightning Imaging Sensor for the Earth Observing System. *Tech. Rep. NASA* TM-4350. NASA, Washington, D. C

Christian, H. J., Blakeslee, R. J., Boccippio, D. J., Boeck, W. L., Buechler, D. E., Driscoll, K.T., Goodman, S. J., Hall, J.M., Koshak,W. J., Mach, D. M. and Stewart, M. F. (2003). Global frequency and distribution of lightning as observed from space by the Optical Transient Detector. *J. Geophys. Res.*, **108** 4005

Cooray, V. (2015). *An introduction to lightning.* (Dordrecht: Springer Science+Business Media)

D'Angola, A., Colonna, G., Gorse, C. and Capitelli, M. (2008). Thermodynamic and transport properties in equilibrium air plasmas in a wide pressure and temperature range. *Eur. Phys. J.* D, **46,** 129-50

Delalondre, C. (1990). *Modélisation aérothermodynamique d'arcs électriques à fort intensité avec prise en compte du déséquilibre thermodynamique local et du transfert thermique à la cathode*. Ph. D. thesis, Université de Rouen

Deron, C. (2003). *Rayonnement thermique des plasmas d'air et d'argon : modélisation des propriétés radiatives et étude expérimentale.* Ph. D. thesis, Ecole Centrale Paris

Djurovic, S. and Konjevic, N. (2009). On the use of non-hydrogenic spectral lines for low electron density and high pressure plasma diagnostics. *Plasma Sources Sci. Technol.*, **87,** 035011

Eichhoff, D., Kurz, A., Kozakov, R., Gött, G., Uhrlandt, D. and Schnettler, A. (2012). Study of an ablation-dominated arc in a model circuit breaker. *J. Phys. D: Appl. Phys.*, **45**, 305204

Elias, P. Q. and Castera, P. (2013). Measurement of the impulse produced by a pulsed surface discharge actuator in air. *J. Phys. D: Appl. Phys.*, **46,** 365204

Fay, A. J. and Bigand, A. (2015). Airbus lightning in service experience vs lightning zoning. *Int. Conf. on Lightning and Static Electricity,* Toulouse, France

Fisher, B., Taeuber, R. and Crouch, K. (1988). Implications of a recent lightning strike to a NASA jet trainer. *AIAA 26th Aerospace Sciences Meeting,* 88-0394, Reno, USA

Freeman, R. A. (1968) Variable-energy blast waves. *Brit. J. Appl. Phys: J. Phys.* D, **1,** 1697-710

Gagné, M. and Therriault, D. (2014). Lightning strike protection of composites. *Prog. Aerosp. Sci.*, **64**, 1-16

Genovese, K., Casaletto, L., Rayas, J. A., Flores, V. and Martinez, A. (2013). Stereo-Digital Image Correlation (DIC) measurements with a single camera using a biprism. *Optics and Lasers in Engineering*, **51**, 278-285

Gilmore, F. R. (1955). Equilibrium composition and thermodynamic properties of air to 24000 K. *Rand Corporation Research Memorandum,* Rm-1543 (Defense Documentation Center, AD-84052)

Gleizes, A., Gonzalez, J. J. and Freton, P. (2005). Thermal plasma modelling. *J. Phys. D: Appl. Phys.*, **38** R153–83

Griem, H. R. (1974). *Spectral Line Broadening by Plasmas.* (New York: Academic)

Griem, H. R. (1997). *Principles of Plasma Spectroscopy.* (Cambridge: Cambridge University Press)

Griem, H. R., Halenka, J. and Olchawa, W. (2005). Comparison of hydrogen Balmer-alpha Stark profiles measured at high electron densities with theoretical results. *J. Phys.* B*: At. Mol. Opt. Phys.*, **38,** 975-1000

Gou, J., Tang, Y., Liang, F., Zhaoa, Z., Firsich, D. and Fielding J. (2010). Carbon nanofiber paper for lightning strike protection of composite materials. *Composites: Part B,* **41**, 192-8

Gonzalez, J. J. (1992). *Modélisation d'un arc transféré de forte puissance (1 Mega-Watt).* Ph. D. thesis, Université Paul Sebatier.

Gurevich, A., Zybin, K. P. and Roussel-Dupre, R. (1999). Lightning initiation by simultaneous effect of runaway breakdown and cosmic ray showers. *Phys. Lett.*, **254**, 79-87

Hargather, M. J. and Settles, G. S. (2010) Natural-background-oriented schlieren imaging. *Experiments in Fluids*, **48**, 59-68

Hsu, K. C., Etemadi, K. and Pfender, E. (1983). Study of the free-burning high intensity argon arc. *J. Appl. Phys.*, **54**, 1293

Jones, Ch., Rowse, D. and Odam, G. (2001) Probabilities of catastrophe in lightning hazard assessments. *Int. Conf. on Lightning and Static Electricity*, 01-2877, Seattle, USA

Kahhali, N., Rivière, Ph., Perrin, M.-Y., Gonnet, J.P. and Soufiani, A. (2010). Effects of radiative transfer modelling on the dynamics of a propagating electrical discharge. *J. Phys. D: Appl. Phys.*, **43**, 425204

Karch, C., Honke, R., Steinwandel, J. and Dittrich, K. W. (2015). Contributions of lightning current pulses to mechanical damage of CFRP structures. *Int. Conf. on Lightning and Static Electricity*, Toulouse, France

Kasemir, H.W. (1960). A contribution to the electrostatic theory of a lightning discharge. *J. Geophys. Res.*, **65** 1873–78

Kepple, P. and Griem, H. R. (1968). Improved Stark profile calculations for the hydrogen lines H_α, H_β, H_γ, and H_δ. *Phys. Rev.*, **173,** 317-25

Konjevic N, Lesage A, Fuhr J R and Wiese W L 2002 Experimental Stark widths and shifts for spectral lines of neutral and ionized atoms *J. Phys. Chem. Ref. Data*, **31,** 819–928

Kramida, A., Ralchenko, Y., Reader, J. and NIST ASD Team (2015). *NIST Atomic Spectra Database* (ver. 5.3) Available: http://physics.nist.gov/asd [2016, April 5] [online] (Gaithersburg: National Institute of Standards and Technology)

Krider, E. P. (1973). Lightning spectroscopy. *Nucl. Instr. Meth.*, **110**, 411-9

Lago, F. (2014). Lightning in aeronautics. *J. Phys.: Conf. Ser.*, **550**, 012001

Lago, F. (2004). *Modélisation de l'interaction entre un arc électrique et une surface: application au foudroiement d'un aéronef.* Ph. D. thesis, Université Paul Sebatier

Lalande, Ph., Bondiou-Clergerie, A. and Laroche, P. (1999) Analysis of available in-flight measurements of lightning strikes to aircraft. *Int. Conf. on Lightning and Static Electricity*, Toulouse, France

Larigaldie, S. (1987). Mechanisms of spark propagation in ambient air at the surface of a charged dielectric: II. Theoretical modelling. *J. Appl. Phys.*, **61,** 102-08

Laroche, P., Blanchet, P., Delannoy, A. and Issac, F. (2012). Experimental studies of lightning strikes to aircraft. *J. Aerosp. Lab*, **5**, AL05-6

Larsson, A., Lalande, Ph., Bondiou-Clergerie, A. and Delannoy, A. (2000a) The lightning swept stroke along an aircraft in flight. Part I: thermodynamic and electric properties of lightning arc channels. *J. Phys. D: Appl. Phys.,* **33**, 1866-75

Larsson, A. (2002) The interaction between a lightning flash and an aircraft in flight. *C. R. Physique*, **3,** 1423-44

Le Besnerais, G. and Champagnat, F. (2005). Dense Optical Flow by Iterative Local Window Registration. *IEEE International Conference on Image Processing*, **I**, 137-140

Le Besnerais, G., Champagnat, F., Plyer, A., Fezzani, R., Leclaire, B. and Le Sant, Y. (2009) Advanced processing methods for for image-based displacement field measurement. *J. Aerosp. Lab*, **1**, AL01-04

Lin, S. C. (1954). Cylindrical shock waves produced by instantaneous energy release. *J. Appl. Phys.*, **25**, 54

Little, P. F. (1978). Transmission line representation of a lightning return stroke. *J. Phys. D: Appl. Phys.*, **11**, 1893-910

Ma, S., Gao, H., Zheng, S. and Wu, L. (2011). Spectroscopic measurement of temperatures in pulsed TIG welding arcs. *J. Phys. D: Appl. Phys.*, **44**, 405202

Macgorman, D. R. and Rust, W. D. (1998). *The Electrical Nature of Storms*. (New York: Oxford Univ. Press) pp. 118–62

Malan, D. J. and Schonland, B. F. J. (1951). The Distribution of Electricity in Thunderclouds. *Proc. Roy. Soc. London*, A 209

Marcuse, D. (1979). Refractive index determination by the focusing method. *Applied Optics*, **18,** 9-13

Marshall, T. C., Mccarthy, M. and Rust, W. (1995). Electric field magnitudes and lightning initiation in thunderstorms. *J. Geophys. Res.*, **100**, 7097-103

Marshall, T. C., Rust, W. D., Winn, W. P. and Gilbert, K. E. (1989). Electrical structure in two thunderstorm anvil clouds. *J. Geophys. Res.*, **94**, 2171-81

Mazur, V. and Ruhnke, L. H. (1998). Model of electric charges in thunderstorms and associated lightning. *J. Geophys. Res.*, **103**, 299–308

Mazur, V. (2002). Physical processes during development of lightning flashes. *C. R. Physiques*, **3**, 1393-409

McKeeman Brown, A.(2005) Evaluating lightning surface protection systems for aerospace composites. *Int. Conf. on Lightning and Static Electricity*, Seattle, USA

Milosavljević, V. and Djeniže, S. (1998). Measured Stark widths and shifts of NII, NIII and NIV spectral lines. *Astron. Astrophys. Suppl. Ser.*, **128**, 197-201

Moreau, J. P., Alliot, J. C. and Mazur, V. (1992). Aircraft lightning initiation and interception from in-situ electric measurements and fast video observations. *J. Geophys. Res.*, **97**, 15903–12

Morgan, D., Hardwick, C. J., Haigh, S. J. and Meakins, A. J. (2012) The interaction of lightning with aircraft and the challenges of lightning testing. *J. Aerosp. Lab*, **5**, AL05-11

Mu, Y., Yuan, P., Wang, X. and Dong, C. (2016). Temperature distribution and evolution characteristic in lightning return stroke channel. *J. Atmos. Sol. Terr. Phys.* **145** 98-105

Needham, C. E. (2010). *Blast Waves Shock: Shock Wave and High Pressure Phenomena*. (Berlin: Springer-Verlag)

Neufeld, R. B. (2015). Lightning direct effects on anisotropic materials from electro-thermal simulation. *Int. Conf. on Lightning and Static Electricity*, Toulouse, France

Orville, R. E. (1966a) High-speed, time-resolved spectroscopic study of the lightning return stroke: part II. A quantitative analysis *J. Atmos. Sci.*, **25** 839-51

Orville, R. E. (1966b) High-speed, time-resolved spectroscopic study of the lightning return stroke: part I. A qualitative analysis *J. Atmos. Sci.*, **25** 827-38

Parmantier, J. P., Issac, F. and Gobin, V. (2012). Indirect Effects of Lightning on Aircraft and Rotorcraft *J. Aerosp. Lab*, **5**, AL05-10

Paxton, A. H., Gardner, R. L. and Baker, L. (1986). Lightning return stroke. A numerical calculation of the optical radiation. *Physics of fluids*, **29**, 2736

Peyrou, B. (2012). *Modélisation MHD d'un arc de Foudroiement d'aéronef*. Ph. D. thesis, Université de Rouen

Peyrou, B., Peyrou, B., Chemartin, L., Lalande, Ph., Cheron, B., Rivière, Ph., Perrin, M.-Y. and Soufiani, A. (2012). Radiative properties and radiative transfer in high pressure thermal air plasmas. *J. Phys. D: Appl. Phys.*, **45**, 1455203

Plooster, M. N. (1970). Shock waves from line sources. Numerical solutions and experimental measurements. *Physics of fluids* **13**, 2665

Plooster, M. N. (1971). Numerical model of the return stroke of the lightning discharge. *Physics of Fluids* **14**, 2124

Price, G. H. and Pierce, E. T. (1977). The modeling of channel current in the lightning return stroke. *Radio Science*, **12**, 381-8

Prueitt, M. L. (1963). The excitation temperature of lightning. *J. Geophys. Res.*, **68**, 803-11

Punekar, G. and Kandashamy, C. (2011). Indirect Effects of Lightning Discharges. *SJEE*, **8**, 245-62

Rakov, V. A. and Uman, M. A. (2003). *Lightning: physics and effects.* (New york: Cambridge university press)

Rakov, V. A. and Uman, M. A. (1998). Review and evaluation of lightning return stroke models including some aspects of their application. *IEEE Trans. Electromagn. Compat.*, **40**, 403-26

Ratovoson, P., Valensi, F., Razafinimanana, M. and Tmenova, T. (2014). Spectroscopic study and high speed imaging of a transient arc. *J. Phys.: Conf. Ser.*, **550**, 012012

Rison, W., Krehbiel, P. R., Stock, M. G., Edens, H. E., Shao, X.-M. Thomas, R. J., Stanley M. A. and Zhang Y. (2016). Observations of narrow bipolar events reveal how lightning is initiated in thunderstorms. *Nature Communications,* **7**, 10721

Roussel, M., Tristant, F., Fustin, F., Even, A., Chazottes, A. and Lalande, P. (2015). In-service Falcon lightning strike events. *Int. Conf. on Lightning and Static Electricity*, Toulouse, France

SAE ARP 5412, Eurocae ED-105 (2005). *Aircraft Lightning Test Methods*, section 5 Review Draft, AE-2 Lightning Committee, SAE International

SAE ARP 5414, Eurocae ED-105 (2005). *Aircraft Lightning Test Methods*, section 5 Review Draft, AE-2 Lightning Committee, SAE International

SAE ARP 5416, Eurocae ED-105 (2005). *Aircraft Lightning Test Methods*, section 5 Review Draft, AE-2 Lightning Committee, SAE International

Sakurai, A. (1954). On the propagation and structure of the blast wave II. *J. Phys. Soc. Jpn.*, **9**, 256–266.

Sedov, L. I. (1959). *Similarity and Dimensional Methods in Mechanics* (London: Infosearch)

Schoene, J. (2007). *Direct and nearby lightning strike with test power distribution lines.* Ph. D. thesis, University of Florida

Settles, G. S. (2001). *Schlieren and Shadowgraph Techniques: Visualizing Phenomena in Transparent Media.* (Berlin: Springer-Verlag)

Solomon, R., Schroeder, V and Baker, M. B. (2001). Lightning initiation - conventional and runaway-breakdown hypotheses. *Q. J. R. Meteorol. Soc.*, **127**, 2683-704

Soula, S. (2012). Electrical Environment in a Storm Cloud. *J. Aerosp. Lab,* **5**, AL05-1

Sousa Martins, R., Chemartin, L., Zaepffel, C., Lalande, Ph. and Soufiani, A. (2015a). Etude expérimental des arcs de foudre simulés en laboratoire. *XII Colloque sur les arcs électriques*, Clermont-Ferrand, France

Sousa Martins, R., Chemartin, L., Zaepffel, C., Lalande, Ph. and Soufiani, A. (2015b). Experimental investigation of lightning arc using optical diagnostics. *Int. Conf. on Lightning and Static Electricity,* Toulouse, France

Sousa Martins, R., Chemartin, L., Zaepffel, C., Lalande, Ph. and Soufiani, A. (2016a). Electrical and hydrodynamic characterization of a high current pulsed arc. *J. Phys. D: Appl. Phys.*, **49**, 185204

Sousa Martins, R., Zaepffel, C., Chemartin, L., Lalande, Ph. and Soufiani, A. (2016b). Characterization of a high pulsed arc using optical emission spectroscopy. *J. Phys. D: Appl. Phys.*, **49**, 415205

Sousa Martins, R., Chemartin, L., Zaepffel, C., Lalande, Ph. and Soufiani, A. (2016c). Experimental characterization of the interaction between a high current arc and aeronautical materials. *21th Int. Conf. on Gas Discharges and their applications*, Nagoya, Japan

Stolzenburg, M. and Marshall, T. C. (2008). Charge structure and dynamics in thunderstorms. *Space Sci. Rev.*, **137**, 355-72

Stehlé, C. and Hutcheon, R. (1999). Extensive tabulations of Stark broadened hydrogen line profiles. *Astron. Astrophys. SuppL. Ser.*, **170**, 93-97

Sweers, G., Birch, B. and Gokcen, J. (2012). Lightning strikes: protection, inspection and repair. *Aero Quarterly*, **4**, QTR 04-12

Takahashi, T. (1978). Riming Electrification as a Charge Generation Mechanism in Thunderstorms. *J. Atmos. Sci.*, **35**, 1536–48

Tanaka, M., Michishita, T. and Uesugi, Y. (2005). Hydrodynamic chemical non-equilibrium model of a pulsed arc discharge in dry air at atmospheric pressure. *Plasma Sources Sci. Technol.*,**14**, 137-51

Taylor, G. I. (1950a). The formation of a blast wave by a very intense explosion. I. Theoretical discussion. *Proceedings of the Royal Society of London*, Series A, *Mathematical and Physical Sciences*, **201**, 159–174.

Tholin, F., Chemartin, L. and Lalande, Ph. (2013). Numerical investigation of the surface effects on the dwell time during the sweeping of lightning arcs. *Int. Conf. on Lightning and Static Electricity*, Seattle, USA

Tholin, F., Chemartin, L. and Lalande, Ph. (2015). Numerical investigation of the interaction of a lightning and an aeronautic skin during the pulsed arc phase. *Int. Conf. on Lightning and Static Electricity*, Toulouse, France

Thottappillil, R. (2002). Electromagnetic Pulse Environment of Cloud-to-Ground Lightning for EMC Studies. *IEEE Trans. Electromagn. Compat.*, **44**, 203-13

Timoshenko, S. (1959). *Theory of plates and shells*. (New York: McGraw-Hill)

Uman, M. A., Orville, R. E. and Salanave, L. E. (1964). The density, pressure, and particle distribution in a lightning stroke near peak temperature. *J. Atmos. Sci.* **21**, 306-10

Uman, M. A. and Orville, R. E. (1965). The opacity of lightning. *J. Geophys. Res.*, **70**, 5491-7

Uman ,M. A. (1966). Quantitative lightning spectroscopy. *IEEE spectrum,* **3,** 102-10

Uman, M. A.,Brantely, R. D., Lin, Y. T., J., Krider, E. P. and McLain, K. (1975). Correlated electric and magnetic fields from lightning return strokes. *J. Geophys. Res.,* 80, 373-4

Ventsel, E. (2001). *Thin plates and shells.* (New York: Marcel Dekker)

Vlastos, A. E. (1969). Restrike Channel Resistance of Thin Exploding Wires. *J. Appl. Phys.*, **40,** 4752-60

Vlastos, A. E. (1972). The resistance of sparks. *J. Appl. Phys.*, **43,** 1987-89

Valensi, F., Pellerin, S., Boutaghane, A., Dzierzega, K., Zielinska, S., Pellerin, N. and Briand, F. (2010). Plasma diagnostics in gas metal arc. *J. Phys. D: Appl. Phys.*, **43**, 434002

Valensi, F., Ratovoson, L., Razafinimanana, M., Masquère, M., Freton, P. and Gleizes, A. (2016). Electrode voltage fall and total voltage of a transient arc. *J. Phys. D: Appl. Phys.*, **49,** 255202

Villa, A., Malgesini, R. and Barbieri, L. (2011). A multiscale technique for the validation of a numerical code for predicting the pressure field induced by a high-power spark. *J. Phys. D: Appl. Phys.*, **44,** 165201

Vlases, G. and Jones, D. (1968). Experimental study of cylindrical magnetohydrodynamics blast waves. *Phys.Fluids*, **11**, 987-92

Weizel, W. and Rompe, R. (1947). Theorie des elektrischen Funkens. *Annalen der Physik*, **436**, 285-00

Xu, A., Lacoste, A., Rusterholtz, L., Elias, P. Q., Stancu, D. and Laux, C. (2011). Experimental study of the hydrodynamic expansion following a nanosecond repetitively pulsed discharge in air. *Appl. Phys. Lett.*, **99**, 121502

Zehar, S. and Zehetmeier, D. (2013). Optimized protection for composite helicopters on system level to minimize effects due to lightning strike. *Int. Conf. on Lightning and Static Electricity*, Seattle, USA

Zel’dovich, Y. B. and Raizer, Y. P. (2002). *Physics of Shock Waves and High-Temperature Hydrodynamic Phenomena.* (Mineola: Dover)

Zhivlyuk, Y. and Mandel’shtam, S. (1961). On the temperature of lightning and force of thunder. *J. Exp. Theor. Phys.*, **13**, 338-40

Appendix A

To calibrate the infrared thermography measurements, we measure the surface temperature with a high accuracy platinum resistance thermometer probe (PT100, 0.2 mm diameter) which is fixed at the panel surface. The IR camera is configured to observe the panel in an area that includes the PT100 probe. The temperature from the IR camera is then measured in area adjacent to the probe. The panel is heated with a heat gun (Bosch GHG-660). The data are acquired when the temperature displayed by the two diagnostics reaches a steady value. The relation between the resistance measured by the micro-ohmmeter R_T and the temperature T in Celsius is given by:

$$R_T = R_0(1 + AT + BT^2) \tag{A.1}$$

where R_0 is the resistance at 0 °C, A and B are two constants which are equal to 3.9083×10^{-3} °C^{-1} and -5.775×10^{-7} °C^{-2}, respectively. Figure A.1 shows the diagnostic setup and figure A.2 shows the measured data.

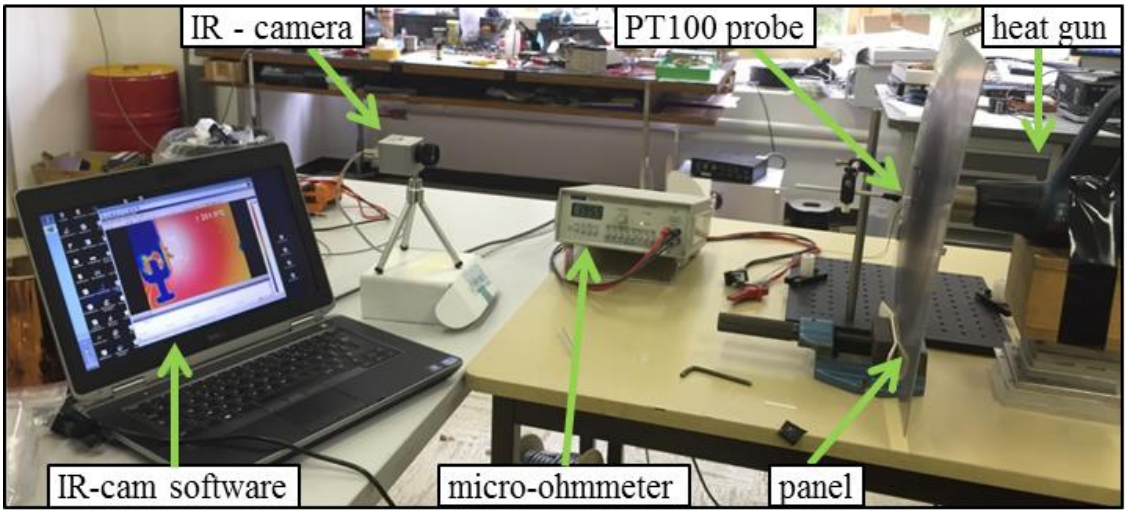

Figure VI.1. Diagnostic setup for infrared thermography measurement calibration.

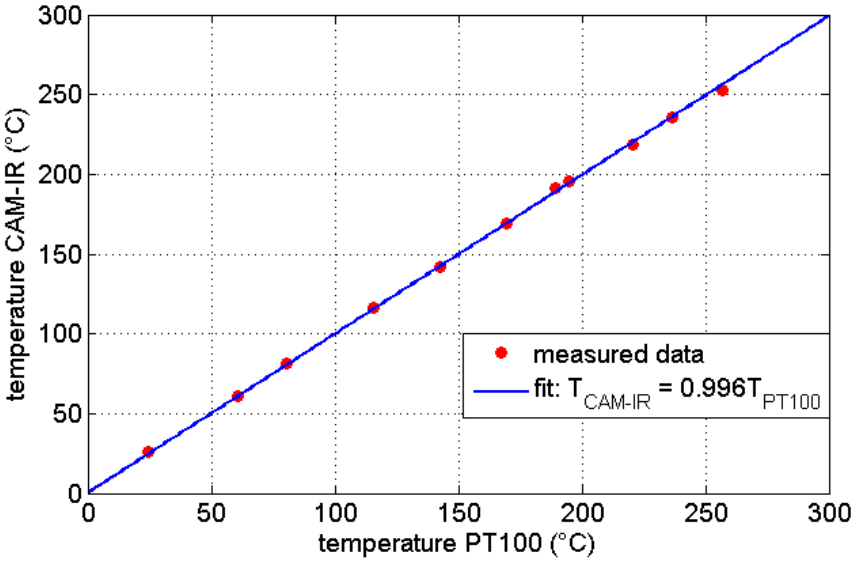

Figure VI.2. Experimental correlation curve between the temperatures measured with the PT100 probe and the IR camera.

Appendix B

Spectroscopic constants and Stark broadening parameters of 192 ionic lines of oxygen and nitrogen are used analysis for the optical emission spectroscopy done in Chapter V. Here, we present two tables with the data used for the calculation of the absorption coefficient of these transitions (Chapter V, equation (V.1)). The spectroscopic constants (central wavelength λ_{line}, Einstein emission coefficient for the transition A_{ul}, energy and degeneracy of the upper transition level E_u and g_u) are taken from the NIST database (Kramida et al. (2015)). The Stark broadening parameters w_S are taken from the experimental data compiled by Konjevic et al. (2002).

There are 113 nitrogen and 79 oxygen ionic lines in the spectral range of measurements, (431.5 nm to 585 nm). Table B.1 presents the data for N II and table B.2 for O II. The estimated accuracies for the transition probabilities are represented in the tables by *Acc.*, which represents:

- AA: ≤ 1%
- A+: ≤ 2% | A: ≤ 3%
- B+: ≤ 7% | B: ≤ 10%
- C+: ≤ 18% | C: ≤ 25%
- D+: ≤ 40% | D: ≤ 50%
- E: > 50%

For the transitions that are listed by NIST but the Stark parameters are not present in Konjevic tables, the Stark parameters is noted with a superscript "a". In these cases, we defined the w_S as the average of the parameters of the same multiplet of the transition that are listed in the Konjevic tables. There are nine cases where the multiplet is not present in the tables. In those cases, noted with a superscript "b", we defined w_S as the average of all other listed transitions. It is important to mention that it occurs for transitions with small A_{ul} (in the order of 10^6 s^{-1}) and high E_u, which leads to terms $g_u A_{ul} e^{-Eu/kT}$ negligible compared to the other studied lines.

Table B.1. Data for ionic nitrogen lines.

N°	λ_{line} (nm)	A_{ul} (s^{-1})	Acc.	E_u (eV)	g_u	Stark broadening parameters		
						w_S (Å)	N_e (10^{17} cm^{-3})	T (kK)
1	444.7030	1.12e+08	B+	23.196373	5	0.387 0.512 1.830	1.00 1.60 4.66	28 31 32.8
2	445.9937	7.99e+06	D	23.425232	1	0.56[a]	1.0	28
3	446.5529	1.59e+06	D	23.421752	3	0.56[a]	1.0	28
4	447.7682	6.44e+06	D	23.421752	3	0.56[a]	1.0	28
5	450.7560	7.39e+06	D	23.415329	5	0.56	1.0	28
6	456.4760	1.65e+06	B+	23.124489	5	0.492	1.0	28
7	460.1478	2.22e+07	B+	21.159916	5	0.354	1.0	28
8	460.7153	3.15e+07	B+	21.152682	3	0.357	1.0	28
9	461.3868	2.12e+07	B+	21.152682	3	0.294 0.422	1.0 1.6	28 31
10	462.1393	9.04e+07	B+	21.148308	1	0.314	1.0	28
11	463.0539	7.48e+07	B+	21.159916	5	0.200 0.326 0.300 0.320 0.36 0.50	0.75 1.00 1.15 1.30 1.45 2.8	30 28 33 35 38 54
12	464.3086	4.39e+07	B+	21.152682	3	0.329 0.52	1.0 2.8	28 54
13	465.4531	1.92e+06	B	21.159916	5	0.343	1.0	28
14	466.7208	2.31e+06	B	21.152682	3	0.343[a]	1.0	28
15	467.4908	8.54e+06	B	21.148308	1	0.343[a]	1.0	28
16	469.4274	1.23e+07	C+	30.368676	3	2.633	1.0	28
17	469.5899	1.29e+07	C+	30.369653	5	2.633[a]	1.0	28
18	469.7638	3.06e+06	C+	30.368676	3	2.633[a]	1.0	28
19	469.8554	3.67e+07	C+	30.368161	1	2.633[a]	1.0	28
20	470.0032	1.05e+07	C+	30.371039	7	2.633[a]	1.0	28
21	470.2503	9.15e+06	C+	30.369653	5	2.633[a]	1.0	28
22	470.4247	2.13e+07	C+	30.368676	3	2.633[a]	1.0	28
23	470.6400	6.09e+06	C+	30.372819	9	2.633[a]	1.0	28
24	470.9584	1.82e+07	C+	30.371039	7	2.633[a]	1.0	28
25	471.2065	1.46e+07	C+	30.369653	5	2.633[a]	1.0	28
26	471.8377	3.02e+07	C+	30.372819	9	2.633[a]	1.0	28

N°	λ_{line} (nm)	A_{ul} (s^{-1})	Acc.	E_u (eV)	g_u	Stark broadening parameters		
						w_S (Å)	N_e (10^{17} cm^{-3})	T (kK)
27	472.1577	7.75e+06	C+	30.371039	7	2.633[a]	1.0	28
28	477.4244	3.07e+06	B	23.242271	5	0.377	1.0	28
29	477.6224	1.03e+07	B	27.661100	3	0.354[a]	1.0	28
30	477.9722	2.49e+07	B	23.239295	3	0.427	1.0	28
31	478.1190	1.92e+06	B	23.246033	7	0.438	1.0	28
32	478.8138	2.50e+07	B	23.242271	5	0.408	1.0	28
33	479.3648	7.73e+06	B	23.239295	3	0.402	1.0	28
34	480.3287	3.17e+07	B	23.246033	7	0.372 0.418 1.36	1.00 1.60 4.66	28 31 32.8
35	481.0299	4.75e+06	B	23.242271	5	0.394	1.0	28
36	486.0167	1.87e+06	B+	23.196373	5	0.306	1.0	28
37	489.5117	3.04e+06	D	20.409133	3	0.456	1.0	28
38	498.7376	6.98e+07	B+	23.425232	1	0.498	1.0	28
39	499.1243	3.54e+07	C+	27.974241	5	0.244	1.0	28
40	499.4360	2.62e+07	C+	27.979665	7	0.244[a]	1	28
41	499.4370	7.11e+07	B+	23.421752	3	0.441	1.0	28
42	499.7224	1.96e+07	C+	27.971269	3	0.244[a]	1	28
43	500.1134	9.65e+07	A	23.124489	5	0.065 0.068 0.083	0.25 0.23 0.31	17.5 18.8 17.1
44	500.1474	1.04e+08	A	23.131853	7	0.068 0.066 0.086	0.25 0.23 0.31	17.1 17.5 18.8
45	500.2703	8.33e+06	B	20.939965	3	2.51[a]	1.0	28
46	500.5150	1.14e+08	A	23.141959	9	0.071 0.064 0.083 0353	0.071 0.064 0.083 0.353	17.1 17.5 18.8 28.0
47	500.5300	6.51e+06	C+	27.974241	5	0.32[a]	1.0	28
48	500.7328	7.43e+07	B+	23.415329	5	0.463	1.0	28
49	501.0621	2.10e+07	B	20.939965	3	2.51[a]	1.0	28
50	501.1314	5.84e+07	C+	27.971269	3	0.32[a]	1.0	28
51	501.2036	5.19e+07	C+	27.979665	7	0.32[a]	1.0	28
52	501.6381	1.59e+07	A	23.124489	5	0.424	1.0	28
53	502.2074	1.09e+06	C+	27.657033	3	0.4[b]	1.0	28

N°	λ_{line} (nm)	A_{ul} (s^{-1})	Acc.	E_u (eV)	g_u	Stark broadening parameters		
						w_S (Å)	N_e (10^{17} cm^{-3})	T (kK)
54	502.3053	3.61e+07	C+	27.974241	5	0.369	1.0	28
55	502.5659	1.04e+07	A	23.131853	7	0.439	1.0	28
56	502.8781	3.27e+06	C+	27.657033	3	0.4[b]	1.0	28
57	504.5099	3.37e+07	B	20.939965	3	0.380 0.452	1.0 1.6	28 31
58	504.6538	5.39e+06	C+	27.657033	3	0.4[b]	1.0	28
59	507.3592	2.43e+06	B	20.939965	3	0.3	1.0	28
60	510.4445	1.01e+07	C	24.531351	3	0.41	1.0	28
61	516.8050	3.06e+07	C+	30.369653	5	0.466[a]	1.0	28
62	517.0156	6.54e+07	C+	30.368676	3	0.466[a]	1.0	28
63	517.1266	8.71e+07	C+	30.368161	1	0.466[a]	1.0	28
64	517.1469	5.81e+07	C+	30.371039	7	0.466[a]	1.0	28
65	517.2344	6.01e+07	C+	30.126518	5	0.466[a]	1.0	28
66	517.2973	5.01e+07	C+	30.124336	3	0.466[a]	1.0	28
67	517.3385	7.36e+07	C+	30.129743	7	0.466[a]	1.0	28
68	517.4462	5.07e+07	C+	30.369653	5	0.466[a]	1.0	28
69	517.5890	8.93e+07	C+	30.133933	9	0.466[a]	1.0	28
70	517.6573	2.17e+07	C+	30.368676	3	0.466[a]	1.0	28
71	517.7058	5.00e+07	C+	30.124336	3	0.466[a]	1.0	28
72	517.9344	8.67e+07	C+	30.372819	9	0.466[a]	1.0	28
73	517.9521	1.07e+08	C+	30.138939	11	0.466[a]	1.0	28
74	518.0358	4.28e+07	C+	30.126518	5	0.466[a]	1.0	28
75	518.3200	2.88e+07	C+	30.371039	7	0.482	1.0	28
76	518.4961	3.20e+07	C+	30.129743	7	0.489	1.0	28
77	518.5087	7.11e+06	C+	30.124336	3	0.466[a]	1.0	28
78	518.6206	5.76e+06	C+	30.369653	5	0.466[a]	1.0	28
79	519.0380	1.77e+07	C+	30.133933	9	0.438	1.0	28
80	519.1965	4.25e+06	C+	30.126518	5	0.466[a]	1.0	28
81	519.9501	1.51e+06	C+	30.129743	7	0.466[a]	1.0	28
82	531.3424	1.41e+07	C+	30.304034	3	0.444	1.0	28
83	532.0202	4.20e+07	C+	30.304034	3	0.444[a]	1.0	28
84	532.0958	2.52e+07	C+	30.300731	5	0.444[a]	1.0	28
85	532.7756	4.65e+06	C+	30.300731	5	0.444[a]	1.0	28

N°	λ_{line} (nm)	A_{ul} (s^{-1})	Acc.	E_u (eV)	g_u	Stark broadening parameters		
						w_S (Å)	N_e (10^{17} cm^{-3})	T (kK)
86	533.8729	1.85e+07	C+	30.295949	7	0.444[a]	1.0	28
87	534.0207	2.59e+07	C+	30.300731	5	0.513	1.0	28
88	535.1232	3.67e+07	C+	30.295949	7	0.534	1.0	28
89	545.2070	9.82e+06	B+	23.421752	3	0.481	1.0	28
90	545.4215	3.70e+07	B+	23.425232	1	0.487	1.0	28
91	546.2581	1.11e+07	B+	23.421752	3	0.498	1.0	28
92	547.5287	4.66e+06	B	25.460177	5	1.163	1.0	28
93	547.8086	5.22e+06	B+	23.415329	5	0.572	1.0	28
94	548.0050	1.44e+07	B+	23.421752	3	0.582	1.0	28
95	549.5655	2.66e+07	B+	23.415329	5	0.553	1.0	28
96	552.6234	2.13e+07	C+	27.733833	5	0.464	1.0	28
97	553.0242	4.04e+07	C+	27.739182	7	0.409	1.0	28
98	553.5347	6.04e+07	C+	27.745867	9	0.444[a]	1.0	28
99	553.5383	4.53e+07	C+	27.730126	3	0.433	1.0	28
100	554.0061	6.03e+07	C+	27.728235	1	0.41	1.0	28
101	554.3471	3.51e+07	C+	27.733833	5	0.41	1.0	28
102	555.1922	2.00e+07	C+	27.739182	7	0.404	1.0	28
103	555.2677	1.50e+07	C+	27.730126	3	0.288	1.0	28
104	556.5255	3.97e+06	C+	27.733833	5	0.444[a]	1.0	28
105	563.172	1.18e+07	B	27.661100	3	0.4[b]	1.0	28
106	566.663	3.45e+07	A	20.653591	5	0.425 0.648 0.750	1.0 1.6 2.8	28 31 54
107	567.602	2.80e+07	A	20.646058	3	0.094 0.120 0.134 0.452 0.648 0.68	0.23 0.31 0.31 1.0 1.6 2.8	17.5 18.8 16.3 28.0 31.0 54.0
108	567.956	4.96e+07	A	20.665517	7	0.077 0.099 0.120 0.430 0.688 0.760	0.17 0.23 0.31 1.0 1.6 2.8	17.0 17.5 18.8 28.0 31.0 54.0

N°	λ_{line} (nm)	A_{ul} (s^{-1})	Acc.	E_u (eV)	g_u	Stark broadening parameters		
						w_S (Å)	N_e (10^{17} cm^{-3})	T (kK)
109	568.621	1.78e+07	A	20.646058	3	0.475 0.606 0.65	1.0 1.6 2.8	28 31 54
110	571.077	1.17e+07	A	20.653591	5	0.455	1.0	28
111	573.066	1.26e+06	A	20.646058	3	0.601	1.0	28
112	574.730	3.27e+06	B+	20.653591	5	0.444[a]	1.0	28
113	576.745	2.39e+06	B+	20.646058	3	0.444[a]	1.0	28

Table B.2. Data for ionic oxygen lines

N°	λ_{line} (nm)	A_{ul} (s^{-1})	Acc.	E_u (eV)	g_u	Stark broadening parameters		
						w_S (Å)	N_e (10^{17} cm^{-3})	T (kK)
1	431.7139	3.68e+07	B	25.8373469	4	0.256	1	40
2	431.9630	2.48e+07	B	25.8487465	6	0.261	1	40
3	431.9866	5.62e+07	D	31.693188	2	0.208	1	40
4	432.5761	1.42e+07	B	25.8316245	2	0.258[a]	1	40
5	432.7460	6.76e+07	D	31.374055	6	0.382	1	40
6	432.7849	7.24e+06	D	31.373797	4	0.382[a]	1	40
7	432.8591	1.12e+08	D	31.693188	2	0.253[a]	0.81	60
8	433.1466	4.82e+06	D	31.374055	6	0.382[a]	1	40
9	433.1857	6.50e+07	D	31.373797	4	0.382[a]	1	40
10	433.6859	1.53e+07	B	25.8373469	4	0.202	1	40
11	434.5560	7.95e+07	B	25.8316245	2	0.259	1	40
12	434.7217	1.19e+07	B+	28.512452	4	0.311	1	40
13	434.7413	9.32e+07	B+	28.512452	4	0.311[a]	1	40
14	434.9426	6.75e+07	B	25.8487465	6	0.253	1	40
15	435.1260	9.89e+07	B+	28.509803	6	0.225	1	40
16	435.1457	5.82e+06	B	28.509803	6	0.225	1	40
17	435.9395	1.44e+06	C+	29.0686696	6	0.328[a]	0.81	60
18	436.6895	3.92e+07	B	25.8373469	4	0.248	1	40
19	436.9272	3.57e+07	B	29.0622427	4	0.328[a]	0.81	60

N°	λ_{line} (nm)	A_{ul} (s^{-1})	Acc.	E_u (eV)	g_u	Stark broadening parameters		
						w_S (Å)	N_e (10^{17} cm^{-3})	T (kK)
20	438.4446	2.29e+06	D	31.650925	2	0.252	0.81	60
21	439.3435	1.14e+06	E	31.650925	2	0.254	0.81	60
22	439.5935	3.91e+07	B	29.0686696	6	0.328[a]	0.81	60
23	440.5978	4.30e+06	B	29.0622427	4	0.328[a]	0.81	60
24	441.4456	2.81e+06	D	31.637492	4	0.253[a]	0.81	60
25	441.4899	8.47e+07	B	26.2490332	6	0.087 0.113 0.133 0.110 0.125 0.135	0.31 0.41 0.46 0.39 0.44 0.47	18.8 19.1 19.5 19.5 19.8 19.9
26	441.6975	7.16e+07	B	26.2253999	4	0.135 0.086 0.121 0.130 0.109 0.124 0.132	0.47 0.31 0.41 0.46 0.39 0.44 0.47	19.9 18.8 19.1 19.5 19.5 19.5 19.8
27	444.3010	5.05e+07	D	31.147904	6	0.343[a]	1	40
28	444.3523	1.89e+06	D	31.147582	8	0.343[a]	1	40
29	444.7676	2.52e+06	D	31.147904	6	0.343[a]	1	40
30	444.8191	5.10e+07	D	31.147582	8	0.343	1	40
31	445.2378	1.37e+07	B	26.2253999	4	0.135 0.086 0.121 0.130 0.109 0.124 0.132	0.47 0.31 0.41 0.46 0.39 0.44 0.47	19.9 18.8 19.1 19.5 19.5 19.5 19.8
32	446.6235	9.00e+07	C+	31.367182	4	0.284[a]	0.81	60
33	446.7465	9.00e+07	C+	31.366419	2	0.284[a]	0.81	60
34	455.773	2.54e+07	D	34.08673	6	0.28[b]	0.81	60
35	455.894	2.12e+07	D	34.08524	4	0.28[b]	0.81	60
36	456.022	4.23e+06	D	34.08524	4	0.28[b]	0.81	60
37	459.0974	8.85e+07	B+	28.361069	8	0.223	1	40
38	459.5957	4.87e+06	B	28.358142	6	0.38	2.8	54

N°	λ_{line} (nm)	A_{ul} (s^{-1})	Acc.	E_u (eV)	g_u	Stark broadening parameters		
						w_S (Å)	N_e (10^{17} cm^{-3})	T (kK)
39	459.6177	8.34e+07	B+	28.358142	6	0.272 0.380	1.0 2.8	40 54
40	463.88558	3.61e+07	B	25.6382317	4	0.22 0.64	1.0 2.8	40 54
41	464.18103	5.85e+07	B	25.6495861	6	0.223 0.620	1.0 2.8	40 54
42	464.91347	7.84e+07	B	25.6650366	8	0.209	1	40
43	465.08384	6.70e+07	B	25.6313476	2	0.225	1	40
44	466.16324	4.04e+07	B	25.6382317	4	0.214[a]	1	40
45	467.37331	1.24e+07	B	25.6313476	2	0.214[a]	1	40
46	467.62350	2.05e+07	B	25.6495861	6	0.214[a]	1	40
47	469.0888	1.86e+07	D	31.466247	4	0.241[a]	0.81	60
48	469.1419	7.43e+07	D	31.465948	2	0.241[a]	0.81	60
49	469.63528	3.15e+06	B	25.6382317	4	0.214[a]	1	40
50	469.8437	6.59e+06	D	31.147904	6	0.343[a]	1	40
51	469.9011	9.88e+07	D	31.147582	8	0.343[a]	1	40
52	469.9218	9.36e+07	B	28.8630622	6	0.24[a]	0.81	60
53	470.1179	9.23e+07	C	31.466247	4	0.241	0.81	60
54	470.1712	3.69e+07	D	31.465948	2	0.241[a]	0.81	60
55	470.3161	9.20e+07	D	31.147904	6	0.343[a]	1	40
56	470.5346	1.13e+08	B	28.8832607	8	0.115 0.170 0.195 0.146 0.174 0.189 0.240	0.31 0.41 0.46 0.39 0.44 0.47 0.7	18.8 19.1 19.5 19.5 19.8 19.9 60.0
57	471.0009	2.98e+07	C	28.8570197	6	0.24	0.81	60
58	474.1704	5.07e+06	C+	28.8630622	6	0.24[a]	0.81	60
59	475.1278	6.39e+06	C	28.8577951	8	0.24[a]	0.81	60
60	475.2691	1.45e+06	C	28.8570197	6	0.24[a]	0.81	60
61	484.4919	1.02e+06	D	28.8630622	6	0.24[a]	0.81	60
62	485.6389	5.58e+06	C	28.8570197	6	0.24[a]	0.81	60
63	485.6762	1.00e+07	C	28.8568237	4	0.24[a]	0.81	60

N°	λ_{line} (nm)	A_{ul} (s^{-1})	Acc.	E_u (eV)	g_u	Stark broadening parameters		
						w_S (Å)	N_e (10^{17} cm^{-3})	T (kK)
64	486.0965	4.70e+07	C	31.373797	4	0.284	0.81	60
65	486.4878	8.07e+06	C	28.8525662	2	0.24[a]	0.81	60
66	487.1523	5.60e+07	C	31.374055	6	0.284	0.81	60
67	487.2017	9.34e+06	D	31.373797	4	0.284[a]	0.81	60
68	489.0856	5.10e+07	C+	28.8390333	2	0.94	2.8	60
69	490.6830	4.78e+07	C+	28.8307830	4	0.94	2.8	60
70	492.4529	5.43e+07	C+	28.8217043	6	0.232	0.81	60
71	494.1072	6.04e+07	B	29.0622427	4	0.328[a]	0.81	60
72	494.3005	7.88e+07	B	29.0686696	6	0.328[a]	0.81	60
73	495.5707	1.81e+07	B	29.0622427	4	0.328	0.81	60
74	515.9941	3.12e+07	B	28.955839	2	0.362[a]	0.81	60
75	517.5903	1.46e+07	B	28.955839	2	0.362[a]	0.81	60
76	519.0498	1.18e+07	B	28.941697	4	0.362[a]	0.81	60
77	520.6651	3.33e+07	B	28.941697	4	0.362	0.81	60
78	558.3217	2.17e+06	D	30.811970	4	0.28[b]	0.81	60
79	561.1072	2.14e+06	D	30.800949	2	0.28[b]	0.81	60

ÉCOLE DOCTORALE
Sciences mécaniques et énergétiques, matériaux et géosciences (SMEMAG)

Titre : Étude expérimentale et théorique d'un arc de foudre et son interaction avec un matériau aéronautique

Mots clés : Foudre, arc électrique, diagnostics optiques, plasma, pied d'arc, matériaux aéronautiques.

Résumé : Aujourd'hui, l'étude des effets directs de la foudre sur les structures aéronautiques pourrait s'appuyer, au moins en partie, sur des outils de simulation. Néanmoins, le manque de données expérimentales sur la phase d'arc impulsionnelle ne permet pas de justifier le caractère prédictif des outils de simulation.
L'objectif de cette thèse est de réaliser une base de données expérimentale en s'appuyant sur la caractérisation des arcs de foudre dans des situations standardisées. Ces données peuvent être utilisées à la fois pour la compréhension des phénomènes observés lors des essais, mais surtout comme référence comparable aux outils de simulation.
Dans un premier temps, on s'intéresse à la colonne d'arc libre dans l'air, hors interaction avec les électrodes. Par ailleurs, les profils spatio-temporels de température et de pression sont évalués par spectroscopie d'émission. On montre ainsi que, pour un arc de 100 kA, la température maximale atteint 37400 K sur l'axe de la colonne à 2 µs après l'amorçage, avec une pression de l'ordre de 45 bars.
Dans un second temps, on s'intéresse à l'interaction de l'arc foudre avec des matériaux aéronautiques. La dynamique du pied d'arc ainsi que les caractéristiques de l'onde de choc sont analysées sur différents matériaux aéronautiques tels que l'aluminium ou des composites à fibres de carbone. Les contraintes thermomécaniques subies par le matériau sont étudiées par thermographie infrarouge, et par des mesures de déflection rapide au centre du matériau, conduisant à une évaluation de la pression exercée par l'arc au point d'impact.

Title: Experimental and theoretical studies of lightning arcs and their interaction with aeronautical materials

Keywords: Lightning, electric arc, optical diagnostics, plasma, arc roots, aeronautical materials.

Abstract: Nowadays, the study of the direct effects of lightning on aeronautical structures could be based, at least in part, on simulation tools. Nevertheless, the lack of experimental data on the transient phase of the lightning arc does not allow us to justify the predictive nature of the simulation tools. The objective of this thesis is to produce an experimental database based on the characterization of lightning arcs in standardized situations. These data can be used both for the understanding of the phenomena observed during the tests, but especially as a reference comparable to the simulation tools.
First, we are interested in the free arc column in air, without interaction with the electrodes. Furthermore, time- and space-resolved profiles of temperature and pressure are evaluated by emission spectroscopy. For a 100 kA arc, it is shown that the temperature reaches 37400 K in the arc axis at 2 µs after arc ignition, with a corresponding pressure of 45 bar.
Second, we are interested in the interaction of the lightning arc with aeronautical materials. The dynamics of the arc roots and the characteristics of the shock wave are analyzed for different aeronautical materials such as aluminum or carbon fiber composites. The thermo-mechanical constraints applied on the material are studied by infrared thermography and by rapid deflection measurements at the center of panel, leading to an evaluation of the pressure exercised by the arc at the attachment point.

Université Paris-Saclay
Espace Technologique / Immeuble Discovery
Route de l'Orme aux Merisiers RD 128 / 91190 Saint-Aubin, France